PUB-5380

The Electromagnetic Calorimeter for the Solenoidal Tracker At RHIC

A Conceptual Design Report

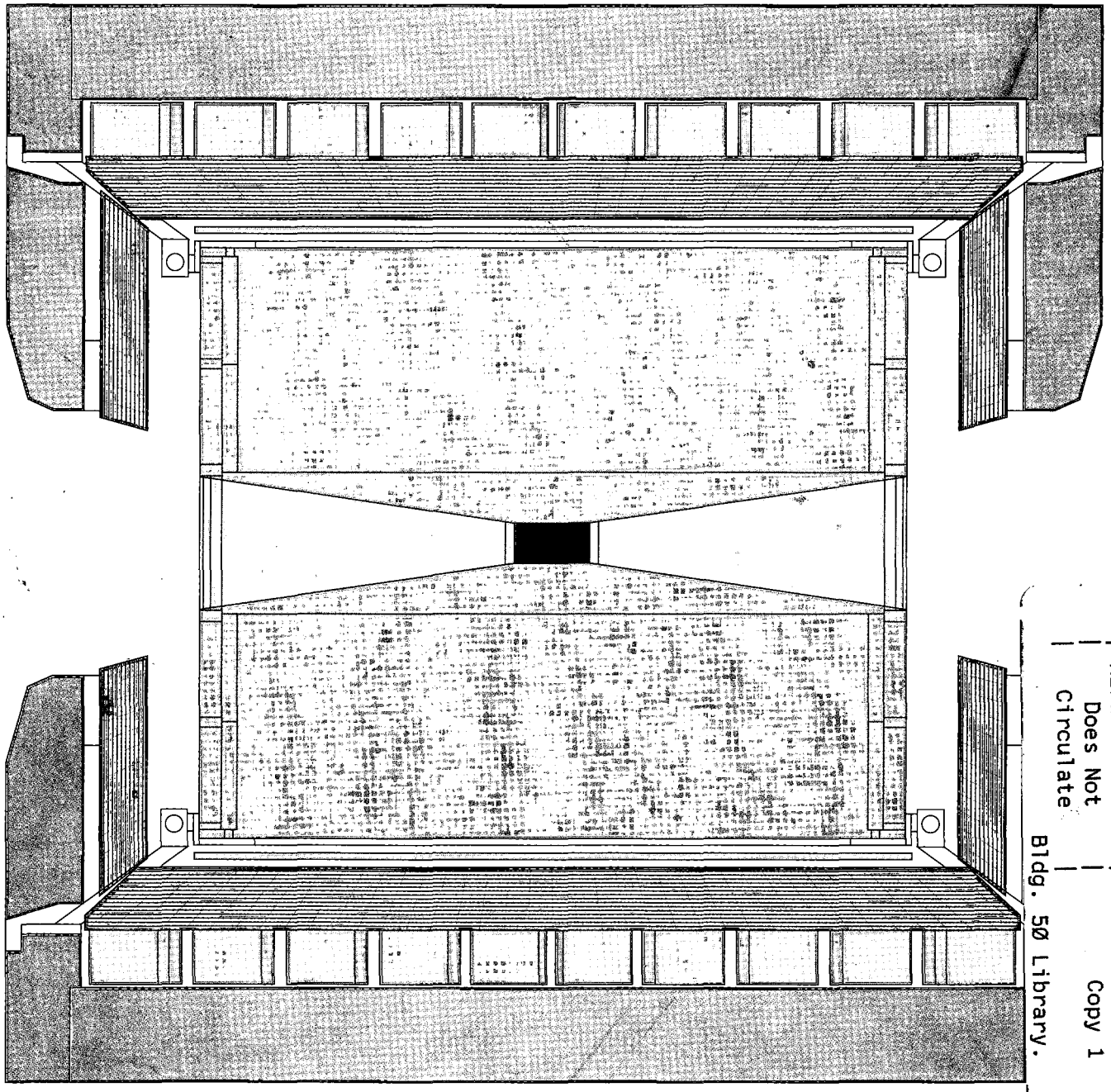

DISCLAIMER

PUB-5380

The Electromagnetic Calorimeter for the Solenoidal Tracker At RHIC

A Conceptual Design Report

September 22, 1993

The STAR EMC Collaboration

This work was supported in part by the Director, Office of Energy Research, Office of High Energy and Nuclear Physics, Division of Nuclear Physics and by the Office of Basic Energy Sciences, Division of Nuclear Sciences, of the U.S. Department of Energy under Contract Nos. DE-AC03-76SF00098, DE-FG03-88ER40424, DE-FG02-88ER40413, W-31-109-ENG-38, DE-FG05-92ER40717, and DE-FG03-93ER40772

The Electromagnetic Calorimeter for the Solenoidal Tracker At RHIC

A Conceptual Design Report

M.E. Beddo, E. Bielick, J. W. Dawson, T. Fornek, D.P. Grosnick, V.J. Guarino, W.N. Haberichter, D.A. Hill, N. Hill, T. Kasprzyk, T. Kicmal, D.X. Lopiano, J. Nasiatka, E. Petereit, H.M. Spinka, D.G. Underwood, and **A. Yokosawa**
Argonne National Laboratory, Argonne, Illinois 60439, U.S.A.

J.B. Carroll, V. Ghazikhanian, T. Hallman, **G.J. Igo**, S. Trentalange, and C. Whitten, Jr.
University of California, Los Angeles, California 90024, U.S.A.

W. Christie, **L. Madansky**, and R. Welsh
The Johns Hopkins University, Baltimore, Maryland 21218, U.S.A.

P.A. DeYoung and G. Peasley
Hope College, Holland, Michigan 49422

W.J. Llope, A.M. Vander Molen, and **G. Westfall**
Michigan State University, East Lansing, Michigan 48824, U.S.A.

A. Aprahamian, N.N. Biswas, **U. Garg**, V.P. Kenny, and J. Piekarz
University of Notre Dame, Notre Dame, Indiana 46556, U.S.A.

S.A. Akimenko, Y.I. Arestov, N.I. Belikov, V.I. Belousov, B.V. Chujko, A.M. Davidenko, **A.A. Dereschikov**, S.V. Erin, O.A. Grachov, A.S. Konstantinov, I. Kotov, Y.A. Matulenko, A.P. Meschanin, A.I. Mysnick, S.B. Nurushev, A.I. Pavlinov, A.Y. Polyarush, A.I. Ronzhin, V.L. Rykov, V.A. Sergeev, K.E. Shestermanov, L.F. Soloviev, O.D. Tsay, A.G. Ufimtsev, and A.N. Vasiliev
Institute of High Energy Physics, Protvino, Russia

V. Baublis, V. Grushin, A. Nazarov, S. Novikov, A. Oltchak, **M. Strikanov**
Moscow Engineering, Physics Institute, Moscow, Russia 115409

D.L. Adams, S. Ahmad, **B.E. Bonner**, J.A. Buchanan, C.N. Chiou, J.M. Clement, M.D. Corcoran, T. Empl, H.E. Miettinen, G.S. Mutchler, J.B. Roberts, and J. Skeens
Rice University, Houston, Texas 77251, U.S.A.

G. Glass, S. Mordechai
University of Texas, Austin, Texas 78712, U.S.A.

T.M. Cormier
Wayne State University, Detroit, Michigan 48201, U.S.A.

CONTENTS

1.

Conceptual Design Summary

1. CONCEPTUAL DESIGN SUMMARY

1.A. Scientific Motivation

Calorimetry plays a central role in modern high energy and nuclear physics. With the advent of inexpensive integrated electronics, it has become possible to construct large devices with full solid angle coverage, sufficiently granular to allow precise measurement of both the energy and position of particles produced in high energy interactions. This ability has led directly to such important advances as the discovery of the intermediate vector boson. Presently, calorimetry plays an essential role in the search for the top quark at FNAL. In the future, it will be a key element in the search for the Higgs boson at the SSC. The indispensable utility in being able to unambiguously trace the transfer of energy from the initial state to the final state is generally understood, and every collider detector ever built has relied upon calorimetry to help provide this capability. In part, this is due to the fact that the deposition of energy through the generation of particle cascades is a statistical process, and the resolution provided by this technique therefore improves with increasing energy as $1/\sqrt{E}$. Calorimeters are sensitive to both charged and neutral particles, and the depth required to contain a shower increases slowly (logarithmically) with energy. Alternatively, for a given momentum resolution $\Delta p/p$, magnetic tracking devices must increase in size as $p^{1/2}$.

The physics goals and collision environment of the Relativistic Heavy Ion Collider (RHIC) are fundamentally different from those of other high energy colliders. The primary physics goal is to collide heavy nuclei together with sufficient energy to produce a transition from hot, dense, hadronic matter to a color deconfined, chirally symmetric plasma of quarks and gluons. This state of matter is thought to have existed early in the history of the universe. While there is a general consensus that QCD at thermodynamic equilibrium must exhibit this transition, the order of the transition, the critical energy density required to reach it, and the time necessary to attain equilibrium are unknown. High charged particle densities ($dn_{ch}/d\eta \approx 700$) are expected to result from these collisions. However, even though the total energy of the projectile particles will be on the order of 20 TeV, the average p_t of the particles produced is expected to be ~400 MeV/c. The experimental landscape at RHIC is therefore strikingly different from that of other colliders built to search for exclusive high energy final states. In this new environment, it is essential that the transfer of energy from beam rapidity to mid-rapidity be understood. The information and capabilities provided by calorimetry are vital to that understanding. In particular, the improved resolution and trigger capabilities provided by electromagnetic calorimetry afford several unique possibilities for scientific discovery when combined with the large acceptance and tracking capabilities of the Solenoidal Tracker At RHIC (STAR).

The STAR detector will search for signatures of quark-gluon plasma (QGP) formation and investigate the behavior of strongly interacting matter at high energy density. The emphasis will be the correlation of many observables on an event-by-event basis. In the absence of definitive theoretical signatures for the QGP, it is imperative that such correlations be used to identify special events and possible signatures. This requires a flexible detection system that can simultaneously measure many experimental observables.

The configuration of the STAR Phase I detector is shown in Fig. 1A-1. Momentum measurements will be made at mid-rapidity over a large pseudo-rapidity range ($|\eta| < 2$) with full azimuthal coverage ($\Delta\phi = 2\pi$). Particle identification will be performed within $|\eta| < 1$. The detection system will consist of a time projection chamber (TPC) and a silicon vertex tracker (SVT) inside a solenoidal magnet to provide tracking, momentum analysis, particle

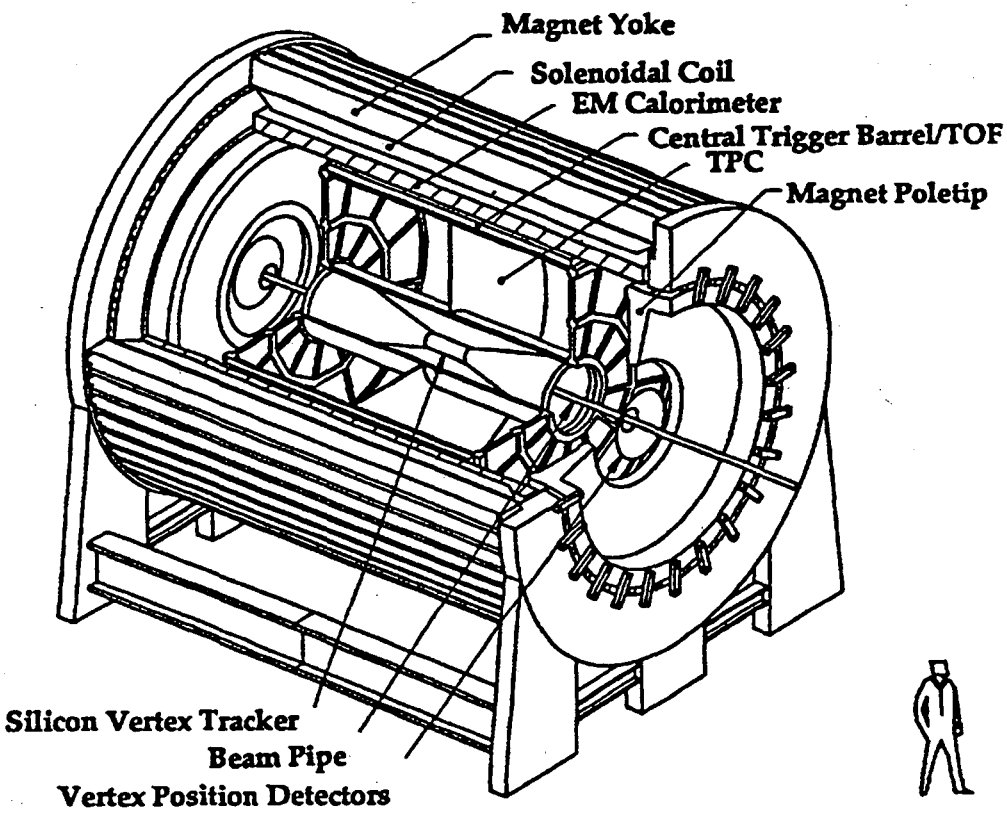

Figure 1A-1. A perspective view of the STAR experimental configuration.

identification via dE/dx, and location of primary and secondary vertices. Detectors will be installed to provide a collision geometry trigger. These include a central trigger scintillator barrel around the TPC, vertex position detectors near the beamline just outside the magnet, and calorimeters located in the region of the beam insertion magnets to selectively veto events according to the number of spectators. Multiplicity information from the charge amplification region near TPC pad planes will extend the coverage provided by the central trigger barrel to $1 \leq |\eta| \leq 2$.

An electromagnetic calorimeter (EMC), herein proposed, would be located inside the STAR magnet. The purpose of the EMC is to measure and trigger on the total (E_t) and local ($d^2E_t/d\eta d\phi$) transverse energy deposition in pp, pA, and AA collisions. As part of the STAR detector the EMC will:

- Improve the resolution for the reconstructed global transverse energy within $|\eta| \leq 2$ to ~2% for central AuAu collisions, affording a more detailed understanding of the transfer of energy from projectile rapidity to mid-rapidity and a more refined estimate of the energy density which is reached
- Measure the global neutral transverse energy with a resolution of ~2% at the trigger level, allowing a sensitive search for rare events

The improved resolution and unique trigger capabilities provided by the calorimeter extend the physics reach of STAR significantly. Specifically, the electromagnetic calorimeter proposed for STAR will:

- Provide a unique capability within STAR to conduct a sensitive search at the trigger level for events exhibiting local fluctuations in isospin abundances that have been predicted[1,2,3,4]to result from coherent pion emission if a disoriented chiral condensate is formed
- Provide a unique capability within STAR to conduct a sensitive search at the trigger level for events exhibiting an unusual correlation between energy density and entropy density at mid-rapidity which might result as a consequence of a transition to a color deconfined plasma of quarks and gluons[5,6,7]
- Provide a unique capability within STAR to trigger above ~5–7 GeV/c on high p_t π^0s, direct photons, and jets in order to study the energy loss of hard scattered partons that traverse the reaction volume and interact with the surrounding medium during the early stages of the collision[8,9]
- Provide a unique capability within STAR to study the gluon structure function in pp and pA interactions in order to correctly determine the incident gluon flux in nucleus-nucleus collisions. This is necessary, for example, in order to correctly determine the yield of open charm at mid-rapidity due to secondary parton scatters, from which the time scale necessary for thermalization may be inferred.[10,11] The contribution to the observed final state hadron spectra from mini-jet production is also strongly dependent on the degree of gluon shadowing.[12,13,14,15,16,17]

Measurement of the gluon structure function in pp interactions and gluon shadowing in pA interactions is of particular importance. One of the primary advantages of RHIC is that unlike the situation at lower energy where only a phenomenological approach was possible, firm predictions as to the evolution of the earliest stages of the collision are possible using perturbative QCD. Simulations of this stage indicate that it is gluons at low Bjorken x which equilibrate first and dominate this phase of the evolution. The manifestation of this phase may be striking, including a dramatic increase in open charm and mini-jet production resulting from semi-hard gluon scatters. Mini-jet production may account for up to 50% of the total transverse

---

[1]J.D. Bjorken, Acta Physica Polonica **B23** (1991) 635.
[2]F. Wilczek, "Chiral Dynamics Near Equilibrium or After Quenching," Proceedings of the Tenth International Conference on Ultra-Relativistic Nucleus-Nucleus Collisions, June 20–24, 1993, Borlänge, Sweden.
[3]A. Panagiotou *et al.*, Phys. Rev. **D45** (1991) 3134.
[4]S. Pratt, Phys. Lett. **B301** (1993) 159.
[5]L. Van Hove, Phys. Lett. **B118** (1982) 138.
[6]M. Kataja *et al.*, Phys. Rev. **D34** (1986) 2755.
[7]S. Nagamiya, Nucl. Phys. **A544** (1992) 5c.
[8]M. Gyulassy and M. Pluemmer, Phys. Lett. **B243** (1990) 432.
[9]X.N. Wang and M. Gyulassy, Phys. Rev. Lett. **68** (1992) 1480.
[10]B. Müller, "Physics of the Quark-Gluon Plasma," Proceedings of the NATO Advanced Study Institute on Particle Production in Highly Excited Matter, Il Ciocco, Italy, July 12–24, 1992.
[11]B. Müller and X.N. Wang, Phys. Rev. Lett. **68** (1992) 2437.
[12]K. Kajantie, P.V. Landshoff, and J. Lindfors, Phys. Rev. Lett. **59** (1987) 2527.
[13]K.J. Eskola, K. Kajantie, and J. Lindfors, Nucl. Phys. **B323** (1989) 37.
[14]P.V. Landshoff, Nucl. Phys. **A498** (1989) 217.
[15]X.N. Wang, Phys. Rev. **D43** (1991) 104.
[16]D. Appel, Phys. Rev. **D33** (1986) 717.
[17]X.N. Wang, Phys. Lett. **B248** (1990) 447.

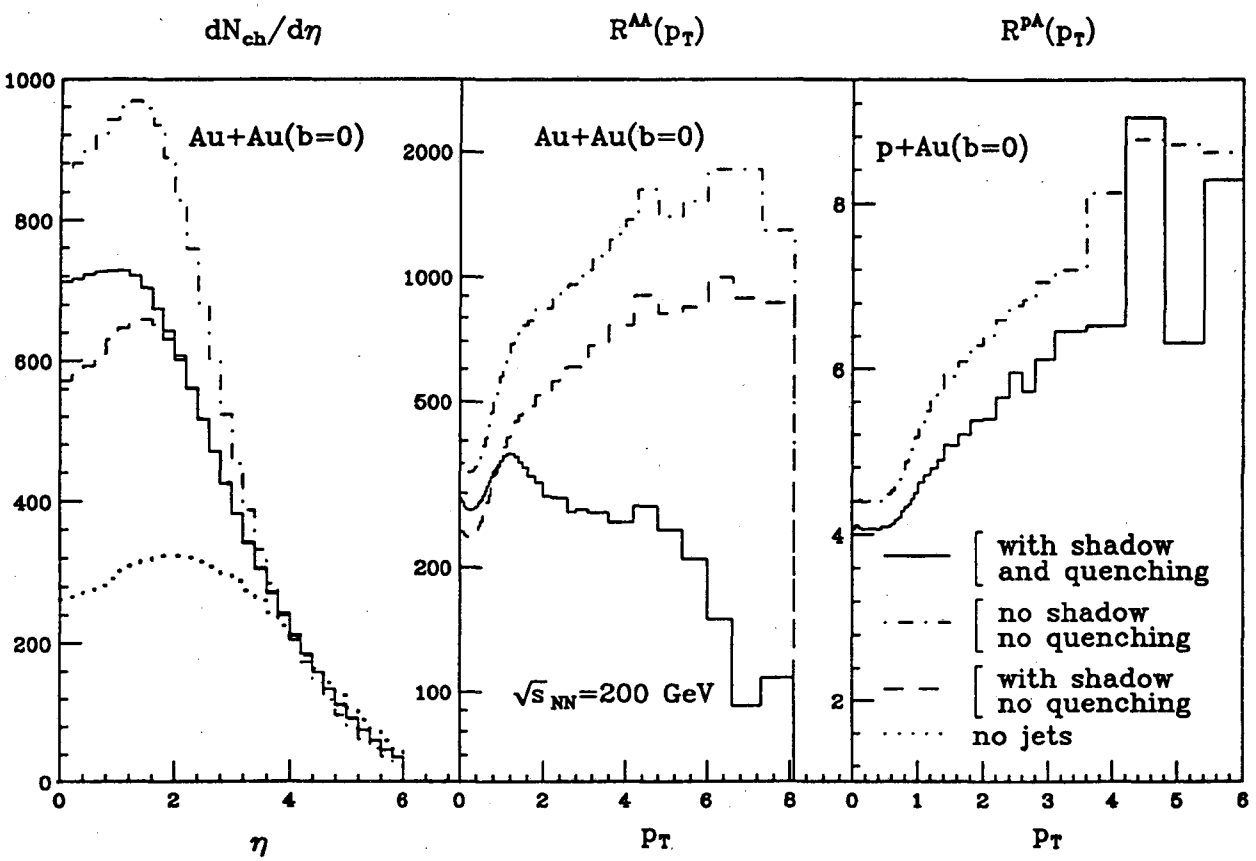

Figure 1A-2. Results from HIJING calculations on the dependence of the inclusive charged hadron spectra in central AuAu and pAu collisions on mini-jet production (dash-dotted), gluon shadowing (dashed) and jet quenching (solid) assuming that gluon shadowing is identical to that of quarks. $R^{AB}(p_t)$ is the ratio of the inclusive p_t spectrum of charged hadrons in A+B collisions to that of pp. Details may be found in Reference 18 in this chapter.

energy observed at mid-rapidity. Without measurement of the degree of gluon shadowing however, the theoretical predictions for $dn_{ch}/d\eta$ and $d^2n/dydp_\perp$, for example, are uncertain by 20–30%[18] (Fig. 1A-2). The interpretation of these data will be much less certain and the understanding seriously compromised in a first round of experiments if the incident gluon flux has not been determined. Some information on the gluon structure function in the nucleus will be provided by the NMC experiment at CERN and Fermilab experiments E665, E772, and E789. Thus far, however, the available data in the low x region of interest ($.01 < x < .05$) tend to be limited either by systematics or low statistics.

High luminosity polarized proton running at RHIC will also provide a unique opportunity for studying parton confinement. Just as the study of heavy ion interactions is put on firm theoretical ground by the energy regime at RHIC, the range of x Bjorken and Q^2 available at RHIC will afford precise perturbative QCD (pQCD) predictions of the influence of spin as a fundamental degree of freedom within the Standard Model.[19] This is in marked contrast to the situation at fixed target experiments, for example, where pQCD is not applicable,

[18]X.N. Wang and M. Gyulassy, Phys. Rev. Lett. 68 (1992) 1480.

[19]For a review of spin physics possible at RHIC, see Proceedings of the Polarized Collider Workshop, AIP Conference Proceedings No. 223, University Park, PA, 1990.

and effective models of QCD have not been able to explain the large polarization asymmetries observed experimentally. In contrast to this regime in which interpretation of experiments has often been problematic, the theory offering predictions for the outcome of single and double helicity experiments at RHIC will be robust, and these studies will contribute important information to our understanding of the confined phase of hadronic matter. This aspect of the RHIC program is complementary to the study of relativistic heavy ion collisions. While the primary goal of RHIC is to produce and study a color deconfined phase of quarks and gluons in relativistic heavy ion collisions, a detailed understanding of the evolution of this phase also requires knowledge of the confined state and how hadrons will be formed during the mixed phase.

For polarized proton running at RHIC, the electromagnetic calorimeter proposed for STAR again plays an essential role. In particular, when combined with the large acceptance and tracking capabilities of STAR , the electromagnetic calorimeter will:[20]

- Provide a capability within STAR for a direct measurement of the spin-dependent gluon structure function of the proton $\Delta G(x)$, using measurements of inclusive jet production, inclusive direct photon production, and jet-direct photon coincidences
- Provide a unique capability within STAR to study the polarization of sea quarks using asymmetries in $W^{\pm}$ production as a probe
- Provide a unique capability within STAR to conduct a deep search for small spin-dependent, parity violating asymmetries which might indicate new physics beyond the Standard Model[21]
- Provide a unique capability within STAR to measure the transverse quark structure function of the nucleon

The possibility of using the STAR EMC to study the polarization of the quark sea via Drell-Yan pair production is also being investigated.

The measurement of the spin-dependent gluon structure function of the proton is, again, of particular interest. When normalized for the range of Q^2 investigated, recent results[22] from both SLAC experiment E142, and the SMC experiment at CERN reconfirm that the proton spin can not be accounted for by the contribution from valence quarks. Other explanations in terms of the angular momentum carried by gluons, orbital angular momentum of quarks, or polarization of the strange quark sea have been postulated, but little insight beyond the need for further study will be provided by the present generation of experiments. A direct measurement of the contribution to the proton spin from gluons is clearly necessary, and with the addition of the proposed electromagnetic calorimeter, the STAR detector will be capable of providing these data. Studies of gluon fusion in which

$$gg \rightarrow \chi_{0,2} \rightarrow \gamma\psi \tag{1.1}$$

[20]For a review of spin physics possible with STAR, see "Proposal on Spin Physics Using the RHIC Polarized Collider," submitted to Brookhaven National laboratory RHIC Spin Collaboration, August 5, 1992.

[21]M.J. Tannenbaum, "Polarized Protons at RHIC," Proceedings of the Polarized Collider Workshop, AIP Conference Proceedings No. 223, University Park, PA, 1990; see also P. Taxil, "Beyond the Standard Model with Polarized Beams at Future Colliders" in the same proceedings.

[22]G. Igo, "Measurement of the Spin-Dependent Structure Function $g_1^d(x)$ of the Deuteron," Proceedings of the Tenth International Conference on Ultra-Relativistic Nucleus-Nucleus Collisions, June 20–24, 1993, Borlänge, Sweden.

in polarized pp interactions can in principle also be used to extract the spin-dependent gluon structure function.[23] Such experiments are difficult, however, due to the contribution to ψ production from other resonances and the complicated nature of the double helicity asymmetry for inclusive ψ production.

In summary, the improved resolution and unique trigger capabilities provided by the electromagnetic calorimeter proposed for STAR extend the physics reach of STAR significantly. In relativistic heavy ion interactions, the addition of this detector uniquely provides the means by which to determine the initial conditions of the collision, allowing STAR to take full advantage of the applicability of perturbative QCD in interpreting experimental results. Additionally, measurements of the hadronic cascades of hard-scattered partons may be used as a penetrating probe of the QGP. The improved resolution provided by the proposed EMC provides several unique possibilities for the discovery of rare events. In polarized proton interactions, the proposed electromagnetic calorimeter will provide STAR with the capability to study the influence of spin as a fundamental degree of freedom of QCD within the Standard Model, and to determine the contribution from gluons to the spin of the proton.

Within STAR the importance of the capabilities provided by the EMC is understood, as evidenced by the fact that the mechanical and electrical interfaces required for installation have already been engineered into the STAR baseline detector. The following sections summarize the conceptual design for the barrel and endcap calorimeter elements designed to provide these capabilities.

1.B. Detector Concept

1.B.1. The Barrel Electromagnetic Calorimeter

The proposed barrel EM calorimeter is a lead-scintillator sampling calorimeter. It is located inside the aluminum coil of the STAR solenoid and covers $|\eta| \leq 1.05$ and 2π in azimuth, thus matching the acceptance for full TPC tracking (Fig. 1B-1). At $\eta \sim 0$, the amount of material in front of the EMC is ~0.5 radiation lengths (X_o). The inner radius is 2.20 meters, and the overall length is 6.20 meters.

The conceptual design of the EMC consists of 120 modules, each subtending ~6° in $\Delta\phi$ and 1.05 in $\Delta\eta$ (Fig. 1B-2). A 20-mm-thick aluminum front plate and 30-mm non-magnetic stainless steel back plate run the full 3.1-meter length of each module. The mechanical construction consists of 20 layers of 5-mm-thick lead. The lead is potentially clad on both sides with .5 mm of non-magnetic stainless steel. Between each clad lead sheet, 6.6-mm-high aluminum spacers of I-beam cross section may be placed to ensure that the scintillator tiles placed between the layers of lead are not subject to undue stress from either the weight of the lead or from compressive forces.

Plastic scintillator tiles of 4-mm nominal thickness are placed between the layers of lead, forming pseudo-projective towers. There are 20 scintillator tiles in each sampling layer corresponding to a tower size of $\Delta\eta \sim .05$. Wavelength shifting optical fibers run along the two edges of the scintillator tiles which are not captured by the I-beam spacers. Aluminized mylar

[23] M.A. Doncheski, "Polarized pp Production of ψ at Low p_t and the Polarized Gluon Distribution Function," Proceedings of the Polarized Collider Workshop, AIP Conference Proceedings No. 223, University Park, PA, 1990.

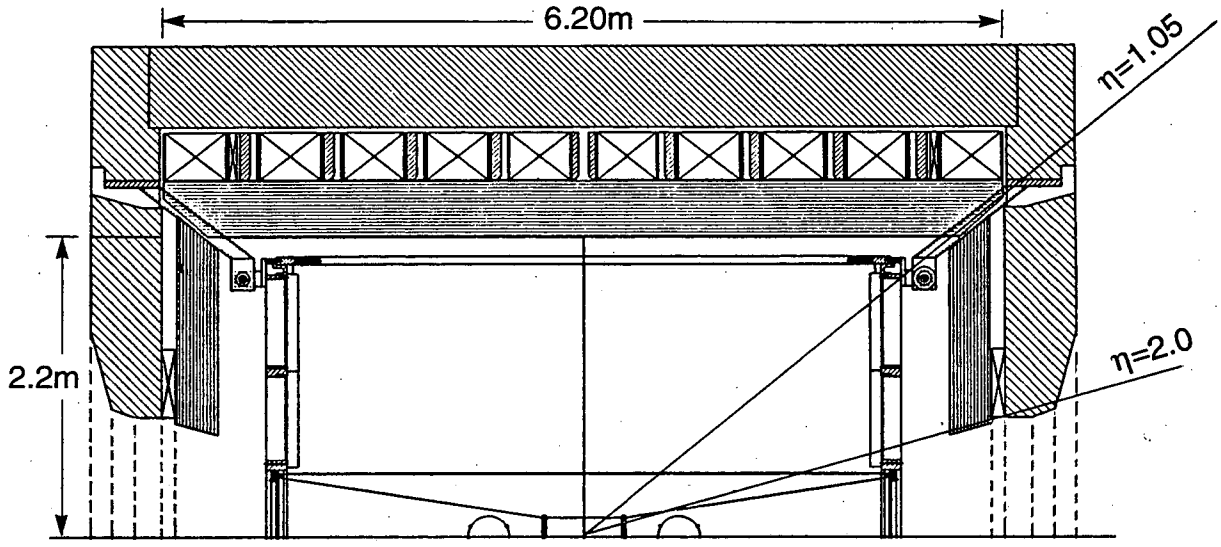

Figure 1B-1. A cross-sectional view of one-half of the STAR detector. The barrel EMC covers $|\eta| \leq 1.05$. The endcap calorimeter subtends $1.05 \leq |\eta| \leq 2.0$. The barrel EMC is supported by aluminum rings located between the coils of the conventional magnet. Fibers from the towers of the barrel pass through spaces between the aluminum rings and the coils and are subsequently routed between the iron flux return bars to the exterior of the magnet.

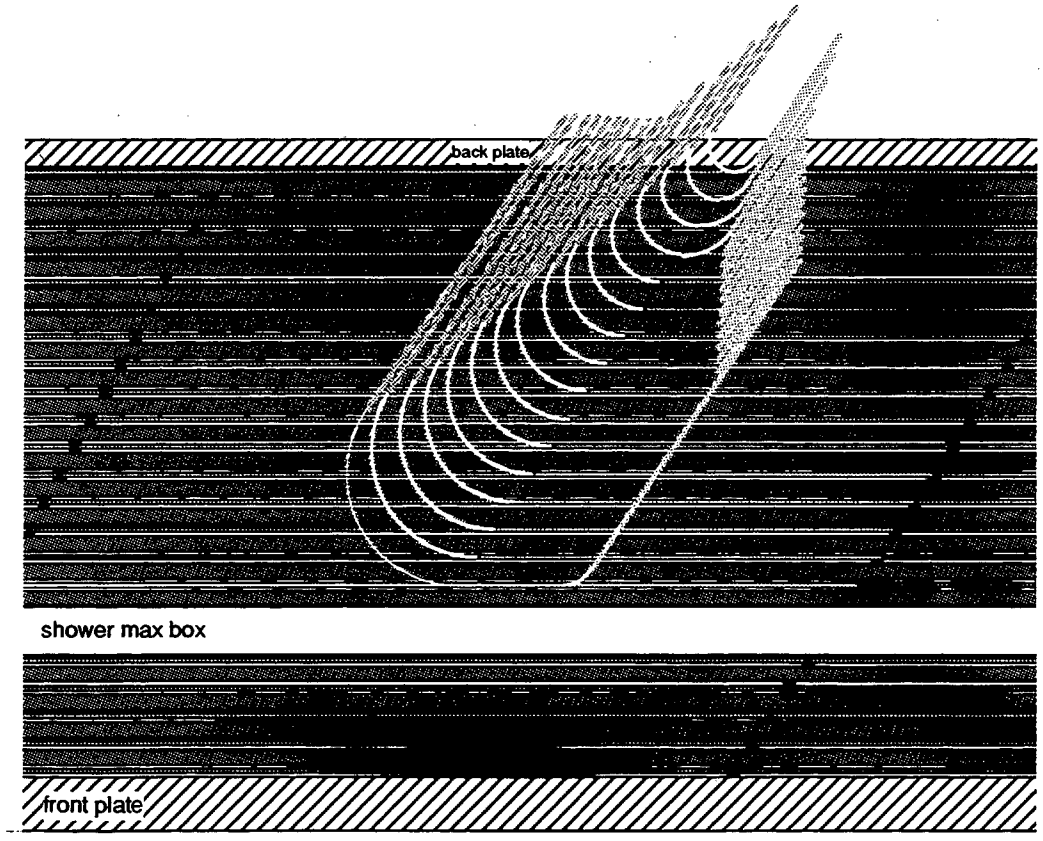

Figure 1B-2. A cross section showing the mechanical construction of a section of a barrel EMC module.

or a highly reflective paper is wrapped around the scintillator in order to maintain contact between the fibers and the tiles. The waveshifting fibers are fused onto clear fibers shortly after leaving the scintillator tiles to increase the effective attenuation length. All the fibers from a given tower are bundled together and routed through the magnet coils to photomultipliers located outside the return iron for the solenoidal magnet. In the Phase I implementation, to reduce the cost, all the fibers from groups of towers adjacent within $\Delta\eta \sim 0.2$ will couple to one PMT.

At a depth of approximately 5 X_o, near the location of the maximum number of shower electrons for photons of 3–5 GeV, a detector with fine spatial resolution will be placed to allow for the detection of direct photons. It will reject background photons emanating from decaying π° mesons having $p_t \lesssim 20$ Gev/c by examining the transverse shower profile at this depth. The radial space allotted for this device is 25 mm.

Each module of the barrel will weigh approximately 1.4 tonnes, including a non-magnetic stainless steel "strongback" attached to the back plate of 30-mm stainless steel. Trapezoidal shaped "keys" will be attached to 70-mm-thick aluminum rings located between the coils of the solenoidal magnet (Fig. 1B-3). The strongback will have a trapezoidal-shaped way machined into it, so that modules can be slid into place from the ends of the STAR detector. A fixture will permit all of the modules except those located behind the TPC supports to be installed after the TPC is in place. This should allow for partial installation of the EMC barrel in the event the full calorimeter is not ready at the start of RHIC operations. The neutral electromagnetic energy resolution in a given tower is expected to be approximately $0.16/\sqrt{E}$. A brief summary of the barrel EMC parameters is presented in Table 1B-1.

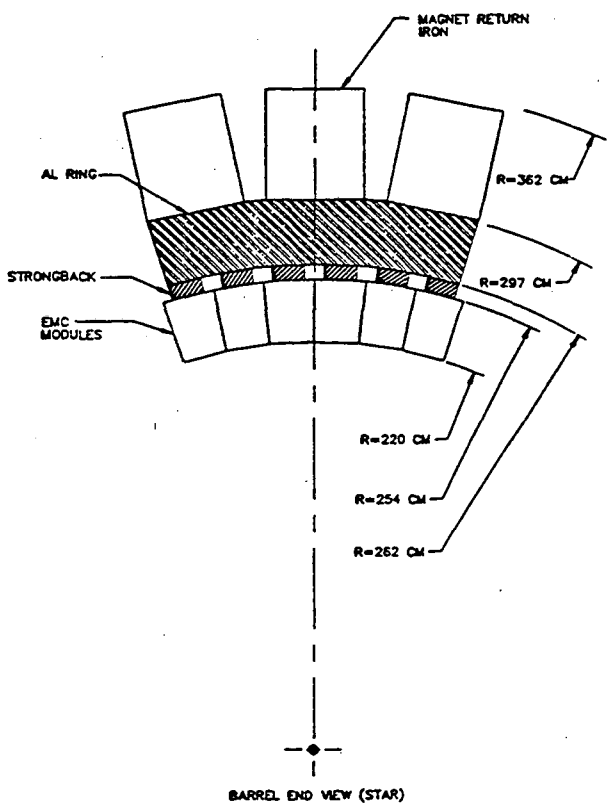

Figure 1B-3. An end view of several modules of the EMC barrel showing the location and arrangement of the aluminum ring and strongback supports.

Table 1B-1. Barrel Electromagnetic Calorimeter Parameters.

Barrel Calorimeter Type	18 X_0 Lead-Scintillator 'EM' Section
Mechanical segmentation	60 azimuthal sectors, $\Delta\phi = 0.105$ (6°) 40 projective towers in $\|\eta\| < 1.05$, $\Delta\eta = 0.0525$
Inner radius	2.20 m
Length	6.20 m
Weight	172.7 tonnes
Readout	Waveshifting fiber (2/tile) to PMT
Towers	1,200
Shower max detector	Scintillator strips or wires/pads parallel and perpendicular to η
Readout	Waveshifting fiber

1.B.2. The Endcap Electromagnetic Calorimeter

A sampling calorimeter constructed of alternating layers of lead and plastic scintillator, similar to the barrel EMC design, was also chosen for the STAR endcap EMC. This choice was found to be an appropriate compromise between cost and resolution. The ϕ segmentation of the endcap calorimeter was chosen to match the barrel EMC. Consequently, $\Delta\phi = 6°$ and there are 60 ϕ towers. This segmentation is an integral multiple (5) of the ϕ segmentation for the TPC. The segmentation in θ corresponds to $\Delta\eta = 0.05$ near $\eta = 1.0$, but increases to $\Delta\eta = 0.1$ near $\eta = 1.4$. This increase avoids scintillation tiles with dimensions less than 80 mm in the η direction. The coarser η segmentation for $\eta \sim 1.4$ also reduces the number of photomultipliers, fibers, and associated readout electronics.

Each of the scintillator tiles is part of a tower of alternating lead and scintillator layers, with boundaries that project to the nominal beam interaction point. This is shown in Fig.1B-4 for a section of the endcap EMC. A total of 25 layers of lead and 26 scintillator tiles are present in each tower. The total absorber thickness is chosen to be 23 X_0 in order to contain essentially

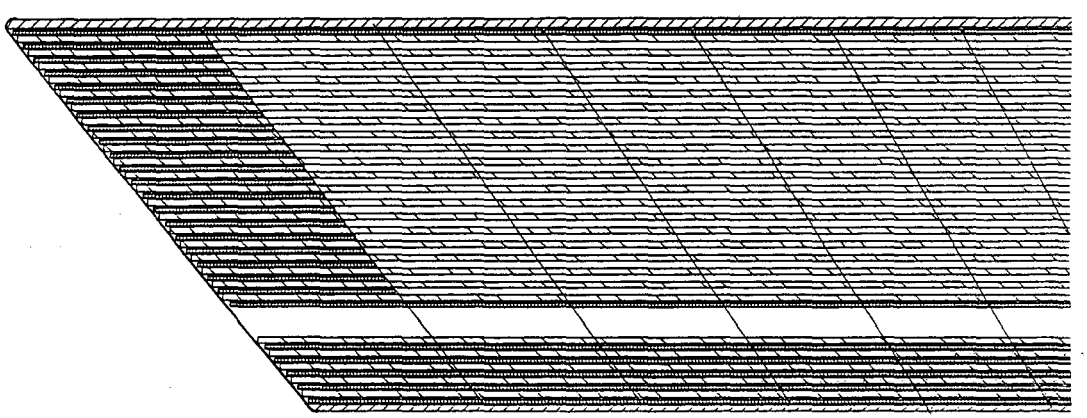

Figure 1B-4. A cross-sectional view of one 180° endcap EMC module. The scintillators are positioned so as to form pseudo-projective towers pointing to the interaction region. A shower maximum detector to distinguish between direct photons and photons from π^0 decay is located at a depth of ~5 X_0. The diagonal lines indicate the tower boundaries.

all of the electromagnetic shower energy. This is somewhat thicker than in the barrel EMC because the particles and showers detected in the endcap region are generally of higher energy. A 25-mm gap is present for a finely segmented shower maximum detector near the depth corresponding to the maximum number of particles in electromagnetic showers.

The mechanical design of the endcap calorimeters consists of two sections of $\Delta\phi = 180°$ per endcap. The endcap sections are reinforced on the back with stainless steel channel and mounted to the magnet poletip with locating pins and mounting bolts. These sections could be mounted to the magnet poletips in the experimental hall without removing the accelerator beam pipe. The weight of each section is ~13.6 tonnes. Preliminary structural analyses suggested the need for additional lead supports besides the inner and outer radial supports and the two sides separated by 180°. The present conceptual design (Fig. 1B-5) has additional radial lead supports every $\Delta\phi = 30°$ in the shadow of the TPC sector boundaries. These sector boundaries correspond to support members on the ends of the TPC and are thus already regions of lower efficiency for detection of charged particles. The radial lead supports and the sides contain tabs to support the lead.

Light from the calorimeter scintillators must be transmitted to photomultipliers or other photon transducers. Optical fibers are routed as shown and exit between the inner and outer end supports. Photomultipliers are presently assumed due to their relatively low cost and extensive experience in their use. These photomultipliers must be mounted outside the main STAR magnetic field for proper operation, with plastic optical fibers of 1-mm diameter connecting the photomultipliers with the scintillators.

There is a shower maximum detector at a depth of ~5 X_0 which will contribute about 7,500 fibers per endcap. This assumes 7-mm-wide scintillator strips oriented at 45° to the center line of each $\Delta\phi = 30°$ section. Two sets of strips perpendicular to each other are assumed. A multi-wire proportional chamber with wires and pads is also being considered for this application. A brief summary of the endcap EMC parameters is presented in Table 1B-2.

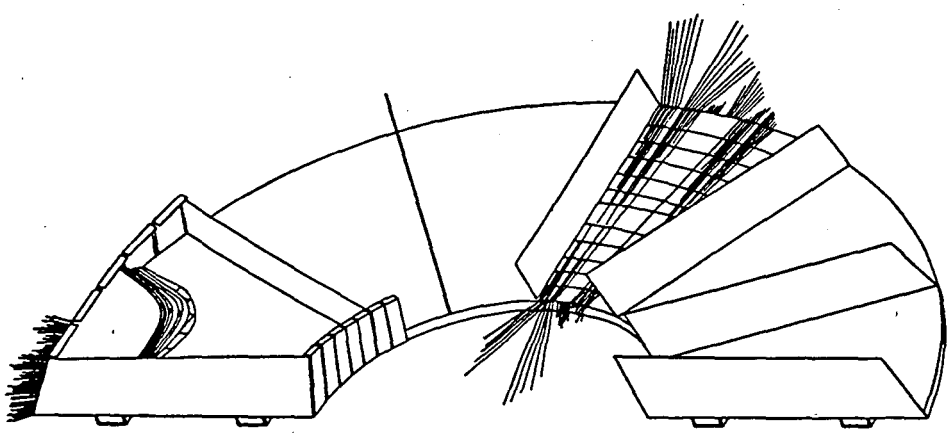

Figure 1B-5. A perspective view showing the internal mechanical support for the endcap EMC. Lead support bulkheads are located at intervals of 30°. Fibers from the scintillator tiles are routed through slots in the walls of the inner and outer circumference, and these fibers are connected to photomultipliers located on the exterior of the magnet poletip.

Table 1B-2. Endcap Electromagnetic Calorimeter Parameters.

Endcap Calorimeter Type	23 X_0 Lead-Scintillator 'EM' Section
Mechanical segmentation	60 azimuthal sectors, $\Delta\phi = 0.105$ (6°) 12 projective towers in $1.1 < \|\eta\| < 2.0$, $\Delta\eta = 0.05$ for $\|\eta\| < 1.4$; $\Delta\eta = .1$ for $1.4 < \|\eta\| < 2.0$
Mean inner radius	.81 m
Mean outer radius	2.32 m
Weight per endcap	27.3 tonnes
Readout	Waveshifting fiber (2/tile) to PMT
Towers per endcap	720
Shower max detector	Scintillator strips or wires/pads oriented at ±45° with respect to η
Readout	Waveshifting fiber

1.C. Cost and Schedule

The modular nature of the calorimeter design makes it possible to stage the construction of this detector in a number of ways. Depending upon which staging plan is adopted, the physics capabilities of the EMC also vary. The present report addresses two possible options, both of which extend the reach of the STAR physics program significantly.

The first option is to construct the 120 modules necessary to complete the full EMC barrel. Each module constructed would contain the hardware for the shower maximum detector, to avoid the difficult problem of retrofitting this detector at a later date. However, the shower maximum detector would not be instrumented with electronics until further funding became available. Construction of the endcap calorimeter would also be deferred. In addition, to reduce the initial cost, fiber bundles from towers adjacent within $\Delta\eta \sim 0.2$ would be coupled to the same photomultiplier. As a consequence, the total number of photomultipliers and electronics channels would be ~600. The cost of this option, which is detailed further in Chapter 6, is $7.5M in FY93 dollars. Several areas have been identified in which contributions from participating institutions could result in significant savings. These include machining of mechanical components, labor for module assembly, and fabrication of the shower maximum detector. The estimated total cost of components and labor which could be contributed is ~$1.5M in FY93 dollars.

The physics provided by this implementation of the calorimeter is significant. Specifically, with the full EMC barrel, the resolution on the reconstructed global transverse energy for AuAu interactions, for example, is improved from ~30% to ~2%. The resolution available at the trigger level for the global neutral transverse energy would be ~2.5%. With this resolution, STAR will be able to search at the trigger level for events exhibiting unusual isospin abundances, or unusual correlations between energy density and entropy density. Additionally, the improved resolution provided by the EMC will afford a more detailed understanding of the transfer of energy from projectile rapidity to mid-rapidity. As the EMC barrel is large compared to a jet radius ($\sqrt{(\Delta\eta)^2 + (\Delta\phi)^2} \lesssim .7$), it will also be possible to measure inclusive jets and high p_t π^0s from parton scatters within $|\eta| \lesssim .3$. This will allow STAR to study the energy loss of hard-scattered partons using inclusive jets as well as γ-jet and jet-jet, coincidences as penetrating probes of the early stages of the collision.

The assembly scenario for this implementation of the EMC leads naturally to a descoped configuration in the event of reduced funding. As the mechanical supports for the TPC capture the modules within $\Delta\phi \sim 12°$ at two locations which are back-to-back, the modules located in these regions of the barrel would be constructed first. A natural consequence is that the EMC barrel would be built up from two sections which are 180° apart. In the event of reduced funding, it would be possible to complete two back-to-back sections comprising half of the EMC barrel for ~$4.5M before contributions. This would allow STAR some capability for all of the physics discussed above, with some reduction in resolution, sensitivity, and acceptance.

The second option considered is to construct the full EMC barrel and one of the endcap calorimeters. The EMC barrel would be instrumented with 1,200 channels of tower electronics. The number of electronics channels for the endcap would be 600. The shower maximum hardware would be completed for installation in both the barrel and endcap calorimeters, but would only be instrumented with electronics in the endcap. The estimated cost for this option before contributions is $13M in FY93 dollars.

This implementation of the STAR EMC provides essentially all the capabilities discussed in Section 1.A. In particular, with the addition of the endcap calorimeter instrumented with shower max, the measurement of gluon shadowing in pA collisions would be possible. This would allow STAR to determine the initial conditions in AA interactions and make full use of perturbative QCD in predicting the pre-equilibrium phase of the collision.

Much of the engineering required to interface the barrel and endcap calorimeters to the STAR detector has already been carried out. In addition, considerable engineering directed at the choice of technology has been accomplished. As a consequence, it is possible given an appropriate funding profile for all of the EMC construction to be completed for the start of RHIC operations. Specifically, it is envisioned that given the choice of technology in summer of 1993, a full-scale prototype would be constructed and tested within a year. Upon completion of this phase, construction of modules would commence. Schedule estimates based upon the construction of similar modules for ZEUS suggest that modules could be completed at the rate of ~30 per year. Consequently, based upon feasibility alone, the full barrel calorimeter would be available for assembly at RHIC in mid-1998.

Assuming a level funding profile of ~$1M per year, the construction of all the modules for the full EMC barrel, including front-end electronics, trigger electronics, and data acquisition, would require approximately 6 years. In this instance, most of the EMC barrel modules would be installed before the start of RHIC in mid-1999, with the remaining modules being installed during the first scheduled RHIC shutdown.

2.

The Physics of Electromagnetic Calorimetry in STAR

2. THE PHYSICS OF ELECTROMAGNETIC CALORIMETRY IN STAR

2.A. Nuclear Physics

2.A.1. Soft Physics

Measurements of Global E_t

The most interesting collisions at RHIC are those that produce the highest densities and temperatures. This is thought to be the most promising environment in which to search for novel phenomena and signatures of a deconfined phase of quarks and gluons. The most characteristic feature of these conditions is expected to be the observation at mid-rapidity of a high multiplicity of particles and high transverse energy deposition (E_t).

The distribution of E_t characteristically observed in relativistic nuclear collisions consists of a plateau region followed by a region of rapidly decreasing probability at the highest E_t values (Fig. 2A-1). The slope of the distribution in the high E_t region is determined by fluctuations in the energy-transferring interactions of the nuclear constituents. It has been suggested that a measurable part of these fluctuations may be due to fluctuations in the partonic states of the incident hadronic systems,[1] and are interesting for this reason. Whatever their origin, the fluctuations in E_t represent variations in the energy density produced in the collisions and must be measured accurately if that range of energy densities is to be understood. Experimental resolutions that are comparable to, or larger than, the natural physics width of the parent distribution lead to a dilution of the sample of high E_t events as shown in Fig. 2A-2 and are therefore undesirable. With the proposed barrel electromagnetic calorimeter, the resolution for determining E_t improves to ~2%, such that ~90% of the events in the top 5% of the observed

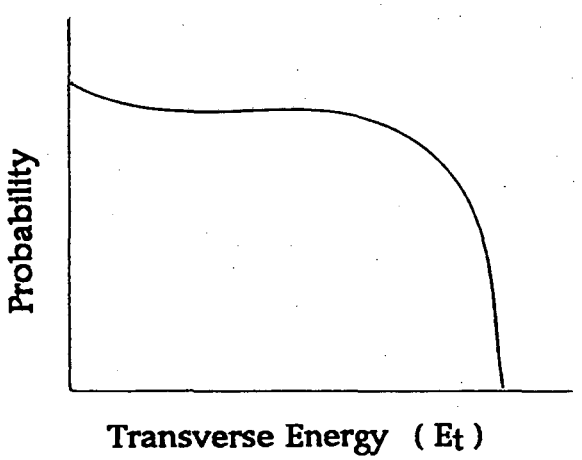

Figure 2A-1. The distribution of E_t characteristically observed in relativistic nucleus-nucleus collisions. The distribution generally exhibits a plateau followed by a region of rapidly decreasing probability at the highest E_t values.

[1] B. Blättel *et al.*, Nucl. Phys **A544** (1992) 479.

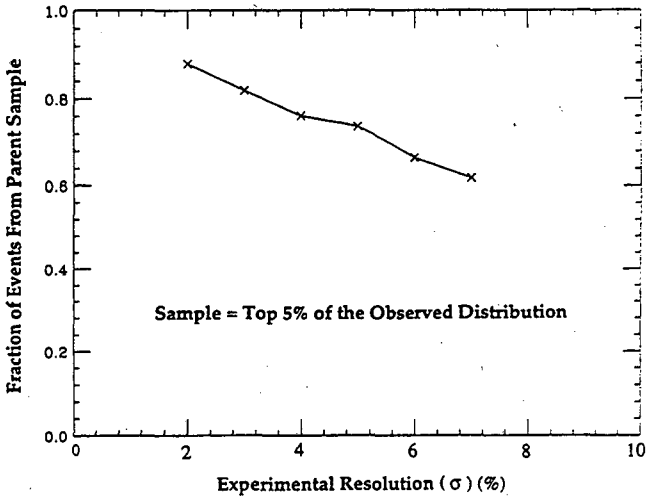

Figure 2A-2. The percentage, as a function of the experimental resolution in E_t, of the number of events in the observed distribution which originate from the top 5% of the parent distribution. The parent distribution is assumed to have a σ of 5%.

distribution will originate from the parent distribution of interest. The parent distribution is assumed to have an intrinsic width of $\sigma \cong 5\%$. This is comparable, for example, to the results obtained for S+Pb collisions at 200 A GeV with the Helios[2] spectrometer. In this instance, the experimental resolution was $\sigma = 3.8\%$, and the observed E_t falloff of 7% could be interpreted in terms of physical processes.

Searching for Rare Events Indicating a Phase Transition

It has been argued[3,4,5] on rather general grounds for some time that the mean transverse momentum, $\langle p_t \rangle$, of particles produced in hadronic interactions, observed as a function of the multiplicity

$$n = \int (dn/dy) \qquad (2.A\text{-}1)$$

in a given rapidity interval, reflects the properties of the equation of state of high temperature hadronic matter. Assuming that a description in terms of hydrodynamics is appropriate, dn/dy is related to the entropy, whereas the p_t spectrum reflects the combined effects of temperature and transverse expansion. Except in the vicinity of a phase transition, higher entropy production in "normal" hadronic matter requires higher temperature, a correlation observed experimentally, for example, at the CERN $p\bar{p}$ collider.[6] In the vicinity of a first order phase transition however, the large latent heat required to "melt" the hadronic matter into a plasma of quarks and gluons leads to a situation in which the energy density and entropy density may increase dramatically, while the temperature and pressure remain essentially constant. In this instance one would expect to observe a departure from the usual correlation between dn/dy

[2]T. Akesson *et al.*, Nucl. Phys. **B353** (1991) 1.
[3]E.V. Shuryak, Phys. Rep. **61** (1980) 71.
[4]E.V. Shuryak and O. Zhirov, Phys. Lett. **89B** (1980) 253; Sov. J. Nucl. Phys. **28** (1978)247.
[5]L. Van Hove, Phys. Lett. **118B** (1982) 138.
[6]UA1 Collaboration, G. Arnison *et al.*, "Transverse Momentum Spectra for Charged Particles at the CERN Proton-Anti-proton Collider," presented XXIth International Conference on High Energy Physics, July 1982, Paris, France.

and $\langle p_t \rangle$, in which the increase in the mean p_t as a function of multiplicity slowed, or even decreased slightly due to reduced transverse expansion in a limited range of dn/dy. Above the transition, one would again recover the standard correlation, the thermodynamic relations for an ideal gas of massless quarks and gluons being similar to that for a gas of massless pions. The behavior one might expect to observed experimentally is indicated qualitatively in Fig. 2A-3.

While this picture suffers from a number of oversimplifications, more detailed studies[7] of the hydrodynamic evolution of matter in ultrarelativistic nucleus-nucleus collisions appear to indicate the behavior expected based on the simple arguments presented above survives the refinement of proper treatment of the longitudinal and transverse expansion which occur during the mixed phase. The mean p_t in this instance does not decrease in any interval of dn/dy, although the increase in the vicinity of the phase transition is once again slowed considerably (Fig. 2A-4). Perhaps the most important conclusion however, is that the correlation between $\langle p_t \rangle$ and dn/dy does in fact reflect properties of the equation of state. While the order and nature of the transition are matters for experiment, the sensitivity of this correlation to the fundamental character of the matter being probed makes this correlation potentially a useful tool in identifying events in which a transition has occurred.

If the transition to a plasma of quarks and gluons occurs with high probability, the correlation between $\langle p_t \rangle$ and dn/dy is best studied within STAR using single particle inclusive data provided by the time projection chamber (TPC). Aside from possible Coulomb effects which should be small, there is no reason to expect *a priori* that the mean p_t measured for charged pions should be different than that for π^0s. In that event, the resolution and systematic uncertainties in determining the mean $\langle p_t \rangle$ using tracks in the TPC will be better than can be obtained by reconstructing low momentum π^0s in the EMC, although some account will need to be taken of the fact that charged pions having $p_t \lesssim 40$ MeV/c spiral in the magnetic field and do not reach the TPC. The effective p_t cutoff may in fact be somewhat higher in nucleus-nucleus collisions due to the high occupancy for the inner pad rows, although the silicon vertex tracker (SVT) will in principle recover most low momentum tracks. Use of the TPC tracking would in

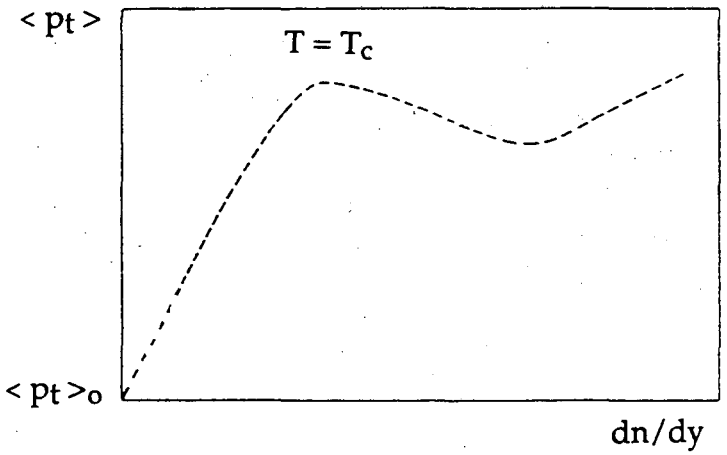

Figure 2A-3. The expected structure in the $\langle p_t \rangle$ versus dn/dy correlation at a given impact parameter resulting from a first order phase transition. Further details may be found in Reference 5.

[7]M Kataja, P.V. Ruuskanen, L.D. McLerran, and H. von Gersdorff, Phys. Rev. **D34** (1986) 2755.

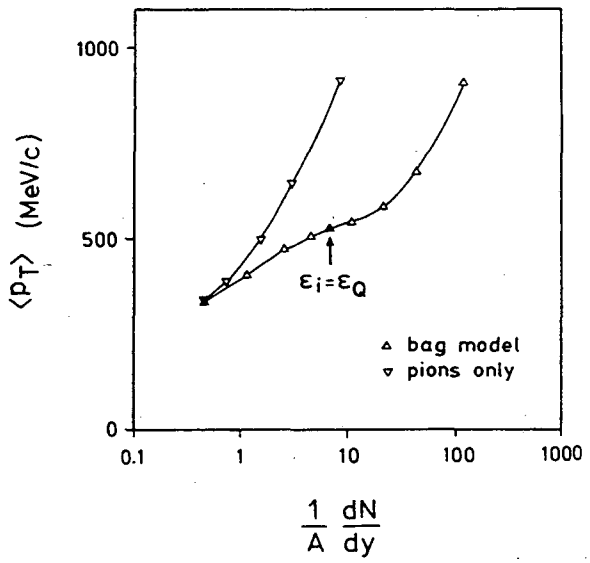

Figure 2A-4. The prediction from Reference 7 for the average p_t as a function of the normalized multiplicity (1/A)dN/dy with (Δ) and without (∇) a first order phase transition. At the point indicated by $\varepsilon = \varepsilon_Q$, pure plasma state at T_c is reached.

any event be preferable for studying this correlation since it would provide the most precise minimum bias data.

If the transition to the deconfined phase is rare however, it will be necessary, due to the overhead in analyzing large data samples, to develop a highly selective trigger to identify such events. Since complete tracking information from the TPC will not be available at the trigger level, the TPC alone can not provide such a trigger. If the correlation between $\langle p_t \rangle$ and dn/dy were known to be similar to that in Fig. 2A-4, for example, this could be accomplished simply by using the STAR central trigger barrel (CTB) to search for events with a given dn/dy. In reality however, the correlation between $\langle p_t \rangle$ and dn/dy is completely unknown even for "normal" events in this energy range. In practice therefore, one would establish the behavior of the correlation for "normal" events, and then develop a trigger to search for a sample of events exhibiting an unusual correlation between $\langle p_t \rangle$ and dn/dy. Since such events might occur as fluctuations in a "normal" range of dn/dy, the most exhaustive search would be conducted by examining the correlation between $\langle p_t \rangle$ and dn/dy at the trigger level, rather than triggering on multiplicity alone.

The STAR EMC provides a useful means to test this correlation at the trigger level. Since the calorimeter is sensitive to the ionization energy loss of charged particles as well as that from electromagnetic showers, the STAR EMC is sensitive to changes in the mean p_t in a given event. When correlated with the multiplicity information provided by the STAR CTB on an event-by-event basis, the EMC provides a unique capability in STAR to search for events with an unusual correlation between energy density and entropy density. If such events are rare, the use of this highly selective trigger may be the only means by which to observe them. The sensitivity at the trigger level to changes in the correlation between $\langle p_t \rangle$ and dn/dy provided by the STAR EMC is discussed further in Section 3.B.

Detection of Centauro Events

A number of conjectures have recently been put forward suggesting that one may expect large fluctuations in the photonic to hadronic ratio in ultra-relativistic heavy ion collisions. The

interest in such possibilities stems from the apparent observation of large fluctuations in this ratio in recent cosmic ray data.[8,9] Although the physical bases for these predictions vary, all depend upon the high density and temperature that can be reached in central nucleus-nucleus collisions at RHIC.

Panagiotou *et al.*[10] consider that, assuming isospin is conserved, the low number of photons from π° decay observed in cosmic ray emulsion data may result from ultra-relativistic nucleus-nucleus collisions in which all pion production is suppressed in a given interval of rapidity. This is noted to be possible if a quark-gluon fireball with non-zero net baryon number is formed, since the high baryochemical potential in such a state suppresses the thermal production of quarks and anti-quarks and therefore the production of pions as well. A fireball of this type would most likely appear in the fragmentation region at RHIC and would be characterized by the suppression of all pion species. A related observation would be that baryons produced in the decay of the fireball would be characterized by a higher than average $\langle p_t \rangle$.

A somewhat less speculative hypothesis by Pratt[11] expands on an earlier possibility suggested by Anslem and Ryskind[12] that a coherent pion field may be produced. More precisely, when the density of possible emission sources of identical bosons within a given volume exceeds a certain critical density, quantum interference effects and symmetrization of the N-body wave function become important. The consequence of symmetrization may be striking. In particular, stimulated emission of pions into low momentum states—pion lasing—might result. The multiplicity of pions is enhanced in general with large fluctuations in the number of pions of a given species possible, due to the fact that the interference depends upon the indistinguishability of bosons of a given isospin. This prediction is especially relevant for π° production where the unknown effects of Coulomb interactions are not a consideration. As a consequence, instead of a low photonic to hadronic ratio, one might expect some events to exhibit "anti-Centauro" behavior, with π° decay photons greatly outnumbering the charged pions observed in a limited region of rapidity ($|\Delta y| \lesssim 1$). Empirical estimates from S + Pb collisions at CERN suggest that the pion densities reached are within a factor of two of the critical density required for stimulated emission, and that in any event, this effect will need to be accounted for in order to understand high-multiplicity events. An enhancement of the observed pion spectra at low p_t, and two-particle HBT correlations indicating coherent production would be other indications that symmetrization was important.

Taking a deeper look at the QCD vacuum, Bjorken[13] suggests that a collision between two ultra-relativistic heavy ions may result in a highly excited, "colorless" system whose isospin orientation may be quite arbitrary. As a consequence, the ratio of neutral to charged pions may fluctuate widely from the normal isospin expectation. Bjorken expects that heavy ions may be the most effective way to produce this phenomeon. This prediction is similar to that of Wilczek,[14] who suggests that a disoriented chiral condensate may be one consequence of a "quench" of the quark-gluon plasma which may be formed.

---

[8]Chacaltaya and Pamir Collaboration, Tokyo University preprint ICRR Report-232-91-1 (1991).
[9]C.M.G. Lattes, Y. Fugimoto, and S. Hawegawa, Phys. Rep. **65** (1980) 151.
[10]A. Panagiotou *et al.*, Phys. Rev. **D45** (1991) 3134.
[11]S. Pratt, Phys. Lett. **B301** (1993) 159.
[12]A.A. Anselm and M. Pyskind, Phys. Lett. **B266** (1991) 482.
[13]J.D. Bjorken, Acta Physica Polonica **B23** (1992) 637.
[14]F. Wilczek, "Chiral Dynamics Near Equilibrium or After Quenching," Proceedings of the Tenth International Conference on Ultra-Relativistic Nucleus-Nucleus Collisions, June 20–24, 1993, Borlänge, Sweden.

Investigation of these phenomena depends entirely on the ability to identify neutral electromagnetic energy (gamma rays) and charged particles over a wide range of acceptance. This study is therefore not possible in STAR without the capabilities provided by the electromagnetic calorimeter. The TPC and charged-particle multiplicity detectors together with the proposed EM calorimeter can accomplish this task with reasonable spatial and energy resolution. The potential for discovery of such wide fluctuations in the photonic to hadronic ratio is therefore a distinct possibility. Simulations designed to determine the limits of the ability of the EM calorimeter to identify, trigger upon, and measure these fluctuations are described in Section 3.B. The results indicate clearly, that with the coverage projected in the STAR EMC proposal, a sensitive search for these exciting possibilities in heavy ion collisions at RHIC is feasible.

2.A.2. Parton Physics

Parton Energy Loss

The measurement of jets, direct photons, and high p_t particles using the STAR electromagnetic calorimeter is essential, since aside from open charm production via gluon fusion, these processes presently represent the only means within STAR of probing the high temperature, gluon-dominated, pre-equilibrium stage of the collision. The goal of studying the products of hard QCD processes in relativistic heavy ion collisions is to use the propagation of quarks and gluons as a penetrating probe of nuclear matter, hot hadronic matter, and quark matter. Since the hard-scattering processes occur at the very earliest stage of the collision ($t < 1$ fm/c), their production rates are dependent only upon the incoming state. Given the quark and gluon structure functions of the colliding nuclei, the rate as a function of p_t of hard parton scattering is entirely calculable using perturbative QCD. This situation is unique to RHIC, which will be the first accelerator to provide nuclear collisions at energies where rates of detectable partonic debris (jets, high-p_t particles, and direct photons) from hard partonic scattering permit accurate measurements.

Various calculations have predicted that the propagation of quarks and gluons through matter depends strongly upon properties of the medium,[15,16,17,18,19] and that a measurement of the yield of hard-scattered partons as a function of transverse energy may be sensitive to the state of the surrounding matter. It has been suggested, for example, that there will be observable changes in the energy loss of propagating partons as the energy density of the medium increases, particularly if the medium passes through a phase transition to the QGP.[20] Interest in this possibility originally focused on the observation that the collisional energy loss of a quark of energy E propagating through an ideal plasma of quarks and gluons at temperature T could be expressed[21] as

$$(dE/dx) \approx \alpha^2_s T^2 \log(4ET/M^2) \exp(-M/T)(1 + M/T) \quad , \qquad (2.A\text{–}2)$$

[15] J.D. Bjorken, Fermilab Report 82/59/59-THY (1982).
[16] D. Appel, Phys. Rev. **D33** (1986) 717.
[17] J.P. Blaizot and L.D. McLerran, Phys. Rev. **D34** (1986) 2739.
[18] M. Rammersdorfer and U. Heinz, Phys. Rev. **D41** (1990) 306.
[19] M. Gyulassy and M. Pluemmer, Phys. Lett. **B243** (1990) 432.
[20] M. Gyulassy *et al.*, Lawrence Berkeley Laboratory Report LBL-31002, to be published in Proceedings of 4th Conference on the Intersections between Particle and Nuclear Physics, Tucson, Arizona, 1991.
[21] J.D. Bjorken, Fermilab Report 82/59/59-THY (1982).

where M is an infrared cutoff on the order of the Debye mass. The strong dependence of this expression on α_s lead to speculation that in the vicinity of a phase transition the normal energy loss experienced by propagating quarks and gluons might be reduced due to decreased coupling between partons in this environment. More recently, it has been noted[22] that another sensitive probe may be the radiative energy loss of propagating partons,

$$(dE/dx) \approx \alpha_s M^2 (\log(s/4M^2))^2 \quad . \tag{2.A-3}$$

Whereas the radiative energy loss for high-energy partons propagating through nuclear matter would normally be strongly suppressed due to the Landau-Pomeranchuk effect, the reduced Debye screening length predicted[23] for the plasma ($\lambda_D = M^{-1} \sim 0.4$) could increase the radiative energy loss significantly (Fig. 2A-5). This same effect is predicted to lead to the suppression of vector meson production (J/ψ, ψ', Υ). Correlation of these results could help determine if effects that might be observed for vector meson production are due to plasma formation, or result instead from propagation within the nuclear medium.

The consequence of parton energy loss in a medium is "jet quenching," or the reduction of the jet yield at a given p_t. This effect, which is most important for intermediate energy jets (5–10 GeV), has already been observed in deep inelastic lepton scattering from nuclear targets.[24] It is most effectively studied using the $qg \rightarrow \gamma q$ Compton subprocess, since for this process complications due to the fragmentation function are not a consideration and the p_t of the parton scatter may be determined unambiguously from the p_t of the direct photon.

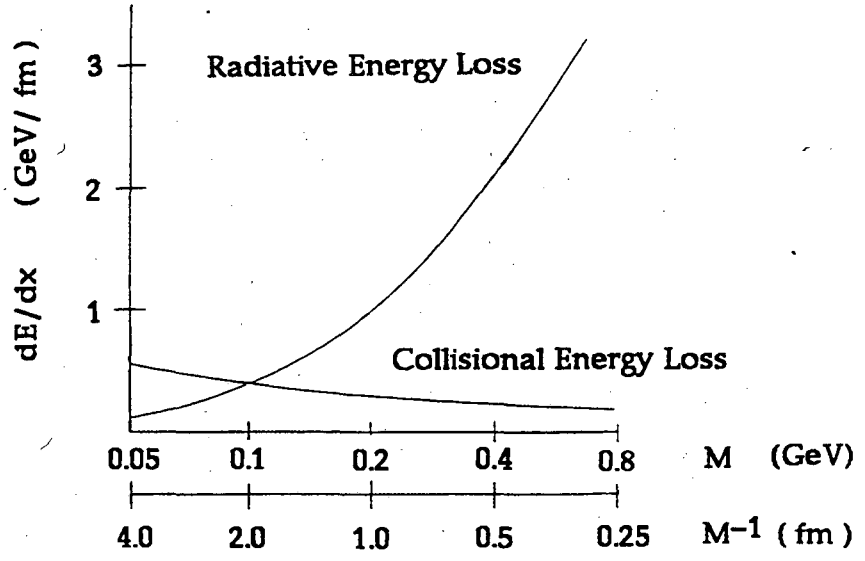

Figure 2A-5. The qualitative behavior predicted for the radiative energy loss as a function of the infrared screening scale M. The radiative energy loss increases significantly as the screening length (M^{-1}) is decreased. The example shown is for a parton of 20 GeV, assuming $\alpha_s = 0.2$.

---

[22]M. Gyulassy, "Nuclear Chromodynamics in eA, pA, and AA Interactions," proceedings of the Future Directions in Particle and Nuclear Physics at Multi-GeV Hadron beam Facilities Meeting, March 4–6, 1993, Brookhaven National Laboratory, Upton, New York.

[23]B. Muller, "Physics of the Quark-Gluon Plasma," Proceedings of the NATO Advanced Study Institute on Particle Production in Highly Excited Matter, July 12–24, 1992, Il Ciocco, Italy; Duke Report No. DUKE-TH-92-36.

[24]L. S. Osborne et al., Phys. Rev. Lett. **40** (1978) 1624; P.B. Renton *et al.*, Oxford Nuclear Physics Laboratory preprint 55/88 (1988); M Gyulassy and M. Plummer, LBL preprint LBL-27234.

It may also be studied using di-jets. In this instance it is essential to measure the energy of both jets in di-jet events. The sum of the jet energies and the di-jet invariant mass are sensitive to interactions of the partons with the medium. The yield as a function of invariant mass of back-to-back jets at mid-rapidity may be the best tool for studying effects of the matter on propagation, since in this case the overall path length in the medium is maximized. The difference of di-jet energies may be sensitive to the difference in path lengths traversed by the partons. In addition, measurement of both jets in a di-jet event suppresses background due to fluctuations of soft production processes that can mimic a jet. A measurement of the di-jet differential cross section for p-nucleus collisions will in itself be of interest for understanding the parton structure functions in nuclear matter.

Jet quenching is also expected to lead to significant effects in the spectra of single high p_t particles, di-hadrons, and jets in AA collisions at RHIC.[25] This is not surprising since above $p_t \sim$ 2–3 GeV/c the particles observed result as fragmentation products from hard parton scatters.

In general, the reconstruction of the parton-scattering kinematics is limited by acceptance and detector resolution effects, and by the superposition of particles from other, incoherent processes which occur during the collision. This last problem is especially serious in high-multiplicity AA collisions, where the jet can be entirely obscured. The technique of jet reconstruction to extract parton information with the STAR EMC in pA and AA collisions is presently being investigated. The yield of jets as a function of p_t, as well as the ability of the STAR EMC to trigger upon jets is discussed further in Section 3.D.

A systematic study of parton energy loss in pA and AA interactions using the STAR EMC will provide a unique tool to search for a transition to a quark gluon plasma in ultra-relativistic nucleus-nucleus collisions. Additionally, events identified as candidates for further study using other signatures may be probed with this technique to determine the nature of the medium in the initial phase of the collision. The STAR EMC is essential for this study of jets and direct photons, since measurement of the neutral electromagnetic energy is necessary to reconstruct jets or detect direct photons. Although the study of single high p_t particles may in principle be accomplished using tracking information from the STAR TPC, without the EMC it is not presently possible to trigger upon high p_t particles.

Mini-Jets and High p_t Tails of Distributions

Mini-jets are expected to be produced copiously in collisions at RHIC.[26,27] As is the case for high p_t jets, the observed yield of mini-jets is expected to be influenced strongly by the state of the high-density medium through which they propagate.[28] However, direct measurement of mini-jets is virtually impossible because of their large opening angle and the strongly varying background. Thus, it is important to study the degree of fluctuation of the transverse energy and multiplicity as a function of pseudo-rapidity and azimuthal angle ($d^2E_t/d\eta d\phi$ and $d^2n/d\eta d\phi$) event-by-event, which should be strongly affected by the mini-jets.[29,30] The STAR EMC is essential for this study since without measuring the neutral transverse energy, the true degree of fluctuation due to mini-jets can not be determined. It is essential that this be systematically studied in pp and pA collisions, as well as AA.

---

[25] X.N. Wang and M. Gyulassy, Phys. Rev. Lett. **68** (1992) 1480.
[26] K. Kajantie, P.V. Landshoff, and J. Lindfors, Phys. Rev. Lett. **59** (1987) 2527.
[27] K.J. Eskola, K. Kajantie, and J. Lindfors, Nucl. Phys. **B323** (1989) 37.
[28] P.V. Landshoff, Nucl. Phys. **A498** (1989) 217; X.N. Wang, Lawrence Berkeley Laboratory Report LBL-28790 (1990), submitted to Phys. Rev. D.
[29] D. Appel, Phys. Rev. **D33** (1986) 717.
[30] X.N. Wang, Lawrence Berkeley Laboratory Report LBL-28789 (1990), submitted to Phys. Lett. B.

Inclusive p_t distributions of hadrons at $p_t > 3$ GeV/c will also be influenced by jets and mini-jets. It should be emphasized that the single particle cross sections fall off more rapidly as a function of p_t than the jet cross sections.[31] However, Wang and Gyulassy[32] have shown that the inclusive single particle yield is very sensitive to the state of the matter through which the parent scattered partons propagate. Figure 2A-6 shows the charged particle pseudorapidity distribution and the ratio of charged particle yields for Au-Au and p-Au collisions compared to p-p collisions as a function of p_t, under various assumptions about the nuclear structure functions (shadowing) and energy loss of the scattered partons (quenching). From the middle panel of Fig. 2A-6, it is seen that the introduction of quenching (in addition to shadowing) leads to a reduction in yield above p_t ~4 GeV/c of a factor 5. Although effects of this magnitude may be observed by examining single particle inclusive spectra provided by the TPC, unfolding the effects of shadowing and quenching in order to interpret these data will require systematic studies using the STAR EMC.

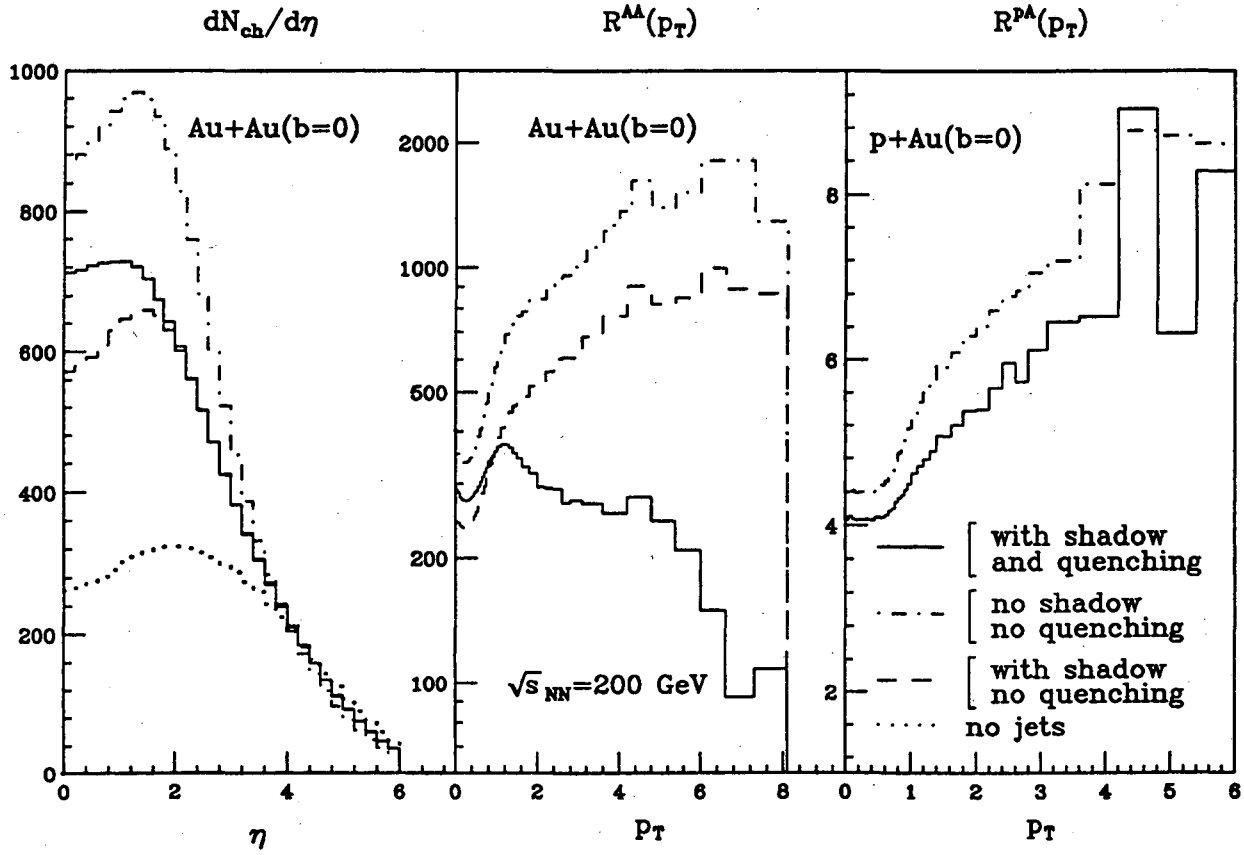

Figure 2A-6. Results from HIJING calculations on the dependence of the inclusive charged hadron spectra in central AuAu and pAu collisions on mini-jet production (dash-dotted), gluon shadowing (dashed) and jet quenching (solid) assuming that gluon shadowing is identical to that of quarks. $R^{AB}(p_t)$ is the ratio of the inclusive p_t spectrum of charged hadrons in A+B collisions to that of pp. Details may be found in Reference 32 in this chapter.

[31] See W. Geist *et al.*, CERN/EP Report 89-159 (1989) to be published in Phys. Rep. (1990).
[32] X.N. Wang and M. Gyulassy, Phys. Rev. Lett. **68** (1992) 1480.

Gluon Shadowing

One of the primary advantages of RHIC is that unlike the situation at lower energy, where only a phenomenological approach was possible, firm predictions as to the early stages of the collision are possible using perturbative QCD. The ability to make full use of this potential, however, depends upon having knowledge of the parton structure functions in the nucleus. Deep inelastic scattering measurements presently underway will provide the necessary measurements for determination of the quark structure functions in nuclei, but little is expected to be known concerning the nuclear structure function for gluons at low Bjorken x. Simulations of the early stage of ultra-relativistic nucleus-nucleus collisions indicate it is precisely gluons at low Bjorken x which make the largest contribution to the energy density of the system produced at mid-rapidity, and dominate this phase of the evolution. The manifestation of this phase may be striking, including a dramatic increase in the production of open charm and mini-jets from semi-hard gluon-gluon scatters. Mini-jet production may account for up to 50% of the total transverse energy observed at mid-rapidity. Without measurement of the gluon shadowing, however, the theoretical predictions for dn_{ch}/d, and $d^2n/dydp_\perp$ are uncertain by $\div$ 30%. The interpretation of these data will be much less certain, and the understanding seriously compromised, if the incident gluon flux has not been determined. Some information on the gluon structure function will be provided by the NMC experiment at CERN, and Fermilab experiments E665, E772, and E789. The available data in the low-x region of interest ($.01 < x < 0.05$) tends to be limited either by systematics or low statistics.

2.B. Spin Physics

After decades of being regarded as an inessential complication to the strong interaction at high energy, spin has again come to the attention of the theoretical community. This is largely due to the fact that recent results from deep inelastic scattering experiments have shown that the spin of the nucleon may not be completely accounted for by that of the quark constituents.[33,34] In fact, recent theoretical work seems to favor a chiral soliton model over a naive quark model.[35]

There is also an abundance of data showing large and inexplicable spin effects at relatively low values of transverse momenta. Some of these effects, such as the polarization of inclusively produced hyperons and analyzing power in pion production persist at the highest energies and transverse momenta that have been studied. Experiments with polarized hadron (and also polarized lepton) beams have been limited to fixed target energies of a few hundred GeV. Perhaps these hadronic spin effects are low energy, low p_t phenomena, which will vanish at higher energies. On the other hand, perhaps they are asymptotic properties of the strong interaction. Continuing these measurements to very high energies would give much-needed answers. In fact, with a complete understanding of QCD and the spin structure of the proton, the spin effects observed in proton-proton collisions at RHIC energies should be calculable.

A critical ingredient in these calculations is the spin distribution of the various constituents of the proton: valence and sea quarks and gluons. The helicity distributions of the valence plus sea quarks in the proton and the neutron are now being measured in deep inelastic scattering of longitudinally polarized muons and electrons from longitudinally polarized proton (deuteron) targets at CERN and SLAC. The separate helicity distributions of sea quarks and gluons and the transversity distribution of quarks are also fundamental properties of the proton that cannot be measured in lepton scattering, but easily could be at RHIC with polarized proton beams. Knowledge of the quark and gluon spin distribution then gives the "beam polarization" for calculation of spin observables in various parton-parton scattering processes, e.g., di-jet production and $W^{\pm}$ and Z° production. All spin observables in $pp \rightarrow jet + jet + X$ should then be calculable, beginning at Q^2 values where higher twist effects must be included and extending out to Q^2 where only leading twist should be important. These measurements can easily be made at polarized RHIC and afford stringent tests of QCD and of current models of the nucleon. Measurement of parity-violating asymmetries in weak boson production can further test the standard model and probe the possible substructure of quarks.

Recent theoretical work (see, e.g., Reference 8) seems to favor chiral soliton models of the nucleon over naive quark model ideas to explain the helicity structure function g_1 measured at CERN and SLAC. On the other hand, the hyperon polarization and spin transfer and the analyzing power in high-x meson production with polarized proton and antiproton beams are nicely fit into a consistent scheme using a constituent quark model.[36] These results have been interpreted as showing the existence of orbiting valence quarks inside polarized protons.[37] We are, therefore, confronted with the challenge of relating constituent quarks to the chiral picture of the nucleon.

---

[33] J. Ashman *et al.*, Phys. Lett. B206 (1988) 364; Nucl. Phys. B328 (1989) 1.
[34] B. Adeva *et al.*, Phys. Lett. B302 (1993) 533.
[35] J. Ellis and M. Karliner, CERN-TH-6898/93, May 1993.
[36] D.L. Adams *et al.*, Phys. Lett. B261 (1991), 201; Z. Phys. C56 (1992), 181; A. Yokosawa, Proc. XXI Int. Symp. on Multiparticle Dynamics, Wuhan, China, Sept. 1991, p. 545.
[37] C. Boros, Liang Zuo-tang and Meng Ta-chung, Phys. Rev. Lett. 70 (1993) 1751.

Measurement of all of the spin structure functions of the proton (quark, gluon, helicity, and transversity) at polarized RHIC would constitute a significant and important physics program.[38,39,40] These structure functions could then be used to make detailed tests of QCD by measurement of spin asymmetries in hadronic scattering processes, which would allow the most detailed test of QCD and our understanding of the nucleon that have ever been made. The addition of the EMC would also increase the capability of STAR for searching for the quark-gluon plasma (QGP) and afford complimentary tests of QCD at modest cost.

2.B.1. Status of Present Knowledge

Experimental programs using polarized beams and/or polarized targets at high energies have been active during the past three decades. Many asymmetry measurements in a number of scattering processes (e.g., elastic scattering, deep inelastic scattering, and inclusive meson production) have been carried out at various laboratories in the world. As unique measurements often bring surprises, many exciting and unexpected results in hadron-hadron and muon-nucleon scattering have been observed using polarized beams and/or targets. These include large spin effects in pp elastic scattering,[41,42,43] inclusive pion production,[44,45,46,47,48,49,50,51,52] and in ρ production.[53] The importance of spin as a fundamental degree of freedom has also been observed experimentally in deep inelastic lepton scattering[54,55] and hyperon production.[56,57,58,59,60,61] Thus far, experiments with polarized proton beams have been limited to about 200 GeV/c. It is extremely important to explore spin effects at much higher energies where high p_t phenomena as well as parity-violating asymmetries in $W^{\pm}$ and Z° production can be studied.

Some information about the spin composition of the proton is obtained from asymmetry measurements in the deep inelastic scattering of longitudinally polarized muons or electrons on longitudinally polarized protons at SLAC and CERN. At present, it is yet to be determined how the spin of the proton is carried by valence quarks, sea quarks, gluons, and orbital angular

[38] C. Bourrely, J.Ph. Guillet, and J. Soffer, Nucl. Phys. **B361** (1991) 72.
[39] M.A. Doncheski, F. Halzen, C.S. Kim, and M.L. Stong, University of Wisconsin report MAD/PH/744 (1993).
[40] For a review of spin physics possible at RHIC, see proceedings of the Polarized Collider Workshop, AIP Conference Proceedings No. 223, University Park, PA, 1990.
[41] R.V. Kline *et al.*, Phys. Rev. **D22** (1980) 553.
[42] G. Fidecaro *et al.*, Phys. Lett. **105B** (1981) 309.
[43] F.Z. Khiari *et al.*, Phys. Rev. **D39** (1989) 45.
[44] L. Dick *et al.*, Phys. Lett. **57B** (1975) 93.
[45] R.D. Klem *et al.*, Phys. Rev. Lett. **36** (1976) 929.
[46] D. Aschman *et al.*, Nucl. Phys. **B142** (1978) 220.
[47] W.H. Dragoset *et al.*, Phys. Rev. **D18** (1978) 3939.
[48] J. Antille *et al.*, Phys. Lett. **94B** (1980) 523.
[49] S. Saroff *et al.*, Phys. Rev. Lett. **64** (1990) 995.
[50] V.D. Apokin *et al.*, Phys. Lett. **243B** (1990) 461.
[51] B.E. Bonner *et al.*, Phys. Rev. Lett. **61** (1988) 1918.
[52] D.L. Adams *et al.*, Phys. Lett. **261B** (1991) 197; Phys. Lett. **261B** (1991) 201; Phys. Lett. **264B** (1991) 462; Phys. Lett. **276B** (1992) 531; Z. Phys. **C56** (1992) 181.
[53] S. Heppelmann *et al.*, Phys. Rev. Lett. **55** (1985) 1824.
[54] J. Ashman *et al.*, Phys. Lett. **B206** (1988) 364; Nucl. Phys. **B328** (1989) 1.
[55] B. Adeva *et al.*, Phys. Lett. **B302** (1993) 533.
[56] G. Bunce *et al.*, Phys. Rev. Lett. **36** (1976) 1113.
[57] S. Erhan *et al.*, Phys. Lett. **82B** (1979) 301.
[58] B.E. Bonner *et al.*, Phys. Rev. **D38** (1988) 729.
[59] L.G. Pondrom, Phys. Rep. **127** (1985) 57 and references therein.
[60] B. Lundberg *et al.*, Phys. Rev. **D40** (1989) 3557.
[61] K.B. Luk *et al.*, Phys. Rev. Lett. **70** (1993) 900.

momentum. It was expected that the valence and sea quarks would account for a substantial fraction of the net proton spin. There is evidence which suggests, however, that the net spin-angular-momentum contributed directly by the quark constituents of the proton is small. On the other hand, when interpreted in terms of quark-antiquark annihilation processes, single spin inclusive meson production using 200 GeV/c polarized proton and anti-proton beams suggests the existence of orbiting valence quarks inside polarized protons.[62] Thus, it is possible that valence quarks may contribute to the proton spin primarily through orbital angular momentum.

Programs to test quantum chromodynamics and explore the electro-weak coupling at CERN and Fermilab have provided a wealth of information on the Standard Model of particle physics. However, these experiments at high-energy colliders do not cover the area of spin physics. Tests involving the spin-dependence in fundamental scattering processes such as jet, direct photon, Drell-Yan, and $W^{\pm}$, Z° boson production are yet to be carried out.

Polarized proton-proton collisions have previously been limited to a relatively low range of $\sqrt{s}$ and Q^2. Large polarization effects have been seen in many different experiments. In spite of this, spin physics has been relegated to a "soft physics" compartment in high energy physics, since interpretation of these data using QCD has been problematic. A comprehensive program of spin physics experiments at RHIC using the STAR EMC would allow measurement of the spin-dependent parton distributions of the proton (both longitudinal and transverse) and would provide fundamental spin tests of QCD and the electro-weak interaction. The high energy and luminosity at RHIC will permit experiments in which an interpretation in terms of perturbative QCD will be unambiguous.

In the following sections, we present estimates of the acceptance of STAR and expected event rates will be discussed for several reactions of interest.

In general, the luminosity at RHIC for pp running is energy dependent. The integrated luminosities used to calculate event rates discussed below are:

$$\int \mathcal{L} dt = 8 \cdot 10^{38} \text{cm}^{-2} \sim 800 \text{ pb}^{-1} \quad , \tag{2.B-1}$$

at 500 GeV, assuming $\mathcal{L} = 2 \times 10^{32}$ cm^{-2} sec^{-1}, and

$$\int \mathcal{L} dt = 3.2 \cdot 10^{38} \text{cm}^{-2} \sim 320 \text{ pb}^{-1} \quad , \tag{2.B-2}$$

at 200 GeV, assuming $\mathcal{L} = 8 \times 10^{31}$ cm^{-2}sec^{-1}. The beam polarization is assumed to be 0.7. The assumed running time is 100 days at 50% efficiency, or 4×10^6 sec.

2.B.2. The Gluon Spin Distribution of the Proton

Information on the gluon spin distribution in polarized protons can be obtained by measuring asymmetries in the cross section for various scattering processes which depend on the helicities of the colliding beams. Such processes include inclusive direct-γ production, inclusive jet production, and direct-γ-jet and jet-jet coincidences. Inclusive direct-γ and direct-γ+ jet production in pp interactions are dominated by a single parton-level subprocess,

$$q + g \rightarrow \gamma + q \quad , \tag{2.B-3}$$

[62] C. Boros, Liang Zuo-tang and Meng Ta-chung, Phys. Rev. Lett. **70** (1993) 1751.

and determining the spin-dependent gluon distribution of the proton from these processes is straightforward. On the other hand, inclusive jet and jet-jet production contain contributions from many parton-level subprocesses (e.g., gg, qq, qg, etc. scattering), and extraction of the spin-dependent gluon structure function using these processes is more difficult, despite their increased cross section. Consider the hadronic reaction, pp → (hadron or gauge boson) + X. When both initial protons are longitudinally polarized with polarization P, we measure an observable A_{LL} defined as,

$$A_{LL} = (1/P^2)(N^{++} - N^{+-})/(N^{++} + N^{+-}) \quad , \tag{2.B-4}$$

where N^{+-}, for example, is the yield observed when the helicities of the two colliding beams are anti-aligned. If one QCD subprocess is dominant, then

$$A_{LL} \sim P_a P_b \hat{a}_{LL(a+b\to c+d)} \quad , \tag{2.B-5}$$

where P_a and P_b are the polarizations of partons a and b in the proton, and $\hat{a}_{LL}$ is the parton-level asymmetry for a given subprocess.

For the determination of the gluon spin distribution, measurements of direct-γ, direct-γ with away-side jet, jet, and di-jet production are proposed.

Direct-γ Production

Direct photons are produced through $q\bar{q}$ annihilation and the q-g Compton subprocess, $qg \to \gamma q$. The Compton process is the dominant one in pp interactions at mid-rapidity since there are no valence antiquarks in the proton. Then,

$$A_{LL} \sim \left\langle [\Delta u(x_1)/u(x_1)] \cdot [\Delta G(x_2)/G(x_2)] \cdot \hat{a}_{LL(qg\to\gamma q)} \right\rangle \quad , \tag{2.B-6}$$

where the u quark polarization is $\Delta u(x)/u(x) = [u_+(x) - u_-(x)]/[u_+(x) + u_-(x)]$, and $\Delta u(x)$ is the u quark helicity distribution. Similarly, the gluon polarization is $\Delta G(x)/G(x) = [G_+(x) - G_-(x)]/[G_+(x) + G_-(x)]$, and $\Delta G(x)$ is the helicity distribution carried by gluon fields. The average in Eq. (2B-6) is taken over the allowed kinematic range for the outgoing quark jet.

From deep inelastic scattering measurements, for example, $\Delta u(x)/u(x) \sim 0.4$ for x Bjorken of $x_q \sim 0.2$. For the Compton process, $\hat{a}_{LL} \approx 0.6$ at $\theta = 90°$ in the parton cm frame. Consequently,

$$A_{LL} \cong 0.2 \times (\Delta G/G) \tag{2.B-7}$$

and the uncertainty in the gluon polarization is related to the uncertainty in the measured asymmetry by

$$\delta(\Delta G/G) \cong 5 \times \delta A_{LL} \tag{2.B-8}$$

With the proposed STAR barrel electromagnetic calorimeter ($|\eta| \leq 1$), using 1-cm-wide scintillator strips for the shower maximum detector, the estimated uncertainty in the measured asymmetry for 10 GeV/c $\lesssim p_t \lesssim$ 20 GeV/c is

$$\delta A_{LL} \sim \pm 0.0012 \sqrt{8 \times 10^{38}\,\mathrm{cm}^{-2} / \int \mathcal{L}\,dt} \quad , \tag{2.B-9}$$

at $\sqrt{s}$ = 500 GeV; at $\sqrt{s}$ = 200 GeV,

$$\delta A_{LL} \sim \pm 0.006 \sqrt{3.2 \times 10^{38}\,\mathrm{cm}^{-2} / \int \mathcal{L}\,dt} \quad . \tag{2.B-10}$$

Theoretical estimates of the asymmetry, A_{LL}, have been performed assuming both large ($\langle \Delta G \rangle \sim$ 2–3 $\hbar$) and small ($\langle \Delta G \rangle \sim \hbar/2$) gluon polarization. The results are presented in Fig. 2B-1, in which it is noted that at $p_t \sim 10$ GeV/c, in order to distinguish between these two cases, it is necessary to reduce the uncertainty in A_{LL} to $\delta A_{LL} \lesssim \pm 0.01$. From Eqs. 2.B-2 and 2.B-10 for example, it is noted that for the design luminosity at $\sqrt{s}$ = 200 GeV, this sensitivity will be achieved by the STAR detector in a run of ~1 month.

Direct-γ Production with Away-Side Jet Detection

In order to measure the x dependence of the gluon helicity distribution, ΔG(x), both the direct-γ and the away-side jet must be detected in coincidence so that the kinematics of the incoming partons can be calculated (see the next section for a discussion of jet detection).

For the STAR barrel EMC, it is possible to study γ-jet events in which $-0.3 < \eta_{jet} < 0.3$ and $-1.0 < \eta_\gamma < 1.0$. (With corrections for missing acceptance, it may be possible to extend the coverage for jets such that $|\eta_{jet}| \leq 0.5$ is possible.) For a p_t acceptance of 10–20 GeV/c, x_1 and x_2 can then vary from 0.05 to 0.2 at $\sqrt{s}$ = 200 GeV. Restricting the p_t interval to 15–20 GeV/c, the corresponding cross section is 28 pb, and the estimated uncertainty in A_{LL} is,

$$\delta A_{LL} \sim \pm 0.034 \sqrt{3.2 \times 10^{38}\,\mathrm{cm}^{-2} / \int \mathcal{L}\,dt} \tag{2.B-11}$$

The acceptance in rapidity for the gamma and jet is shown in Fig. 2B-2 for both the STAR EMC barrel and the barrel with the addition of a pair of endcap calorimeters. For reference, the momentum fractions for the quark and gluon have been noted as well. From Fig. 2B-2, it is evident that to study ΔG(x) in the x range of interest ($x_q \gtrsim .2$–.3), the additional acceptance

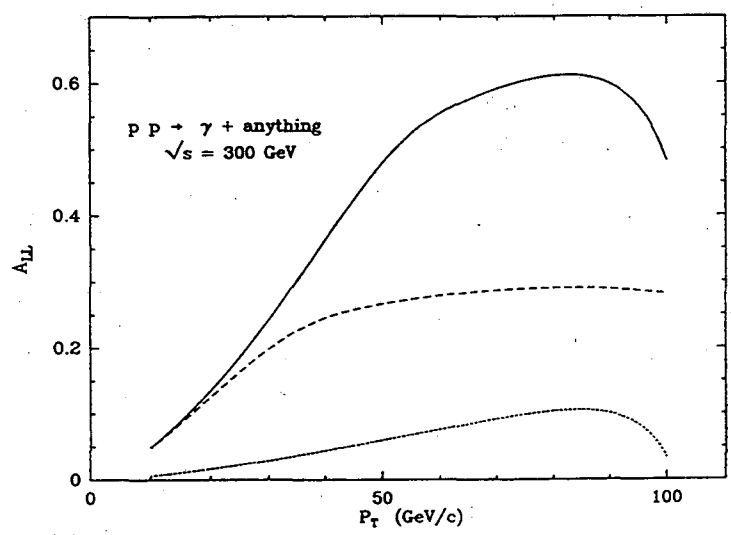

Figure 2B-1. The asymmetry A_{LL} predicted for inclusive direct-γ production at $\theta_{cm} = 90°$ in the parton center of mass frame in the event of large (dashed) and small (dotted) gluon polarization ΔG. The asymmetry for large gluon polarization is also shown for $\theta_{cm} = 45°$ (solid). At $p_t \sim$ 10 GeV/c, an uncertainty $\delta A_{LL} \approx \pm .01$ is required to distinguish between large and small gluon polarization. This sensitivity will be achieved with the proposed STAR barrel EMC in a run of ~1 month. Details of the calculation may be found in Reference 6.

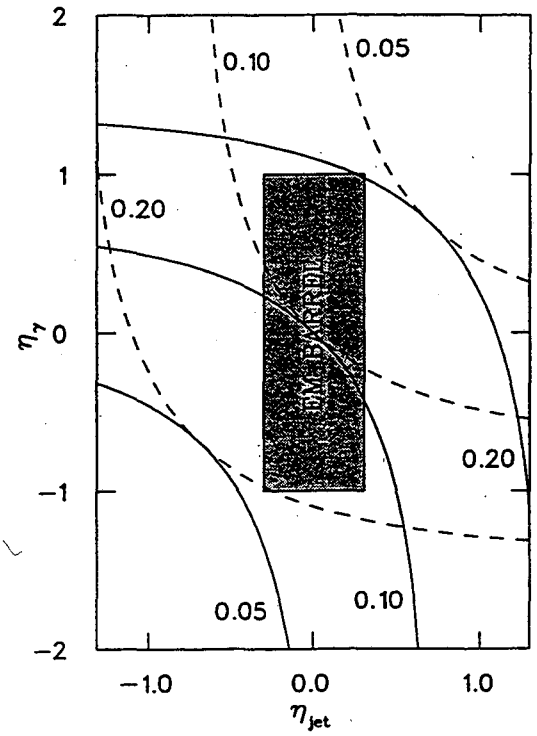

Figure 2B-2. The momentum fractions x_1 (solid) and x_2 (dashed) of the quark and gluon plotted as a function of the direct-γ and jet pseudorapidities. Data shown are for $p_t \cong 10$ GeV/c at $\sqrt{s} = 200$ GeV, and assume the full acceptance of the barrel and endcap calorimeters. The dark region in the center of the plot indicates the acceptance of the EMC barrel alone.

provided by the endcap calorimeters is necessary. The x acceptance for the gluon, assuming $x_q \gtrapprox .2$–.3, is shown for the STAR EMC with and without the endcap calorimeters in Fig. 2B-3 and Fig. 2B-4 respectively, from which it is again evident that the acceptance for direct-γ + jet events of interest (i.e., $x_q \sim 0.2$–0.3, $p_t \sim 10$ GeV/c) is improved substantially with the addition of the endcap calorimeters. The yield as a function of x_{BJ} for the gluon is shown in Fig. 2B-5, assuming the acceptance is that of the barrel and endcap calorimeters and x_{BJ} of the quark is 0.2–0.3. From Fig. 2B-5 it is noted that the yield of direct-γ + jet events in the most interesting kinematic region for studying $\Delta G(x)$ is ~6500 per month. The data shown in Fig. 2B-5 are for $\sqrt{s}$ = 200 GeV and p_t = 10–20 GeV/c. The following table (Table 2B-1) gives the estimated uncertainty (δA_{LL}) in the asymmetry for direct-γ+ jet production for various combinations of x Bjorken for the quark and the gluon. From Table 2B-1, it is noted that in a standard 100-day run, the value of the gluon polarization, $\Delta G(x)/G(x)$, can be measured with an uncertainty of ~±(5–15)% in a range of x from ~0.05–0.2.

Single-Jet Production

Several QCD subprocesses contribute to the cross section for jet production:

- Gluon-gluon scattering at low p_t ($gg \rightarrow gg$)
- Gluon-quark scattering at medium p_t (above ~20 GeV/c), ($gq \rightarrow gq$), and
- Quark-quark elastic scattering at high p_t ($qq \rightarrow qq$)

At low p_t, gluon-gluon scattering is expected to be the largest contribution to inclusive jet production, and to first order, therefore,

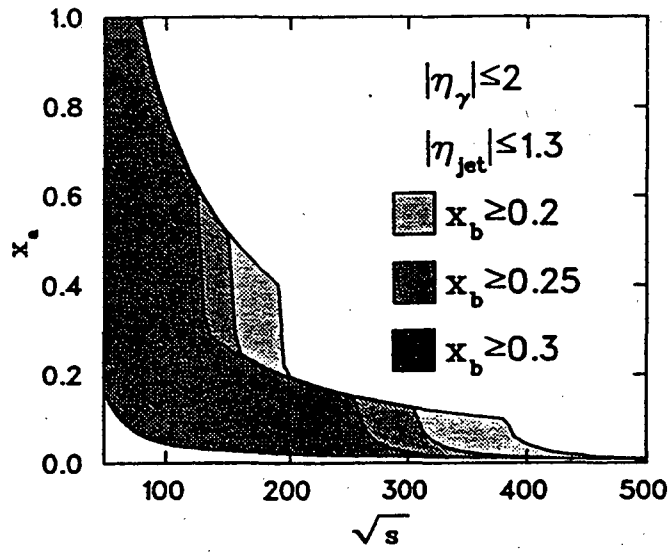

Figure 2B-3. As a function of $\sqrt{s}$, the range of x_{BJ} of the gluon (x_a) in which the STAR detector has acceptance assuming the momentum fraction of the quark is $x_{BJ} \gtrsim 0.2$–0.3. The data shown are for $p_t \equiv$ 10 GeV/c, and assume the full acceptance of the barrel and endcap calorimeters. The acceptance in x_a determines the kinematic region in which the Compton subprocess, $q + g \rightarrow \gamma + q$, can be studied.

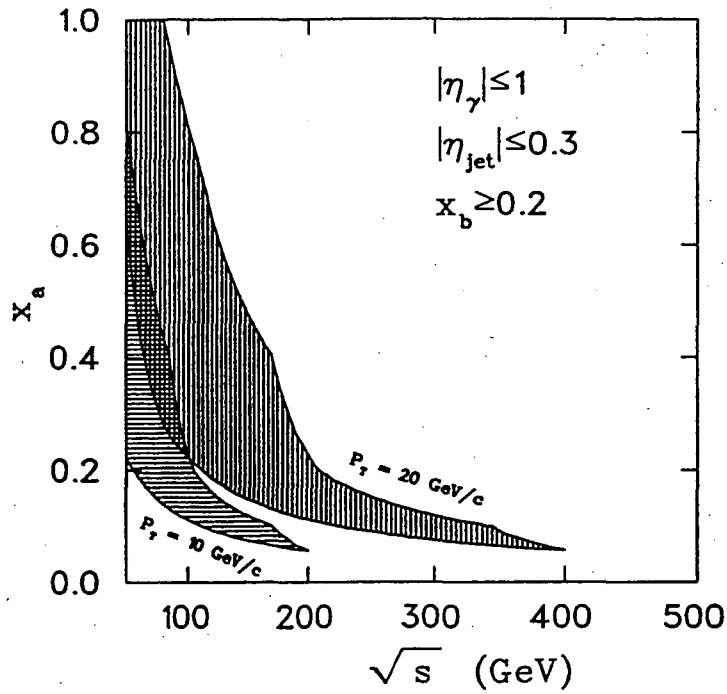

Figure 2B-4. As a function of $\sqrt{s}$, the range of x_{BJ} of the gluon (x_a) in which the STAR detector has acceptance, assuming the momentum fraction of the quark is $x_{BJ} \gtrsim 0.2$. The data shown are for $p_t \equiv$ 10 GeV/c and $p_t \equiv$ 20 GeV/c and assume the acceptance of the barrel calorimeter only. The acceptance in x_a determines the kinematic region in which the Compton subprocess, $q + g \rightarrow \gamma + q$, can be studied.

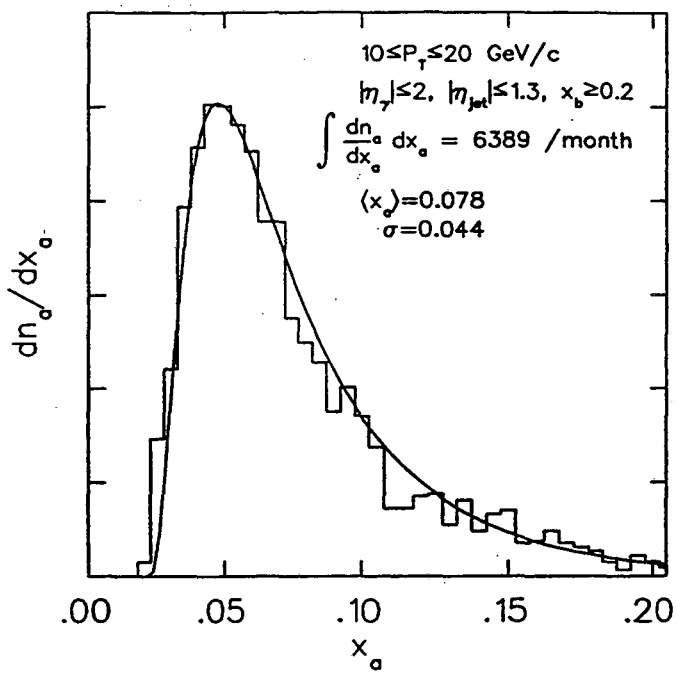

Figure 2B-5. The yield, as a function of x_a of the gluon, of events in which the momentum fraction of the quark is $x_b \gtrsim 0.2$. Data shown are for 10 GeV/c $\leq p_t \leq$ 20 GeV/c at $\sqrt{s}$ = 200 GeV, and assume the full acceptance of the barrel and endcap calorimeters. Interpretation of the yield indicates there are ~6500 direct-γ+ jet events per month in the kinematic region of interest.

$$A_{LL} = [\Delta G(x_1)/G(x_1)] \times [\Delta G(x_2)/G(x_2)] \times \hat{a}_{LL(gg \to gg)} \quad , \qquad (2.B\text{-}12)$$

where $\hat{a}_{LL}$ is ~0.8 for scattering at 90° in the parton cm frame.

Jets will be reconstructed in STAR using the EM calorimeter to measure the electromagnetic component, and the TPC to detect charged particles (see, for example, Section 4.A.2). Monte Carlo studies of the rates, acceptance, and resolution were made using the ISAJET program using the EHLQ1 structure functions and GEANT.

Table 2B-1. The Estimated Uncertainty in the Direct-γ+ Jet Asymmetry, δA_{LL}, for Various Combinations of the Quark ($max(x_1,x_2)$) and Gluon ($min(x_1,x_2)$) Kinematics.

		$max(x_1,x_2)$			
		≤0.2	0.2–0.3	0.3–0.4	>0.4
$min(x_1,x_2)$	0.00–0.05		0.012	0.009	0.007
	0.05–0.10	0.006	0.006	0.010	0.012
	0.10–0.15	0.007	0.010	0.020	0.030
	0.15–0.20	0.021	0.019	0.038	0.060
	>0.20		0.035	0.049	0.073

In the calculations, it was assumed that particles within a core of radius $\sqrt{(\Delta\eta)^2 + (\Delta\phi)^2} \lesssim 0.7$ were part of the jet. Further discussion of jets in the STAR EMC may be found in Sections 2.A.2 and 3.D. The yield is quite high, as indicated in the following section.

Di-Jet Production

Since, in general, several QCD subprocesses contribute to the cross section for jet production, and the relative importance of each varies with the kinematic region which is studied, direct-γ + jet production from the Compton subprocess $qg \rightarrow \gamma q$ provides the best means of studying the spin-dependent gluon distribution $\Delta G(x)$. However, for di-jets of low invariant mass (M_{JJ}), gluon-gluon subprocesses dominate, and the measured asymmetry, A_{LL}, may then be used to provide information similar to that extracted for direct-γ + jet production (c.f., Equations 2.B-12 and 2.B-6).

When two back-to-back jets are detected, the kinematics of the incoming partons can be reconstructed to within a small correction which depends upon their intrinsic p_t. The reconstructed value of x_{BJ} for each parton may then be used to compute the parton-level subprocess asymmetry, $\hat{a}_{LL}$. The measured value of A_{LL} then determines the parton polarization. Thus, di-jet production may be used to provide an independent measurement of the spin-dependent structure functions such as $\Delta G(x)$, and in general, provides useful tests of QCD. The yield of di-jet events having $M_{JJ} \geq 20$ GeV was estimated for the STAR acceptance using the Monte Carlo discussed in the previous section. The results for $\sqrt{s} = 200$ GeV are presented in Table 2B-2.

2.B.3. Asymmetries in Inclusive $W^{\pm}$ and Z° Production

Inclusive $W^{\pm}$ and Z° production at RHIC will be a powerful tool for investigating some parton distributions in the proton, and perhaps also in light nuclei. This is due in part to the large cross section for $W^{\pm}$ and Z° production—which is much larger than for Drell-Yan production in the x range of interest—and in part to the V-A coupling of the W. With polarized beams, the sea quark polarization and the difference between the valence u and d quark polarizations can be measured through the study of asymmetries which depend upon these distributions such as

$$A_{Lpv} = \frac{\Delta u(x_1)\bar{d}(x_2) - \Delta\bar{d}(x_1)u(x_2)}{\Delta u(x_1)\bar{d}(x_2) + \Delta\bar{d}(x_1)u(x_2)} \qquad \text{(2.B-13)}$$

It is noted that the parton momentum fraction x for production of a "transverse mass" $M_T \sim 40$ GeV at RHIC is approximately $x = M_T/\sqrt{s} \sim 0.1$–$0.25$. On the other hand, because of the increased energy range studied, LHC and SSC will probe much smaller x values. Thus, RHIC is unique for studying some parton distributions in this kinematic region using inclusive $W^{\pm}$ and Z° production as probes.

Table 2B-2. The Yield of Di-Jet Events in the STAR Acceptance Having $M_{JJ} \geq 20$ GeV.

	M_{JJ} (GeV)	$\lvert\eta\rvert$	N_{pair}
Barrel EM	≥20	≤0.3	$3 \cdot 10^6$
Barrel plus endcaps	≥20	≤1.3	$1 \cdot 10^8$

With the addition of an electromagnetic calorimeter, the STAR detector is especially well suited for the measurement of inclusive $W^{\pm}$ and Z° production due to its large acceptance for electrons produced by high mass particle decays. The rates for $W^{\pm}$ and Z° decays to electrons within the STAR detector acceptance have been calculated by Derevschikov and Rykov.[63] At $\sqrt{s} = 500$ GeV, these cross sections were estimated from the PYTHIA program to be

$$\begin{aligned} \sigma(pp \rightarrow W^+ + X \rightarrow e^+ + \nu + X) &= 120 \text{ pb} \\ \sigma(pp \rightarrow W^- + X \rightarrow e^- + \nu + X) &= 43 \text{ pb} \\ \sigma(pp \rightarrow Z^{\circ} + X \rightarrow e^+e^- + X) &= 10 \text{ pb} \quad . \end{aligned} \tag{2.B-14}$$

The corresponding total number of events detected at $\sqrt{s} = 500$ GeV in an idealized detector for the integrated luminosity 800 pb^{-1} are

Boson	STAR (Barrel)	STAR (Barrel+Endcaps)
$W^+ + W^-$	83,000	110,000
W^+	61,000	80,000
W^-	22,000	30,000
Z°	3,840	7,200

Background simulations, using the depth segmentation capabilities of the STAR EMC design for electron/hadron separation, are in progress. It is anticipated that STAR will be able to detect adequate numbers of W and Z events for much of the physics described below.

Two recent theoretical papers describe interesting results that can be obtained on parton distributions from $W^{\pm}$ and Z° production. Bourrely and Soffer[64] calculate the unpolarized cross sections for $W^{\pm}$ and Z° production at RHIC using various assumptions for the sea quark distributions. The sensitivity of this measurement to the sea quark distribution is shown in Fig. 2B-6 in which differences of a factor of 2–3 are seen in the central region, where the cross sections are largest. Doncheski *et al.*[65] compute a charge asymmetry from single lepton production with unpolarized beams

$$\varepsilon^{\ell} = \frac{\frac{d\sigma}{d\eta}(\ell^-) - \frac{d\sigma}{d\eta}(\ell^+)}{\frac{d\sigma}{d\eta}(\ell^-) + \frac{d\sigma}{d\eta}(\ell^+)} \quad , \tag{2.B-15}$$

which is compared to recent measurements at CDF.[66] From this analysis, it is shown that at SSC, LHC, and Tevatron energies, ε^{ℓ} is sensitive to the difference $d_v - u_v$ in the valence quark distributions. In contrast, this asymmetry is shown to be sensitive to the difference $d_s - u_s$ in the sea quark distributions at RHIC. Furthermore, the charge asymmetry for W production at $\bar{p}p$

[63] A.A. Derevschikov and V.L. Rykov, Brookhaven National Laboratory report RSC-BNL/IHEP-4 (1992).
[64] C. Bourrely and J. Soffer, Marseille preprint CPT-93, p. 2865 (1993), submitted to Phys. Lett.
[65] M.A. Doncheski, F. Halzen, C.S. Kim, and M.L. Stong, University of Wisconsin report MAD/PH/744 (1993).
[66] F. Abe *et al.*, Phys. Rev. Lett. **68** (1992) 1458.

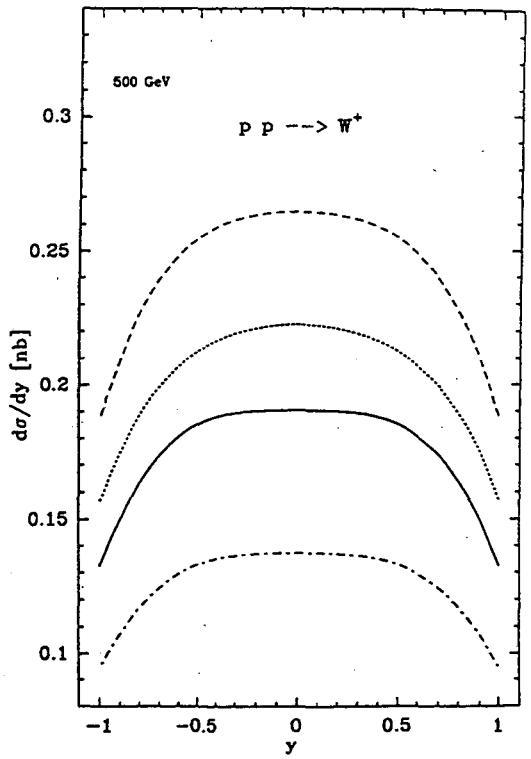

Figure 2B-6. $d\sigma/dy$ versus y for W^+ production at $\sqrt{s}$ = 500 GeV, for different choices of the sea antiquark distributions. The solid line corresponds to Eichten et al.,[67] the dashed dotted line to Bourrely et al., [68] and the dashed line to Martin et al.[69] The small dashed line corresponds to Martin et al. with the number of u and d antiquarks being equal.

colliders is shown to be small at small η, where the cross section is large. Thus, measurements of ε^{ℓ} at RHIC offer a unique sensitivity to the difference $d_s - u_s$ in the distribution of sea partons.

A number of other asymmetries can be computed when one or both of the proton beams are polarized. A practical advantage of measuring asymmetries is that certain systematic errors, such as detector efficiencies and absolute luminosities, cancel. A second asymmetry calculated by Doncheski *et al.* is similar to that for ε^{ℓ} and A_{LL} above:

$$\varepsilon^{e}_{LL} = \frac{\left[\frac{d\sigma^{++}}{d\eta}(e^+) - \frac{d\sigma^{+-}}{d\eta}(e^+)\right] - \left[\frac{d\sigma^{++}}{d\eta}(e^-) - \frac{d\sigma^{+-}}{d\eta}(e^-)\right]}{\left[\frac{d\sigma^{++}}{d\eta}(e^+) + \frac{d\sigma^{+-}}{d\eta}(e^+)\right] + \left[\frac{d\sigma^{++}}{d\eta}(e^-) + \frac{d\sigma^{+-}}{d\eta}(e^-)\right]} \quad , \tag{2.B-16}$$

where $d\sigma/d\eta(e^+)$, for example, is the cross section for e^+ production and the + and − superscripts on $d\sigma/d\eta$ correspond to the helicities of the colliding beams. In this case, it is shown that with appropriate cuts to eliminate $e^{\pm}$ background from sources other than $W^{\pm}$ decay, ε^{e}_{LL} is sensitive to both the spin distribution of the sea quarks and to the difference $\Delta d - \Delta u$ of the d and u quark spin distributions. A measurement of the gluon spin distribution using

[67] E.J. Eichten, I. Hinchliffe, and C. Quigg, Phys. Rev. **D45** (1992) 2269.
[68] C. Bourrely *et al.*, Phys. Rep. **177** (1989) 319.
[69] A.D. Martin *et al.*, Preprint **RAL**-92-021 (1992).

inclusive direct-γ + jet production, should reduce uncertainties in the sea quark spin distribution sufficiently to permit the determination of $\Delta d - \Delta u$ from ε_{LL}^{e}.

Besides the usual two-spin asymmetries which depend only on the helicities of the colliding beams, there are spin asymmetries that depend on both the helicity and the charge and momenta. The single spin longitudinal asymmetry

$$A_{pv} = \frac{\frac{d\sigma^-}{d\eta} - \frac{d\sigma^+}{d\eta}}{\frac{d\sigma^-}{d\eta} + \frac{d\sigma^+}{d\eta}} \tag{2.B-17}$$

is the best known example. There is also a two-spin parity-violating asymmetry

$$A_{LL,pv} = \frac{\frac{d\sigma^{++}}{d\eta} - \frac{d\sigma^{--}}{d\eta}}{\frac{d\sigma^{++}}{d\eta} - \frac{d\sigma^{--}}{d\eta}} \quad , \tag{2.B-18}$$

which is zero by reflection symmetry for parity conserving processes. Note that $(d\sigma/d\eta)^{--}$ has purely left-handed current inputs, and $(d\sigma/d\eta)^{++}$ has only right-handed current inputs.

These last two parity-violating asymmetries are discussed by Bourrely and Soffer.[70] Calculations for the energy range at RHIC are presented using various assumptions about the sea quark polarization. In the central region near $\eta = 0$, large differences are seen between the predictions for $\Delta\bar{u} \neq 0$ and $\Delta\bar{u} = 0$, given the constraints imposed by measurements of deep inelastic lepton scattering at CERN and SLAC.[71,72] Measurement of these parity-violating asymmetries should therefore be useful in obtaining information about the sea quark spin distributions in the proton.

2.B.4. High-Energy Drell-Yan Electrons and the Sea Quark Polarization

The study of Drell-Yan pair production appears to be another way to determine the polarization of sea quarks. The $q\bar{q}$ annihilation into a vector boson gives a large asymmetry on a partonic level and selects sea antiquarks along with valence quarks.

The asymmetry A_{LL} for Drell-Yan production in pp collisions is related to the sea quark helicity distribution $\Delta q(x)$,

$$A_{LL} = \hat{a}_{LL} \frac{\sum_i e_i^2 \left[\Delta q_i(x_1)\Delta\bar{q}_i(x_2) + \Delta q_i(x_2)\Delta\bar{q}_i(x_1)\right]}{\sum_i e_i^2 \left[q_i(x_1)\bar{q}_i(x_2) + q_i(x_2)\bar{q}_i(x_2)\right]} \quad , \tag{2.B-19}$$

where $x_1 - x_2 = x_F$, $x_1 x_2 = M^2/s$, M is the mass of the pair, e^2 is the square of the parton charge, and $\hat{a}_{LL} = -1$. The sum in Equation 2.B-19 is taken over parton flavor.

---

[70] C. Bourrely and J. Soffer, Marseille preprint CPT-93, p. 2865 (1993), submitted to Phys. Lett.
[71] J. Ashman *et al.*, Phys. Lett. **B206** (1988) 364; Nucl. Phys. **B328** (1989).
[72] B. Adeva *et al.*, Phys. Lett. **B302** (1993) 533.

To determine if the study of Drell-Yan production might be possible, the PYTHIA event generator was used to estimate the yield in an **ideal** detector with the same total acceptance as the STAR barrel and endcap calorimeters. The results are presented in Table 2B-3 for a standard 100 day running period at $\sqrt{s}$ = 200 GeV. Further simulation is necessary to determine the feasibility of observing Drell-Yan pair production given the STAR tracking and trigger capabilities for $|\eta| \gtrsim 1.6$.

2.B.5. Transverse Quark Structure Functions of the Proton

From deep inelastic scattering, one can measure the structure function $f_1(x)$ which is related to the longitudinal momentum distribution of quarks in the nucleon and $g_1(x)$ which is related to the helicity distribution in a polarized nucleon. There exists a third fundamental partonic structure function, $h_1(x)$, which is a leading-twist (twist-2) distribution function like $f_1(x)$ and $g_1(x)$. This distribution can be determined by measuring the transverse spin asymmetry A_{NN} in Drell-Yan processes.

$$A_{NN} = \left(\frac{1}{P^2}\right)\left(N^{\uparrow\uparrow} - N^{\uparrow\downarrow}\right) / \left(N^{\uparrow\uparrow} + N^{\uparrow\downarrow}\right) \tag{2.B-20}$$

where P is the transverse polarization of the beam and $N^{\uparrow\downarrow}$, for example, is the yield of Drell-Yan pairs when the beams are transversely polarized in opposite directions. In terms of $h_1(x)$, A_{NN} is given as:

$$A_{NN} = \hat{a}_{NN}\left[\sum_a e_a^2 h_1^a(x_1) h_1^{\bar{a}}(x_2)\right] / \left[\sum_a e_a^2 f_1^a(x_1) f_1^{\bar{a}}(x_2)\right] \quad , \tag{2.B-21}$$

where e_a^2 is the square of the electric charge for a given parton flavor a, $\hat{a}_{NN}$ is the partonic double-spin asymmetry, and the sum is over parton flavor.

Simulations performed with PYTHIA indicate that for an **ideal** detector the yield of Drell-Yan pairs entering the combined acceptance of the STAR barrel and endcap calorimeters would be ~28,000 in the mass region of 5–9 GeV. Further simulation is necessary to determine the feasibility of observing Drell-Yan pair production given the STAR tracking and trigger capabilities for $|\eta| \lessapprox 1.6$.

2.B.6. Higher Twist Effects

Single transverse spin asymmetries are expected to vanish in lowest order, perturbative QCD. Even though the asymmetries vanish at the leading, or "twist-2" level, this is no longer true when higher order, "twist-3" diagrams are taken into account. For example, a large single spin asymmetry has been predicted in inclusive direct-γ production ($p^{\uparrow}p \rightarrow \gamma + X$) by Qiu and

Table 2B-3. The Estimated Yield of Drell-Yan Pairs into the Acceptance of the STAR Barrel and Endcap Calorimeters.

M_{ee}, GeV/c^2	5–9	9–12	12–15	15–20
	28,000	20,000	8,400	5,400

Sterman.[73] Experimentally, large single spin asymmetries were found in Fermilab experiments on inclusive π° production ($p^\uparrow p \rightarrow \pi^\circ + X$) up to $p_t = 4$ GeV/c. Qiu and Sterman interpret these data in terms of a twist-3 parton distribution, which involves the correlation between the quark and gluon field strength.

The event rate for direct-γ production can be estimated for the EMC barrel as in Section 2.B-2. The corresponding estimate for the uncertainty in the single transverse spin asymmetry is

$$\delta A_N \sim \pm 0.006 \sqrt{3.2 \times 10^{38}\,\mathrm{cm}^{-2} / \int \mathcal{L} dt} \qquad \text{(2.B-22)}$$

[73] J. Qiu and G. Sterman, Phys. Rev. Lett. 67 (1991) 2264.

3.

Trigger Capability

3. TRIGGER CAPABILITY

3.A. Use of the STAR EMC for Event Selection in AA Interactions

The most interesting collisions at RHIC are those that produce the highest densities and temperatures. This is thought to be the most promising environment in which to search for novel phenomena and signatures of a deconfined phase of quarks and gluons. The most characteristic feature of these conditions is expected to be the observation at mid-rapidity of a high multiplicity of particles ($dn\pi/d\eta \sim 1000$) and high transverse energy deposition. If the mean p_t per particle and the global ratio of neutral to charged energy do not vary significantly from event to event, central triggers based upon the multiplicity of charged particles at mid-rapidity or the total energy deposited in the electromagnetic barrel calorimeter are essentially equivalent, as has been found in heavy ion experiments at low energies. Thus, the most interesting physics may be found by triggering on events in which this assumption is violated and the correlation between the multiplicity and transverse energy at mid-rapidity departs significantly from that which is characteristically observed. This possibility will be discussed further below.

In the realm of conventional physics which may be predicted with existing event generators, the equivalent sensitivity of using either $N_{ch}|_{y=0}$ or $E_t|_{y=0}$ to trigger on central collisions is clearly demonstrated in Fig. 3A-1, in which the response of both the central trigger barrel (CTB) and electromagnetic barrel calorimeter are shown as a function of impact parameter for AuAu collisions at $\sqrt{s_{nn}}$ = 200 GeV/A. These data were derived by using FRITIOF[1] to generate the necessary events and by determining the response of the STAR

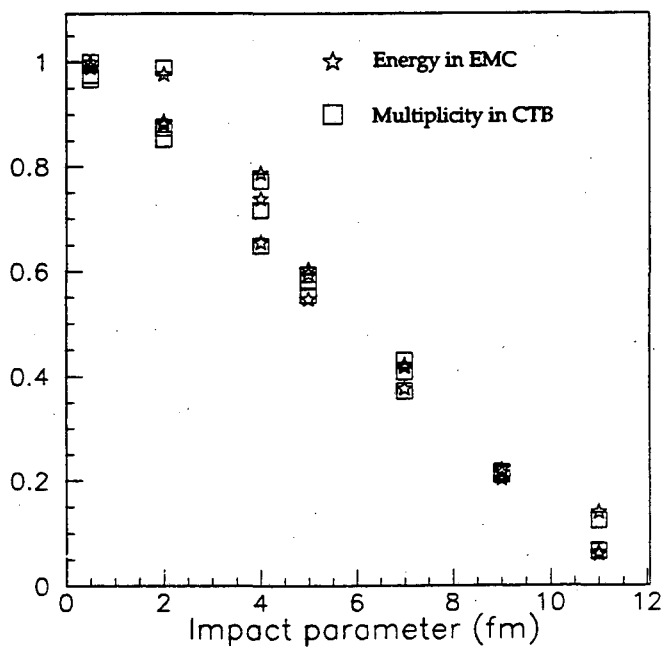

Figure 3A-1. A comparison as a function of impact parameter of the particle multiplicity and transverse energy within $|\eta| \leq 1.05$ for AuAu collisions at $\sqrt{s_{nn}}$ = 200 GeV. Both distributions are plotted as a ratio of the value at a given impact parameter to the maximum of the distribution.

[1]Bo Nilsson-Almquist and E. Stenlund, Computer Physics Communications 43 (1987).

detector system through a full GEANT simulation. The equivalent sensitivity to impact parameter using triggers based upon either observable is apparent.

In real operation, the STAR detector will trigger not only upon the most interesting central collisions, but will accept a prescaled sample of minimum-bias collisions as well. The efficiency and trigger bias of the central collision-selection criteria may then be determined.

3.B. Use of EMC for Selection of Rare Events in AA Interactions

It is in the selection of rare events in AA interactions that some of the unique capabilities provided by the electromagnetic calorimeter become apparent. As noted above, some of the most interesting physics may be found by triggering on events in which the average p_t per particle[2,3] and/or the ratio of charged to neutral energy[4,5] depart significantly from that which is characteristically observed. If these events occur at low cross section and their observation therefore requires significant rejection of "background events" at the trigger level, they will not be observed unless the characteristic correlation between the charged-particle multiplicity and transverse energy can be tested at the trigger level. In the present circumstance in which full event reconstruction (i.e., tracking) will take longer than 10 ms, this can not be accomplished for events having an unusual $\langle p_t \rangle$ without the electromagnetic calorimeter. Of course, searching for events exhibiting an unusual charged-to-neutral energy ratio cannot be accomplished in any circumstance without measurement of the neutral electromagnetic energy. With partial coverage of the electromagnetic calorimeter it would still be possible to search for rare events in selected regions of the STAR acceptance, although the sensitivity would be reduced.

To test the sensitivity of the STAR EMC to events exhibiting unusual isospin abundances, the response of this detector was examined in a full GEANT simulation of the STAR detector, using 10 "normal" central AuAu events at $\sqrt{s_{nn}}$ = 200 GeV/A and the same 10 events with 50% of the π° mesons changed to $\pi^\pm$ mesons. This was accomplished by interchanging the particle ID presented to GEANT in order to conserve both momentum and energy. In this instance, the average number of charged particles incident upon the central trigger barrel increased from 2,086 for standard events generated by FRITIOF to 2,284 for events having an anomalous charged-to-neutral isospin abundance.

The results of this simulation are shown in Fig. 3B-1, in which the total sampled energy deposited in the EMC barrel has been plotted versus the charged particle multiplicity detected in the central trigger barrel for both the normal and anomalous AuAu collisions. With the resolution afforded by high-statistics AuAu interactions, the two classes of events clearly exhibit different correlations in this observable.

The ratio of the energy deposited in the EMC barrel to the charge multiplicity detected in the CTB has been histogrammed in Fig. 3B-2 for the same events. The data in this projection again cluster into distinct groups corresponding to standard FRITIOF events (mean = 0.2878, rms = 0.0099) and events having an anomalous isospin abundance (mean = 0.2395, rms = 0.0051). If one assumes these distributions are gaussian and that the standard deviation is

[2]L. Van Hove, Phys. Lett. 118B, (1982) 138.
[3]M. Kataja *et al.*, Phys. Rev. D34, (1986) 2755.
[4]J.D. Bjorken, Acta Physica Polonica B23, (1992) 635.
[5]F. Wilczek, {Chiral Dynamics Near Equilibrium or After Quenching," Proceedings of the Tenth International Conference on Ultra-Relativistic Nucleus-Nucleus Collisions, June 20–24, 1993, Borlänge, Sweden.

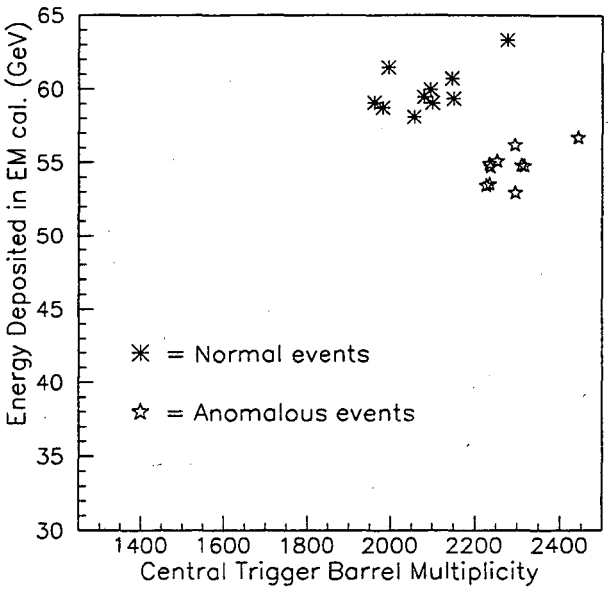

Figure 3B-1. A scatterplot of the charged particle multiplicity detected in the CTB versus the transverse energy in the EMC for 1) standard FRITIOF AuAu events at $\sqrt{s_{nn}}$ = 200 GeV, and 2) FRITIOF AuAu events in which 50% of the $\pi^{\pm}$ mesons have been changed to π° mesons. Both distributions lie along lines of constant slope that pass through the origin.

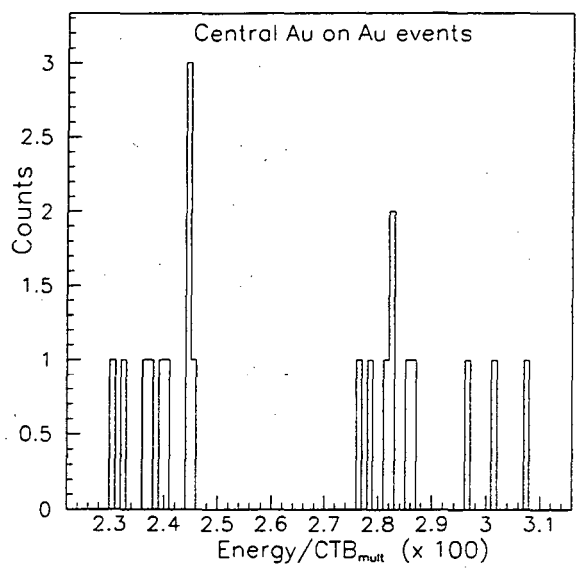

Figure 3B-2. A projection of the data in Fig. 3B-1 indicating the slope parameters calculated for individual data points. The points for the standard AuAu events (left) and AuAu events in which 50% of the $\pi^{\pm}$ mesons have been changed into π° mesons (right) separate into two distinct distributions. Assuming the distributions are Gaussian, the selectivity of this trigger is at the level of 1 in 10^4.

equivalent to the rms value for each distribution, the ability to unambiguously select events having this anomalous charged-to-neutral fraction is on the order of 1 in 10^4. This crude estimate is perhaps unrealistic, insofar as the true nature of these distributions is a matter for experiment and there is no reason to expect *a priori* that events will fall into only two distinct categories. However, the sensitivity to this observable provided by the EMC barrel and the corresponding ability to select this particular type of rare event at the trigger level appears promising. It also can not be accomplished within STAR by other means. It is noted that the width of the ratio distribution for the normal AuAu events is ~1.7%, in good agreement with the neutral energy resolution discussed in Section 4.B.1. As the mass of the colliding system is reduced, however, the corresponding reduction in $dn_\pi / d\eta$ will result in some compromise of the trigger sensitivity to this observable.

A second class of events for which the information provided by the EMC would afford a unique trigger capability are those in which the mean p_t per particle were substantially less than normal. Such an observation might correspond, for example, to an increase in entropy at fixed total energy. In this instance, the ratio of the energy deposited in the EMC barrel to the number of charged particles detected in the CTB would be reduced compared to that in a normal AuAu event. The change in this observable in this instance is in a different direction from that expected for the Centauro-type events[6] discussed above. Figure 3B-3 shows the ratio determined for 10 AuAu events, in which the average p_t per pion has been reduced by 30%, and

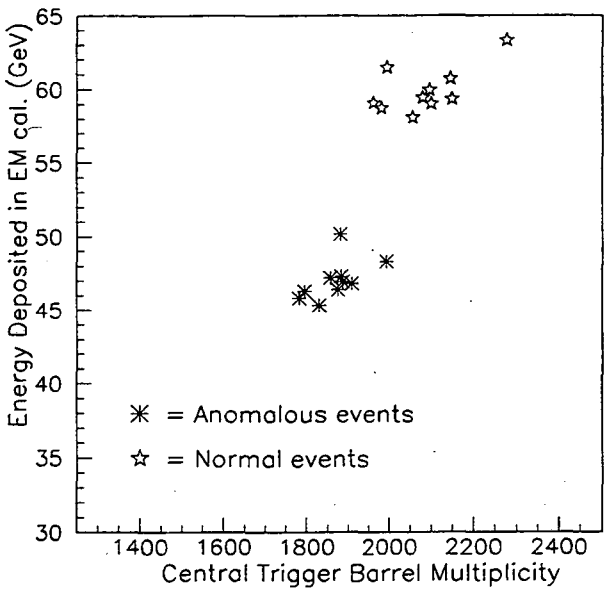

Figure 3B-3. A scatterplot of the charged particle multiplicity detected in the CTB versus the transverse energy in the EMC for 1) standard FRITIOF AuAu events at $\sqrt{s_{nn}}$ = 200 GeV, and 2) FRITIOF AuAu events in which the average p_t per pion has been reduced by 30%. Using the EMC, STAR is sensitive at the trigger level to fluctuations in this correlation.

[6]C.M.G. Lattes, Y. Fugimoto, and S. Hawegawa, Phys. Rep. 65, (1980) 151.

for 10 normal interactions. Once again, the two classes of events exhibit different correlations in this observable, and the sensitivity at the trigger level afforded by the EMC is evident.

3.C. Use of EMC for Selection of High P_t Particles

Another important capability provided by the STAR EMC is the ability to trigger on high p_t particles produced either directly or as the result of secondary fragmentation by hard ($p_t \geq 10$ GeV/c) or semi-hard ($p_t \geq 5$ GeV/c) parton scattering. This capability is essential in order to trigger on direct photons or leading particles from jets. It may also be used to select an enriched sample of events containing single high p_t particles in pA interactions, for example, to test the effects of shadowing on multiple mini-jet production in AA collisions (e.g., Section 2.A.2). It is also the case that **the EMC is presently the only means by which to reliably trigger on high p_t particles**, which is essential if the trigger conditions for pp, pA, and AA interactions are to be matched in order to investigate systematic differences between these colliding systems.

Without the EMC, the present STAR trigger system selects events primarily on the basis of charged particle multiplicity which is conventionally associated with impact parameter. As the multiplicity and transverse energy have until now been found to be correlated, selection upon multiplicity is normally related to selection based upon transfer of energy from the projectile frame to mid-rapidity. In pp and pA collisions, the primary consideration for matching trigger criteria is how many binary collisions the proton participates in, and how much energy it transfers to the target nucleus. These are again correlated with multiplicity. However, the situation may become confused without a trigger detector capable of recognizing events in which a large energy transfer produces a relatively small number of high p_t particles.

Specifically, using an appropriate tower threshold, the EMC will enable STAR to trigger on high energy photons which are either produced directly, or as the product of high p_t π° decay. The efficiency and selectivity for triggering upon photons of a given energy depends upon which interactions are studied, how high the threshold is set, and what segmentation is chosen for the calorimeter. The last consideration relates to how large a region in η and ϕ one integrates background particles from the underlying event and how likely it is that all of the energy from the high p_t photon is deposited in a single tower.

High p_t charged particles will in general deposit the energy typical of a minimum ionizing particle before exiting the rear of the calorimeter. Consequently, although the EMC will detect some of the energy from high p_t charged particles, a simple tower threshold would not be sufficient for an efficient trigger. The full energy of such particles can be recovered for the purpose of jet reconstruction and tower correction from tracking in the STAR TPC.

For pp and pA interactions the "pedestal" energy deposited in a given tower by background particles from the underlying event is minimal. For AA collisions, the situation becomes more difficult. In all cases, further simulation is necessary to quantify precisely how efficient and selective a simple tower threshold discrimination trigger would be for photons of a given energy. A related question is how low in p_t the trigger would remain selective before introducing a substantial background due to statistical fluctuations in the distribution of tower energies. An estimate can be made for AA collisions from Fig. 3C-1 in which the tower by tower distribution of transverse energies has been plotted for one fully simulated AuAu collision at $\sqrt{s_{nn}} = 200$ GeV. The quantity plotted is sampled energy deposited in the calorimeter towers. The sampled energy deposited by a 5 GeV/c π°, as well as that for photons of 10 and 15 GeV, is also shown. This simulation suggests that with a simple tower threshold trigger, one could begin to enhance the selection of events containing single high p_t π° mesons and direct photons having $p_t \geq 5$–7 GeV/c.

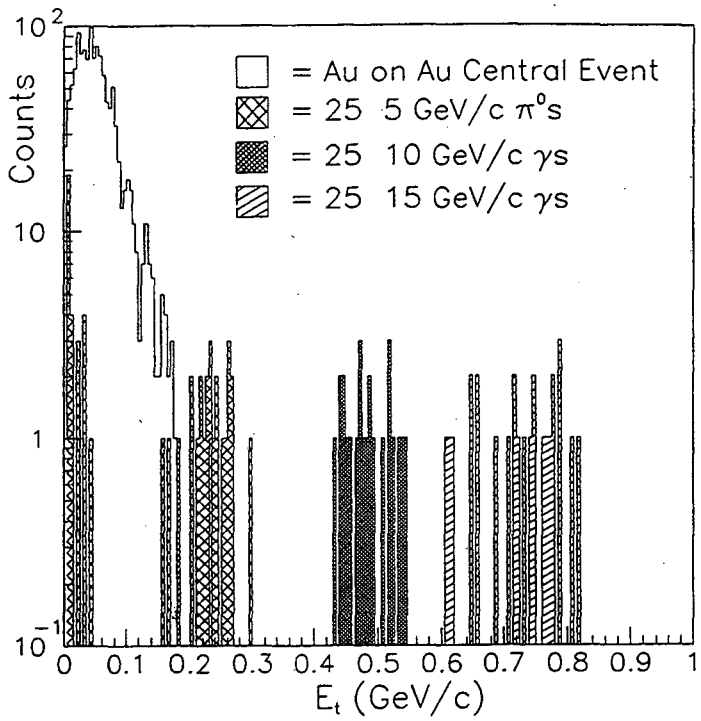

Figure 3C-1. A histogram of the tower by tower distribution of sampled energy for a central AuAu event. The response of the EMC for 5 GeV π^0 mesons as well as direct photons of 10 and 15 GeV is indicated as well.

3.D. Use of EMC for Selection of Jets

An important question in the study of jets and direct photons in pp, pA, and AA reactions is the ability of the STAR EMC to trigger efficiently on events containing hard parton scatters, while rejecting minimum bias events. This is particularly important in pp studies where the design luminosity for $\sqrt{s} = 200$ yields approximately $6 \cdot 10^5$ minimum bias events per second.

To examine the efficiency of a calorimeter trigger based on discriminating energy on a tower by tower basis, jets having p_t values of 10–50 GeV/c were generated in pp, pAu, and AuAu collisions using the Heavy Ion Jet Interaction Generator (HIJING).[7] HIJING was developed specifically to account correctly for the effect upon high p_t parton scatters of interactions with the surrounding medium. It is tuned to reproduce the essential features of pp multi-particle production data over a wide range of $\sqrt{s}$ and includes, for example, the effects of multiple mini-jet production and nuclear shadowing of parton distribution functions. It therefore calculates all the partonic debris resulting from partonic scatters and reliably predicts not only the high p_t particles, but the underlying event as well. Using the exclusive particle spectra predicted by HIJING, the energy deposited in the calorimeter towers was estimated on a particle by particle basis using a GEANT parametrization of the response of the towers to particles of a given type and momentum. This parametrization was used instead of a full GEANT simulation to reduce the computing required to accumulate adequate statistics. At the time of this simulation, the size of the calorimeter towers considered was $\Delta\eta \approx \Delta\phi \approx .035$. This segmentation was subsequently reduced ($\Delta\eta \approx .05$, $\Delta\phi \approx 6°$) due to considerations of cost.

[7]X.-N. Wang and M. Gyulassy, LBL-31036; X.N. Wang and M. Guylassy, Phys. Rev. D41, 350 (1991).

Consequently, for example, a cluster of 3 × 3 towers considered for the purpose of this simulation corresponds roughly to the same size as two towers of the presently designed system.

The results for pp interactions are presented in Fig. 3D-1 for the RHIC design luminosity of $\mathcal{L}_0 \sim 10^{31}$ cm^{-2}sec^{-1}. From the data presented, it is evident that for a simple 3 × 3 cluster discrimination threshold of 3 GeV, the trigger rate for minimum bias events has been reduced by a factor of ~10^3. For the same threshold, the efficiency of detecting a parton scatter with p_t = 10 GeV/c is ~20% (Fig. 3D-2). In general, the detection efficiency increases with p_t becoming ~60% for parton scatters having p_t = 20 GeV/c. The trigger rate for parton scatters having p_t values of 10 GeV/c or more is approximately 100 per second.

The results for pAu interactions are presented in Fig. 3D-3 for a luminosity of $\mathcal{L}_0 \sim 10^{29}$ cm^{-2}sec^{-1}. Aside from the difference in luminosity, the results for pAu interactions are qualitatively very similar to those for pp. One difference, however, is that because of the increased background in the underlying event in this instance, the 3 × 3 cluster threshold necessary to obtain the same rejection for low p_t minimum bias events is increased from 3 GeV to 6 GeV. For this threshold, the trigger rate for minimum bias events is reduced by a factor of ~10^2. The efficiency of detecting a parton scatter with p_t = 10 GeV/c is ~10% (Fig. 3D-4). The

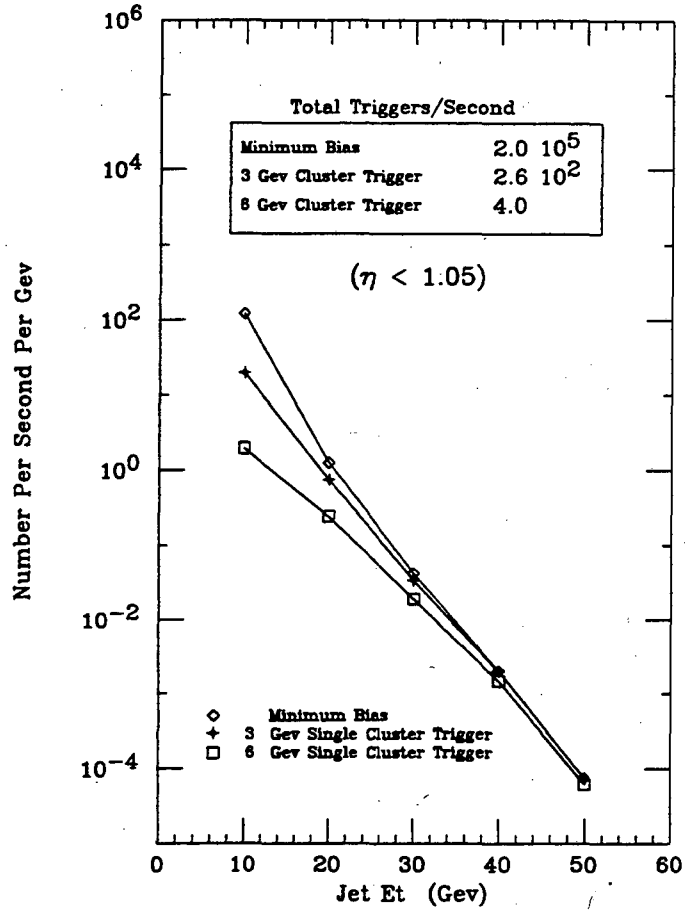

Figure 3D-1. The rate per second per GeV of events containing jets of a given E_t for various single tower discrimination thresholds. Data shown are for pp collisions at $\sqrt{s}$ = 200 GeV ($|\eta| \leq 1.05$).

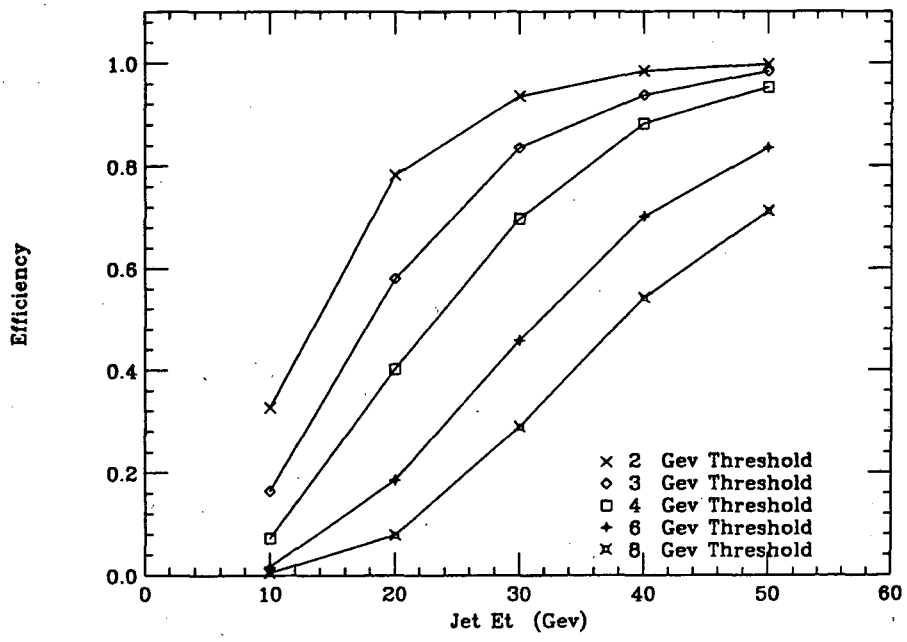

Figure 3D-2. The efficiency as a function of jet energy for triggering on an event containing a jet, for a given single tower discrimination threshold. Data shown are for pp collisions at $\sqrt{s}$ = 200 GeV.

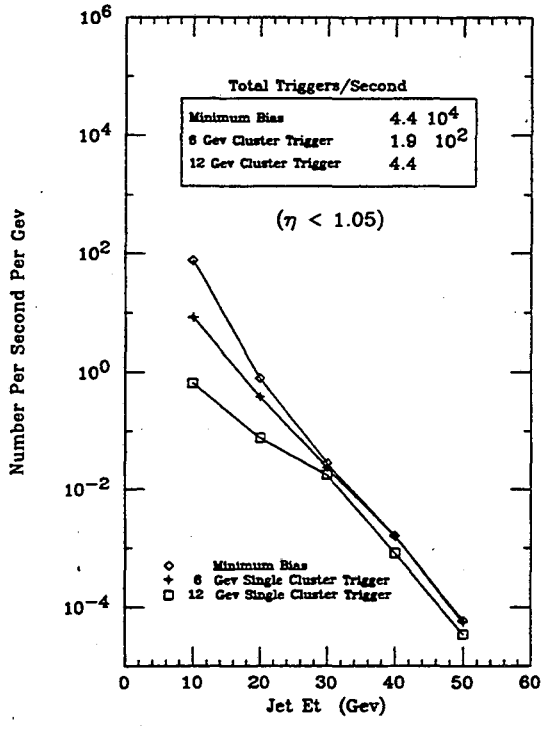

Figure 3D-3. The rate per second per GeV of events containing jets of a given E_t for various single tower discrimination thresholds. Data shown are for pAu collisions at $\sqrt{s_{nn}}$ = 200 GeV ($|\eta| \leq 1.05$).

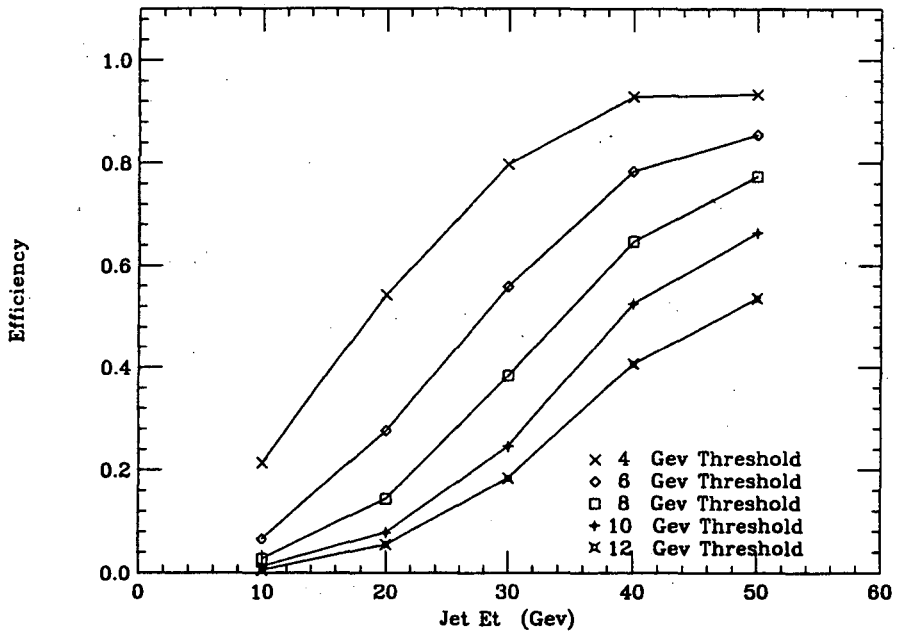

Figure 3D-4. The efficiency as a function of jet energy for triggering on an event containing a jet, for a given single tower discrimination threshold. Data shown are for pAu collisions at $\sqrt{s_{nn}}$ = 200 GeV.

detection efficiency again increases with p_t becoming ~25%, for example, for parton scatters having p_t = 20 GeV/c. The trigger rate for parton scatters having p_t values of 10 GeV/c or more is approximately 100 per second.

The corresponding plots for AuAu collisions are presented in Figs. 3D-5 and 3D-6. In this case, the trigger threshold has been increased to 7 GeV to account for the increased energy deposited in the towers by the large number of secondaries in the underlying event. Despite this increase however, the efficiency is somewhat higher for AuAu than pAu interactions below p_t = 20 GeV. Also, below 20 GeV/c, the shape of the efficiency curve is flat. To interpret these results correctly, it is necessary to understand the limitations of the calculation.

The efficiency curves in Fig. 3D-6 are derived by generating a known number of events with a parton scatter of a given p_t, embedding those events in a minimum bias or untagged sample of AuAu events **which may or may not contain jets**, and subsequently determining how many of the events known to contain jets are recovered using a given 3 × 3 cluster threshold. The efficiency for detecting a given event known to contain a jet ($p_t \leq$ 20 GeV/c) appears to be increased compared to pAu. A subtlety of this calculation, however, is that the energy deposited on average by the underlying event is high because the probability that the underlying minimum bias event contains a jet in this energy range has increased dramatically. Consequently, because the average AuAu event is much more likely to contain such a jet, the increased probability of selecting a given tagged event in a larger sample of minimum bias events is also increased coincidentally.

Further simulation is necessary to determine if a more efficient trigger can be devised for AuAu interactions. The trigger rate for AuAu events containing a parton scatter with a p_t of 10 GeV or more is approximately 1 per second which is well within the STAR capability. This is a consequence primarily, however, of the reduced luminosity for Au. It is noted with regard to triggering, that the STAR EMC is presently the only detector in the STAR Phase I baseline capable of triggering on high p_t particles.

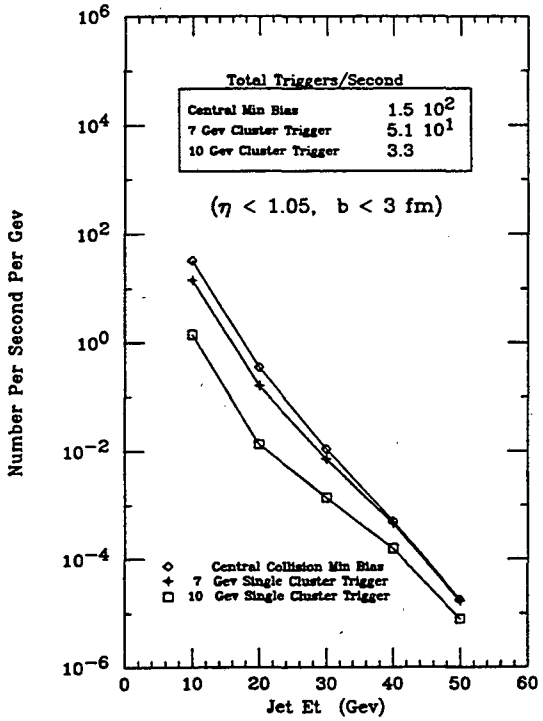

Figure 3D-5. The rate per second per GeV of events containing jets of a given E_t for various single tower discrimination thresholds. Data shown are for AuAu collisions at $\sqrt{s_{nn}}$ = 200 GeV ($|\eta| \leq 1.05$).

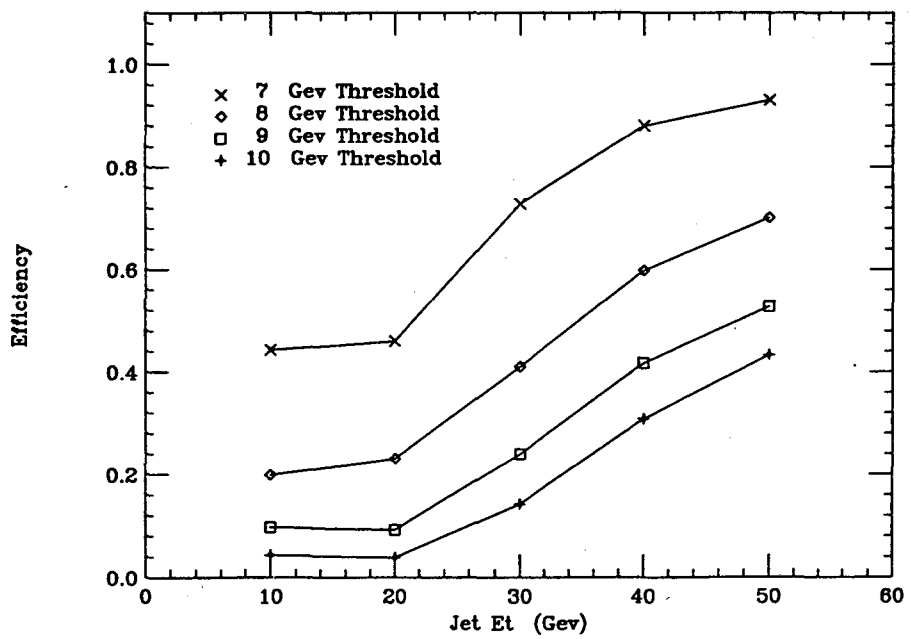

Figure 3D-6. The efficiency as a function of jet energy for triggering on an event containing a jet, for a given single tower discrimination threshold. Data shown are for AuAu collisions at $\sqrt{s_{nn}}$ = 200 GeV.

4.

Conceptual Design

4. CONCEPTUAL DESIGN

4.A. Overview of STAR

The Solenoidal Tracker At RHIC (STAR) is designed to search for signatures of quark-gluon plasma (QGP) formation and to investigate the behavior of strongly interacting matter at high energy density in relativistic nucleus-nucleus collisions. High-luminosity polarized proton beams at RHIC and the corresponding sensitivity to small spin-dependent asymmetries will also provide a unique opportunity to study the importance of spin as a fundamental variable in elementary QCD interactions.

In relativistic heavy ion collisions, the emphasis will be on the measurement and correlation of global observables on an event-by-event basis and the use of hard scattering of partons to probe the properties of high-density nuclear matter. The event-by-event measurement of global observables—such as temperature, flavor composition, collision geometry, reaction dynamics, and energy or entropy density fluctuations—is possible because of the very high charged-particle densities, $dn_{ch}/d\eta \approx 700$, expected in nucleus-nucleus collisions at RHIC. Event-by-event fluctuations are expected in the vicinity of a phase transition, so this experiment will be sensitive to threshold behavior of the experimental observables as a function of energy density. Since there is no clearly established theoretical signature of the QGP, access to many observables simultaneously will be critical for identifying rare events in which the QGP may be formed. The STAR detector has been designed to provide tracking, momentum analysis, and particle identification over a large pseudo-rapidity range with full azimuthal coverage to minimize fluctuations due to losses in acceptance. The experiment will therefore be sensitive to critical dynamic fluctuations at the single-event level and be capable of detecting and correlating fluctuations in particle ratios, energy density, entropy density, temperature, flavor content, and particle-production dynamics. Correlations between identical bosons (HBT) will provide additional information on the freeze-out geometry, the expansion dynamics, and the possible existence of a QGP.[1]

Measurement of jets produced by hard-scattered partons will be used as a penetrating probe of the collision volume and will also provide important new information on the nucleon structure function and parton shadowing in nuclei. Since hard-scattering processes are directly calculable in QCD, a measurement of the yield of hard-scattered partons as a function of transverse energy should be sensitive to their interaction with the surrounding matter.[2,3] The energy loss of these propagating quarks and gluons is predicted to be sensitive to the medium and may be a direct method of observing the QGP, provided the "initial conditions" and the influence of mini-jet production[4,5,6,7,8,9] have been determined in a systematic study of pp and pA interactions. The measurement of gluon shadowing in nuclei is of particular interest since the yield of mini-jets is strongly influenced by the density of gluons at small x. Although data exist on quark shadowing in the nucleus, the degree of gluon shadowing is presently unknown.

---

[1]For a full discussion of the STAR detector, see *The STAR Conceptual Design Report*, LBL PUB-5347 (1992).
[2]M. Gyulassy and M. Pluemmer, Phys. Lett. **B243** (1990) 432.
[3]X.N. Wang and M. Gyulassy, Phys. Lett. **68** (1992) 1480.
[4]K. Kajantie, P.V. Landshoff, and J. Lindfors, Phys. Rev. Lett. **59** (1987) 2527.
[5]K.J. Eskola, K. Kajantie, and J. Lindfors, Nucl. Phys. **B323** (1989) 37.
[6]P.V. Landshoff, Nucl. Phys. **A498** (1989) 217.
[7]X.N. Wang, Phys. Rev. **D43** (1991) 104.
[8]D. Appel, Phys. Rev. **D33** (1986) 717.
[9]X.N. Wang, Phys. Lett. **B248** (1990) 447.

In polarized proton interactions, the ability to detect jets and direct photons will provide unique data on the origin of the proton spin. Recent results[10] on the spin-dependent structure function of the neutron are consistent with the Bjorken sum rule when combined with corresponding data taken earlier for the proton.[11,12,13] These results confirm the surprising observation that the intrinsic spin angular momentum of the proton can not be accounted for by the contribution from constituent quarks. Another possibility is that a substantial contribution to the spin of the proton is carried by gluons. The measurement of inclusive jets, inclusive direct photon production, and direct photons in coincidence with an away-side jet in polarized pp interactions at RHIC will allow a determination of the contribution to the proton spin from the gluon sea, $\Delta G(x)$. This information is essential if the origin of the proton spin is to be understood. It will also be possible using the STAR detector to search for compositeness and unexpected single-spin asymmetries due to parity violation and to verify the parity violation in the decay of the $W^{\pm}$ boson. The possibility of investigating the polarization of sea quarks using $W^{\pm}$, Z°, and Drell-Yan pair production is also under study.

To meet the design criteria and fulfill the physics objectives, tracking, momentum analysis, and particle identification of most of the charged particles at mid-rapidity are necessary. In heavy ion interactions, the tracking must operate in conditions at higher than the expected maximum charged-particle multiplicities ($n_{ch} = 3000$ in the range $|\eta| < 1$ within the acceptance of the experiment) for central AuAu collisions.

The detection system (Fig. 4A-1) will consist of a time projection chamber (TPC) and silicon vertex tracker (SVT) located inside a solenoidal magnet with a 0.5-T field to provide tracking, momentum analysis, and particle identification of most of the charged particles at mid-rapidity. Momentum measurements will be made over a large pseudo-rapidity range ($|\eta| < 2$), with full azimuthal coverage ($\Delta\phi = 2\pi$). Particle identification via ionization energy loss (dE/dx) of pions/kaons for $p < 0.7$ GeV/c and kaons/protons for $p < 1$ GeV/c will be performed within $|\eta| < 1$. In addition, measurement of decay particles and reconstruction of secondary vertices will be possible. A two-track resolution of 2 cm at 2-m radial distance from the interaction is expected. Momentum resolution of $\Delta p/p \approx 0.02$ at $p_t = 0.1$ GeV/c is required to accomplish the physics, and $\Delta p/p$ of a few percent at $p_t = 10$ GeV/c is sufficient to accurately measure the rapidly falling spectra at high p_t and particles from mini-jets and jets. The momentum resolution at low p_t is limited by multiple scattering. To minimize multiple scattering and photon conversion after π° decay, which also creates nonprimary vertex tracks, detector material will be kept to a minimum throughout the tracking system.

The TPC will be divided into two longitudinal drift regions, each 2.1 m in length (Fig. 4A-2). The two drift regions are separated by a high voltage membrane at $\eta = 0$. Electrons created from track ionization drift in the longitudinal direction along the TPC electric-field lines to the endcaps of the TPC. Each endcap is instrumented with 70,000 pads, and each pad read out in 512 time samples during the ~50 μs required to drift the ionization from the midplane to the pad plane of the TPC volume. The inner radius of the TPC will be 50 cm, and the outer radius 202 cm. Neglecting energy loss, singly ionized particles having $p_t \leq 40$ MeV/c spiral inside the TPC inner radius and do not reach the active volume of the TPC. For these particles, the silicon vertex tracker will be used as a standalone device. Particles having $p_t \geq 150$ MeV/c

[10]G. Igo, "Measurement of the Spin-Dependent Structure Function $g_1^d(x)$ of the Deuteron," Proceedings of the Tenth International Conference on Ultra-Relativistic Nucleus-Nucleus Collisions, June 20–24, 1993, Borlänge, Sweden.
[11]J. Ashman, *et al.*, Phys. Lett. **B206** (1988) 364.
[12]J. Ashman *et al.*, Nucl. Phys. **B328** (1989) 1.
[13]B. Adeva *et al.*, Phys. Lett. **B302** (1993) 533.

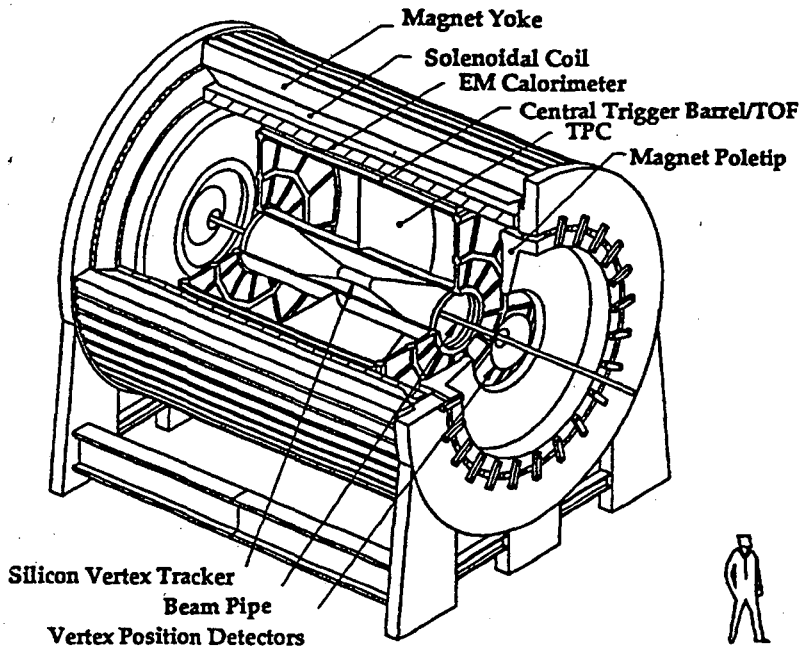

Figure 4A-1. Perspective view of the STAR experimental configuration.

traverse the TPC and exit at the outer radius. Given the simulated response of the TPC and the high charged-particle densities expected in nucleus-nucleus collisions at RHIC, it will be possible, for example, to accurately determine the slope of the pion p_t distribution on an event-by-event basis (Fig. 4A-3) and to search for critical dynamic fluctuations in a narrow range of conditions as a possible indicator of a transition to a deconfined phase of quarks and gluons.

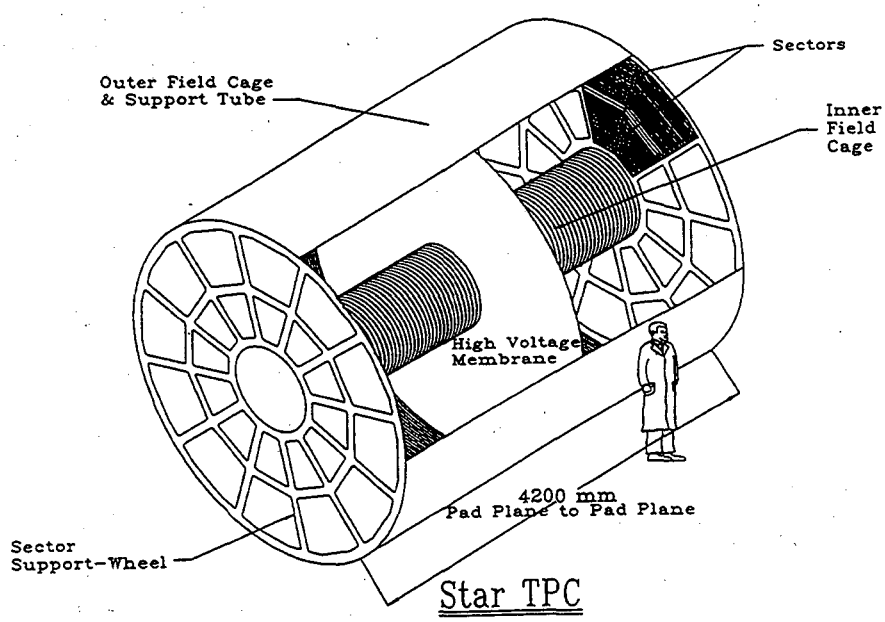

Figure 4A-2. Perspective view of the STAR Time Projection Chamber.

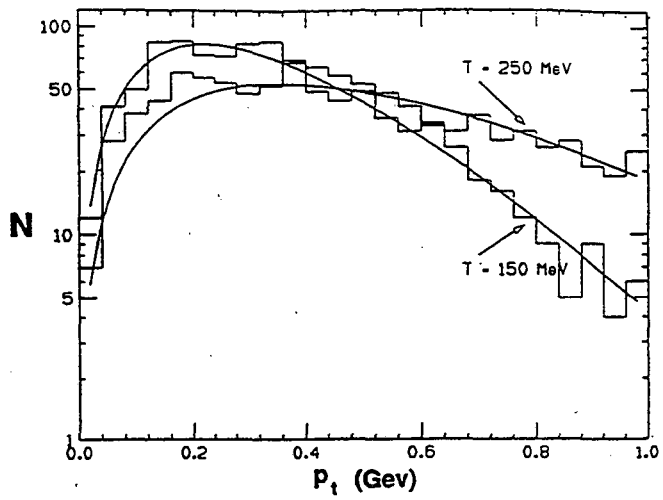

Figure 4A-3. Simulation of the p_t spectrum for one event generated using a Boltzmann distribution of 1000 pions. The histograms correspond to single events generated with T = 150 MeV and 250 MeV. The curves are fits to the histogram using a Maxwell-Boltzmann distribution.

The silicon vertex tracker (SVT) coupled with the TPC will locate the position of the primary vertex to high accuracy, improve the momentum and dE/dx resolutions, and locate secondary vertices to an accuracy of better than 100 μm. It presently consists of ~200 silicon drift detectors arranged in three concentric barrels around the interaction point at radii of 5, 8, and 13 cm, respectively. It is designed to provide three-dimensional space points for track segments within its acceptance and therefore will provide a powerful tool for extending the acceptance of the TPC to low momenta. Additionally, vertex information from the SVT significantly improves the momentum resolution at high p_t (see, for example, Section 4.A.3). The improved vertex resolution of the SVT will also make it possible to measure the decay of baryons and anti-baryons having multiple strangeness (e.g., Ξ^-, Fig. 4A-4), whose yield is

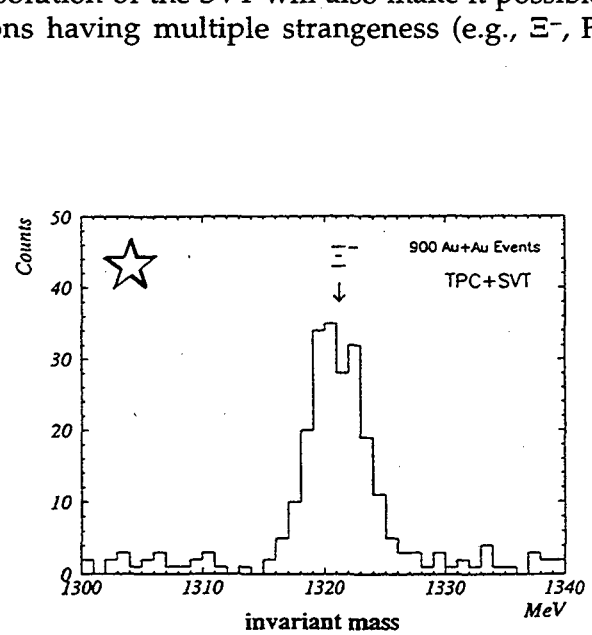

Figure 4A-4. Invariant mass distribution of Ξ^- (TPC+SVT) with TPC momentum resolution taken into account.

sensitive to the strangeness density reached in nucleus-nucleus collisions and is therefore a possible signature of QGP formation.

A central trigger barrel around the TPC and veto calorimeters located in the region of the beam-insertion magnets will provide the information necessary for a collision-geometry trigger by measuring the multiplicity at mid-rapidity and the energy carried forward by spectator nucleons, respectively. Vertex position detectors near the beamline at either end of the solenoidal magnet have been designed to localize the interaction to within ±6 cm in ≲100 ns by determining the mean time of flight (TOF) of particles produced in the interaction. Precise determination of the vertex position will be accomplished using the TPC and SVT detectors. The integrated charge from the anode wires of the TPC will be used as a measure of the prompt charged particles traversing the region $1 \leq |\eta| \leq 2$ and will provide a coarse trigger on $dn/d\eta$ in this region. A similar capability for $d^2n/d\eta d\phi$ will be provided by the central trigger barrel in the region $0 \leq |\eta| \leq 1$.

A portion of the central trigger barrel will be instrumented with a highly segmented TOF array. Each TOF scintillator will be approximately 1.5 cm × 2.6 cm × 23.5 cm in dimension and will provide TOF resolution on the order of 100 ps. For particles within the acceptance of the TOF array, the pion/kaon separation will be extended from ~0.7 GeV/c to ~1.3 GeV/c, and the kaon/proton separation will be extended from ~1 GeV/c to ~2.4 GeV/c. Studies are also in progress to determine if Cerenkov plastic used in combination with scintillator plastic in this segmented array may be used to provide a coarse separation of pions and kaons at the trigger level and the means for an enhanced-strangeness trigger.

An electromagnetic calorimeter (EMC) located outside the central trigger barrel will be used to trigger on local ($d^2E_t/d\eta d\phi$) and global (E_t) transverse energy and to measure jets, direct photons, and leading-π^0 production. Correlation of the information from the EMC and central trigger-barrel detector systems will also enable STAR to trigger on events exhibiting unusual pion isospin abundances (e.g., Centauro events), which have been suggested[14,15,16,17] as a signature of exotic nuclear matter in nucleus-nucleus collisions at high energy. The STAR EMC is a sampling calorimeter ~18 X_0 thick, constructed of alternating layers of lead absorber and scintillator tiles read out with waveshifting fibers. It is located inside the magnet coil and is designed to have a resolution of $\sim 16\%/\sqrt{E}$. Full calorimetry in STAR will be accomplished using a combination of TPC tracking and electromagnetic calorimetry.

External TPCs located at ±7 m from the interaction point along the beamline will be used to study the transfer of energy from the projectile rapidity to mid-rapidity by following the fate of the incident baryons rescattered in the collision. These chambers extend the pseudorapidity coverage of STAR from $|\eta| \leq 2$ to $|\eta| \lesssim 4$. By analyzing the difference in the distribution of positively and negatively charged particles in this acceptance, nuclear stopping and possible collective effects in spectator matter will be investigated. Extension of the tracking acceptance to $|\eta| \lesssim 4$ should enhance the ability of STAR to resolve events and regions of anomalously high particle production that could result from the hadronization of a quark-gluon plasma.

---

[14]D. Bjorken, Acta Physica Polonica **B23** (1991) 635.
[15]F. Wilczek, "Chiral Dynamics Near Equilibrium or After Quenching," Proceedings of the Tenth International Conference on Ultra-Relativistic Nucleus-Nucleus Collisions, June 20–24, 1993, Borlänge, Sweden.
[16]A. Panagiotou *et al.*, Phys. Rev. **D45** (1991) 3134.
[17]S. Pratt, Phys. Lett. **B301** (1993) 159.

4.A.1. STAR Phase I Components

Magnetic Field

The magnet will be a solenoid with uniform magnetic field along the beam direction. It will be designed to be able to provide uniform fields with strengths of 0.25–0.5 T. An iron return yoke and shaped pole pieces will transmit the magnetic flux and shape the magnetic field. The magnet design is chosen for high tracking accuracy and azimuthal symmetry. Small correction coils will be used to further improve the field uniformity. A field strength of 0.5 T will provide adequate resolution for momenta as high as 10 GeV/c with only modest spiraling of low p_t particles. The magnetic coil mean radius will be 2.81 m, and the radius of the yoke will be 3.31 m. The total magnet length will be 7.25 m. A room-temperature Al coil is being designed in an attempt to reduce construction costs. A brief summary of the magnet parameters is presented in Table 4A-1.

Time Projection Chamber (TPC)

The TPC will be divided into two longitudinal drift regions, each 2.1 m long. Electrons created from track ionization will drift in the longitudinal direction, along the TPC electric field lines, to the endcaps of the TPC. Each endcap is instrumented with ~70,000 pads. Two pad sizes will be used, one for the inner sectors (50 cm < radius < 125 cm) and one for the outer sectors (125 cm ≤ radius < 202 cm), as described in Table 4A-2. Each pad will be read out into 512 or 1024 time samples, depending on the choice of TPC gas. The TPC geometrical acceptance for particles reaching the outer radius is $|\eta| < 1$ and that for particles reaching the inner radius (i.e., multiplicity with partial dE/dx and tracking) is $|\eta| < 2.0$. A summary of the TPC design can be found in Table 4A-2.

The pad plane configuration is designed to maximize the recorded track length for good momentum resolution, minimize the required number of electronics, and provide sufficient dE/dx sampling along the track to achieve particle identification in the $1/\beta^2$ region. The inner-radius pad-plane sectors are composed of small pads arranged in separated rows. These small pads improve the two-track resolution permitting position measurements along the track in the high-track-density region closer to the interaction. These position measurements at the inner-radius region are important for extending the measured track, for improving momentum resolution, and for accurate projection to the SVT. The outer-radius pad sectors are designed with larger pads to achieve continuous sampling along the track for dE/dx. R&D is currently

Table 4A-1. Magnet Properties.

Solenoid field strength	0.25–0.5 T
Length	7.25 m
Aluminum coil	
Mean radius	2.81 m
Yoke	
Mean radius	3.31 m
Weight	729 tonnes
Pole tips	
Weight of each	65.9 tonnes
Total weight of Fe	861 tonnes

Table 4A-2. Time Projection Chamber.

Drift volume	Coaxial cylinder —
Inner radius	0.5 m
Outer radius	2.02 m
Length	4.2 m
PID acceptance	$\|\eta\| < 1$
Tracking acceptance	$\|\eta\| < 2$
Drift gas	Under study
Pressure	Atmospheric
Sampling rate	12.3 MHz
Time samples	512 or 1024
Total number of pad rows	45
Pad sectors	Two types
Type, number of rows	Inner, 13
Pad size	2.85 mm × 11.5 mm
Type, number of rows	Outer, 32
Pad size	6.2 mm × 19.5 mm
Total number of pads	136,368
Total # pixels	77,000,000
Dynamic range for dE/dx	8 bits, non-linear
Position resolution ($p_t > 1$ GeV/c)	460 μm in x,y and 700 μm in z
Drift time	40 μs

under way to identify the TPC gas with the optimal compromise with respect to longitudinal diffusion, transverse diffusion, multiple scattering, and ionization energy loss.

Silicon Vertex Tracker (SVT)

The silicon vertex tracker (SVT) coupled with the TPC will locate the position of the primary interaction vertex to high accuracy, improve the momentum and dE/dx resolutions, and locate secondary vertices to an accuracy better than 100 μm. It also provides a powerful tool to extend the acceptance of the TPC to low momenta. The lower TPC limit for fully efficient track reconstruction is 150 MeV/c. Therefore, a considerable part of the event will be measured by inclusion of tracking in the SVT alone. Thus, the SVT must be able to provide three-dimensional space points and tracking vectors with high spatial resolution, so that the tracks measured in the TPC can be linked to those in the SVT. The SVT must be of low mass so as to minimize secondary-particle production, photon conversion, and multiple scattering.

The SVT will consist of ~200 silicon drift detectors (SDD). Individual detectors are grouped into ladders. Each ladder consists of six SDDs. The ladders are arranged in three concentric barrels around the interaction at radii of 5, 8, and 13 cm, as shown in Fig. 4A-5. The SVT contains 70 K–100 K channels of electronics. Each barrel is 42 cm in length. Each SDD is made from a 10-cm-diameter wafer. The thickness of a wafer is 300 μm, a good compromise between signal strength (24k electrons are created by minimum ionizing particle) and

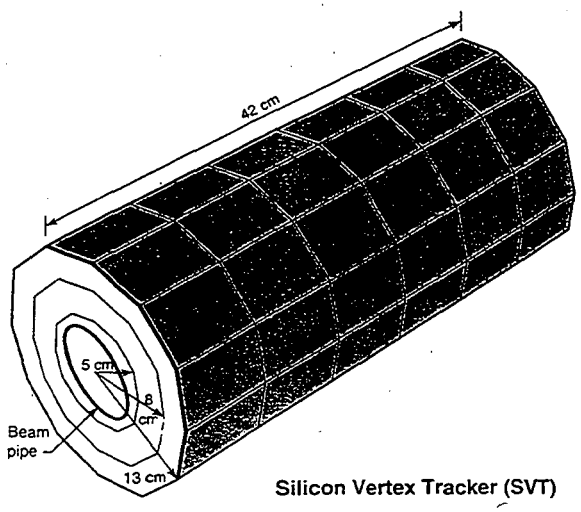

Figure 4A-5. Conceptual layout of the SVT.

acceptable values of multiple scattering and secondary-particle production for particles traversing the detector. A brief summary of the SVT parameters can be found in Table 4A-3.

Electromagnetic Calorimeter (EMC)

The purpose of the EMC is to measure and trigger on the total (E_t) and local ($d^2E_t/d\eta d\phi$) transverse energy deposition in pp, pA, and AA collisions. It is also possible to use the EMC to trigger on jets, high-energy direct photons, and high p_t particles. In nucleus-nucleus collisions, this provides a unique opportunity to study the interactions of hard-scattered partons in the hot nuclear medium and thus infer its properties. In polarized pp collisions, the information provided by the EMC can be used to study the spin structure of the proton as well as single-spin transverse asymmetries.

The barrel EM calorimeter is a lead-scintillator sampling calorimeter located inside the STAR solenoidal coil. It covers $|\eta| \leq 1.05$ and 2π in azimuth. At $\eta \sim 0$, the amount of material in front of the EMC is ~0.5 X_0. The inner radius is 2.22 m, and the length is 6.82 m. It consists of 60 wedge segments of 6° in ϕ and is subdivided into 40 pseudo-projective towers over the full η range. Each tower has 20 layers of lead and 21 layers of scintillator. Each scintillator tile will be read out with two wavelength-shifting optical fibers. In the Phase I implementation, all the fibers from pairs of towers adjacent within $\Delta\eta \lesssim 0.2$ will couple to one PMT to reduce the cost. There will be 1200 PMTs, and the effective tower size will initially be 0.20×0.105 ($\Delta\eta$, $\Delta\phi$), similar to many existing calorimeters used in studies of jets and direct photons in high energy physics. The physical construction will permit various kinds of upgrades as increased funds become available for more PMT channels. This includes a fourfold increase in η segmentation and flexible depth segmentation to optimize the separation of hadronic and electromagnetic energy components. The Phase I calorimeter will also include a detector with higher granularity at ~5 X_0 to increase the two-photon resolution of the EMC and thus the ability of the detector to separate high-energy direct photons from those coming from π^0 decays. The EM energy resolution is expected to be approximately $0.16/\sqrt{E}$. A brief summary of the EMC parameters is presented in Table 4A-4.

Table 4A-3. Silicon Vertex Tracker.

Length	42 cm
Inner barrel (radial distance)	5 cm
Middle barrel (radial distance)	8 cm
Outer barrel (radial distance)	13 cm
Thickness of detectors (SDD)	300 μm
Total effective thickness	~4.0% X_o
Number of detectors	~200
Diameter of Si wafer	10.00 cm
Length of detector (SDD)	7.05 cm
Width of detector (SDD)	5.68 cm
Drift length of detector	3.50 cm
Average drift time	~3.5 μs
Time samples	256
Sampling rate	40 MHz
Anode pitch	250 μm
Number of channels	72576
Position resolution	25 μm

Triggering and Trigger Detectors

The STAR trigger is designed to cover the dynamic range from pp to central AuAu collisions in an architecture that allows continuous upgradeability, as more becomes known about the RHIC environment. It is important to note that no universally accepted unambiguous signature of quark-gluon plasma events has been identified. Thus the trigger must allow exploration of various paths in the search for these signatures and be flexible enough to

Table 4A-4. Electromagnetic Calorimeter Parameters.

Barrel calorimeter type	18 X_o lead-scintillator 'EM' section
Mechanical segmentation	60 azimuthal sectors, $\Delta\phi = 0.105$ (6°) 40 projective towers in $\lvert\eta\rvert < 1.05$, $\Delta\eta = 0.0525$
Inner radius	2.22 m
Length	6.20 m
Weight	172.7 tonnes
Readout	Waveshifting fiber (2/tile) to PMT
Towers	1,200
Shower max detector	Scintillator strips or wires/pads parallel and perpendicular to η
Readout	Waveshifting fiber

implement continuous upgrades as our understanding grows. The trigger is designed with redundancy to allow for application of independent selection criteria in order to understand and eliminate trigger biases. At the beginning, STAR will operate with high dead time until sufficient information is obtained to be able to safely increase the selectivity of the trigger and thus increase the overall live time. The minimum-bias interaction rates are expected to be 1 kHz for AuAu and 1 MHz for pp. The key aspect of the design of the STAR trigger system is that information from all trigger counters will be digitized completely within four crossing periods and placed in a digital pipeline clocked synchronously with the RHIC machine. This feature allows a high degree of flexibility in developing more sophisticated second- and third-level triggers to pursue the most interesting physics as it becomes possible to develop more selective trigger criteria. The STAR Phase I trigger system will consist of the set of detectors described in Table 4A-5. All detectors cover the full azimuth.

Data Acquisition (DAQ)

The DAQ subsystem will provide two major functions in STAR. First, it will act as an event builder by assembling data originating from each detector subsystem into a form suitable for recording and distribution to analysis and monitoring tasks via a network. Second, it will provide for higher-level triggering on a time scale short compared with the time required for event building and third-level triggers. Rates >50 events/s will enter the trigger processors. The data-recording rate is limited by available taping speed at reasonable cost.

The DAQ subsystem has been engineered based on an architecture that uses the newest transputer family members, the T9000 RISC processor, and the C104 packet router. This technology has been chosen for two reasons. First, the total cost/MIPS (including all necessary ancillary components, interfaces, etc.) is much lower than for any other processor family. Second, the overhead in hardware and in software to network large numbers of processors is virtually nonexistent. Both issues are important in the STAR application. An alternative technology is that of the Fiber Channel. This technology would provide the transport from the readout boards on the detector to an event builder that would be constructed from Fiber Channel components.

The event size for central AuAu collisions is expected to be 96 MB. After reduction by the average occupancy factor expected for the TPC (10%) and inclusion of a 20% overhead for encoding, this becomes approximately 12 MB per event. Events of this size will be recorded on magnetic tape at a rate of one event/second. Though pp collisions have substantially lower multiplicity than AuAu collisions, their event-recording rate is limited by the occupancy in the TPC due to overlapping events at high luminosity. Recording rates for pp collisions are 30 events/sec at $\sqrt{s}$ = 200 GeV and 10 events/s at $\sqrt{s}$ = 500 GeV.

Table 4A-5. STAR Trigger System Detectors.

Detector	$\lvert\eta\rvert$	Number of channels
Central trigger barrel (CTB)	0–1	240
TPC endcap MWPC	1–2	96
Vertex position detectors (VPD)	3.3–3.8	48
Veto calorimeter (VC)	> 5	4
EM calorimeter (EMC)	0–1	1200

Additional compression through on-line analysis of the data can reduce the event size and increase the overall event rate. It is possible that, with some developments in on-line data reduction and compression through track-finding and fitting, the event-recording rate could be increased, possibly as much as tenfold.

4.A.2. EM Plus Tracking Technique

Full calorimetry in STAR is accomplished by using a combination of TPC tracking and electromagnetic calorimetry. To examine the feasibility of this technique, a comparison was made between the response expected for tracking plus electromagnetic calorimetry versus electromagnetic plus hadronic calorimetry. This question was studied by simulating jet events in pp collisions at $\sqrt{s_{nn}} = 200$ GeV using the HIJING generator, decaying all produced particles with lifetimes shorter than the K°_{L}, and considering the energy produced in the form of photons, charged particles, and hadrons (both charged and neutral). The effect of the STAR solenoidal field on the location of the energy deposited by the charged particles was taken into account, and then the energies of the hadrons and photons were binned into an η-ϕ grid with bin sizes of 0.1 and 0.028, respectively. (These bins are much larger than necessary for the 'tracking' and EM components, but are used for comparison with the bin sizes typical of collider calorimeters.) The resulting binned energies were folded with resolutions of $0.40/\sqrt{E}$ for the hadron calorimeter, and $0.22/\sqrt{E}$ for the EM calorimeter. The spatial resolution, momentum resolution, and reconstruction efficiency of the tracking system were assumed to be perfect. An implementation of the CDF cluster-finding algorithm was then applied to the binned data sets and, for each found cluster, E_t was summed within $R = \sqrt{((\Delta\eta)^2 + (\Delta\phi)^2)} \sim 0.7$ of the apparent centroid of the jet for both the [EM + hadronic] and [EM + tracking] data sets. The mean detected jet energies and fractional RMS widths for these data are listed in Table 4A-6. The energy resolutions in [EM + tracking] are not appreciably worse than those in [EM + hadronic] for the higher-p_t jets, and are even somewhat better for the lowest p_t jets, presumably because of the rapidly decreasing hadronic-calorimeter resolution.

Further results of this study are presented in Figs. 4A-(6–7), where the energy of clusters found using the CDF-style cluster-finding algorithm in 40-GeV pp jet events is compared for [EM + tracking] and [EM + hadronic] calorimetry on an event-by-event basis. The primary losses in the former technique are a consequence of transverse energy carried by neutrons and K°_{L} mesons, which are detected with low probability in the EMC section. There is a clear correspondence between the energy of clusters found using these two techniques, which is

Table 4A-6. pp Jet Resolution Study.

E_t (jet)	20 GeV	40 GeV	80 GeV
EM + hadronic			
Mean detected (GeV)	13.77	29.70	65.32
Detected/generated	0.83	0.65	0.65
rms width (GeV)	6.60	9.59	13.99
% rms width	40	24	14.5
EM + tracking			
Mean detected (GeV)	13.98	26.79	59.01
Detected/generated	0.81	0.76	0.79
rms width (GeV)	5.21	8.49	13.50
% rms width	32	25	17

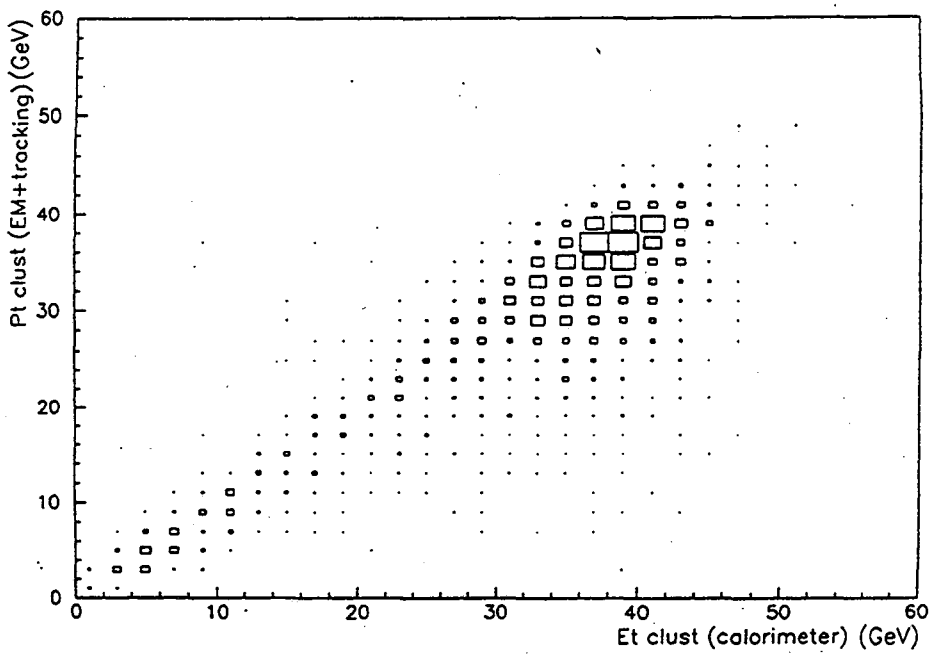

Figure 4A-6. A scatterplot of the energy of clusters found using electromagnetic energy from the STAR EMC plus tracking and momentum information from the TPC versus EM plus hadronic calorimetry. Data shown are for 40 GeV jet events from pp collisions at $\sqrt{s}$ = 200 GeV. The asymmetry in the distribution is due primarily to the transverse energy of neutrons and K_L^0 mesons which are detected using EM plus hadronic calorimetry but are detected in the EMC alone with low probability.

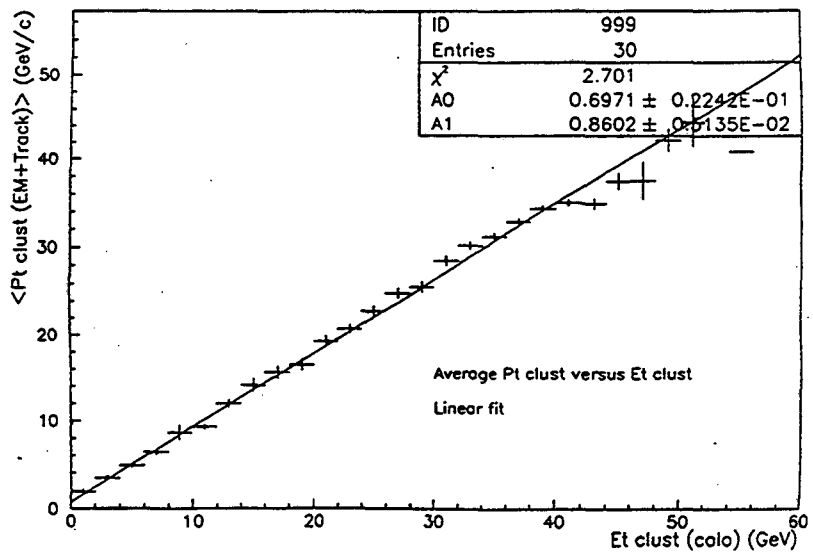

Figure 4A-7. A plot of the average energy of clusters found using EM plus tracking versus the average energy found using EM plus hadronic calorimetry for 40 GeV jet events from pp collisions at $\sqrt{s}$ = 200 GeV.

further evident in Figs. 4A-(8–9), in which slices in energy from 10–12 GeV and 38–40 GeV on the [EMC + hadronic] calorimetry axis have been projected onto the [EMC + tracking] axis. The resulting rms widths as a percentage of the mean are 20% and 17%, respectively. There are also data from a recent experiment at KEK that support the feasibility of studying jets and direct photons using tracking and electromagnetic calorimetry.[18]

For nucleus-nucleus collisions, it is also envisioned the [EM + tracking] technique will be used, both for high p_t and soft physics studies. For the latter, accurate measurement of the local transverse energy flow ($d^2E_t/d\eta d\phi$) is complicated by the fact that the response of the EMC to low-energy hadrons entering the detector is subject to fluctuations, despite the information available from the TPC tracking. Correction of the measured energy flow will require test-beam calibrations to document the response to low-energy hadrons and will, in any event, be subject to some loss of resolution due to this effect.

Recently, significant progress has been made towards reconstructing jets in AA collisions by filtering out all particles below a minimum transverse energy, E_c ~ 2–3 GeV, and making optimum use of correlations between the remaining leading particles which result as a consequence of the parton fragmentation function.[19] This technique is particularly well suited to the STAR TPC in which the momenta of all charged particles can be determined simultaneously. Additionally, it requires the use of a segmented neutral energy calorimeter to avoid loss of information due to missing neutral energy.

Although preliminary, it appears that even with the high multiplicity of charged particles expected in nucleus-nucleus collisions at RHIC, changes in the spectrum of leading hadrons resulting from modifications to the fragmentation function or to the average energy loss in the nuclear medium can be detected. This technique appears promising, and further

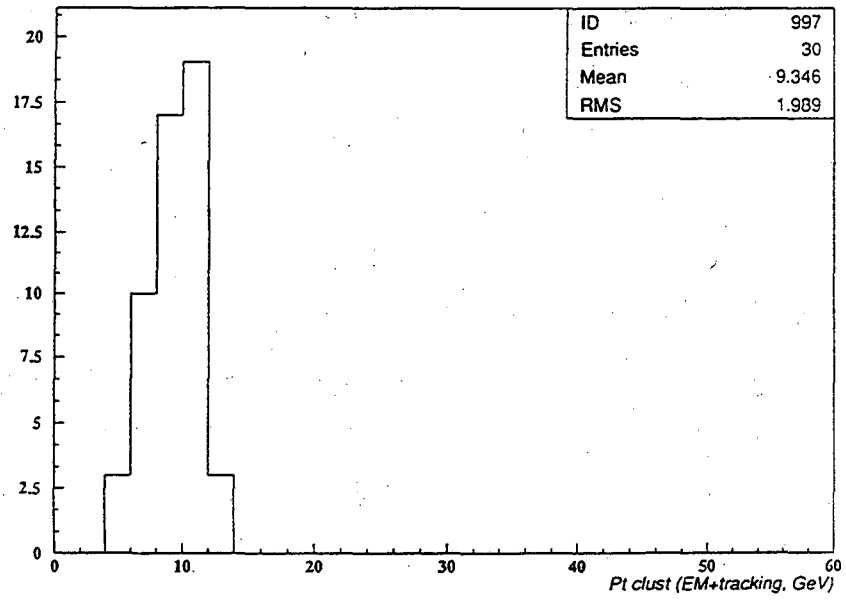

Figure 4A-8. A projection on the EM plus tracking axis of a slice of the EM plus hadronic calorimetry axis from 10 to 12 GeV.

[18]Y. Kim, University of Rochester Report UR-1182; I. H. Park, Ph.D. dissertation, Rutgers University, 1989, unpublished.

[19]D.W. Dong and M. Gyulassy, Phys. Rev. E47 (1993) 2913.

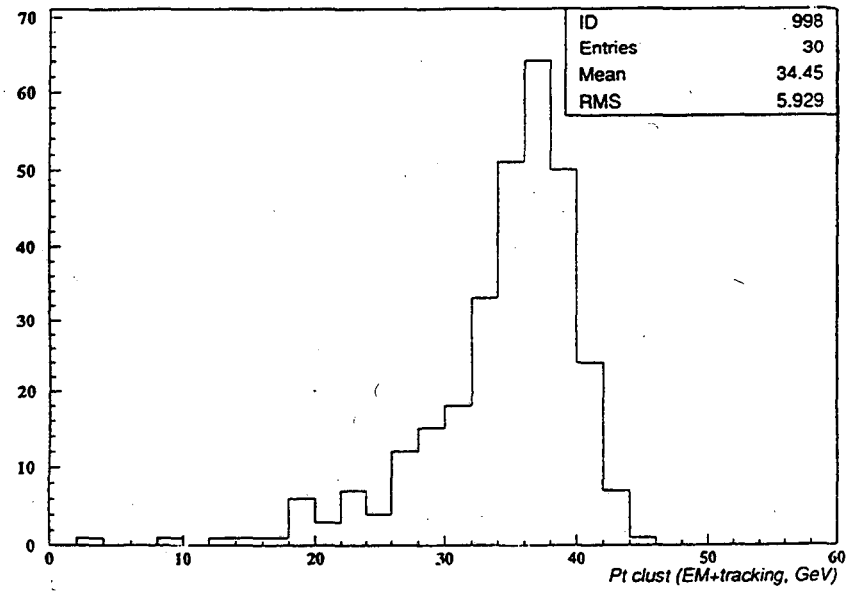

Figure 4A-9. A projection on the EM plus tracking axis of a slice of the EM plus hadronic calorimetry axis from 38 to 40 GeV.

study will be devoted to determine the extent to which jets can be fully reconstructed in AuAu collisions.

4.A.3. STAR Tracking Parameters

Transverse Momentum Resolution

An axial magnetic field like that of STAR allows a measurement of the transverse component of the momentum, p_t. Low p_t particles ($p_t \leq 1$ GeV/c) are important for the thermodynamic observables and HBT analysis. Higher p_t particles come from the fragmentation of jets and mini-jets. The ratio of inclusive p_t spectra at large p_t for pp, pA, and AA collisions at RHIC will enable one to investigate the effects of nuclear shadowing and quenching on jet and mini-jet production.[20] The ability to make these physics measurements depends crucially on the single-particle momentum resolution at both small and large p_t.

A realistic study of the p_t resolution using the standard STAR TPC Monte Carlo and track reconstruction algorithm was carried out in order to ascertain the ability of the TPC, with and without the SVT, to meet the physics objectives of STAR. Particles from central AuAu FRITIOF events were tracked through the STAR detector setup with all physical processes turned on. In order to enhance the statistics of high p_t tracks, a finite number of high p_t particles were superimposed onto the FRITIOF AuAu events. For this calculation, the TPC geometry was simulated using straight pad rows with 8×20 mm^2 pads. The momentum resolution was evaluated by comparing the transverse momentum of reconstructed and generated tracks.

Figure 4A-10 shows the p_t resolution ($\Delta p_t/p_t$) as a function of p_t. The inset frame is a blow-up of the results for $p_t < 1$ GeV/c. Track fitting was performed for two cases: (1) using hit information from the TPC alone (shown as black dots), and (2) using hit information from both the TPC and the SVT (shown as open triangles). For the low p_t tracks ($p_t < 1$ GeV/c), the

[20]M. Gyulassy and M. Pluemmer, Phys. Lett. **B243** (1990) 432; X.N. Wang and M. Gyulassy, Phys. Lett. **68** (1992) 1480.

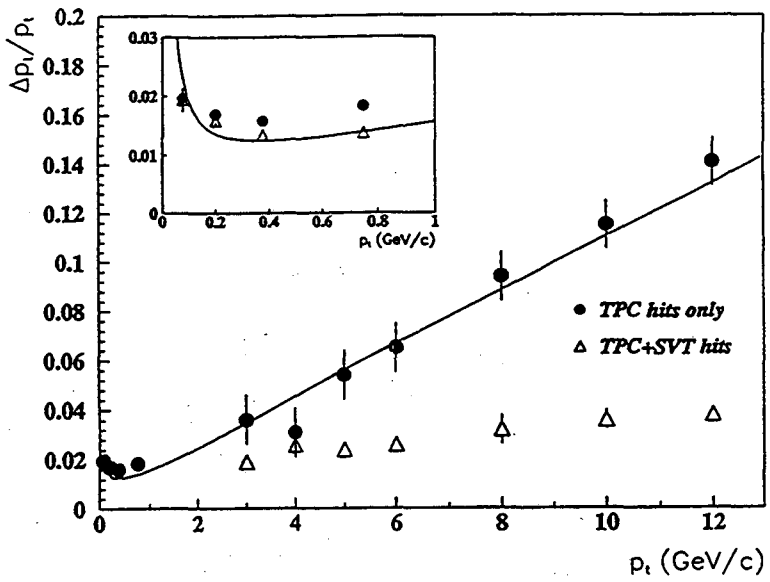

Figure 4A-10. The resolution, $\Delta p_t/p_t$, as a function of p_t for both the TPC only and the TPC plus the SVT.

momentum resolution (dominated by multiple scattering) reaches a minimum of 1.6% at $p_t \leq$ 0.4 GeV/c, where the bulk of particles are produced in nucleus-nucleus collisions. Below $p_t =$ 0.4 GeV/c, $\Delta p_t/p_t$ grows due to the $1/\beta$ factor in the multiple-scattering term. As p_t increases beyond 1 GeV/c, $\Delta p_t/p_t$ grows linearly with p_t and is dominated by the position resolution of the TPC hits. The p_t resolution increases from 3% at a p_t of 3 GeV/c to 14% at 12 GeV/c. The curve represents an analytical formula for the p_t resolution,[21] where some adjustment of the parameters of the curve has been made to optimize the fit.

The pad size of 8×20 mm^2 is not small enough to differentiate hits from close tracks in the inner rows of the TPC for the high-particle-density environment of AuAu collisions. Hence the usable path length for track reconstruction is reduced, and the momentum resolution deteriorates. Quantitatively, a track with a p_t of 5 GeV/c has a resolution of 2.9% when it is tracked alone in the TPC. The resolution deteriorates to 5.4% when it is superimposed on a central AuAu event. The SVT has a much smaller pixel size than the TPC, which significantly enhances the hit-position resolution close to the primary vertex. The inclusion of SVT hits in the track fitting improves the p_t resolution by a factor of two or more for the high p_t tracks. This improvement is a consequence of the addition of a few well defined hits close to the primary vertex, which increase the effective path length for track fitting. Perfect matching of TPC hits with the SVT hits was assumed. Inclusion of the primary vertex as a point in the helix fit will provide an improvement in the momentum resolution that is comparable to that observed when the SVT points are added. This technique is only helpful for primary tracks.

For high p_t tracks, the main effect of the momentum resolution on inclusive p_t spectra is to skew the distribution toward higher p_t values. This effect is shown in Fig. 4A-11, which displays the ratio of a momentum resolution "smeared" distribution to the same "unsmeared" distribution, using the p_t resolution of the TPC with and without SVT hits as shown in Fig. 4A-10. The unsmeared distribution is $p_t(1 + p_t/1.8)^{-12.14}$, which is a parameterization of the inclusive charged particle spectrum for $p\bar{p}$ collisions at $\sqrt{s}$ = 200 GeV. Note that the ratio

[21]Data Analysis Techniques for High Energy Physics Experiments, R.K. Bock, H. Grote, D. Notz, M. Regler (Cambrigde: Cambridge University Press, 1990) pp. 310-3.

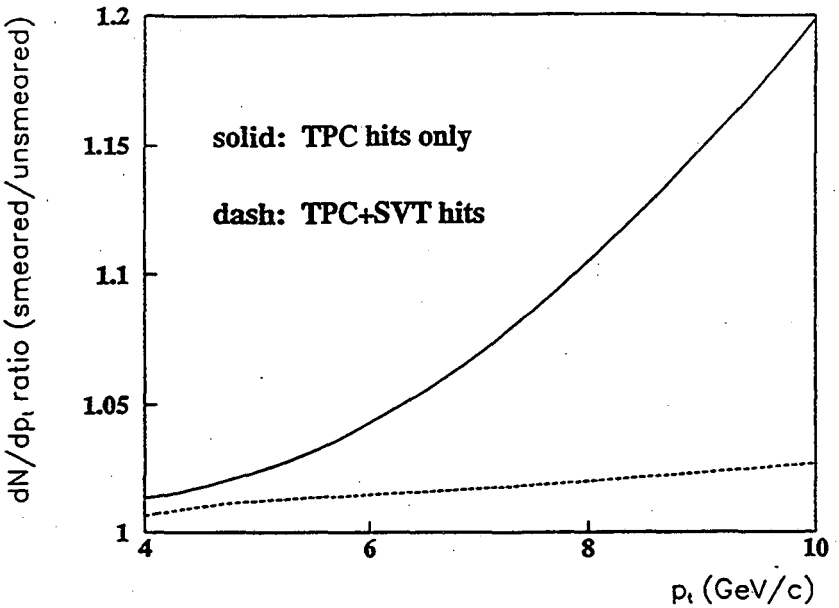

Figure 4A-11. The effect of momentum resolution on the measured yield assuming measurement with the TPC alone (solid) and with the TPC plus the SVT (dashed).

increases monotonically with p_t. Gluon shadowing and jet quenching are expected to reduce dramatically the yield of charged particles for $p_t > 2$ GeV/c from central AuAu collisions. In order to disentangle gluon shadowing from jet quenching, it is necessary to study single particle inclusive spectra from pp and pAu collisions up to $p_t = 6$ GeV/c. The deviation of the smeared distribution from the unsmeared parent distribution is on the order of a few percent in the p_t region of 2–6 GeV/c for TPC tracks without SVT hits. If the SVT hits are included, the effect of smearing is minimal out to $p_t = 10$ GeV/c. With the present simulation, we conclude that the TPC alone should provide sufficient p_t resolution for a study of inclusive spectra up to $p_t = 6$ GeV/c, and the addition of SVT hits extends this p_t limit to above 10 GeV/c. Note that for stiff tracks that originate from the primary vertex, use of the reconstructed primary vertex location would have an effect comparable in magnitude to that observed when SVT hits are included.

4.A.4. Rates and Pileup in the TPC

Full calorimetry in STAR will be accomplished with electromagnetic calorimetry plus tracking. An immediate concern, therefore, despite the fact that the electromagnetic calorimeter is inherently a fast device, is the relatively long time (50 μs) required to drift electrons created by track ionization to the TPC endcaps. The potential for pileup from different events during the TPC drift time is dependent primarily on the luminosity for a given species and is therefore quite different for AA and pp interactions. *In neither case, however, does pileup in the TPC fundamentally compromise the performance of the STAR detector.*

For AuAu interactions, the design luminosity is $\mathcal{L}_0 \sim 10^{26}$ cm^{-2}s^{-1}. Given this luminosity, minimum-bias AuAu collisions will occur approximately once every millisecond. As the TPC pad planes can potentially receive charge as soon as the gated grid is open and will continue to accept charge for 50 μs, it is possible for an event occurring up to 50 μs before the triggered event, or 50 μs after it, to deposit some charge (and therefore create some track segments) during the time required to drift the ionization from the event of interest. The total time during which the TPC is sensitive to pileup in this instance is 100 μs, although the degree of confusion

as a consequence of pileup tracks clearly diminishes the further the pileup event is separated in time from the triggered event. The probability of two minimum-bias events occurring within the time the TPC is sensitive is therefore less than

$$(N_1 \cdot N_2) \cdot \sigma/(N_1) \sim (1000\ s^{-1}) \cdot (100 \cdot 10^{-6}\ s) \sim 0.10\ , \qquad (4.A\text{-}1)$$

where $N_1 = N_2$ is the rate of minimum bias AuAu collisions and σ is the time during which the TPC is sensitive. The probability that both events appear to be in the interaction diamond at the same time is much smaller, $\sim 10^{-3}$ per interaction. Given that minimum-bias collisions will occur throughout the interaction diamond, ($\sigma_{rms} \sim 20$ cm) and that the vertex resolution afforded by the combined tracking in the TPC and SVT is ~200 μm, it is apparent that, for charged secondaries, the relevant probability of unresolvable event pileup is $\sim 10^{-9}$. Since the probability that only neutral particles are produced is negligibly small, this is also the probability that the neutral energy detected in the calorimeter could arise from undetected multiple events. For approximately 0.1% of the AuAu collisions that occur, some ambiguity in the measurement of neutral energy will remain since the proposed calorimeter will not, in general, be able to determine the vector of a neutral energy deposit with sufficient resolution to differentiate between two different sources which both appear to be in the interaction diamond. Provided fast tracking algorithms can be developed for the third-level trigger, it is possible that this source of pileup could be essentially eliminated at the trigger level.

For pp interactions, the design luminosity is $\mathcal{L}_0 \sim 10^{31}\ cm^{-2}s^{-1}$. The rate of minimum-bias pp collisions is therefore one per microsecond. As a consequence, many events will occur and be registered during the ~50 μs in which the TPC gated grid is open. These events will show up in addition to the triggered event and will produce what appear to be secondary tracks. In this instance, the topology of tracks other than those from the event of interest is somewhat different than in AuAu interactions, insofar as the apparent vertices of pileup events will be distributed more or less uniformly along the axis of the TPC. A slight clustering, or lumpiness, in this distribution will result from the fact that events can only occur during crossing periods which are ~110 ns or 0.55 cm of TPC drift apart. Additionally, tracks originating from pileup events will in general either appear not to project back to the region of the interaction diamond (Fig. 4A-12) or will appear not to be complete—part of the track information having been lost due to the closing of the gated grid at a time random with respect to the time at which the pileup event occurred.

To study the feasibility of analyzing compound events in order to distinguish them, a tracking analysis and GEANT simulation of the performance of the TPC under these conditions were performed.[22,23] The number of events occurring within the time during which the gated grid of the TPC is open was calculated using the published cross section for minimum-bias pp interactions (45 mb) and the pp design luminosity for RHIC ($1.4 \times 10^{31}\ cm^{-2}s^{-1}$). The resulting number of minimum-bias events is 6.3×10^5 per second. Consequently, within the 100 μs the TPC is sensitive, 63 minimum-bias events would occur. An appropriate number of minimum-bias FRITIOF pp events were generated, and the resulting events were processed by GEANT. A fast TPC simulator was used to assign each point a spatial resolution and diffusion corresponding to its true position in the chamber. Finally, the z coordinates of hits corresponding to tracks from pileup events were modified to reflect an appropriate drift time

[22]M.A. Bloomer, P.G. Jones, and I.M. Sakrejda, *Evaluation of the STAR TPC Performance for Detecting pp Collisions at RHIC*, STAR Note No. 57.

[23]P.G. Jones, *Update on the Study of pp Collisions* in STAR, STAR Note No. 80.

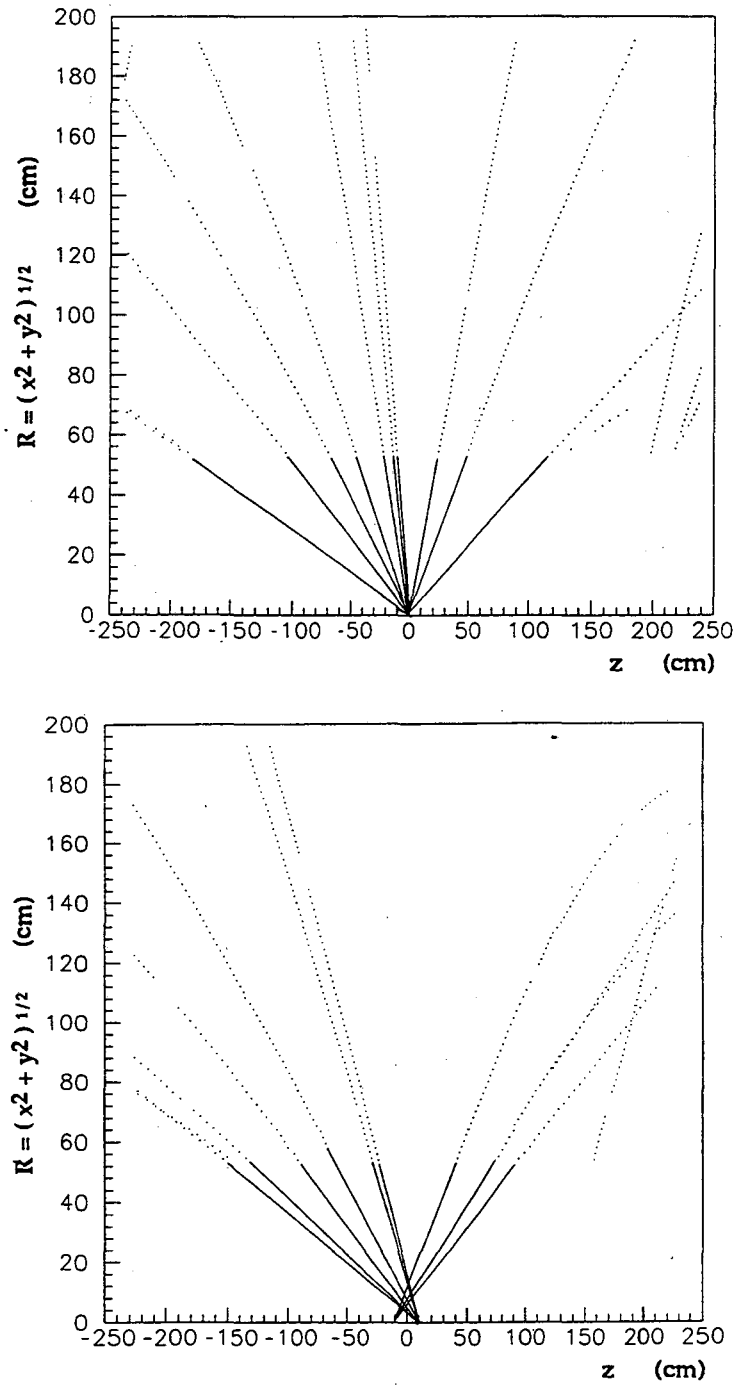

Figure 4A-12. A projection in the plane of $R = \sqrt{x^2 + y^2}$ vs z of hits in the TPC (dotted) for a triggered pp interaction (top), and a pileup interaction occurring one RHIC crossing (220 ns) later (bottom). Both interactions occur at z = 0 in the TPC. However, tracks from the pileup event do not project to the proper vertex at z = 0 since this event occurred at a time random with respect to the opening of the TPC gated grid. For a finite interaction diamond, out-of-time tracks will be distinguished by a lack of hits on the inner pad rows due to incomplete drifting.

for "out of time" tracks, and all events were merged into a composite event to fully simulate the track loading of the TPC in this circumstance. Overlapping pad plane hits from different tracks were merged together, and the STAR pattern recognition program was run on the simulated TPC data.

Evaluation of these data shows that tracks in multi-pp events are reconstructed well. Comparison of Figs. 4A-13 and 4A-14 shows that most of the available hits were assigned to tracks and that the level of the confusion due to hits from different Monte Carlo tracks being assigned to the same reconstructed track is low (Fig. 4A-15). The momentum resolution was not affected (Fig. 4A-16).

Another crucial question, however, is whether different events can be distinguished. In order to investigate this problem, the position of the vertex for each reconstructed track of $p_t >$ 150 MeV/c was calculated. Figure 4A-17 shows a histogram of the z coordinates of the vertices reconstructed in this manner. From these data it is noted that the vertices from different events cluster in groups spaced by approximately 10 cm. This corresponds to the average spacing between consecutive events. It is concluded from these data that high p_t tracks may be properly assigned to the events from which they originate. Further study of lower-momenta tracks needs to be completed. Finally, it is noted that these events were analyzed using tracking in the TPC alone. Using information from the SVT and TOF systems together is expected to enhance the ability of the STAR spectrometer to deal with multi-event pileup in pp interactions.

To exploit the full potential of a polarized-proton program at RHIC, it is necessary to achieve as high a sensitivity as possible to small, spin-dependent asymmetries. It is also attractive in general to extend the measurement of jets and direct photons to as high a p_t as possible by maximizing the integrated luminosity. To examine the suitability of tracking with the STAR TPC at higher luminosity, the above calculation was repeated for the top RHIC

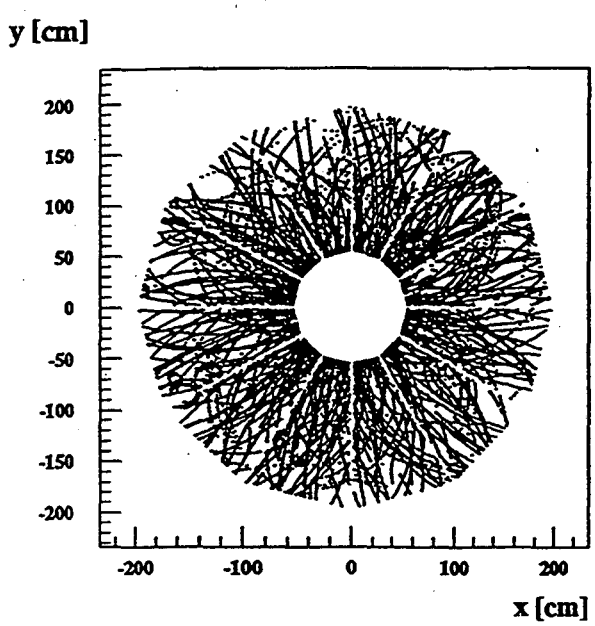

Figure 4A-13. A projection along the z axis of all TPC hits resulting from the ~60 minimum bias pp events occurring within ±50 μsec of a triggered pp interaction. Data shown are for the design luminosity of $\mathcal{L} = 1.4 \times 10^{31}$ $cm^{-2}s^{-1}$. The radial lines in which there are no hits correspond to the location of structural elements which support the TPC pad planes.

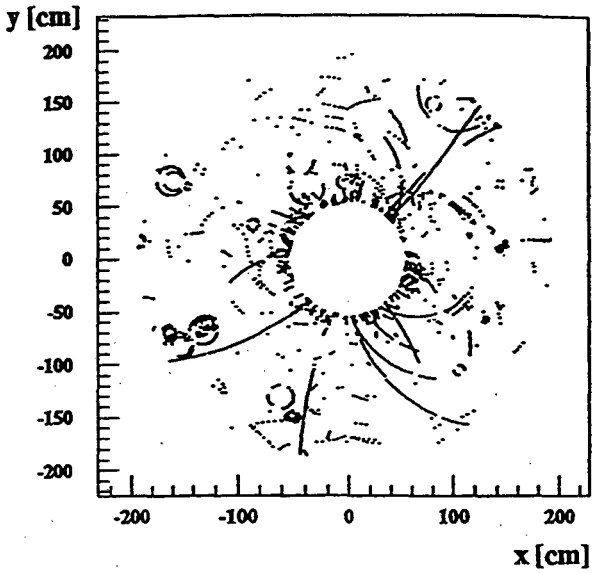

Figure 4A-14. A projection along the z axis of TPC hits in Fig. 4A-13 which were not assigned to a track in reconstructing the ~60 minimum bias pp interactions occurring with ±50 μsec of a triggered pp interaction. Data shown are for the design luminosity of $\mathcal{L} = 1.4 \times 10^{31}\ cm^{-2}s^{-1}$.

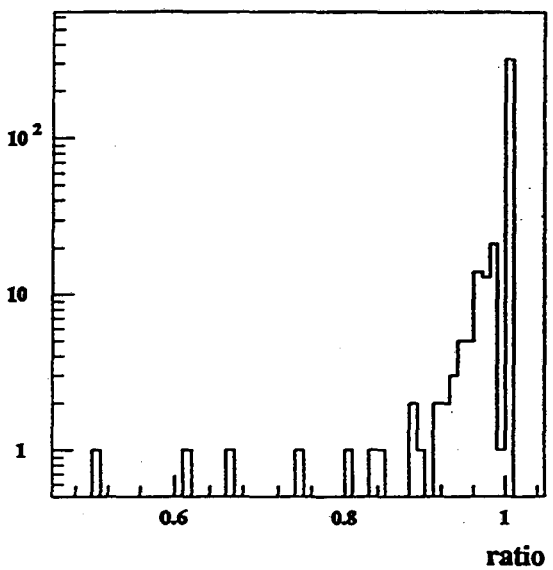

Figure 4A-15. For a given reconstructed track, the ratio of the number of "good" hits assigned to the track which in fact originated from it to the total number of hits assigned to the track after GEANT simulation and tracking reconstruction. For ~97% of the tracks reconstructed, more than 90% of the hits comprising the track were assigned correctly.

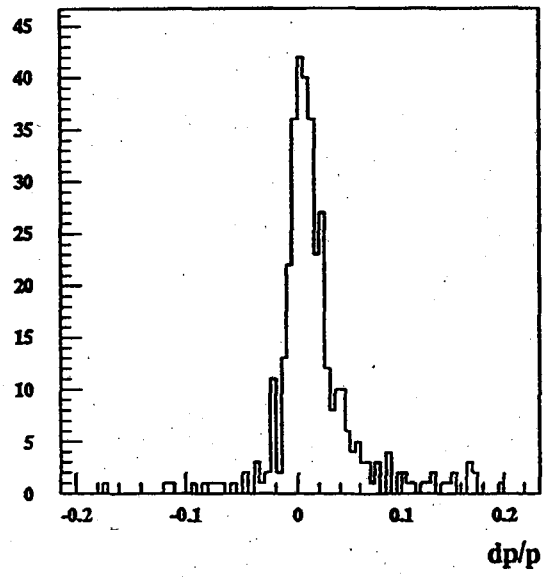

Figure 4A-16. The momentum resolution, Δp/p, for tracks reconstructed in a full GEANT and tracking simulation of the ~60 minimum bias pp interactions occurring ±50 μsec of a triggered pp interaction. Data shown are for the design luminosity of $\mathcal{L} = 1.4 \times 10^{31}\ cm^{-2}s^{-1}$. The distribution is similar to that obtained for AA interactions and does not exhibit any degradation due to track loading from multiple minimum bias pp interactions.

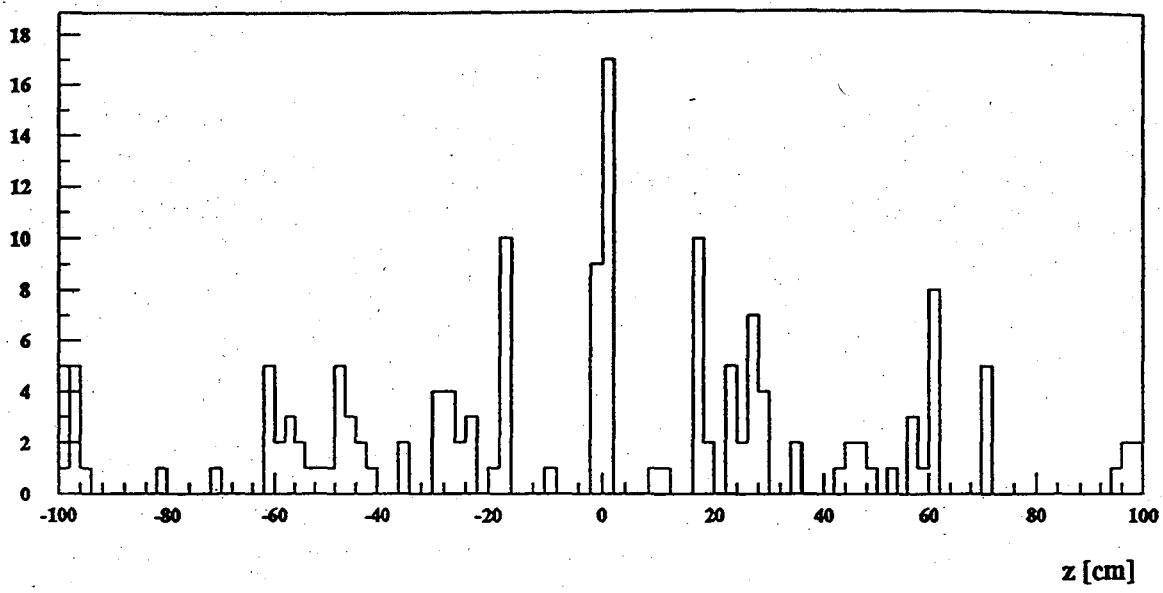

Figure 4A-17. The reconstructed z coordinate of the vertex for all tracks having $p_t \geq 0.15$ GeV/c from the ~60 minimum bias pp interactions occurring within ±50 μsec of a triggered pp interaction. Data shown are for the design luminosity of $\mathcal{L} = 1.4 \times 10^{31}\ cm^{-2}s^{-1}$. Vertices from different tracks tend to cluster into groups spaced by ~10 cm corresponding to the average spacing between consecutive events at this luminosity.

luminosity of $\mathcal{L}_0 \sim 2 \times 10^{32}$ cm^{-2}s^{-1} . Once again, a procedure was derived to test the ability of the STAR spectrometer to identify tracks originating from the triggered event. In this instance, however, timing information from the central trigger-barrel scintillators was also used to tag in-time tracks and separate them from background tracks resulting from minimum-bias events occurring up to 50 μs before or after the triggered event.

Several additional changes to the simulation chain were also made. Most importantly, a new TPC pad plane designed to improve tracking efficiency was included as part of the GEANT simulation. This pad plane consisted of 50 radial pad rows, employing 3.35×12 mm^2 pads at the innermost rows (1 through 18) and 6.7×20 mm^2 pads at the outer rows. The radial design improves the momentum resolution for high p_t tracks by minimizing the track-crossing angle with respect to the pads, while the placement of smaller pads on the innermost pad rows improves the two-track resolution in the highest-track-density region.[24]

A further improvement was the inclusion of a finite-interaction region or "diamond" in the GEANT simulation. As a consequence, events were generated with an rms width of 7.5 cm (half the proton-bunch length[25]) along the beam direction. In principle, a smaller diamond may be achieved by colliding the beams at a non-zero crossing angle. The transverse size of the beam was taken to be 0.5 cm. All interactions, including the generation of delta electrons, were enabled in the GEANT simulation.

The primary problem investigated was the feasibility of correctly identifying and reconstructing tracks that originate from the triggered event. At the top RHIC luminosity, the rate of minimum-bias pp interactions increases to 9 MHz, which corresponds to an average rate of almost one event per bunch crossing. Noting that the drift velocity in the TPC is $v_d \approx 5$ cm/μs, it is evident that consecutive minimum-bias events will be separated by only 6 mm along the drift direction. For this reason, the retrieval of the TOF information from the STAR central trigger-scintillator barrel (CTB) was also investigated.

The central trigger barrel was modeled as a single cylinder for the purpose of this simulation. Its efficiency was assumed to be perfect, and losses due to incomplete azimuthal coverage between adjacent slats and multiple hits were not addressed. Particles reaching the CTB were assigned an absolute time stamp corresponding to their TOF and the crossing period in which they were produced. This information was then used to determine whether the trigger-barrel system could be used to flag tracks from the triggered event and whether the interaction vertex deduced from these tracks might be used to localize the search for the remaining tracks in the event.

The fundamental elements of the simulation used in this instance were the same as those discussed above. Minimum-bias pp events were generated using the Lund-FRITIOF model. These were processed by GEANT using a full simulation of the STAR detector geometry. The output of GEANT was input to the fast-TPC simulation program (FST) in order to generate a pad response for each elementary GEANT pad crossing and to assign each point a spatial resolution according to the track geometry and the track position in the detector.[26,27] The response of the pads was then examined by the program to determine whether close hits should be merged to form a single cluster, simulating the performance of the cluster-finding

[24]Since the time of this study, the design of the TPC sectors has been changed such that straight pad rows are used. This decision was a consequence both of practical considerations (layout) and of the fact that the improvement in the momentum resolution for high p_t tracks using radial pad rows was marginal.
[25]RHIC Conceptual Design Report, BNL Report No. BNL-52195.
[26]P.G. Jones and G. Rai, *The STAR TPC Pad Response Function*, STAR Note No. 33.
[27]P.G. Jones and G. Rai, *The STAR TPC Pad Response Function*, STAR Note No. 34.

algorithm.[28] FST was also modified to extract the time of flight information for all hits registered in the trigger barrel scintillator. Tracks from successive GEANT events were displaced appropriately in time and space relative to the triggered event. Finally, the reconstructed tracks were compared with the GEANT input using an evaluation program written for this task.

In Fig. 4A-18, the resulting hit densities in the TPC are shown as a function of row for both the design and upgraded pp luminosities at RHIC. The three curves shown indicate the ideal number of elementary GEANT pad crossings, the number of resolved hits (including merged clusters) from the FST program, and the number of merged hits. At the design luminosity for pp interactions, the hit density is similar to that of a central SiSi event. At the top

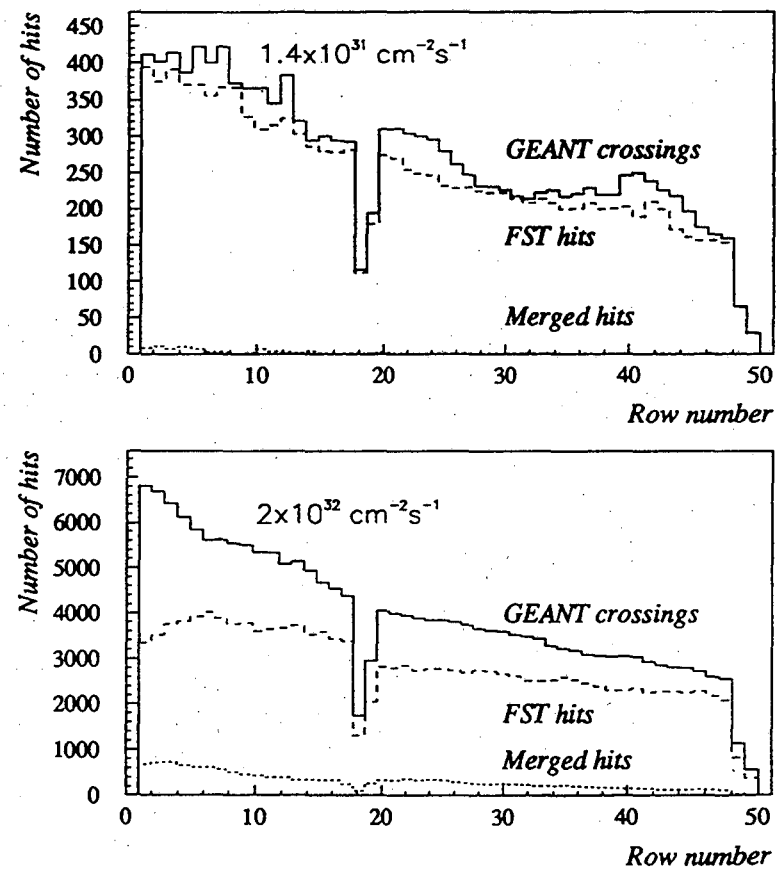

Figure 4A-18. The frequency, as a function of pad row, of hits in the TPC from tracks resulting from multiple pp interactions occurring within ±50 μsec of a triggered pp interaction. Data shown are for the design luminosity of $\mathcal{L} = 1.4 \times 10^{31}\ cm^{-2}s^{-1}$ (top) and the upgrade luminosity of $\mathcal{L} = 2.0 \times 10^{32}\ cm^{-2}s^{-1}$ (bottom). The GEANT hits (solid) and FST hits (dashed) represent respectively the a priori hits and the hits reconstructed by the FaSt TPC Simulator. The difference between these curves results from hits which are merged (dotted) due to the intrinsic space-time resolution of the TPC pixels. For the design luminosity, tracks are well separated in space and time, and the loss of information due to the merging of hits is minimal. For the upgrade luminosity, some loss of information due to track loading is evident for the inner pad rows. The gap occurring at pad row 18 is a consequence of incomplete pad rows resulting from the transition from the inner TPC sectors to the outer ones when radial pad rows are used. Straight pad rows are used in the present sector design.

[28] P.G. Jones and I.M. Sakrejda, *The STAR FaSt TPC Simulation*, STAR Note No. 56.

luminosity, it is closer to that of a central AuAu event (Fig. 4A-19). The loss of information due to merging hits as a consequence of track loading in the high-luminosity environment is clearly evident, especially for the inner pad rows. However, it is also apparent that, except for the innermost pad rows, the percentage of merged hits is not significantly different than for central AuAu events for which the tracking efficiency has been shown to be adequate.

It should be noted that in developing these results, no attempt was made to deconvolute hits using detailed information on the response of the pads. Hits falling closer together in space or time than certain conservative criteria were simply merged together. It may therefore be possible to recover some of the information lost due to the merging of hits once a more realistic pad-response program is developed.

As noted above, results at both the design luminosity and upgrade luminosity for RHIC were generated with a realistic distribution of events in the beam diamond. The interaction region is characterized by an RMS width of 7.5 cm, corresponding to a drift time equivalent to approximately 14 beam crossings. Consequently, the z coordinate of the interaction vertex alone can not be used to identify tracks from the triggered event if there is a high probability another event will occur within ±14 beam crossings. On the other hand, particle production can only occur during successive crossing periods separated by approximately 100 ns. A TOF system with even modest resolution should therefore be able to distinguish tracks emanating from the crossing of interest.

In Fig. 4A-20, the TOF information is shown for all tracks from both the triggered event and pileup events for a luminosity of $\mathcal{L}_0 = 2.0 \times 10^{32}\ \mathrm{cm^{-2}s^{-1}}$. Events occurring before and after the triggered event are clearly seen at multiples of the 110-ns bunch spacing. The triggered event is situated at time t = 0. In Fig. 4A-21, the z coordinate of the distance of closest approach to the beam axis is shown for all reconstructed tracks from both the trigger and pileup events. In Fig. 4A-22, the same plot is shown, but in this case the hatched histograms show only tracks that registered a hit in the trigger barrel scintillator in the time interval ($|\Delta t| < 55$ ns)

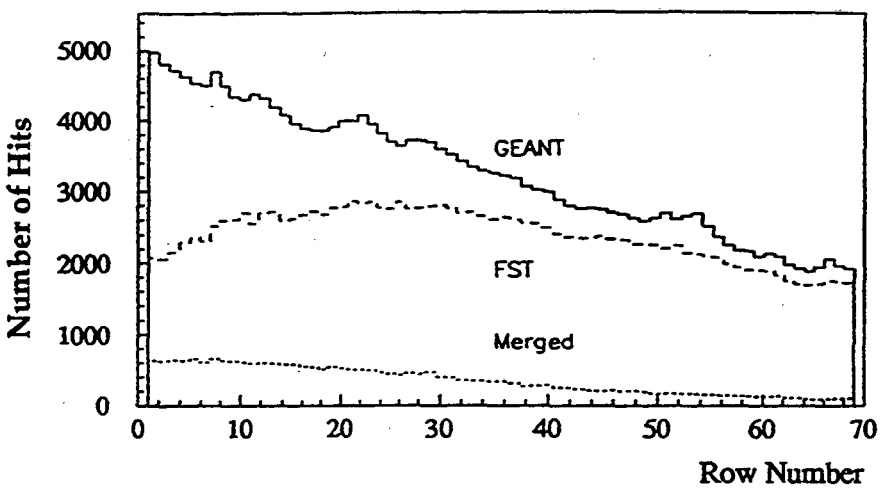

Figure 4A-19. The frequency, as a function of pad row, of hits in the TPC from tracks resulting from a central AuAu interaction. The GEANT hits (solid) and FST hits (dashed) represent respectively the a priori hits and the hits reconstructed by the FaSt TPC Simulator. The difference between these curves results from hits which are merged (dotted) due to the intrinsic space-time resolution of the TPC pixels. Some loss of information due to track loading is evident for the inner pad rows. Straight pad rows are used in the present sector design.

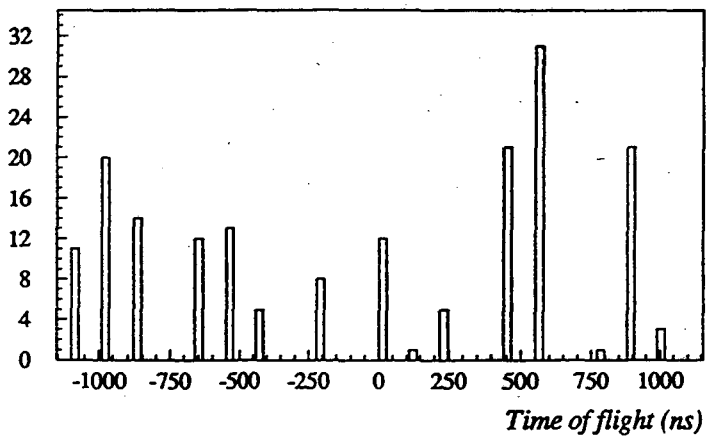

Figure 4A-20. The time of flight (TOF) spectrum for tracks having $p_t \geq 0.15$ GeV/c resulting from some of the multiple pp interactions occurring within ±50 μsec of a triggered pp interaction. Data shown are for the upgrade luminosity of $\mathcal{L} = 2.0 \times 10^{32}\ cm^{-2}s^{-1}$. Tracks from different events are well separated in TOF.

corresponding to the triggered event. Although some low momentum tracks are lost, it is evident that even at the higher luminosity, the timing information of the trigger-barrel scintillator may be employed to flag tracks ($p_t \geq 150$ MeV/c) from the triggered event. This results in the elimination of a considerable number of background tracks in the vicinity of the triggered events that would not be rejected on the basis of position information alone. It is also noted, however, that it is not possible to discriminate different events that occur in the same beam crossing using the timing information of the trigger barrel alone. The triggered crossing in Fig. 4A-21 in fact contains two separate events from the same beam crossing: one with two tracks that hit the trigger barrel and one with 10 tracks. Table 4A-7 lists the frequency of beam crossings in which multiple events occur at the two luminosities.

It is concluded from this study that there is evidence that TOF information from the trigger-barrel scintillator may provide a useful mechanism for flagging the in-time tracks from a

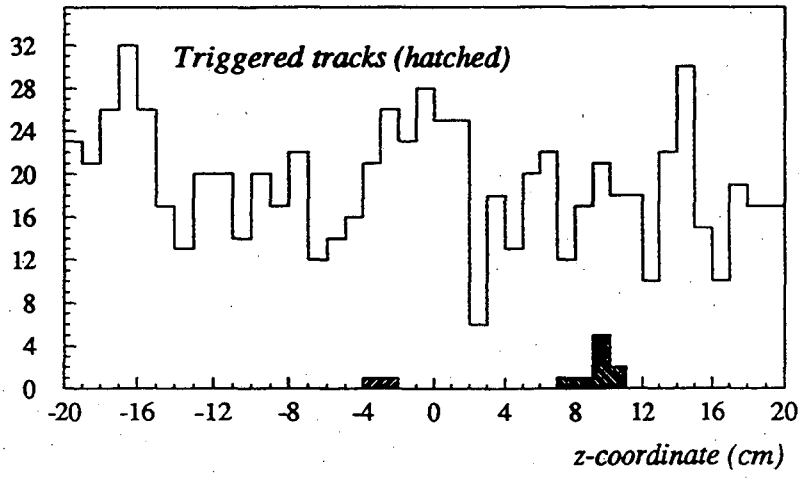

Figure 4A-21. The reconstructed z coordinate of vertices within $|z| \leq 20$ cm for all tracks from multiple minimum bias pp interactions occurring within ±50 μsec of a triggered pp interaction. Data shown are for the upgrade luminosity of $\mathcal{L} = 2.0 \times 10^{32}\ cm^{-2}s^{-1}$. Tracks from the triggered event are hatched. In this particular instance, two pp interactions have occurred in the same triggered event.

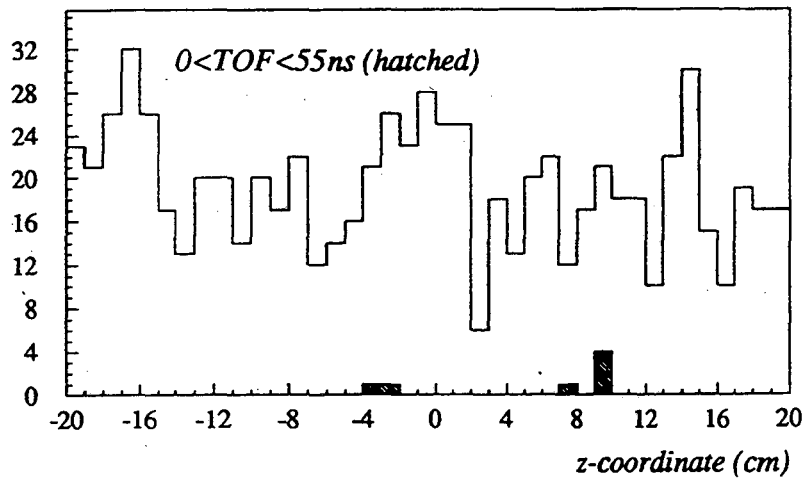

Figure 4A-22. The reconstructed z coordinate of vertices within $|z| \leq 20$ cm for all tracks from multiple minimum bias pp interactions occurring within ±50 μsec of a triggered pp interaction. Data shown are for the upgrade luminosity of $\mathcal{L} = 2.0 \times 10^{32}$ cm^{-2}s^{-1}. Tracks having $p_t \geq 0.15$ GeV/c are identified as originating from the from the triggered event using time of flight (hatched). Tracks from the triggered event having insufficient momentum to reach the time of flight counters are lost.

triggered pp event in the midst of a considerable number of background events at $\mathcal{L}_0 = 2.0 \times 10^{32}$ cm^{-2}s^{-1}. However, it is not possible to resolve multiple events originating from the same beam crossing (Δt = 500 ps) using TOF information alone. In this instance, a cut on the interaction vertex in addition to a TOF cut may be adequate if the events are well separated in the interaction diamond. A remaining difficulty, however, is that of resolving tracks from the triggered crossing that may not reach the trigger-barrel scintillators. The signal-to-background ratio is of the order of 1 to 15 for these low-momentum tracks at $\mathcal{L}_0 = 2.0 \times 10^{32}$ cm^{-2}s^{-1} based on vertex information alone. Consequently, while the unambiguous assignment of tracks with sufficient transverse momentum to reach the central trigger barrel appears to be possible ($p_t \geq 150$ MeV/c, $|\eta| < 1$), the correct assignment of lower-momentum tracks is still to be determined at this luminosity.

Table 4A-7. Frequency of Multiple-Event Beam Crossings for Minimum-Bias pp Events at the Design and Upgrade Luminosities for RHIC.

Events/Crossing	Frequency for $\mathcal{L}_0 = 1.4 \times 10^{31}$ cm^{-2}s^{-1}	Frequency for $\mathcal{L}_0 = 2.0 \times 10^{32}$ cm^{-2}s^{-1}
0	810	290
1	61	358
2	0	152
>2	0	72

4.B. Physics Requirements on EMC Performance

4.B.1. Physics Requirements on Energy Resolution

Nucleus-Nucleus Interactions

Accurate determination of the neutral electromagnetic energy improves the resolution in determining the total transverse energy, thus allowing better global-event characterization. It also provides unique possibilities for triggering on rare events (see, for example, Chapter 3). To study the neutral energy resolution provided by the EMC, the response of this detector was followed through a full GEANT simulation of the STAR detector for a number of colliding systems.

For AA collisions, the RHIC environment is characterized by a large multiplicity of primary charged particles at mid-rapidity ($dn_{ch}/d\eta \approx 700$). Secondary particles from decays and delta rays increase this number by as much as a factor of two. In principle, to achieve the best resolution in determining the neutral electromagnetic energy, it is therefore necessary to subtract the energy deposited by charged particles in the EMC on a particle-by-particle basis. One could accomplish this by parameterizing, as a function of momentum and angle of incidence, the energy deposited in the EMC by charged particles. Using tracking information from the STAR TPC, one might then calculate on a tower-by-tower basis how much of the total energy deposited was due to charged particles and subtract that contribution.

A first-order estimate of the neutral electromagnetic energy resolution afforded by the STAR EMC may be derived more simply. To accomplish this, the full response of the STAR detector was followed through GEANT for a number of colliding systems. The total data set used for this investigation is shown in Table 4B-1.

Figure 4B-1 shows the average multiplicity in the central trigger barrel (CTB) for the different systems studied. Figure 4B-2 indicates the corresponding average total energy deposited in the scintillator layers of the EMC, with and without consideration of local light-saturation effects (Birk's Law). It is noted that the energy deposited in the scintillator layers represents ~5.6% of the total energy incident upon the EMC.

Various quantities from the GEANT output were saved, including the kinematics of all produced particles, all "hits" in the STAR CTB, and all hits in the STAR electromagnetic calorimeter. For all particles that traversed or stopped in a given layer of scintillator in the STAR EMC, the energy deposited in the layer and the parent-particle ID number were also saved. With this information, the total energy deposited in the EMC (E_{tot}), the total neutral energy deposited in the EMC ($E_{neutral}$), and the total charged-particle multiplicity detected in the STAR CTB (M_{CTB}) were extracted for each event. The average correlation between the charged-

Table 4B-1. Data Set Used for GEANT Simulation of the Energy Resolution of the STAR EMC.

System	Events
pp	600
^{12}C ^{12}C	100
^{28}Si ^{28}Si	50
^{197}Au ^{197}Au	10

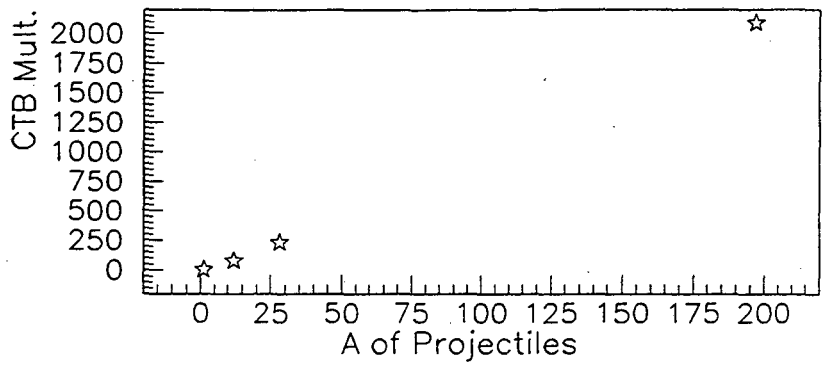

Figure 4B-1. The average multiplicity detected in the STAR central trigger barrel (CTB) plotted vs mass for pp, $^{12}C^{12}C$, $^{28}Si^{28}Si$, and $^{197}Au^{197}Au$ interactions.

particle multiplicity and the total energy deposited in the EMC was then used to extract the neutral energy deposited by finding the best fit to the relationship

$$E_{neutral} = (\alpha \cdot E_{tot} - \beta M_{CTB}) \qquad (4.B\text{-}1)$$

for all events of a given type (e.g., AuAu). The resulting best-fit parameters were used to calculate the neutral energy in each event, and the calculated value was compared to the known value saved from GEANT. Figure 4B-3 shows qualitatively how well this simple procedure works for the SiSi sample. The squares show the total sampled energy deposited in the EMC for each of 50 central SiSi events ($\sqrt{s_{nn}}$ = 200 GeV), while the stars indicate the corresponding total sampled neutral energy. The results of the fit procedure are indicated by circles. Corresponding data for AuAu interactions are presented in Fig. 4B-4.

The difference between the known and fit values of the neutral energy was used to derive a percent resolution for each event. The average neutral energy resolution for each sample was then plotted as a function of the average multiplicity detected in the CTB for each colliding system (Fig. 4B-5). These results have again been plotted both with and without consideration of local light-saturation effects. For reference, the size of the statistical error resulting purely from the multiplicity in the CTB is indicated as well.

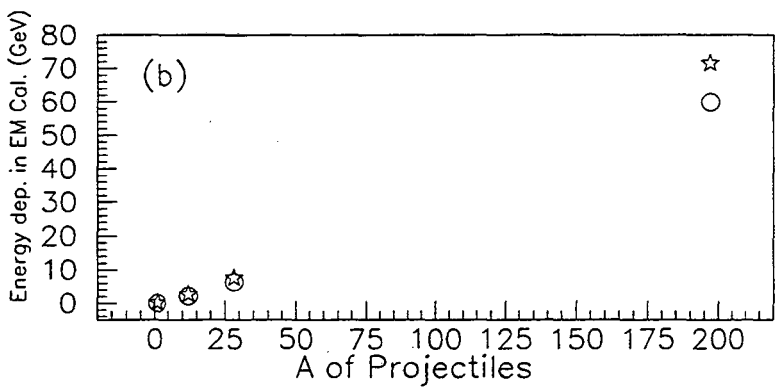

Figure 4B-2. The total sampled energy deposited in the STAR electromagnetic calorimeter (EMC) plotted vs mass for pp, $^{12}C^{12}C$, $^{28}Si^{28}Si$, and $^{197}Au^{197}Au$ interactions. Data are shown both with (circles) and without (stars) the inclusion of local light saturation effects (Birk's law).

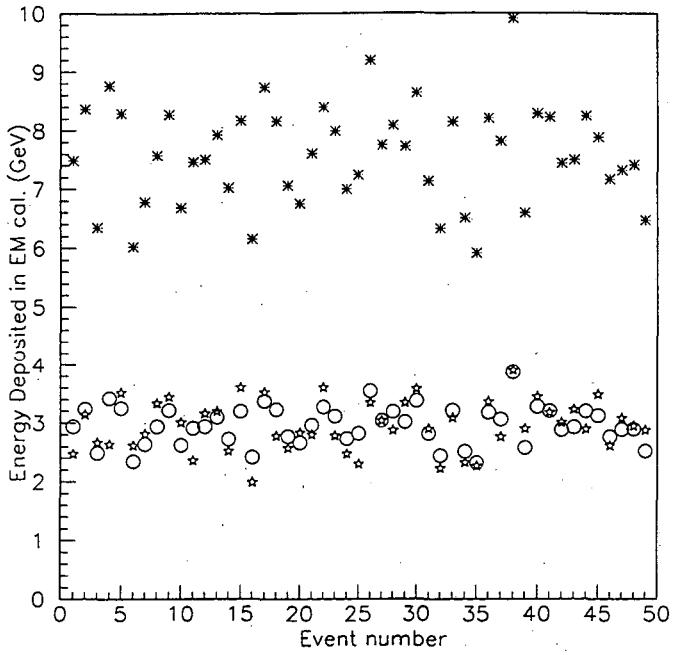

Figure 4B-3. A comparison, for 50 central $^{28}Si^{28}Si$ interactions, of the total sampled energy deposited in the EMC (asterisks), the neutral energy deposited in the EMC as determined from GEANT (stars), and the neutral energy deposited in the EMC determined by extrapolating from the total sampled energy and the measured multiplicity in the STAR CTB using Eq. (4.B-1) (circles). Event-by-event comparison of the value of the neutral energy calculated using Eq. (4.B-1) and the known value from GEANT was used to compute the effective neutral energy resolution.

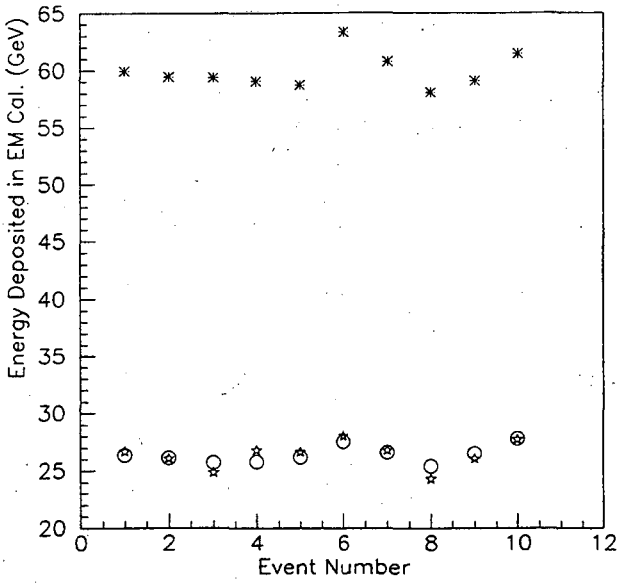

Figure 4B-4. A comparison, for 10 central ^{197}Au ^{197}Au interactions, of the total sampled energy deposited in the EMC (asterisks), the neutral energy deposited in the EMC as determined from GEANT (stars), and the neutral energy deposited in the EMC determined by extrapolating from the total sampled energy and the measured multiplicity in the STAR CTB using Eq. (4.B-1) (circles). Event-by-event comparison of the value of the neutral energy calculated using Eq. (4.B-1) and the known value from GEANT was used to compute the effective neutral energy resolution.

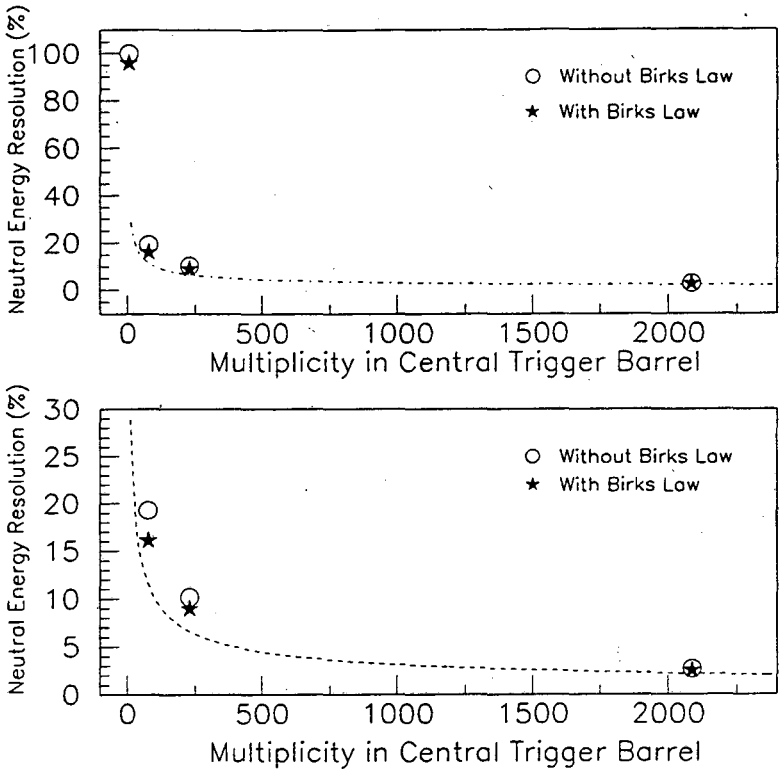

Figure 4B-5. The neutral energy resolution available at the trigger level plotted vs multiplicity in the STAR central trigger barrel for pp, $^{12}C^{12}C$, $^{28}Si^{28}Si$, and $^{197}Au^{197}Au$ interactions (top). Data are shown both with (stars) and without (circles) the inclusion of local light saturation effects. An expanded scale for $^{12}C^{12}C$, $^{28}Si^{28}Si$, and $^{197}Au^{197}Au$ interactions is shown as well (bottom).

What is evident from this study is that for high-multiplicity events, such as those expected at RHIC, the neutral energy resolution afforded by this simple technique works quite well. For AuAu interactions, this simulation suggests that one can achieve a neutral energy resolution of ~2.5%, which is available at the trigger level. The qualitative agreement between the extracted resolutions and the statistical error for a given multiplicity indicates that even though on a particle-by-particle basis there is a large variation in the energy deposited in the EMC, when considered over many particles, the fluctuations average out.

To test the effect upon the neutral energy resolution of partial coverage, this study was repeated for two scenarios in which only a portion of the EMC barrel was implemented. The two configurations considered were one in which the EMC covered two wedges, each covering $\Delta\phi = 90°$ and $|\eta| \leq 1.05$, and a second in which the EMC covered only one wedge having the same acceptance. The results of this simulation indicated that for AuAu interactions, the neutral energy resolution for the first configuration decreased from ~2.5% for the entire EMC barrel to ~2.7%, given the assumption that the neutral energy is distributed uniformly at mid-rapidity. For the second configuration considered, the corresponding resolution was ~4.5%, given the same assumption.

pp Interactions

The limiting resolution of a sampling EM calorimeter depends on the frequency of sampling. This resolution has been parameterized as shown in Fig. 4B-6. The choice of 5-mm-thick lead (0.9 X_0) and 3- to 4-mm scintillator (0.01 X_0) will provide approximately

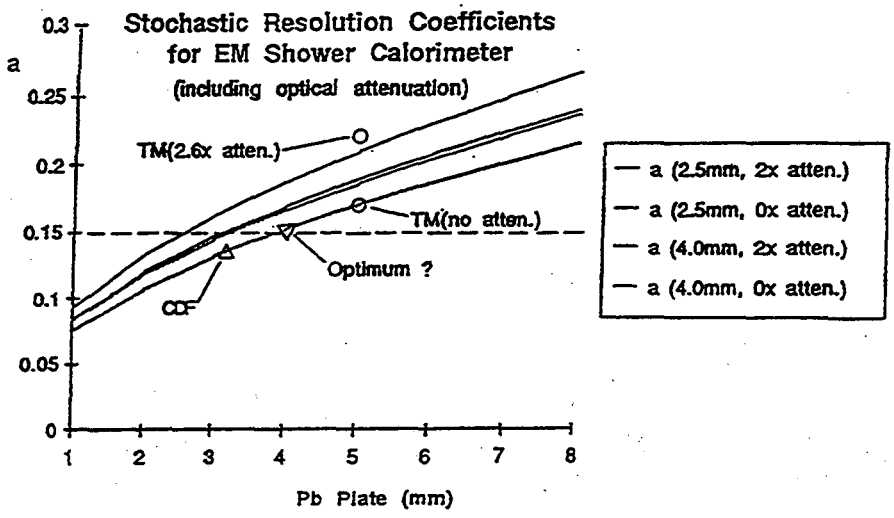

Figure 4B-6. Scaling of the stochastic term in EM shower counter geometries and comparison to the ANL/WSTC test modules and CDF shower counters. For the lead absorber thickness (5 mm) in the present design, the resolution expected is ~16%/$\sqrt{E}$.

$\Delta E/E = 16\%/\sqrt{E}$. This resolution is adequate for direct gamma and jet physics above p_t of 10 GeV/c, based on experience with previous collider detectors that have successfully studied similar physics. Other limiting factors in jet resolution come from the TPC resolution ($\Delta p/p$ ~ 1.5% at high momentum) and from missing neutrals such as K°_L's, Λ°'s, and neutrons. The sampling depth of 18 X_0 is adequate, based on experience with 19 X_0 lead glass at FNAL and from EGS calculations done for other experiments. Contributions to the resolution from fluctuations in energy loss through the back of the calorimeter are expected to be negligible below 50 GeV/c. The coupling scheme between the scintillator and fiber has been shown to give 2–4 photoelectrons/MIP and does not contribute significantly to the overall stochastic resolution.

Tile-to-tile or tower-to-tower variations in response lead to degraded resolution as an energy-independent term and can also lead to poor trigger selectivity (hot-spots). These effects can be controlled by proper calibration procedures before, during, and after assembly of the detector.

4.B.2. Segmentation Required for Physics

The mechanical segmentation for the proposed barrel calorimeter is 40 towers in η ($\Delta\eta \approx 0.05$) and 60 towers in ϕ ($\Delta\phi \approx 0.1$). Each tower is read out via a bundle of optical fibers. The effective segmentation in η and ϕ can therefore be reduced by joining the fiber bundles from more than one tower to a single phototube. Similarly, the longitudinal segmentation can be increased by grouping fibers from a given tower. The segmentation that is ultimately used will be determined by how many readout channels are available.

The global neutral transverse energy (E_t) is one important observable that will be measured with the EMC barrel. This measurement does not place any significant requirement on segmentation. To achieve some measure of asymmetries in the transverse energy, a somewhat finer segmentation is required (e.g., six to eight bins in η and four to six bins in ϕ).

Use of the EMC barrel is also important in jet studies. A typical jet has a radius of about $\sqrt{(\Delta\eta)^2+(\Delta\phi)^2} \sim 0.7$. A few bins in η and ϕ are required within this radius in order to get the

shape and the centroid for the jet. The segmentation necessary for jet studies is thus about 0.1 in both η and ϕ. This segmentation is typical of that used for jet studies at existing collider detectors.

The physics requiring the highest degree of segmentation is the study of inclusive direct photons and direct-γ + jet coincidences. In these studies, the photon energy and direction must be determined as accurately as possible. High segmentation leads to better angular resolution, as the uncertainty in the angle is determined by the size of the tower. High segmentation also leads to smaller occupancy and a reduced probability that a given tower is hit. This reduces the probability that the tower in which the γ deposits its energy is also hit by charged hadrons. Consequently, the uncertainty in the photon energy is decreased. Further simulation is required to determine the extent to which jets and direct photons can be measured in AuAu collisions using the present segmentation of the STAR EMC.

Longitudinal segmentation of the towers may be used to help differentiate between hadronic and electromagnetic energy in the EMC. Charged hadrons loose energy primarily through ionization energy loss (dE/dx). Hadrons with sufficiently high energy may pass completely through the EMC. Consequently, the profile of energy deposited versus depth in the calorimeter is relatively flat for charged hadrons. The electromagnetic energy deposited in the calorimeter results from photons, electrons, and positrons. In this case, the dominant process in the development of showers is bremsstrahlung, which leads to a rapid increase in the transverse size of the EM shower at a relatively shallow depth in the EMC modules. As a consequence, the EMC is very efficient for absorbing all the electromagnetic energy.

The difference in these profiles is illustrated in Fig. 4B-7 in which the electromagnetic and hadronic energy deposited in the EMC barrel are shown as a function of depth. These data result from an integration over all towers for all particles which strike the barrel in a GEANT simulation of one central AuAu event at $\sqrt{s_{nn}}$ = 200 GeV. The electromagnetic energy profile is

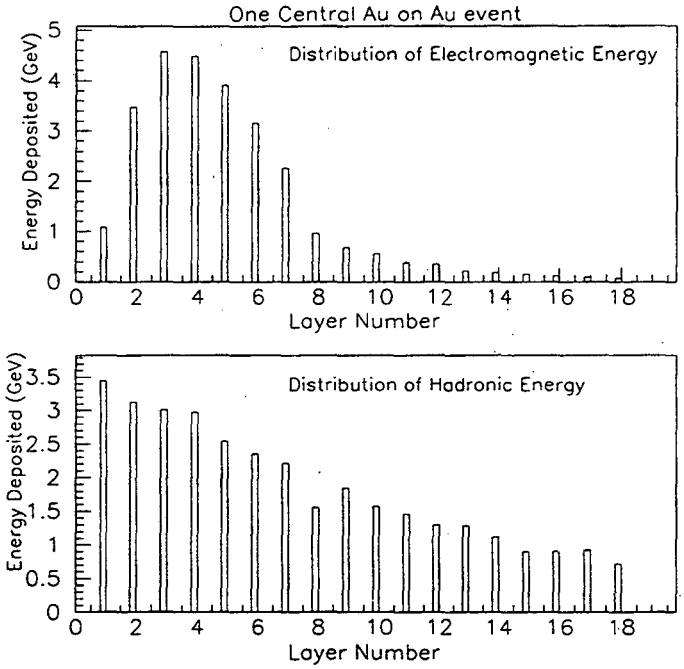

Figure 4B-7. For a central AuAu event, the energy deposited as a function of depth in the calorimeter (sampling layer) from electromagnetic (top) and hadronic (bottom) sources.

peaked towards the front of the EMC as expected from the discussion above. The profile for the hadronic energy deposition shows a monotonic decrease with depth in the EMC. This shape results from folding the incident momentum distribution of the charged hadrons with their energy loss. Low momentum hadrons lose all of their energy and stop at a shallow depth in the EMC leading to a relatively large value at the start of the energy deposition profile. High energy hadrons pass completely through the EMC which results in more energy being deposited late in the profile relative to that from electromagnetic showers.

Separation of electromagnetic and hadronic energy in the EMC is also important for the study of $W^{\pm}$ and Z° production. In this instance, there are several different kinds of background which must be considered in identifying electrons. These include real electrons from π° dalitz decay and electrons from γ conversions in the materials of the SVT and TPC. These show up as tracks in the TPC and are accepted as valid electrons. A more serious background at high p_t results from pions, which are produced at a rate two orders of magnitude higher than that for electrons from $W^{\pm}$ decay. One way in which this background arises is from overlaps of charged pions with neutral pions. In this instance, a track is seen and the observed energy is high due to the neutral energy that is deposited. Another type of background is from hadronic interactions of charged pions in the calorimeter which deposit a large fraction of the energy of the π. These are more serious because the energy is observed at the same location as the track in η and ϕ and the shower max spatial resolution does not eliminate them. In these cases, the pion either produces neutral energy through charge exchange or creates a hadronic shower near the front of the EMC.

In some collider detectors this type of background is eliminated by vetoing events in which shower particles from the EMC leak into a hadronic calorimeter located immediately behind it. In the present design however, identification of this type of background requires examining the profile of the energy deposited as a function of depth in the calorimeter.

Figure 4B-8 shows the energy profiles for twenty-five 30 GeV/c electrons and twenty-five 30 GeV/c π^{-}. In this case, the profiles expected characteristically from previous high

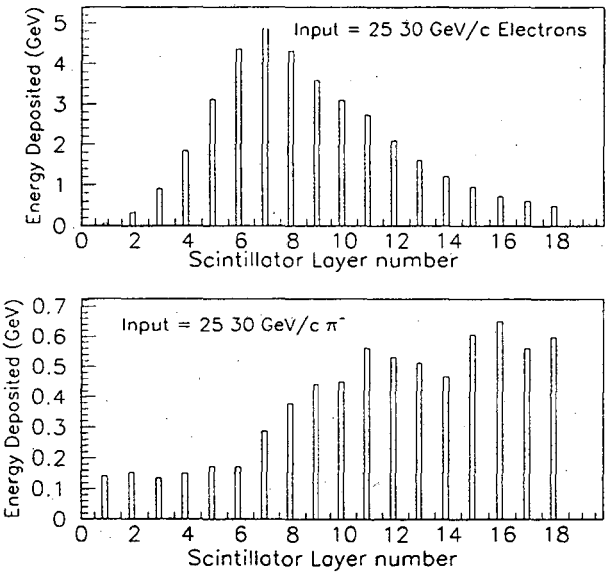

Figure 4B-8. The energy deposited as a function of depth (sampling layer) in the EMC for twenty-five 30 GeV/c electrons and π^{-} mesons.

energy results are recovered. Electrons lose essentially all of their energy in the EMC, while the π^- lose relatively little. By segmenting the towers longitudinally, one can use the difference in the energy deposition as a function of depth to aid in particle identification. This is particularly important in the study of $W^{\pm}$ production, since the STAR EMC is not hermetic, and determination of the cross section for $W^{\pm}$ production will therefore require careful measurement of the inclusive electron spectrum at high p_t. The ability to trigger on high energy electrons or photons is also improved.

The segmentation required in the shower max detector to differentiate between direct γs and those resulting from π° decay is discussed in Section 4.B.4.

4.B.3. Physics Requirements on Acceptance

The improved resolution and unique trigger capabilities provided by the EMC afford a rich program of scientific research in pp, pA, and AA collisions. In general, the acceptance of the EMC required to accomplish this program depends upon the specific study which is discussed.

For the study of rare events exhibiting unusual isospin abundances for example, the most promising kinematic region in which to search is unknown. Although existing cosmic ray data[29] support the existence of isospin fluctuations at forward rapidities ($|y| \gtrsim 2$), it has been suggested[30] that given the uncertainty in the present state of knowledge, a sensitive search at mid-rapidity should also be made. In this instance, therefore, the acceptance of the EMC should be as large as possible, consistent with constraints of funding. Alternatively, a search for this type of unusual event may be performed in a limited region of acceptance in the event the full calorimeter is not ready at the start of RHIC operations. Similar arguments apply to the search for events exhibiting an unusual correlation between energy density and entropy density, which might result as a consequence of a transition to a color-deconfined plasma of quarks and gluons. In this instance however, the acceptance at mid-rapidity would be favored, since it is in this region the highest densities and temperatures will be reached.

For the study of the energy loss of hard-scattered partons which traverse the reaction volume and interact with the surrounding medium during the early stages of the collision, the primary consideration is the ability to reconstruct jets from direct-γ + jet coincidences. As the jet typically has a radius $\sqrt{(\Delta\eta)^2 + (\Delta\phi)^2} \lesssim .7$, the minimum acceptance of the EMC required for this study is at least as large. This corresponds roughly to the acceptance of a segment of the barrel EMC which is full length in η, and subtends one-fourth of the full azimuthal acceptance ($\Delta\eta = \Delta\phi \sim 1.4$). Given this radius and acceptance, the direction of the outgoing parton is confined to $|\eta| \lesssim 0.3$. (With corrections for missing acceptance, it may be possible to extend the coverage for jets to $|\eta| \lesssim 0.5$.) Since the transverse size of a photon shower is relatively small (~3 cm), the minimum acceptance required for its detection at $\phi = \phi_{jet} + 180^\circ$ is $|\eta| \lesssim 0.3$, $\Delta\phi \sim 45^\circ$. Although some study of direct-γ + jet coincidences would be possible with the minimum acceptance, the yield of such events is low enough[31] at high p_t that there is a clear advantage in having the full acceptance of the EMC barrel. To a good approximation, the observed yields are in fact proportional to the acceptance in η and ϕ.

The acceptance required for the study of $W^{\pm}$ and Z° production is presently under study. The fact that the yield of $W^{\pm}$ production is rather flat as a function of rapidity in pp

[29] C. M. G. Lattes, Y. Fugimoto, and S. Hasegawa, Phys. Rep. 65 (1980) 151.
[30] J. D. Bjorken, "Baked Alaska", AGS/RHIC Users Meeting, June 2–3, 1993, Brookhaven National Laboratory, Upton, New York 11973
[31] See, for example, Sections 2.B.2 and 3.D.

interactions suggests however, that the acceptance of the EMC barrel may be adequate (see, for example, Fig. 2B–6).

The physics that places the most restrictive requirements on the acceptance of the electromagnetic calorimeter is the study of the gluon structure function G(x) in pp and pA interactions.

Restricting the acceptance in η and ϕ limits the coverage in x and the effective range over which G(x) can be studied. One way to measure G(x) for nucleons or nuclei is to use inclusive direct-γ + jet production.[32] Both the direct-γ and the "away-side" jet must be detected in coincidence so the kinematics of the incoming partons can be calculated. Thus, the STAR EMC acceptance must include coverage near a given ϕ for the jet, and also near $\phi + 180°$ for the γ. The remainder of this section deals with these kinematics and, in particular, the impact on the η coverage.

The two main contributions to inclusive direct-γ + jet production are the Compton ($q + g \rightarrow \gamma + q$) and annihilation ($q + \bar{q} \rightarrow \gamma + g$) subprocesses, assuming isolated direct-γs.[33,34,35] Both of these subprocesses involve $2 \rightarrow 2$ scatterings, and the kinematics can be determined as follows. The incoming partons are assumed to have fractions x_1 and x_2 of the beam momenta p_1 and p_2, respectively, and to have negligible transverse momenta so that they collide collinearly. The outgoing partons have momenta p_3 and p_4, and angles θ_3 and θ_4 relative to the incoming direction of parton #1. Conservation of momentum transverse to the beam gives

$$p_t = p_3 \sin\theta_3 = p_4 \sin\theta_4 \ , \tag{4.B-2}$$

and along the beam gives

$$\begin{aligned} p_1 x_1 - p_2 x_2 &= p_3 \cos\theta_3 + p_4 \cos\theta_4 \\ &= p_t \left(\frac{\cos\theta_3}{\sin\theta_3} + \frac{\cos\theta_4}{\sin\theta_4} \right) \ . \end{aligned} \tag{4.B-3}$$

Ignoring quark masses, energy conservation at the parton level leads to

$$\begin{aligned} p_1 x_1 + p_2 x_2 &= p_3 + p_4 \\ &= p_t \left(\frac{1}{\sin\theta_3} + \frac{1}{\sin\theta_4} \right) \ . \end{aligned} \tag{4.B-4}$$

Expressed in terms of pseudorapidity $\eta = -\ln(\tan(\theta/2))$, and using the expressions above, gives

[32] T. Akesson, *et al.*, Z. Phys. **C34** (1987) 293.
[33] J.F. Owens, Rev. Mod. Phys. **59** (1987) 465.
[34] T. Ferbel and W.R. Molzon, Rev. Mod. Phys. **56** (1984) 181.
[35] E.L. Berger, E. Braaten, and R.D. Field, Nucl. Phys. **B239** (1984) 52.

$$x_1 \equiv \frac{p_t}{p_1}\left(\frac{e^{(+\eta_3)}+e^{(+\eta_4)}}{2}\right)$$
$$x_2 \equiv \frac{p_t}{p_2}\left(\frac{e^{(-\eta_3)}+e^{(-\eta_4)}}{2}\right) . \qquad (4.B\text{-}5)$$

In the special case of equal incoming momenta and high energies,

$$p_1 = p_2 = \sqrt{s}/2 \qquad (4.B\text{-}6)$$

For collisions at RHIC, the annihilation subprocess ($q + \bar{q} \rightarrow \gamma + g$) will be small since there will be no valence antiquarks in either beam. The dominant contribution to the inclusive direct-γ + jet production cross section will be from the Compton subprocess ($q + g \rightarrow \gamma + q$). Note that the final state in both cases involves a direct-γ plus either a quark jet or a gluon jet. Considering the Compton subprocess only, then the cross section for pp interactions will be approximately

$$\frac{d^2\sigma(pp \rightarrow \gamma + jet + x)}{d(p_t^2)\, d\phi\, dy_\gamma\, dy_{jet}} \propto \sum_f \left[q_f^p(x_1) G^p(x_2) \frac{d\sigma_{(q_f g \rightarrow \gamma q)}}{d\hat{t}} + q_f^p(x_2) G^p(x_1) \frac{d\sigma_{(q_f g \rightarrow \gamma q)}}{d\hat{t}} \right] , \qquad (4.B\text{-}7)$$

and similarly for proton-nucleus or nucleus-nucleus collisions, where the sum in Eq. (4.B-7) is over parton flavor. The quantities y_γ and y_{jet} are the rapidities of the direct-γ and jet, respectively. $G^p(x)$ is the gluon structure function of the proton, which is of particular interest in pA interactions, since the modification of this structure function in the nucleus has important consequences for the spectra of particles observed in AA interactions. The $q_f(x)$ are the quark structure functions in the proton. For example, $q_f(x) = u(x), d(x), s(x), \bar{u}(x), \ldots$ for u, d, and s quarks and for u antiquarks, respectively. Information on these quark structure functions can be obtained from deep inelastic electron and muon scattering and from neutrino scattering. The parton level cross sections $d\sigma/d\hat{t}$ can be calculated from perturbative QCD when the process is a hard scattering. For the purposes of this section, the onset of hard scattering will be assumed to correspond to $p_t = 10$ GeV/c.

A number of corrections need to be applied to the simple relation in Eq. (4.B-7), corresponding to annihilation, higher order subprocesses, and bremsstrahlung effects.[36,37,38] In addition, there are corrections caused by isolation cuts on the experimental data[39] and other effects. Nevertheless, the gluon structure function $G^p(x)$ of the proton has been determined as a function of x from inclusive direct-γ + jet experimental data at the ISR,[40] and work is in progress to obtain $G^p(x)$ from recent data at the Tevatron collider detector CDF. Therefore, such a procedure should also be possible at RHIC.

[36] J.F. Owens, Rev. Mod. Phys. **59** (1987) 465.
[37] E.L. Berger, E. Braaten, and R.D. Field, Nucl. Phys. **B239** (1984) 52.
[38] P. Aurenche *et al.*, Phys. Lett. **140B** (1984) 87.
[39] E.L. Berger and J. Qiu, Phys. Rev. **D44** (1991) 2002.
[40] T. Akesson *et al.*, Z. Phys. **C34** (1987) 293.

For collisions of identical beams of particles (pp, SiSi, etc.), the sum in Eq. (4.B-7) involves seven structure functions (u, $\bar{u}$, d, $\bar{d}$, s, $\bar{s}$, G) if heavy quarks are ignored. In the proton, these structure functions are reasonably well determined[41] from many high energy experiments. However, much less is known about these structure functions, and especially $G^A(x)$, for nuclei. It is expected that $G^A(x)$ can be determined using inclusive direct-γ + jet production cross sections from proton-nucleus (pA) collisions.

Assume that the pA inclusive direct-γ + jet production data are subdivided into L bins of x_p for partons from the proton beam, and M bins of x_A for partons from the beam of nuclei. Then for each x_A bin, Eq. (4.B-7) would give L linear equations in terms of the seven structure functions (q_f^A, G^A) for the nucleus, assuming the proton structure functions and the perturbative QCD cross sections $d\sigma / d\hat{t}$ are known. Additional information on $q_f^A(x)$ can be obtained from deep inelastic electron and muon scattering from the nucleus and other data. This information will add constraints to the linear equations from Eq. (4.B-6). Therefore, $G^A(x)$ for the nucleus A can be obtained for sufficiently large L and accurate inclusive direct-γ + jet cross section data. (In principle, all of the structure functions for the nucleus could be obtained this way, though the results might be strongly correlated.) The extension of this procedure to nucleus-nucleus interactions is straightforward.

The two colliding beams at RHIC will have equal velocities so that the interaction points do not precess around the accelerator. Thus, to good approximation, the momenta per nucleon for the two beams will be the same. For example, for pA collisions of protons with nuclei containing A nucleons,

$$p_A \equiv A p_p \quad . \tag{4.B-8}$$

As a result, Eq. (4.B-5) gives $x_p \approx A x_A$. In other words, in a hard-scattering process for beams of the same momentum per nucleon, a parton from a proton with momentum fraction x_p will give the same scattering as the same parton from a nucleus with a momentum fraction $x_A = x_p/A$.

To some approximation, the parton structure functions in nuclei should be similar to those for protons and neutrons. For nuclei with N neutrons and Z protons, and assuming $x_A = x_p/A = x_p/(N + Z)$,

$$\begin{aligned} q_f^A(x_A) &\approx N q_f^n(x_p) + Z q_f^p(x_p) \\ G^A(x_A) &\approx N G^n(x_p) + Z G^p(x_p) \quad . \end{aligned} \tag{4.B-9}$$

Figure 4B-9 shows three structure functions from the proton — u(x), $\bar{u}$(x), and G(x).[42] The sea-quark structure functions are all quite small for $x_p \gtrsim 0.2$. In this same region, the valence quark structure functions are comparable to or larger than the gluon structure function. If Eqs. (4.B-9) are approximately correct, then the process of deriving $G^A(x)$ from inclusive direct-γ + jet production in pA collisions becomes particularly clean for $x_A \gtrsim 0.2/A$. In this case, u^A and d^A can be determined from deep inelastic scattering data, $\bar{u}^A$, $\bar{d}^A$, s^A, and $\bar{s}^A$, are all approximately zero, and the only unknown in Eq. (4.B-7) will be G^A.

The same kinematic region that is relevant for measurement of the gluon structure function of a nucleon within the nucleus is also of interest for measuring the spin-dependent

[41] J.G. Morfin and W.K. Tung, Z. Phys. **C52** (1991) 13.
[42] J.G. Morfin and W.K. Tung, Z. Phys. **C52** (1991) 13.

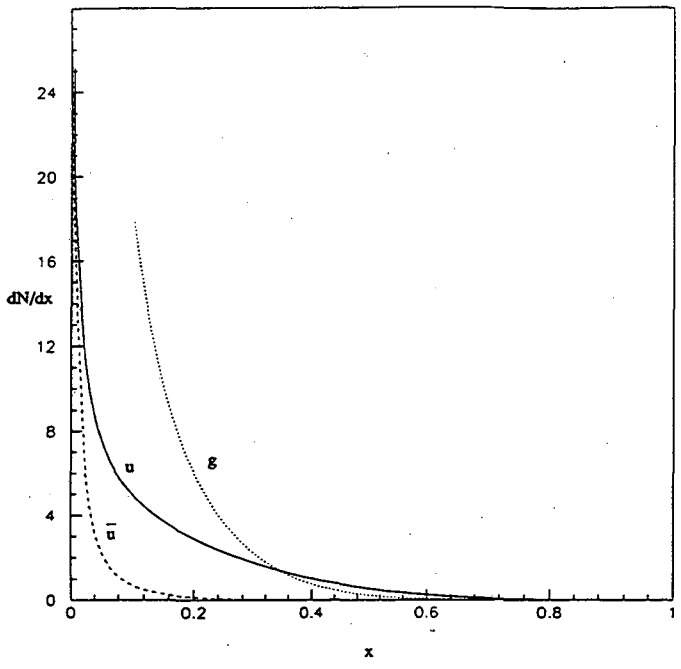

Figure 4B-9. As a function of x_{BJ}, the structure functions for u quarks, $\bar{u}$ anti-quarks, and gluons (G(x)) in the proton. Further details may be found in Reference 42.

gluon distribution in polarized pp interactions (see Section 2.B). The gluon polarization, $\Delta G(x)$, can be found most easily when the quark from the dominant Compton process, $qg \rightarrow \gamma q$, has $x_{BJ} > 0.2$.

The kinematic region of interest for pp and pA collisions is shown in Fig. 4B-10, where $x_T = 2\ p_t/\sqrt{s} = 0.1$ corresponds to $p_t = 10$ GeV/c at $\sqrt{s_{nn}} = 200$ GeV. These data were derived assuming that the direct-γ could be detected over the range $-2 \leq \eta \leq +2$ with the barrel and two endcap EMCs. However, the jet acceptance is smaller since all particles within a radius $R_j = (\sqrt{(\Delta\eta)^2 + (\Delta\phi)^2} \leq 0.7)$ of the jet center must also be detected. Figure 4B-10 shows that an endcap calorimeter will be essential to measure $x \gtrsim 0.2$. Studies of rates, cross sections, and acceptances for inclusive direct-γ + jet production with at least one of the partons having x larger than 0.2 in pp collisions indicate that the RHIC energy range is ideal for performing these measurements.[43] As noted above, similar kinematics apply for pA collisions, and thus the endcap calorimeter is also needed to study $G^A(x)$.

Another way of illustrating the effects of the EMC acceptance is shown in Figs. 4B-11 and 4B-12. The first gives the coverage in $x_a = \min(x_1, x_2)$ of the gluon when x_{BJ} of the quark is $x_b = \max(x_1, x_2) \geq 0.2$ for the case of the barrel calorimeter alone. Figure 4B-12 shows the same quantity for the combined barrel and endcap EMC acceptance. It can be seen that both the barrel and the endcap will be required to measure the gluon structure function over a wide range of x.

[43] M.E. Beddo, H. Spinka, and D.G. Underwood, "Estimates of Rates and Errors for Measurements of Direct-γ and Direct-γ + Jet Production by Polarized Protons at RHIC," ANL Report No. ANL-HEP-TR-92-59; STAR Note No. 77.

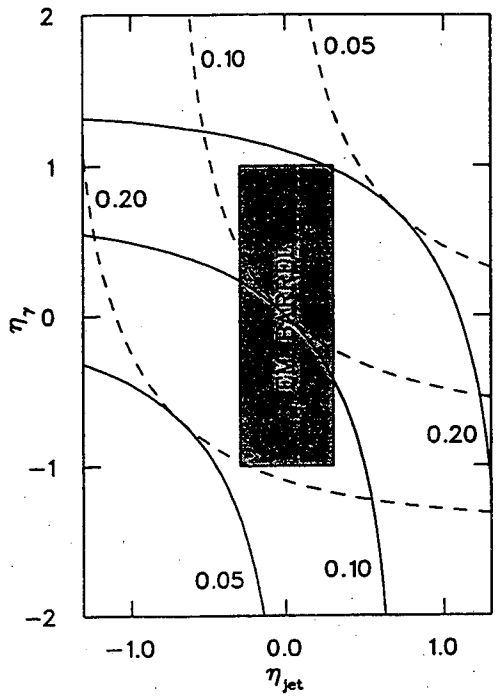

Figure 4B-10. The momentum fractions x_1 (solid) and x_2 (dashed) of the quark and gluon plotted as a function of the direct-γ and jet pseudorapidities. Data shown are for $p_t \cong 10$ GeV/c and $\sqrt{s} = 200$ GeV, and assume the full acceptance of the barrel and endcap calorimeters. The dark region in the center of the plot indicates the acceptance of the EMC barrel alone.

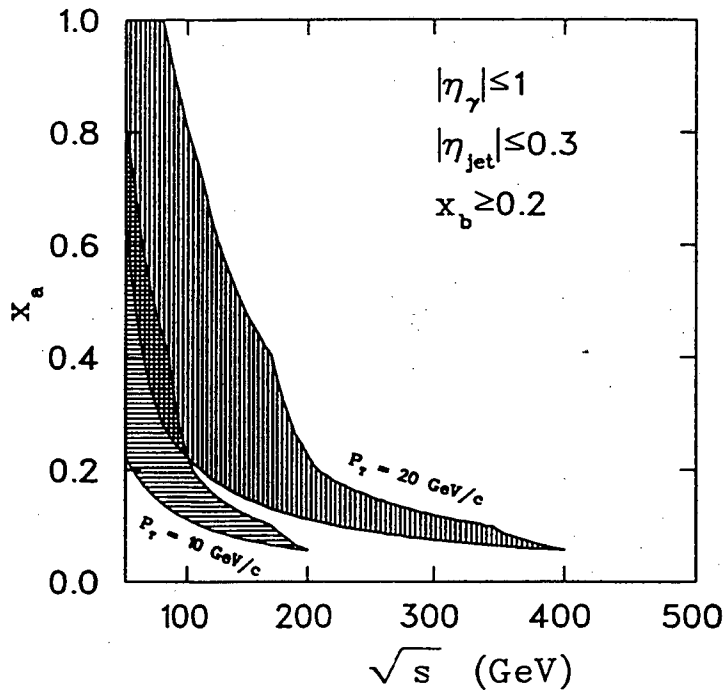

Figure 4B-11. As a function of $\sqrt{s}$, the range of the gluon (x_a) in which the STAR detector has acceptance, assuming the momentum fraction of the quark is $x_{BJ} \gtrsim 0.2$. The data shown are for $p_t \cong 10$ GeV/c and $p_t \cong 20$ GeV/c and assume the acceptance of the barrel calorimeter only. The acceptance in x_a determines the kinematic region in which the Compton subprocess, $q + g \rightarrow \gamma + q$, can be studied.

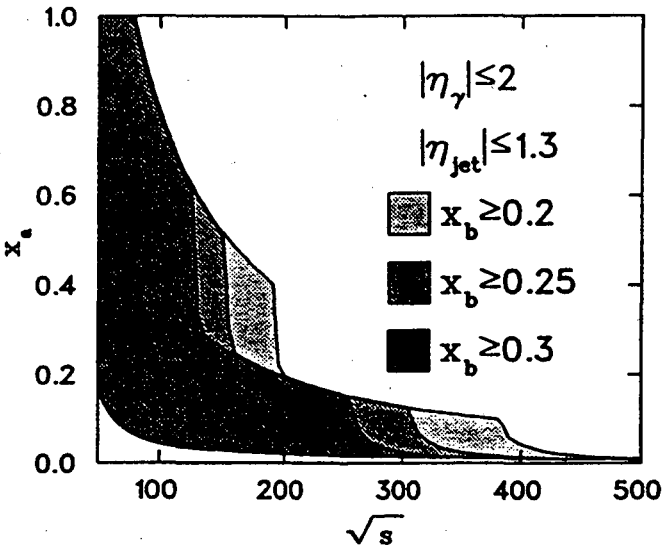

Figure 4B-12. As a function of $\sqrt{s}$, the range of x_{BJ} of the gluon (x_a) in which the STAR detector has acceptance assuming the momentum fraction of the quark is $x_{BJ} \gtrsim 0.2$. The data shown are for $p_t \cong 10$ GeV/c, and $p_t \cong 20$ GeV/c and assume the acceptance of the barrel and calorimeter only. The acceptance in x_a determines the kinematic region in which the Compton subprocess, $q + g \rightarrow \gamma + q$, can be studied.

4.B.4. Rejection of Fake Direct Photon Signatures

The major background for the measurement of direct-γ events is the electromagnetic decay of π° and η° mesons. If the two photons from such a decay cannot be resolved, if one of the photons is missed because it is outside the detector acceptance, or if one of the photons has a low energy and cannot be distinguished from noise, then the event will appear to be a direct-γ. As shown below, the electromagnetic calorimeter towers alone are too large to distinguish the two showers for π° decays in the p_t region of interest. Instead, a finely segmented detector must be placed near the location at which the number of electrons in the shower is a maximum to distinguish two photon showers in the energy range of interest for hard-parton scattering.

The minimum laboratory angle between photon pairs produced through the electromagnetic decay of mesons is given by

$$\Delta\theta_{min} = 2\frac{m}{E} \quad , \tag{4.B-10}$$

where m is the mass and E is the laboratory energy of the decaying meson. For meson momenta p_m in the range 10 GeV/c $\leq p_m \leq$ 20 GeV/c, $\Delta\theta_{min}$ varies from about 14 –27 mr for π° decay. Expressed in terms of transverse momentum, 10 GeV/c $\leq p_t \leq$ 20 GeV/c and $|\eta| \leq 1$ corresponds to 10 GeV/c $\leq p_m \leq$ 31 GeV/c and to $9 \leq \Delta\theta_{min} \leq 27$ mr. Figure 4B-13 shows the distribution, as a function of the radial distance from the centroid of the shower, of energy deposited in polystyrene scintillator by 10 GeV photons. These results were calculated using the EGS electromagnetic shower Monte Carlo. With fine segmentation and/or large distances, the two photons from a π° decay can be distinguished from a single, direct-γ event. However, for a fixed acceptance, the cost generally increases dramatically if the segmentation or distance to the photon detector is increased. Furthermore, highly asymmetric decays of mesons may cause the loss of one photon from the detector acceptance in any event due to the inability to

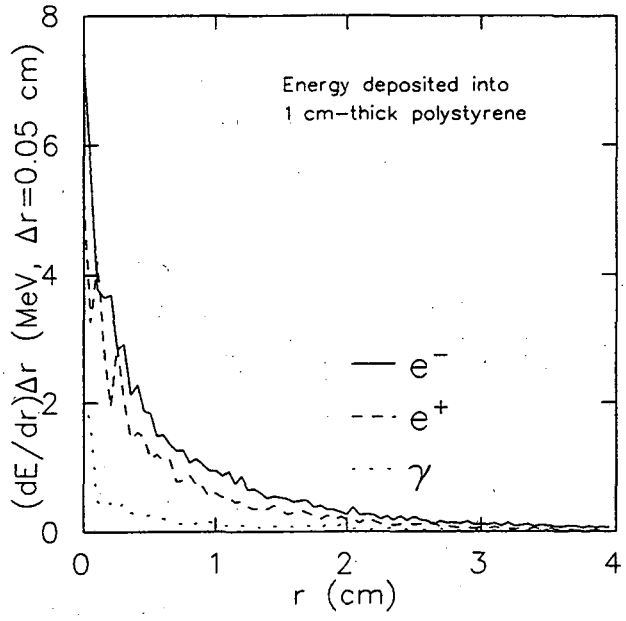

Figure 4B-13. The distribution, as a function of the radial distance from the centroid of the shower, of the energy deposited in polystrene scintillator by 10 GeV photons.

identify the low-energy photon because of detector noise. Thus, realistic detectors cannot always distinguish true direct-γ events from electromagnetic decays of mesons. A convenient figure of merit in this regard is the ratio R_{fake} of the number of photons from unresolved π° and η° decays to the number of true direct-γ events. The background and, therefore, the measurement uncertainties grow with R_{fake}.

The STAR electromagnetic calorimeter design has towers with cross-sectional area 12×24 cm^2 near $\eta = 0$. The inner radius is expected to be about 2.22 m, which gives a lower limit to the angular resolution for separating two showers of 53 mr. This is not sufficient for resolving π° decays with $10 \text{ GeV/c} \leq p_t \leq 20 \text{ GeV/c}$. Algorithms, such as analysis of the moments of the deposited energy, will probably not improve the resolution by more than a factor of two. Since the tower size and the corresponding angular resolution are large compared to values required, the electromagnetic calorimeter towers alone will not be useful for direct-γ measurements. (R_{fake} will be too large to give meaningful results.)

The spatial resolution for separating electromagnetic showers in the STAR calorimeter could be significantly improved by adding a charged particle detector made of narrow strips. The optimum depth for this finely segmented detector is near the shower maximum, where the number of electrons and positrons is a maximum and the statistical determination of the shower center is the best. The width of the strips should be comparable to the transverse radius of the showers at this depth, or ~5 mm. However, it may be necessary to use wider strips due to considerations of cost. Ideally, two sets of perpendicular strips would be used.

Simulations to investigate the feasibility of measuring direct photons using a shower maximum detector of this design were performed using 0.5-, 1.0-, and 1.5-cm-wide strips having lengths corresponding to $\Delta\eta = 0.1$ at a radius R = 260 cm (slightly larger than the presently expected radius for the shower maximum detector of 230 cm). In the simulations, it was assumed that the photons could be resolved if $R\,\Delta\phi \gtrsim 1$, 2, and 3 cm, respectively. The results of this conservative calculation for the ratio R_{fake} are displayed in Fig. 4B-14. What is noted from

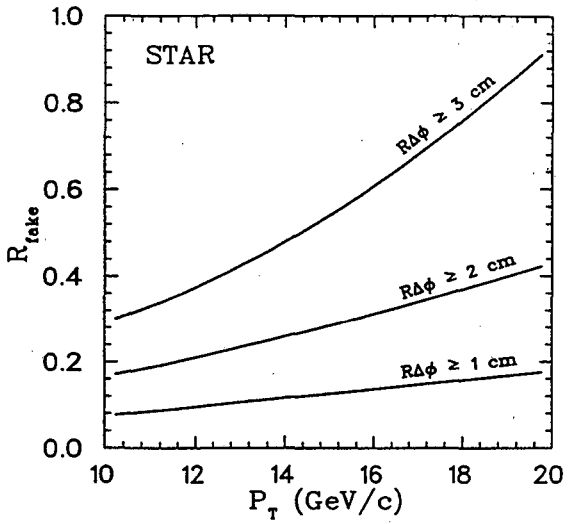

Figure 4B-14. As a function of p_t, the ratio, R_{fake}, of the number of photons from unresolved π° and η° decays to the number of direct photons for shower maximum detector strips of 0.5, 1.0, and 1.5 cm in width. These widths correspond to values of $R\Delta\phi$ of 1, 2, and 3 cm respectively.

these data, for example, is that R_{fake} increases from ~18% at p_t ~ 10 GeV/c to ~40% at p_t ~ 20 GeV/c. It is noted that $R\,\Delta\theta_{min}$ = 3.5 cm for E = 20 GeV, suggesting that a strip width near 1.0 cm may be near optimum when a trade-off between cost and spatial resolution is considered. This is borne out to some extent by estimates of the error on spin asymmetries for $pp \rightarrow \gamma+X$ reactions using the three strip widths above. Compared to the error for 1-cm strips, the error increased by a factor of 1.2 for 1.5-cm strips and decreased by a factor of 1.3 for 0.5-cm strips. The present conceptual design for the shower maximum detectors for the barrel and endcap calorimeters is discussed in Sections 4.C.6 and 4.D.6, respectively.

4.C. The Barrel Electromagnetic Calorimeter

4.C.1. Choice of Technology

A priori, there are many available technologies for an electromagnetic calorimeter. Crystals such as NaI, CsI, and BGO have excellent resolution for individual low energy photons. Lead glass has better energy resolution than most sampling calorimeters. The primary problem with these detectors is cost, particularly for the depth, area, and geometry needed in STAR. The area that must be covered outside the TPC is over 100 square meters for $|\eta| \lesssim 2$. To accomplish all physics goals, the depth must be adequate to contain 40 GeV showers within a couple of percent, including leakage fluctuations. This implies a total depth of approximately 20 X_o. The geometrical constraint imposed by the solenoidal STAR geometry implies the EMC elements must be wedge-shaped at a minimum, if not truncated pyramid shapes as used in VENUS and UA2.

Gas calorimetry with wire chamber sampling between layers of lead has been used in some applications, but in general has demonstrated problems with non-uniform gain and extremely large signals from neutrons. Other sampling detectors have used liquid argon or some other liquid to detect the ionization caused between plates of converter or absorber by the passage of charged particles. Generally, the cryogenic vessels used to contain the liquid take up an unacceptable amount of space. This leads to a lack of hermiticity and cracks within the sensitive volume of the detector. Liquid argon calorimeters also typically require more time to

integrate signal than, for example, scintillator tiles, although recent SSC development efforts have resulted in at least one liquid krypton prototype calorimeter with a comparable time constant[44] for high energy showers. Although detailed studies of a liquid argon calorimeter were not performed, both the cost and GeV equivalent noise level are expected to be higher than for a lead-scintillator sampling calorimeter. The noise level can be a particularly serious problem in the present application, since for heavy ion interactions, the average p_t of the charged particles and photons that reach the calorimeter is ~400 MeV.

A sampling calorimeter using lead and plastic scintillators has been chosen for the detection of electromagnetic energy in STAR. A significant advantage of this technology is that the calorimeter can be constructed from a number of relatively small modules. If necessary, this will permit part of the calorimeter to be constructed and installed after the STAR baseline components (TPC, magnet, etc.) are complete. This would be significantly more difficult, for example, with liquid argon technology. Calorimeters of this design have been successful in a number of colliding beam and fixed target experiments, and as a consequence, the technology is well known. Recent examples of detectors incorporating this technology include the endcap upgrade calorimeter for CDF and the barrel calorimeter for SDC. In particular, the use of a lead-scintillator sampling calorimeter is a cost effective way to cover the necessary square area, employing a mechanical design flexible enough to accommodate the constraints imposed by the closed STAR geometry. The resolution is adequate for individual high energy photons and electrons above a few GeV. For heavy ion physics where the energy of a very large number of low energy photons is to be summed, the resolution is also adequate (see Section 4.B.1). With typical photostatistics (two photoelectrons/sampling layer/minimum ionizing particle) and a typical sampling frequency (once every 0.9 X_0) , the intrinsic resolution expected from sampling calorimeters is ~14%/$\sqrt{E}$. The resolution typically achieved is 16%/$\sqrt{E}$, plus a 1–1.5% constant term added in quadrature. The constant, or so-called "stochastic" term comes from tower-to-tower variations in the calibration, and both transverse and longitudinal non-uniformities in light collection from the pieces of scintillator.

The light generated by charged particles passing through the scintillator must be brought to photon detectors such as photomultipliers. In the present STAR design, the electromagnetic calorimeter will be located inside the solenoidal magnet. The photomultipliers must be located outside the magnet to avoid high magnetic fields, and to minimize the radius and cost of the magnet. The use of waveshifter plates such as those used in the ZEUS calorimeter would not be practical, since they would take up an unacceptable amount of space in traversing the magnet coil pancakes. Consequently, plastic optical fibers that take up less space and require less labor to prepare have been selected for the STAR design. The use of fibers also allows for the possibility of upgrading the longitudinal and transverse segmentation of the calorimeter towers if more photomultipliers and readout electronics become available. The flexibility to segment longitudinally may be particularly useful in discriminating between hadronic and electromagnetic showers.

Once the decision is made to use a sampling calorimeter with scintillator, the next concerns are how best to accomplish efficient light collection, what segmentation should be used, and how the mechanical structure should be designed. These choices are intricately related to each other and are discussed in detail in the sections that follow.

[44]O. Benary *et al.*, Nucl. Instr. and Methods **A232** (1993) 78.

4.C.2. Mechanical Structure

The present conceptual design for the barrel electromagnetic calorimeter includes 120 calorimeter modules, each subtending ~6° in $\Delta\phi$ and 1.05 in $\Delta\eta$. The calorimeter is a sampling calorimeter, and the mechanical construction of each module consists of 20 layers of 5-mm-thick lead. The lead is potentially clad on both sides with 0.5 mm of nonmagnetic stainless steel. Between each clad lead sheet, 6.6-mm-high aluminum spacers of I-beam cross section may be positioned to ensure that the scintillator tiles placed between the layers of lead are not subject to undue stress from either the weight of the lead or compressive forces. Plastic scintillator tiles with a nominal thickness of 4 ± 0.4 mm are placed between the layers of lead, forming pseudo-projective towers, as shown in Fig. 4C-1. There are 20 scintillator tiles in each sampling layer, corresponding to a tower size of $\Delta\eta \sim 0.05$. A 20-mm-thick aluminum front plate and 30-mm nonmagnetic stainless steel back plate run the full length of each module. Wavelength-shifting optical fibers run along the two edges of the scintillator tiles that are **not** captured by the I-beam spacers. Aluminized mylar or a highly reflective paper called TYVEK is wrapped around the scintillator in order to maintain contact between the fibers and the tiles. The waveshifting fibers are routed as shown in Fig. 4C-2 and are fused onto clear fibers shortly after leaving the scintillator tiles. All the fibers from a given tower are bundled together and routed to a photomultiplier located outside the return iron for the solenoidal magnet.

Finite element calculations of stresses in the lead in a stacked arrangement indicated that the modules could not be held together with compressive forces by relying upon the friction between the I-beam spacers and the lead. In this instance, the stresses in either clad or unclad lead would be high enough (~21 MPa) that it would deform (Fig. 4C-3), leading to a reduction in the compressive loads and failure of the module assembly. In order to avoid creep problems

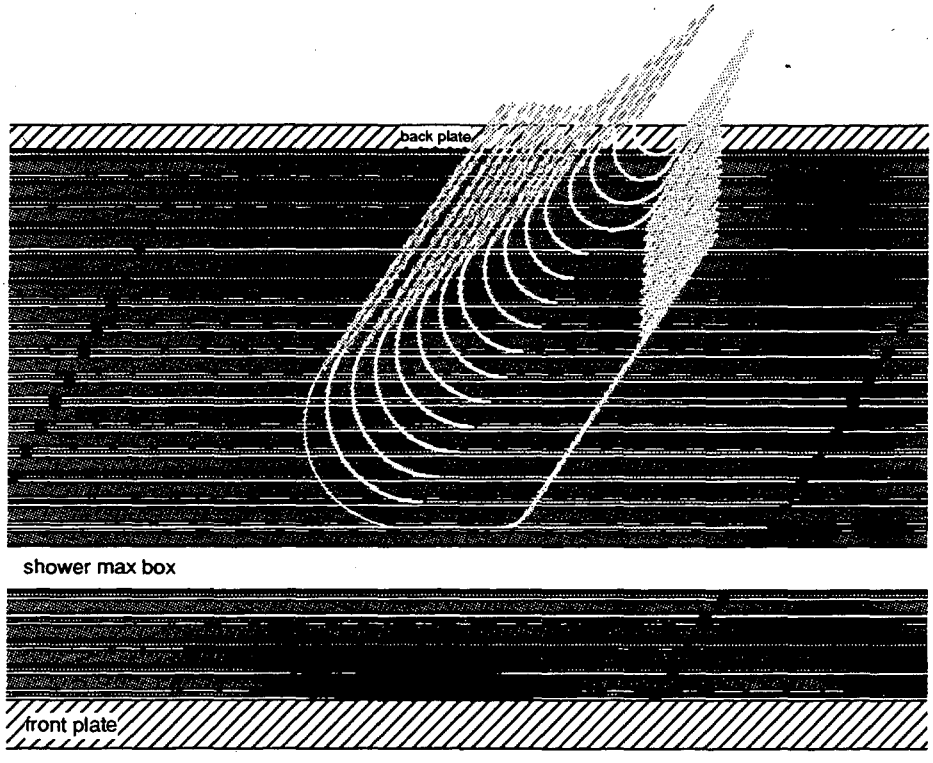

Figure 4C-1. A cross section showing the pseudo-projective towers of a section of a barrel EMC module. At a depth of ~5 X_o, a space of ~25 mm is allocated for a shower maximum detector.

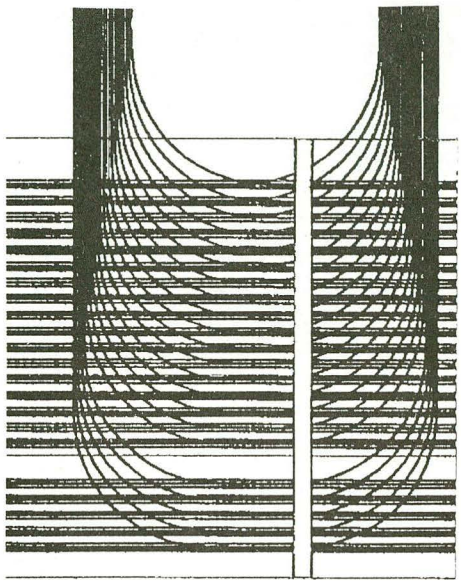

Figure 4C-2. A schematic diagram indicating the routing of the optical fibers used to conduct light from the EMC towers to the photomultipliers located on the exterior of the magnet return steel. The waveshifting fibers are fused onto clear fibers shortly after leaving the scintillator tiles. All the fibers from a given tower are bundled together for routing during assembly.

in the lead over the 10–20 year lifetime estimated for the calorimeter, the maximum stress in the lead would have to be ≲6.9 MPa, depending on the average temperature of the calorimeter and the particular choice of lead alloy. A similar mechanical design based on compression of the converter/absorber plates was acceptable for the ZEUS calorimeter due to the use of depleted uranium plates as absorber material. Depleted uranium was not considered for the STAR EMC for reasons of cost and safety.

A second design also consisted of lead plates and scintillator tiles in a stacked arrangement, held together by compressive loads. In this instance, however, the size of the compressive load was reduced by eliminating the I-beam spacers and stacking the lead and scintillator on top of one another. The effective surface area between sampling layers is greatly increased in this design, reducing the compression required for module stability to about 0.1 MPa. Experience with similar designs at CDF and UA2 has been favorable.

This option has not been eliminated. However, concern over the long-term response of the scintillator under pressure and the possibility that the success of this design at CDF and UA2 might be specific to a particular type or batch of scintillator has prompted the investigation of other designs as well.

A cast lead option similar to that currently planned for the SDC electromagnetic calorimeter was found to be too costly compared to an option with stacked lead sheets. The cost of labor for cutting, handling, and assembling the individual lead sheets in the stacked option was more than offset by the cost of machining the mold parts, performing the casting operation, and preparing molds for subsequent castings. Additional costs would result from machining and assembling the structural elements (bulkheads, tubes, front and back plates) for each module before casting the lead. A further concern is how many times the mold parts could be

Figure 4C-3. A finite element analysis of the stress in lead absorber plates clad with stainless steel at the location of the base of the I-beam spacers used to prevent compression of the scintillator in a stacked module arrangement. The calculations indicate the stresses in clad or unclad lead would be high enough that the lead would deform, leading to a reduction in the compessive loads and failure of the module assembly.

reused. Recent tests[45] have shown that thermal cycling of the aluminum plates used to maintain space for the scintillator tiles during casting of the lead results in warping of the plates beyond the acceptable tolerance for flatness. The warping occurs after a relatively small number of cycles (~10–15), suggesting the mold parts used for the cast lead design would need to be replaced after a limited number of castings. The machining of replacement parts would also lead to an increase in the total cost for this option.

The conceptual design adopted incorporates lead plates and scintillator tiles in a stacked arrangement. The mechanical structure utilizes a back plate of 30-mm thickness, and a front plate of 20-mm-thick aluminum. Type 304 stainless steel end plates 3-mm thick and a 6-mm-thick stainless steel central bulkhead at $\eta \sim 0.5$ provide additional support (see Fig. 4C-4). In this design, the lead absorber sheets are half the full module length, and are captured by fixtures at the ends and middle of the module. This eliminates the need for high compressive forces. If necessary for mid-span support, I-beam spacers will be attached to bands that are connected to the front and back plates. Both the spacers and the lead should experience negligible compressive loads.

At a depth of approximately 5 X_o, near the location of the maximum number of shower electrons for a photon of energy 1–3 GeV, a detector with fine spatial resolution will be placed to allow for the detection of direct photons. It will also provide for the rejection of background photons emanating from decaying π° mesons having $p_t \lesssim 20$ GeV/c. The radial space allotted for this device is 25 mm (Fig. 4C-5).

Each module will weigh ~1.4 tonnes, including a nonmagnetic stainless steel "strongback" attached to the back plate of 30-mm stainless steel. Trapezoidal shaped "keys" will be attached to 76-mm-thick aluminum rings located between the coils of the solenoidal magnet (Fig. 4C-6). The strongback will have a trapezoidal-shaped way machined into it, so that modules can be slid into place from the ends of the STAR detector. A fixture (Fig. 4C-7) will permit all of the modules except those located behind the TPC supports to be installed after the TPC is in place. This should allow for partial installation of modules in the event the full calorimeter is not ready at the start of RHIC operations. The fibers from the calorimeter towers will be pulled in bundles during installation through spaces between the magnet coils and the magnet return iron. Engineering tests with fiber bundles have shown that this procedure will work within the geometrical constraints of the STAR magnet.

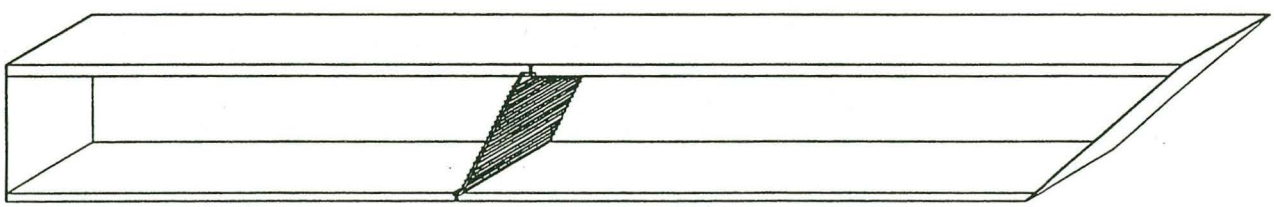

Figure 4C-4. The design chosen for the structural support of the barrel EMC modules. The mechanical structure utilizes back plates of 30-mm stainless steel and a 20-mm-thick aluminum front plate. Type 304 stainless steel end plates 3-mm thick and a 6-mm-thick stainless steel bulkhead at $\eta \sim 0.5$ provide additional support. The lead absorber sheets (not shown) are half the full module length and are captured by fixtures at the ends and middle of the module.

[45]E. Bielick, T. Fornek, A. Spinka, and D. Underwood, "Thermal Distortion Tests of Aluminum and Stainless Steel Plates," STAR Note No. 118; ANL Report No. ANL-HEP-TR-93-55.

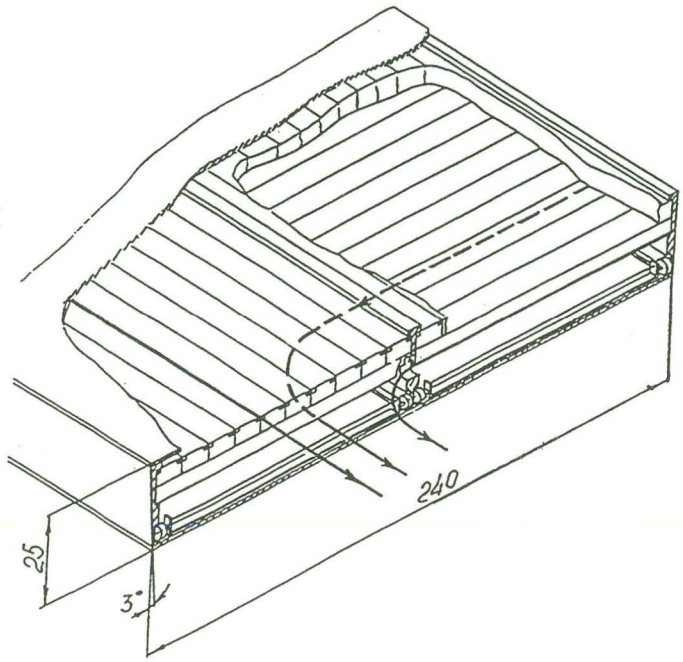

Figure 4C-5. A schematic drawing showing the radial space allocated for the shower maximum detector in a barrel EMC module.

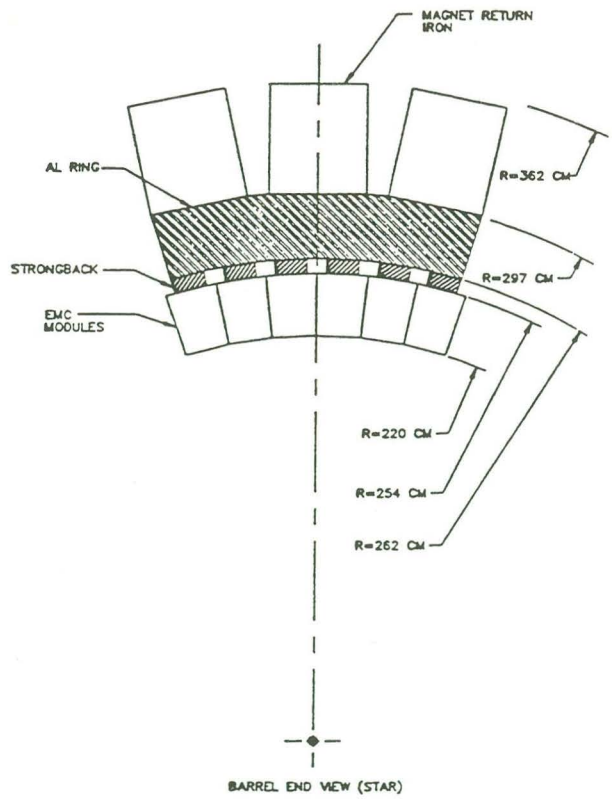

Figure 4C-6. An end view of several modules of the EMC barrel showing the location and arrangement of the aluminum ring and strongback supports.

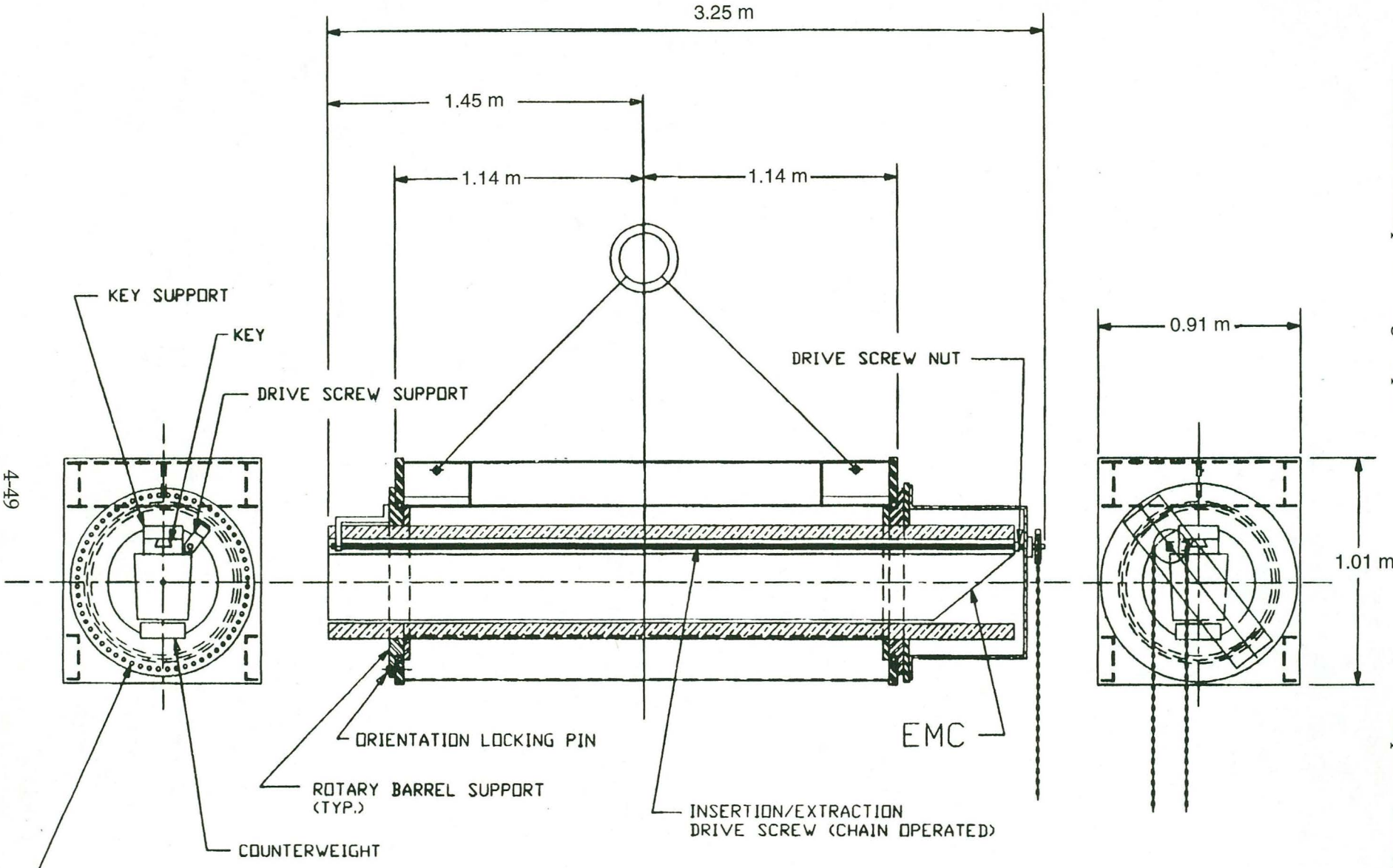

Figure 4C-7. The installation fixture used to insert modules of the EMC barrel.

Finite Element Calculations

Mechanically, the conceptual design for the barrel electromagnetic calorimeter modules relies upon a thick back plate supported by large aluminum rings that are connected to the STAR magnet flux return bars. Two end plates and a central bulkhead are connected to both the back plate and a front plate of 20-mm-thick aluminum. The gravitational load from the lead and scintillators is distributed primarily to these five structural elements. No compression of the lead sheets is used. In addition, there are "shelf supports" for the lead, which are presently envisioned to be I-beams welded to thin-gauge metal strips ~1.0-mm thick. These strips run from the front plate to the back plate near boundaries of the projective towers. Finally, side sheets are used to reinforce the assembly, protect the optical fibers, and provide stability against buckling when the modules are located near the 12 o'clock position in the STAR detector.

Finite element models were constructed to evaluate the stresses and deflections in the barrel modules (Fig. 4C-8). One pair of models investigated behavior at the 3 and 9 o'clock locations in the calorimeter. In the first, point gravitational loads were applied at the intersections of the front plate with the ends and central bulkhead. The weight of the lead sheets was split evenly between the central bulkhead and one end, giving loads of 170, 376, and 209 kg at $\eta = 0$, 0.5, and 1.0, respectively. The maximum stress was 44.13 MPa at the central bulkhead, and the maximum deflection was 1.60 mm at the $\eta = 1$ end of the module, away from the support ring. In a second model, the point loads were replaced by the equivalent total loads distributed uniformly on the ends and central bulkhead. In this case, the maximum stress and deflection were reduced to 31.03 MPa and 0.89 mm. Both models used aluminum back plates and neither incorporated side sheets, yet the deflections and calculated stresses were acceptable in both cases.

A third model of the barrel modules included two side sheets of 0.5-mm stainless steel. In this case, the loads were uniformly distributed as above, using a back plate of stainless steel. The maximum deflection in the side sheets was 0.76 mm. Although the side sheets are not required for strength and are not overstressed in the 3 and 9 o'clock positions, the calculated deflection of 0.8 mm may present difficulties with installation due to the tolerance between adjacent modules. As a cross check, an analytical calculation of the deflection of the side plate under its own weight was performed. The side plate was modeled as a beam with a span of 31.6 cm between the front and back plates. The computed deflection was 0.48 mm for a beam with fixed ends and 2.39 mm for a simply supported beam. These values bracket that computed with the finite element model. It is presently thought that this problem can be solved without seriously impacting the barrel calorimeter module design or the tolerances between adjacent modules.

The need for the side sheets is most important for the modules located near 12 o'clock. In this case, assuming point loads, the maximum stress for the module with front and back aluminum plates, stainless steel ends, and a central bulkhead is 234.43 MPa without the side sheets, and 58.61 MPa with the side sheets included. The maximum allowable stress in Type 304 stainless steel is ~124.11 MPa. In these models, the side sheets are continuously connected to the front plate, ends, and central bulkhead, but have slots near the back plate for the routing of fibers to the photomultipliers. Thus, the modules near 12 o'clock require the side sheets for structural integrity, whether the shelf supports are used, or the lead and scintillator are loosely stacked on the module front plate. The modules near 6 o'clock only require bracing with side sheets if the shelf supports are used.

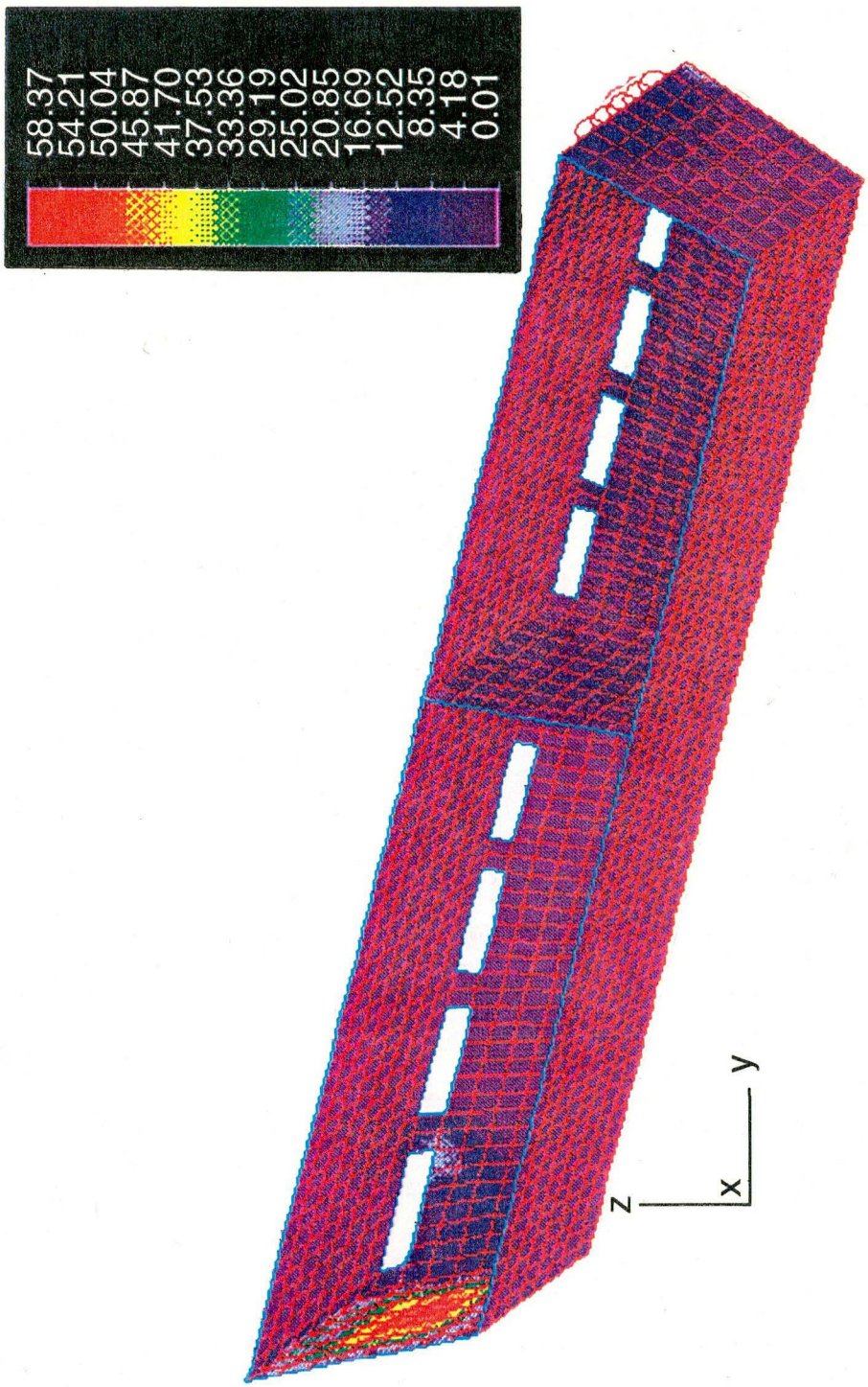

Figure 4C-8. A finite element analysis of the stresses in the structural support members for the barrel EMC modules. The assumed loading of the elements is discussed in the text.

More refined models of the barrel calorimeter modules are planned, in order to examine in detail the loading of the ends and central bulkhead due to the lead. A full-size engineering model of a module to verify these calculations is also being constructed. Scintillators and fibers will not be included in this model.

4.C.3. Optical System

The purpose of the optical system is to collect light as uniformly as possible from the scintillator and to transmit as much as possible to an optical transducer such as a photomultiplier. Given that the optical readout device is typically located exterior to the active region of the calorimeter, it is generally necessary to transmit the light collected through a 90° bend. The optical system is additionally constrained in that it should not create unacceptably large insensitive areas within the acceptance of the calorimeter.

The use of waveshifting plates or fibers is a classic way in which to make a right angle transition in a minimal amount of space. The absorption of blue scintillator light and subsequent re-emission of green light by the waveshifting material has two important aspects. The first is that light incident at any angle is re-emitted into 4π once it has been absorbed. This tends to collect light that would otherwise be lost and to average out variations in the light collection efficiency due to geometry, improving the overall uniformity of collection. The second important benefit is that light shifted from blue to green subsequently has a much longer attenuation length within the waveshifter material, and it is therefore collected with greater efficiency. Waveshifting plates generally cost more than fibers due to the labor-intensive process of cutting and bending adiabatic light pipes that will fit within given mechanical constraints. Waveshifting fibers have a longer attenuation length, and above a minimum bend radius, may be routed as necessary to couple with the optical readout device. In most applications, both plates and fibers must be still be spliced to clear light guides to improve the effective attenuation length further.

A considerable development effort has gone into all aspects of optical systems of this type. The conceptual design for the optical system for the STAR EMC makes optimal use of advances in this area.

Scintillator tiles in the barrel EMC will be coupled to photomultipliers using optical fibers (Fig. 4C-9). A short length of wavelength shifting (WLS) fiber (~50 cm) will be coupled directly to the two edges of the scintillator tiles not captured by the mechanical constraints used to form the scintillators into pseudo-projective towers. These fibers will each be spliced onto ~3 meters of clear optical fiber that will be routed between the return steel bars for the STAR solenoid in order to complete the coupling of the scintillators to the photomultiplier tubes. The transmission of light across the splice between fibers joined in this manner is typically on the order of 95%. It is presently envisioned that the scintillator tiles will be constructed of Kuraray SCSN38 polystyrene. This material emits at a wavelength well matched to both Kuraray Y7 or Bicron K27 waveshifting fibers. Bicron PVT scintillator is known to produce more light for a given thickness. However, it is generally more expensive, and its mechanical properties and optical degradation when placed under pressure for extended periods are not as well known.

A number of tests have been performed to determine the optimum configuration for coupling light from the scintillator to the WLS fibers. One option considered was that of machining a groove in either the edge or face of the scintillator tile into which a WLS fiber would be inserted and possibly glued. This technique has been used successfully, for example,

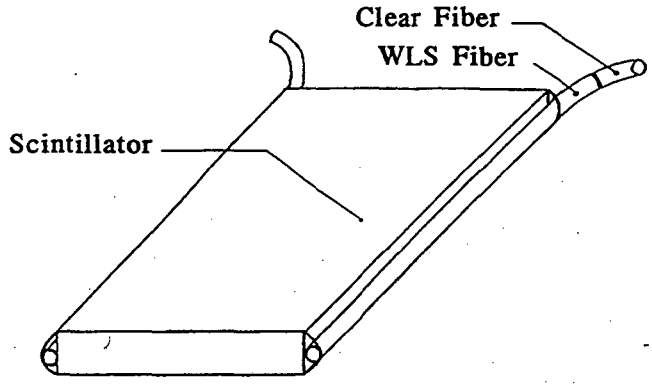

Figure 4C-9. A schematic drawing showing the coupling of the scintillator tiles of the barrel EMC to photomultipliers using wavelength shifting and clear optical fibers.

in the CDF endcap upgrade calorimeter[46] and in prototype testing for SDC.[47] The participant calorimeter in AGS experiment E814 successfully used the edge groove technique as well.[48] In the event the fibers are glued into place, care must be exercised in the choice of glue, to ensure that it does not age or darken prematurely when exposed to radiation and that it will not attack the cladding of the fiber. The primary drawback to this solution is the expense associated with the labor-intensive machining of the groove, which can increase the per tile fabrication cost by more than a factor of two.

A more economical solution with adequate collection efficiency involves constraining the WLS fibers to lie along the edge of the scintillator tile by wrapping them tightly, for example, in aluminized mylar. At the location of the fibers, the mylar roughly forms a parabolic mirror, which helps redirect light into the fiber where it can be captured. Using this technique, the light output from a 4-mm-thick BC408 tile coupled to 50 cm of WLS fiber spliced onto 3 meters of clear fiber was found to be ~2 photoelectrons per minimum ionizing particle (mip). (A similar test with Kuraray SCSN38 scintillator yielded ~1.3 photoelectrons per minimum ionizing particle.) This result, obtained using a Hamamatsu R580 photomultiplier, indicates the light collection using this technique is adequate to meet the design goal for resolution insofar as photostatistics are concerned.

Other factors influencing light collection efficiency include the diameter of the WLS fiber used, the preparation of the edges through which light must pass before entering the WLS fibers, and the reflective wrapping placed around the scintillator tiles.

To test the sensitivity of the light-collection efficiency to the fiber diameter, WLS fibers of 1, 1.5, and 2 mm in diameter were placed in contact with a 4-mm-thick scintillator tile in the manner discussed above. The results indicated that the increase in the light output per mip was much less than the corresponding increase in diameter (~20% for the 2-mm fiber) and that the benefit of increasing the fiber diameter was marginal. Alternatively, 1-mm fiber is less expensive, and more importantly, more flexible than fibers of larger diameter. The latter consideration is important, since it is presently envisioned that bundles of fibers from a number of towers must be simultaneously "fished" through pathways in the return steel as a calorimeter module is being slid into position. Having fibers with greater flexibility makes this process

[46]P. deBarbaro *et al.*, "R&D Results on Scintillating Tile/Fiber Calorimetry for the CDF and SDC Detectors," Rochester Report No. UR1229; NIM **A315** (1992) 317.
[47]SDC Technical Design Report, SDC-92-201/SSCL-SR-1215, pgs. 6-18 to 6-25.
[48]J. Simon-Gillo *et al.*, Nucl. Instr. and Methods **A309** (1991) 427.

easier. The use of 1-mm fibers also minimizes the space required for fiber routing between both adjacent wedge-shaped modules, and the calorimeter and the magnet coil.

The preparation of the edges of the scintillator tiles to which the WLS fibers couple also has a large influence on the light collection efficiency. Depending on the means of preparation, the labor involved in this process may also represent a substantial fraction of the cost of fabrication. In general, it has been known for some time that plastic may be machined to a near-optical finish in a minimal number of passes, provided the cutting tool remains sharp, the pitch between successive cuts is chosen appropriately, and there is little chatter in the contact between the cutting tool and the stock being machined. Recent attempts to reduce the labor associated with more traditional cut and polish techniques have focused upon this type of surface preparation using a milling machine equipped with a diamond cutting tool. To test this possibility for the STAR EMC, a diamond mill was used to machine the edges of the scintillator tiles to be used in a small four-tower prototype EMC. For selected tiles, the edges were also polished. Figure 4C-10 shows a comparison of the light output from both polished tiles and tiles machined with the diamond mill. What is noted from these data is that for both tiles, the

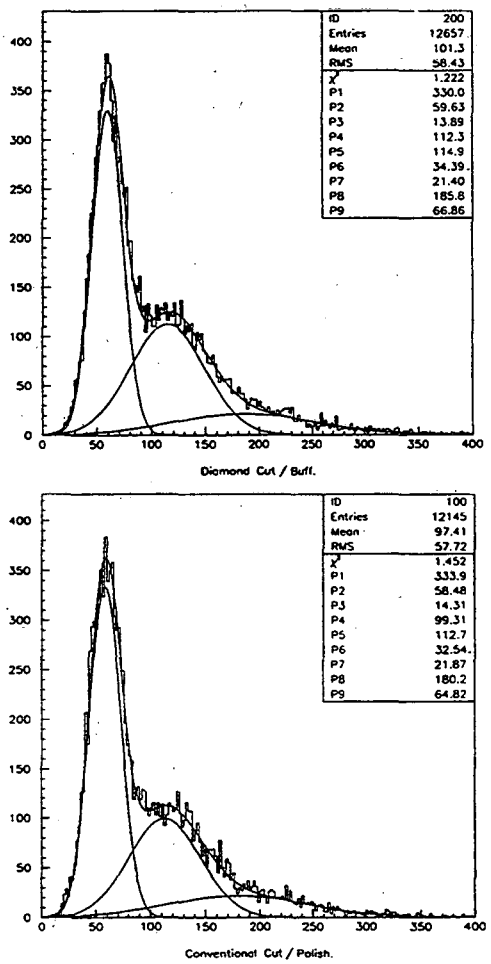

Figure 4C-10. A comparison of the light output of a scintillator tile prepared with a diamond mill (top) to the corresponding output for a tile prepared by traditional cut and polish technique (bottom). Although the average number of photoelectrons per minimum ionizing particle (~1.3) is less than the design goal (~2–3), the light output is approximately the same for both methods of tile preparation. The tiles were read out by optical fiber. The curves shown represent fits to the peaks for one, two, and three photoelectrons.

total light output is less than that required for the desired photostatistics (2–3 photoelectrons/mip) indicating that further improvement in the light collection efficiency is necessary. However, the response of both tiles is the same, indicating that preparation by machining with a diamond cutter provides a surface finish equivalent to that obtained by polishing. Accordingly, it is presently envisioned that the preparation of the edges of the scintillator tiles will be accomplished using a diamond mill. The resulting surface finish will provide total internal reflection at the scintillator air boundary in addition to the specular reflection provided by the parabolic-shaped aluminized mylar stretched around the tile-fiber interface.

The wrapping of the scintillator can also influence the light collection efficiency by as much as a factor of two. It has been found that either TYVEK or aluminized mylar works best on the large surface of the scintillators. TYVEK is a form of paper that is made of polyethylene fibers. It does not optically wet the surface of the scintillator even when under pressure. Consequently, it is a better choice for the primary wrapping of the large surface of the scintillator. The scintillator tiles will additionally be wrapped with aluminized mylar outside of the TYVEK, since a single layer of TYVEK is not optically opaque, and because mylar is still needed at the edges.

Finally, it is noted that the 7-meter attenuation length characterizing clear fiber is the key factor in routing the optical fibers from the scintillator tiles between the magnet coil pancakes and through the return steel as opposed to running them along the half length of the EMC barrel to an exit near the magnet pole tips (Fig. 4C-11). With this routing of fibers, the standard fiber length will be ~3 meters, and the average number of photoelectrons per mip will be

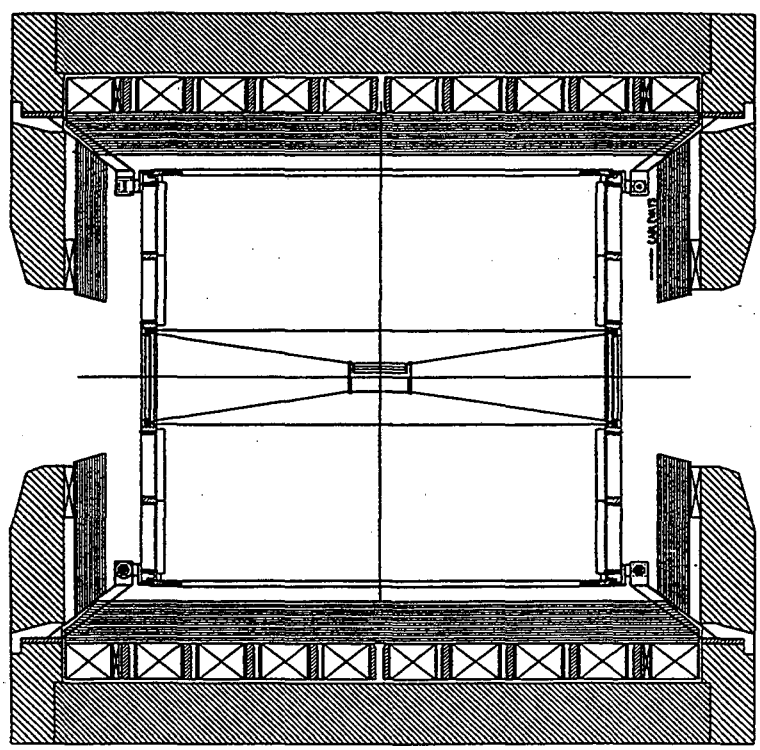

Figure 4C-11. A cross section of the STAR detector showing the spaces between the coil pancakes of the magnet through which optical fibers will be routed to photomultipliers mounted on the exterior of the return steel. The fibers could not be run along the half length of the magnet to an exit at between the poletip and the iron end ring, since this would require use of fibers ~7 m in length resulting in a reduction in light output of a factor of 2.

approximately two per tile. A 7-meter fiber would result in a loss in light collection of a factor of two, which is unacceptable.

4.C.4. Electronics

High Voltage Generation

In order to reduce power consumption, reduce the number of high voltage cables, and improve the linearity of the photomultiplier response, the tube bases for the barrel and endcap photomultipliers will be designed to generate their own high voltage. The circuitry required for this application will be self-contained and will include the necessary components to generate, regulate, and monitor the high voltage for the photomultipliers used in the STAR EMC. It will further be interfaced to the "slow control" system for the STAR detector and will therefore allow one to set and monitor the high voltage settings remotely.

Figure 4C-12 is a block diagram indicating the function of the EMC high voltage (HV) system and its interface to the slow control system using VME. The slow control computer and the HV system will communicate via Ethernet. Ethernet was chosen for this application as it is a readily available, well-established technology that allows for future expansion with a minimum of change to existing hardware. Furthermore, it reduces the network cabling and R&D effort associated with the development of a new bus system. As noted in Fig. 4C-12, the high voltage system is designed to produce and control the HV for the barrel and endcap photomultipliers, the shower maximum detectors, and any future additions to the electromagnetic calorimeter. The Ethernet interface for each of these systems will branch off from the main Ethernet segment using a first layer multiplexer. A second layer of multiplexing will be added if necessary.

Presently, the Ethernet multiplexing has been limited to two layers in order to allow compatibility with TCP/IP protocol. The VME-Ethernet interface, as well as the two Ethernet multiplexers for each subsystem, will reside in a crate located outside of the experimental area. Intelligent local controller (ILC) cards will be located on the detector, possibly on the exterior of the magnet return steel. Each ILC will contain a programmable microcontroller, and 16–32 channels of multiplexed digital-to-analog (D/A) and analog-to-digital (A/D) converters. The microcontrollers will perform the task of decoding (encoding) the address, data, and instructions received (to be sent) via Ethernet, and will apply them to a particular PMT base. While it is possible to incorporate the D/A and A/D converters within the PMT base, removing this capability to the ILC cards reduces the number of D/A and A/D converters required and therefore the cost of the system. It also reduces the per-base power consumption, allowing for operation at lower temperature with reduced electronic noise. The ILC cards will contain some local nonvolatile memory to store preloaded values of the high voltage for each PMT. The system will therefore be capable of recovering from a sudden power loss. There will also be a few kilobytes of memory available per channel so that a short history (several hours) of the high voltage of each PMT may be stored. This will allow the slow controls system to constantly monitor the PMT voltages and initiate an alarm if long-term drifts or deviations occur.

The number of nodes on each segment has been limited to less than 32 (ideally less than 29) to reduce the loading and therefore the error rate on the Ethernet. It is noted that, in this design, the use of two Ethernet multiplexers (fanouts) and 32 ILCs makes it possible to address up to 1024 PMTs per segment. The total number of PMTs that can be addressed with the two multiplexers is 8192 (assuming no ILC on the first layer segment). This will be accomplished using eight RG58 cables running the length of the detector, each cable attached to up to 32 ILCs in a daisy-chain configuration.

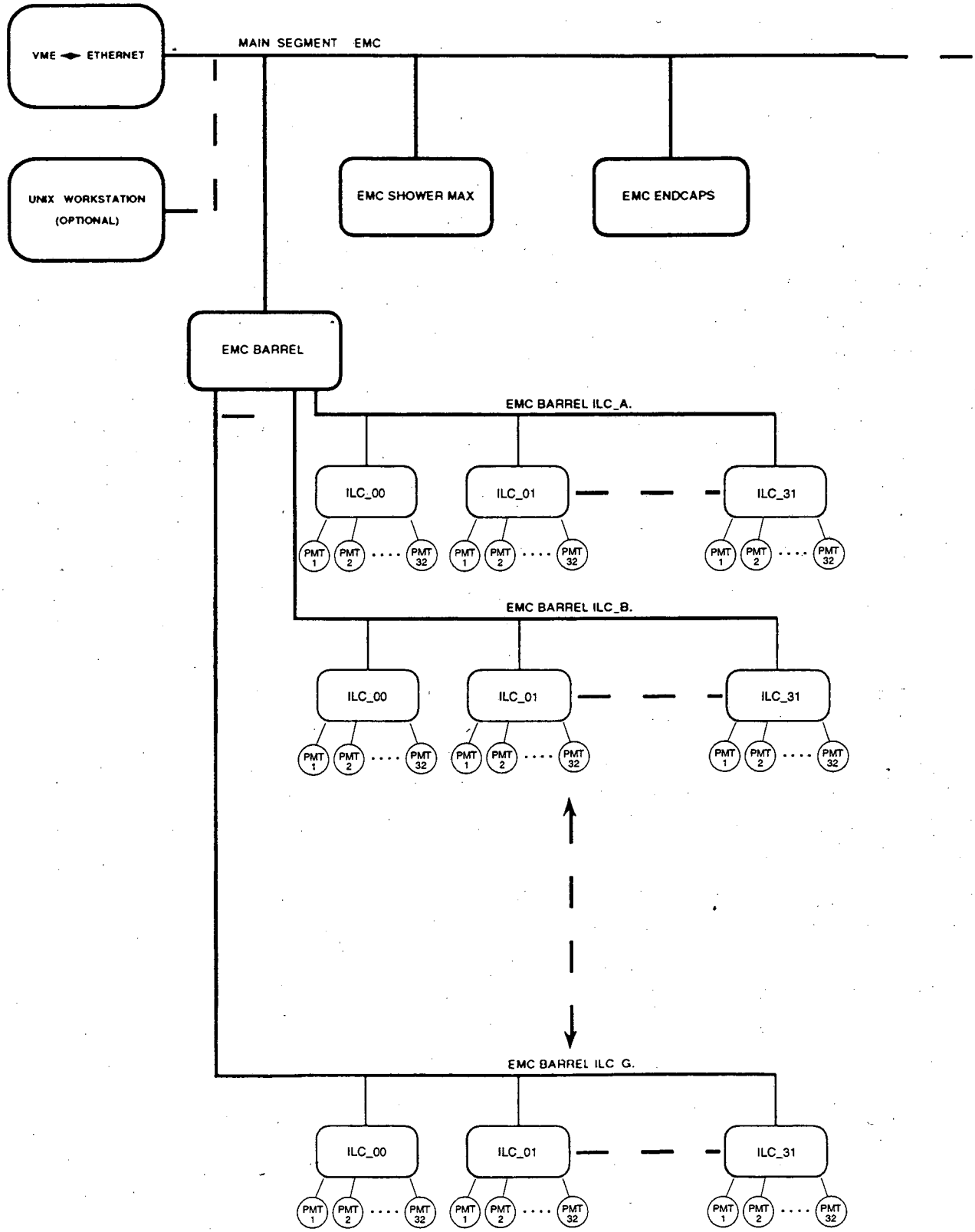

Figure 4C-12. A block diagram indicating the function of the EMC high voltage (HV) system and its interface to the slow control system using VME.

The High Voltage PMT Base

Three different designs are being considered for generating the high voltage for the EMC photomultipliers. Since the photomultiplier tubes for the calorimeter will be located outside the region of high magnetic field, the use of magnetic components (e.g., transformers, inductors) is possible.

The first two designs use step-up transformers to generate an intermediate HV, which feeds a Cockroft-Walton (CW) chain. A schematic diagram of a pulse-width modulation (PWM) HV system is shown in Fig. 4C-13. In this design, a fixed-frequency, square-wave oscillator feeds the primary of a step-up transformer. In tests performed to date, the frequency used was 50 kHz. The output of the transformer "pumps" the CW chain until the desired voltage is achieved. This high voltage is "sensed" using a 1000:1 divider. The divider voltage is then fed back into the PWM system, which varies the width of the square-wave pulses, thereby regulating the effective current in the primary and ultimately the voltage of the system. The advantage of this design is that all the necessary components (e.g., error amplifiers, current-limiting system, soft-start system oscillator, drivers) required to implement the PWM system exist within commercially available integrated circuits.

Tests on the PWM system using the bipolar integrated circuit (SG3526) resulted in a power dissipation of 360–400 mW, higher than that expected. Additional tests using the BiCMOS version of this chip (e.g., Teledyne TC25C25) are expected to result in a power dissipation of less than 50 mW.

The disadvantage of this design is that a relatively high level of rf noise is generated when the square waves used for pulse-width modulation are switched on and off. This noise is typically of the order of a few tens of millivolts. It may easily couple to the PMT signal, thereby reducing the signal-to-noise ratio and compromising the 16 bits of dynamic range required for the EMC tower ADCs.

A second design (Fig. 4C-14) addresses this problem by utilizing a sine-wave system. This design is less efficient than the saturated switched-mode operation of the PWM system, but is also less noisy. The basic design philosophy is the same. A sine-wave oscillator feeds the primary of the transformer, which in turn supplies current to the CW chain. However, in this design, a sine-wave oscillator with a fixed frequency of ~60 kHz is used instead of square waves with a variable duty factor. The oscillator consists of a second-order low-pass active filter, which oscillates because of a positive feedback. The amount of feedback is controlled by the difference between a reference voltage supplied by the external D/A converter and the sensed voltage from the output of the system. This feedback loop varies the amplitude of the sine waves in the primary transformer to correct the output of the system in order to minimize the difference between the set point and the high voltage output. Due to the number of components used and the 100% duty cycle of the oscillator, this design dissipates ~0.5 watt. The noise level expected is on the order of a few hundred microvolts.

In order to standardize the design for several STAR systems that require photomultipliers, as well as reduce the overall cost, an attempt is being made to develop a base that is suitable for both the EMC and CTB systems. This places an additional constraint on the design, since the photomultipliers for the CTB will be located in a 0.5-T magnetic field, which would ordinarily saturate the magnetic cores of the transformer components, making them inoperable. A preliminary design that uses no magnetic components is being prototyped. A DC-DC converter chip (e.g., Linear Technologies LT1054) converts a 12–15 VDC supply voltage

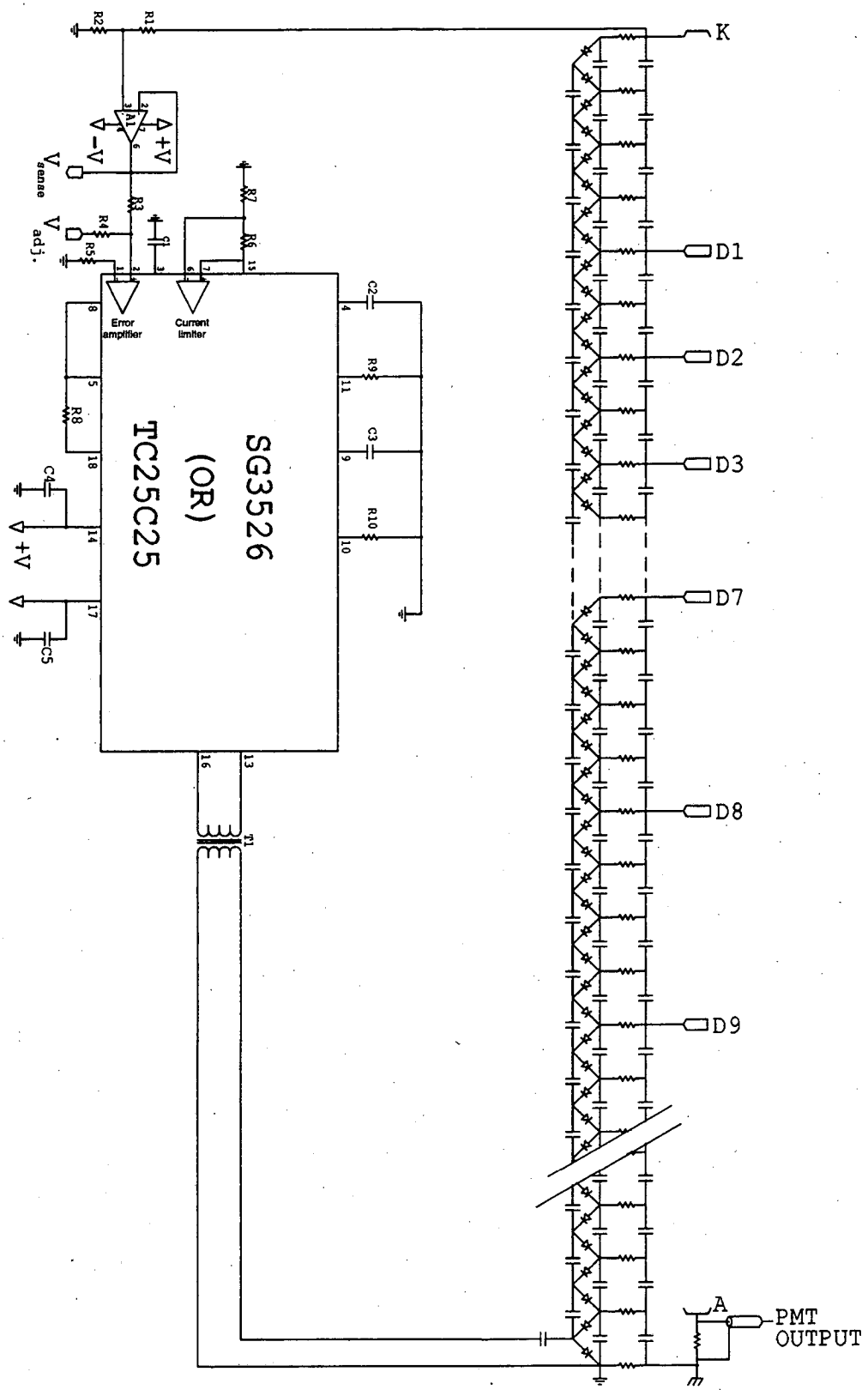

Figure 4C-13. A schematic diagram of a saturated switched-mode pulse width modulation system used to feed a Cockroft-Walton chain.

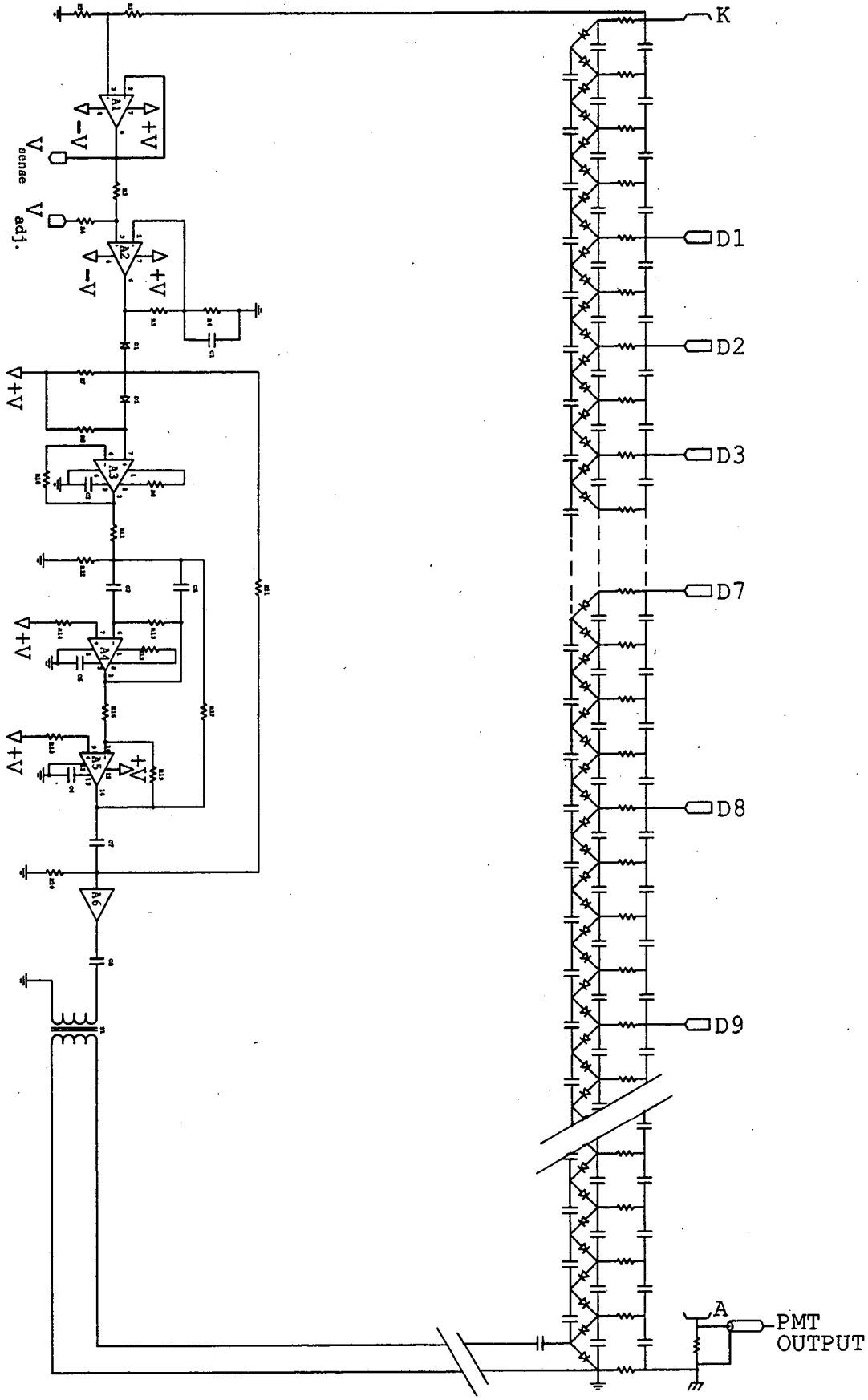

Figure 4C-14. A schematic diagram of an amplitude modulated sine wave system used to feed a Cockroft-Walton chain.

to ±50 VDC. A sine-wave oscillator with a high voltage booster circuit then drives the CW chain. An error-amplifier scheme, such as the one described above, regulates the output of the high voltage driver by modulating the amplitude of the high voltage sine wave.

Digitization of the Analog Signal

Lead-scintillator sampling calorimeters typically detect particles over a wide range of energy. The largest pulse heights are expected to correspond to ~30–50 GeV. These result from direct-γs, or from electrons from $W^{\pm}$ and Z° decays. Small pulse heights are expected from π°s in central heavy ion collisions (~100–200 MeV), and from muons and other minimum ionizing particles which pass completely through the EMC depositing a relatively small amount of energy (~400 MeV equivalent). These particles will be used for one of several calibrations of the calorimeter towers. The number of bits corresponding to this range of energies is 7. If 3 bits are allocated for the pedestal, and the separation between the pedestal and minimum ionizing peaks is also 3–4 bits, the effective dynamic range required is 14 bits. Allowing two additional bits for matching photomultiplier and integrator gains to the ADCs, noise, pedestal drift, etc., a total of 16 bits is needed for the digitization of the analog signal from the EMC towers.

Digitization of the analog signal from the towers of the electromagnetic calorimeter will be accomplished using two 10-bit flash ADCs. A current splitter divides the current input to the charge-integrating system into two units of charge with a predetermined ratio of e.g., 1:64. Two integrators, each of which integrates the charge on one side of the split, subsequently provide that information as input to a corresponding 10-bit flash ADC (FADC) (Fig. 4C-15). The current

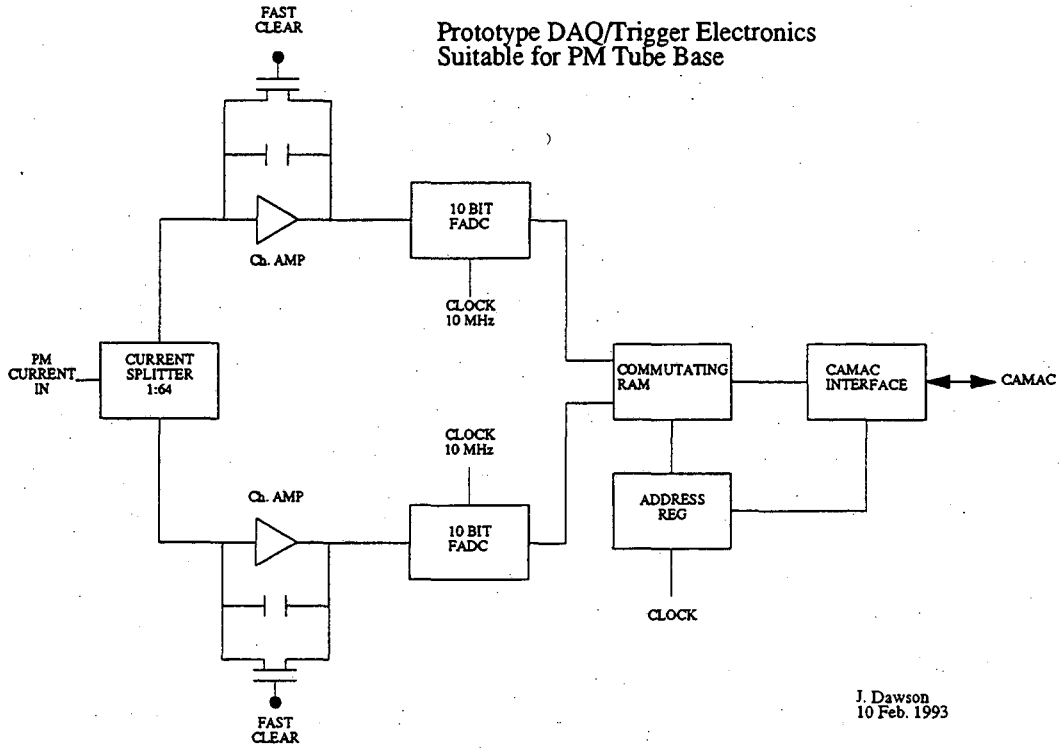

Figure 4C-15. A schematic diagram of the electronics used to digitize 16 bits of analog information from the EMC towers within 3–4 RHIC crossings. A current splitter divides the current input to the charge integrating system into two units of charge in a predetermined ratio (e.g., 1:64). Two integrators, each of which integrates the charge on one side of the split, subsequently provide that information as input to a 10-bit flash ADC (FADC). The two 10-bit words are then concatenated, using a look-up table to resolve the 4 bits of ambiguity.

integrators are equipped with a fast clear. Given a current split of 1:64, the two 10-bit words contain 16 bits of unambiguous dynamic range with 4 bits of overlap. The two 10-bit words are then concatenated, a process in which a look-up table is used to resolve the 4 bits of ambiguity. In the event the two FADC channels can be appropriately calibrated, the look-up table may be unnecessary. With this technique, full digitization of 16 bits of information should be accomplished in less than 3–4 RHIC crossings. Once digitized, the information will be placed in a 10-μs-deep pipeline where it is available to both the trigger and data-acquisition systems.

In one implementation, the trigger and DAQ functions are performed on 9U VME cards located in iron boxes on the magnet return steel. In principle, these boxes also house the phototubes and FADC electronics for the calorimeter towers. Each card has 16 inputs. Digitized pulse-height information from the FADCs is latched into a pipeline with a clock frequency of 110 ns, corresponding to one RHIC crossing period. Latched data are then input into both a layer of Xilinx Field-Programmable Gate Arrays (FPGAs) and into a main memory of static RAM (Fig. 4C-16).

The Xilinx FPGAs execute card-wide trigger algorithms and test, for example, for total energy within a cluster, for the highest energy within a single tower, or for any tower exceeding a given threshold. Summary trigger data are then latched once again at the same frequency for further processing. The output latches are tied together using the 64 unused J2 and 128 unused J3 pins of the VME crate bus and are captured on a card designed to implement crate-wide trigger algorithms. Summary trigger information at the crate-wide level is then latched again and forwarded to a second crate designed to implement global trigger algorithms. Data acquisition would be accomplished by interfacing directly to the static RAM through the VME crate bus.

Various permutations of this concept are possible. For example, the bits from the FADCs could be brought off the FADC card and the detector using multiplexed differential ECL pairs or optical fibers to a more centralized location having trigger logic consisting of large

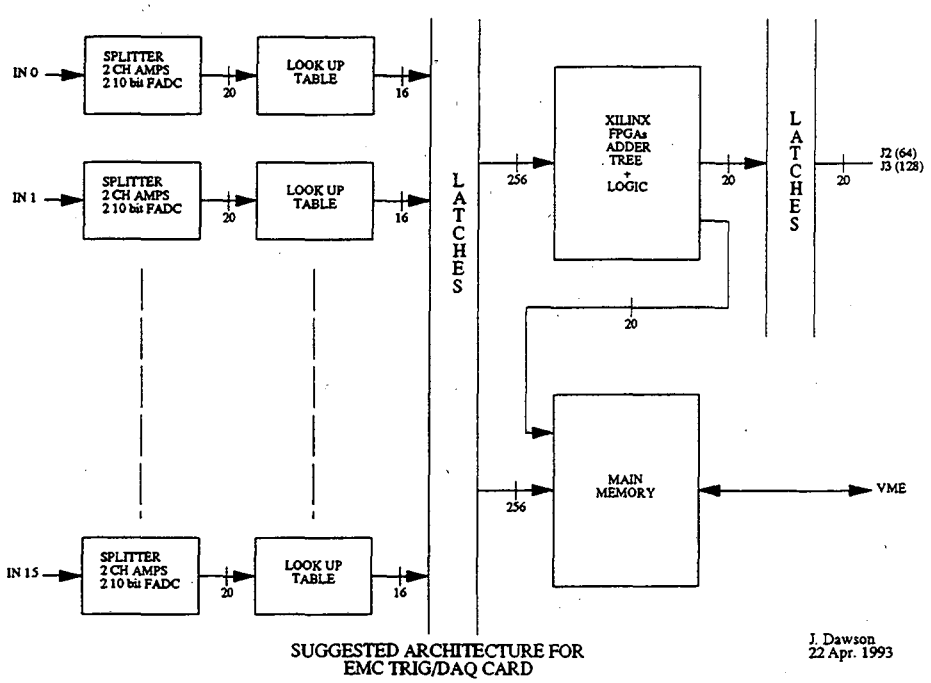

Figure 4C-16. A schematic representation of the Xilinx logic used to make trigger decisions in less than 1 μsec.

arrays of Xilinx FPGAs. This architecture would facilitate the implementation of global trigger algorithms, which are required to look across card or crate boundaries. Additionally, considerations of access and serviceability may require bringing the digitized FADC information to a remote location for processing. Alternatively, placing as much functionality as possible on the same card and in the same crate minimizes the number of signals that must be transported.

Digitization of the Analog Signal From the Shower Maximum Detector

Presently it is not envisioned that information from the shower maximum detector will be used in the trigger. As a consequence, the electronics used to digitize the analog signal from this detector may be substantially different from that used for the EMC towers. Furthermore, the dynamic range for the ADC can be substantially less, probably corresponding to 10 or 11 bits. Given the present design of the STAR EMC, the maximum number of minimum ionizing particles in 0.64 cm of scintillator located at a depth of ~5 X_0 is ~320 for a 40 GeV electromagnetic shower. Assuming 1–2 photoelectrons per minimum ionizing particle per scintillator layer, this corresponds to a maximum of ~640 photoelectrons. Thus, 8–9 bits dynamic range is adequate, allowing one photoelectron per bit. Allocating 1–2 additional bits for matching photomultiplier gains, noise, pedestal drift, etc., a total of 10–11 bits is required for the shower maximum detector.

In the event the shower maximum detector for the barrel and endcap calorimeters is constructed of scintillator strips and waveshifting fibers, the corresponding channel counts will be 9600 and 4000, respectively. In this circumstance, the electronics necessary for digitization may be freely adapted from the amplifier-shaper IC currently planned for the SVT. This amplifier will produce a pulse of 2 V for an input signal of 20k electrons. The input signal is first integrated and then differentiated with a time constant of 9 ns. It then passes through a semi-gaussian filter, producing an effective peaking time of 32 ns. The output nominally returns to zero after an additional 60 ns. Use of this type of electronics appears to be well suited to adaptation of the SVT-style SCA chips as well. The control and housekeeping circuitry would also be similar to that for the SVT in order to make the use of electronics already under development.

The SCA chip used for this application would optimally be clocked somewhat faster than that for the SVT (~50 MHz) in order to allow for 5–6 samples during the pulse duration. The output of the SCA would be presented to a multiplexed ADC ~ 5 μs after the triggered beam crossing, allowing that amount of time for trigger formation before digitized data are removed to external buffers for further processing. The cost of this electronics implementation would be comparable to that of the SVT ($10–$20 per channel) and would therefore represent a small percentage of the overall cost of this implementation of the SMD.

In the event the shower maximum detector is constructed of proportional wire chambers (PWCs) containing wires and pads, the corresponding channel counts for the barrel and endcap detectors will be 30,000 and 13,000, respectively. In this instance, a more appropriate amplifier would be the transresistance amplifier currently under development by Dorfan.[49] It is characterized by a peaking time of 50 ns and fast-recovery pulse-tail suppression. The consequence of the latter characteristic is that the tail of the amplified pulse is completely restored to zero within three RHIC crossings after the one of interest. The baseline restoration is estimated to be fast enough that even a second hit on the same channel one crossing after the triggered crossing would clearly be evident in the digitized data.

[49]D. Dorfan, Dept. of Physics, University of California, Santa Cruz, Santa Cruz, CA 95064.

The Dorfan preamp is characterized by a gain of 2×10^5 and will therefore provide pulses of the right amplitude for use by the SCA presently under development by the SVT. The IC package contains 40 channels, allowing for optimal use of space. For this implementation of the SMD, the SCA would also be clocked at ~50 MHz, yielding 8–10 samples during the full duration of the amplified pulse.

4.C.5. Calibration

A number of different systems will be used to test the EMC hardware after installation. In particular, it will be necessary to monitor the gain in the photomultipliers and electronics and determine the energy calibration for each channel. To monitor the electronics, charge will be injected into each channel. LEDs, xenon flash tubes, and/or lasers will be used to generate light pulses sent on optical fibers to the photomultipliers. Radioactive sources will be placed near some scintillators of each tower to provide an energy calibration. Various physical processes may also be used to monitor the performance of the system.

The injection of charge into each electronics channel will be done to test electrical continuity, search for cross-wirings and cross-talk, and identify channels with abnormal gain. Some gain variation is expected due to differences in the capacitors used for charge integration. However, the observation of abnormal gain generally indicates problems with the electronics or connections. Charge injection may therefore be used to search for electronics channels that are not functioning properly.

Photomultiplier gain can be monitored with light pulses from LEDs, xenon flash tubes, or lasers. This type of gain change can occur, for example, due to temperature changes or changes to the high voltage. As there are advantages and disadvantages for each of these systems, a combination of two or three may be adopted. For example, although LEDs can be very stable for periods up to a year, their total light output and long-term stability are limited. Consequently, the light from each LED will be split or fanned out to ~7–8 photomultipliers, with some photomultipliers receiving light from two LEDs for cross calibration. Xenon flash tubes generate sufficient light to pulse all 1,200 photomultipliers in the barrel EMC simultaneously. However, with this type of system there are typically pulse-to-pulse amplitude variations of a factor ~2, and special tubes are needed to obtain short enough pulses to fit within ADC gates. One advantage of flash tubes is that the light emitted is of the proper wavelength to excite the waveshifter fibers used to transmit light, and may therefore be used to test another component of the detector if injected near the scintillator instead of directly into the photomultipliers. Lasers can generate short, intense light pulses, but distributing these pulses uniformly to all photomultipliers simultaneously is difficult.

Radioactive sources will be used for absolute calibration of the energy deposited in the EMC towers. To accomplish this they will be passed through tubes located at the shower maximum gap in each tower. The sources will be small cylinders containing ^{60}Co or ^{137}Cs. As part of the calibration, the DC currents will be measured in individual photomultipliers. For some EMC towers, calibration using radioactive sources may provide the only long-term absolute calibration possible since it may not be feasible for all of the individual modules to be calibrated in a test beam.

Some physics processes may also provide useful energy calibrations. For example, the pulse height from muons traversing the EMC will correspond to minimum ionization in each scintillator of a given tower and should result in the same signal for all towers at a given η. The reconstruction of η° and low energy π° decays will also provide a useful absolute energy calibration. Normally, high energy π° decays are not used because the position resolution

required to determine the opening angle between the two photons is insufficient to reconstruct the mass of the π° accurately. J/ψ and Z° decays may also be used for calibration, although the rates for these processes will be low.

Finally, calibration will also be necessary to determine the change in response due to the STAR magnetic field. This result may occur because of magnetic effects on the photomultipliers, mechanical effects causing the movement of optical components, or changes in the properties of electronics components such as power supplies. The total change in the output signal due to such effects is typically ~5%, based on experience at CDF. These changes could be isolated and corrected using the LED, Xenon flash tube, and source systems discussed above. For example, the LEDs could be used to test for changes in photomultiplier gain with the magnetic field on and off. The xenon flash tube system would be used to check for changes in light transmission from the scintillator to the photomultiplier, and the radioactive source calibration system would monitor changes in scintillator light output.

4.C.6. Shower Maximum Detector

The basic purpose of the shower maximum detector is to provide fine spatial resolution for electromagnetic showers, in order to distinguish direct photons from photons resulting from π° decay. For example, to distinguish a π° from a direct-γ at $p_t \sim 20$ GeV/c, it is necessary to resolve two showers which are only 3 cm apart. The size of the calorimeter towers, on the other hand, is effectively limited to 24 cm × 24 cm by considerations of cost. Consequently, a device with fine spatial resolution costing much less per channel for electronics than the EMC towers is required.

Two different technologies are being considered for the construction of the barrel shower maximum detector. One technology is a wire chamber with perpendicular wires and strips, and the other is scintillator strips with optical fiber readout. Issues affecting the decision between the two technologies include:

- Efficiency for detecting single electrons in a low energy shower
- Compatibility with the barrel EMC mechanical design
- Cost per channel
- Availability of existing Russian components and construction labor
- Experience in the CDF experiment and in tests performed at IHEP, Protvino.

The design considered for the wire chamber shower maximum detector is essentially identical to that in CDF (see Fig. 4C-17). An aluminum extrusion, 24-cm-wide with 6-mm × 6-mm channels that are open at the top, forms the basic structure of the detector. The extrusions would be approximately half the length of a barrel module given the module design in Section 4.C.2, with square channels running parallel to the beam, along the η direction. The wires would be constructed of 20-micron-diameter gold-plated tungsten, and would be centered in the channels with small supports made of plastic, G10, or foam. Strips running in the ϕ direction would be etched onto thin PC board. They would cover the open side of the extrusion and run at right angles to the channels for a length of 24 cm. The strip widths would be 1.2 cm at $\eta = 0$ and would increase in width with increasing $|\eta|$.

Pulse heights would be recorded for both the wires and the induced signals on the strips, giving two-dimensional information on the shower location. Electrical components such as high voltage isolation capacitors and current-limiting resistors for the wires would be located at the ends of the extrusions producing small (~7 mm) dead regions in the detector. To reduce

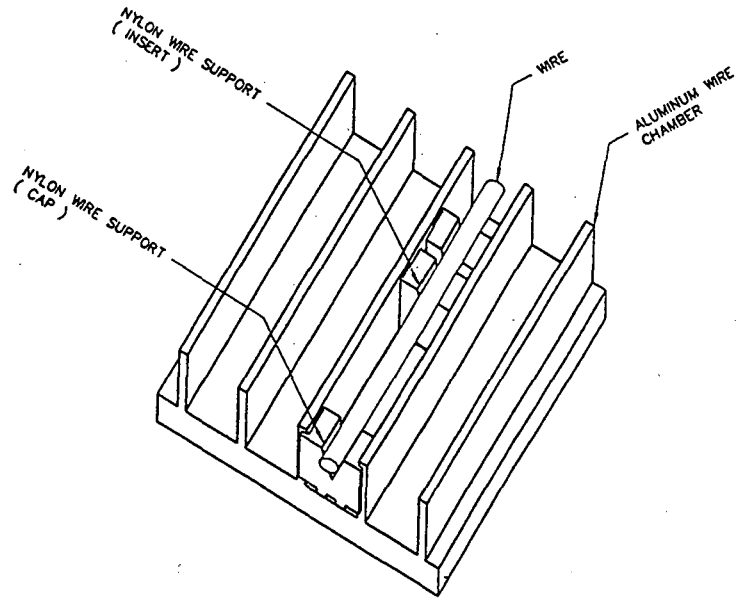

Figure 4C-17. A conceptual design for the mechanical construction of a wire/strip shower maximum module for the barrel EMC. An aluminum extrusion with 6-mm × 6–mm channels that are open at the top forms the basic structure of the detector. Strips running in the ϕ direction are etched onto a thin PC board, which forms the cover of the extrusion. The wires running down the middle of the channels would be 20 μm gold-plated tungsten.

the cost of electronics, pairs of wires would be connected together after the isolation capacitors, giving an effective segmentation in the ϕ direction of 1.2 cm. This coarser segmentation can not be accomplished mechanically, since the drift time for electrons becomes excessive in a mechanical cell 1.2 cm square. The signals from the wires would be routed to preamplifiers, ADCs, and other electronics located on the outside of the magnet flux return bars using ribbon cable. Similarly, the signals from the strips would travel on ribbon cable as well. The capacitance of a strip pulse cable ranges from ~680 pf for the 1.2 cm strips near $\eta = 0$, to ~900 pf for the wider strips at high $|\eta|$. The preamplifiers would be designed to collect the charge and shape the output pulse within 100 nsec to allow for high rate operation. Alternatively, it would also be possible to take several ADC samples over a time period of ~200 ns. The electronics for digitization of the analog signal would be identical to those used for the TPC.

The top of the wire chamber shower maximum detector would consist of a plastic cover. The cover would be machined to route ribbon cables to the end of the module and would also position the tube containing the radioactive source used for calibration. It would fit above the PC board for the strips and would prevent compression of the cables or source tube by other elements in the barrel module. The total radial space allocated for this detector is 25 mm, including the extrusion and plastic cover.

An alternative design for the shower maximum detector consists of two sets of 1-cm-wide, 5–6-mm-thick scintillator strips, which are perpendicular to each other. The set parallel to ϕ has a length of 12 cm, since two strips, offset slightly in depth, are used to span the full 24-cm width of a barrel EMC module. The waveshifting fibers used for readout are placed in grooves machined into the strips, and are bonded to clear optical fibers soon after leaving the scintillator. These are then routed to the back plate of the module as shown in Fig. 4C-18. All the fibers from this set of strips are run to a single photomultiplier. The other set of scintillator strips is parallel to η, with lengths varying from 24 cm at $\eta = 0$ to 36 cm at $|\eta| = 1$ in order to match the size of the EMC towers. The routing of fibers for strips running in the η direction

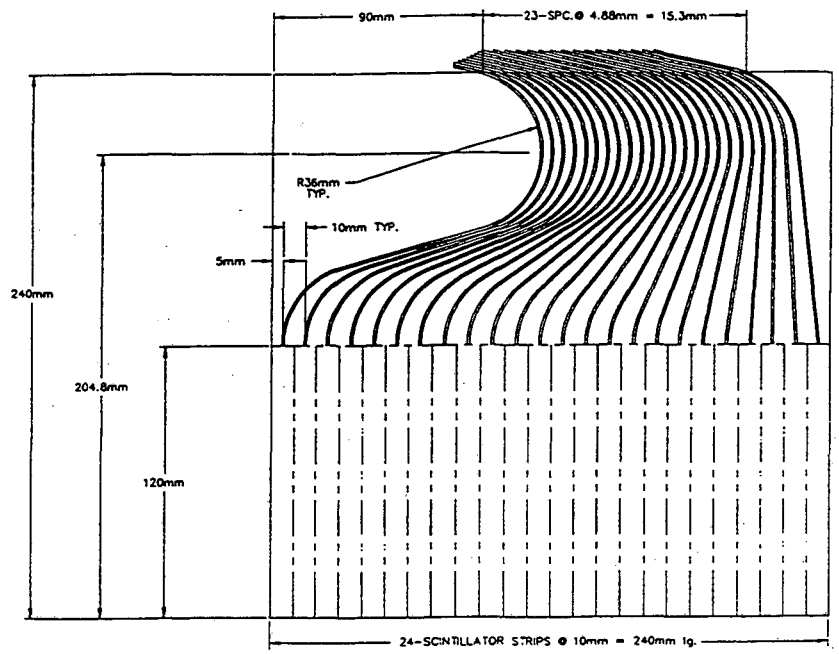

Figure 4C-18. A schematic diagram showing the routing of the optical fibers from a scintillator strip shower maximum detector to the back plate of a barrel EMC module. This technology, as well as wire/strip chambers, is being considered for this application.

would be similar to that discussed above. All the scintillator strips necessary for the shower maximum detector for two towers would be located in a single aluminum box designed to fit into a barrel EMC module. This box would protect the scintillators and fibers from possible compression by the lead plates.

The advantages of the wire chamber shower maximum technology include good efficiency for the detection of single minimum ionizing particles, successful operation in the CDF detector, and low cost per channel. Advantages of the scintillator strip technology include good compatibility with existing designs for the EMC modules and the availability of existing photomultipliers. Recent tests[50,51,52] of the scintillator strip technology at IHEP, Protvino have demonstrated a light collection efficiency corresponding to ~2 photoelectrons per minimum ionizing particle using the same photomultiplier planned for the detector. This observation indicates that the efficiency for single electrons should be high. A possible advantage of fiber readout is immunity to electrical noise. This is a concern, since the ribbon cables for a wire chamber shower maximum detector would potentially be routed through the gap between the magnet iron end ring and the magnet pole tip, where many power cables for the TPC and SVT will also be located. The sensitivity of the ribbon cables to noise from these power cables is under study to see whether pickup noise is a potential problem.

One possible limitation of the shower maximum detector is its effectiveness in eliminating asymmetric π^0 decays in which the energy of the two decay photons differs by a significant amount. One measure of this effectiveness is to plot detection efficiency vs the ratio

[50]S.A. Akimenko, *et al.*, "Study of the Module of a Shower Maximum Detector," STAR Note No. 123.
[51]S.A. Akimenko, *et al.*, "Second Module of a Shower Maximum Detector," STAR Note No. 124.
[52]B.V. Chuiko, *et al.*, "Some Parameters of the Basic Element of the SMD for STAR at RHIC," STAR Note No. 122.

R, where R is defined as (E1–E2)/(E1+E2) and E1, E2 are the energies of the two decay photons. A Monte Carlo simulation of a four-tower segment of the EMC with a one-dimensional scintillator shower max detector was performed to look at this variable. The results are presented in Fig. 4C-19, from which it is noted that the detection efficiency is essentially 100% from R = 0 to R = 0.8–0.9, above which it falls linearly to zero at R = 1.0. This performance is better than that of some liquid argon detectors used for the detection of direct-γs, although it is not quite as good as that of some finely segmented lead glass arrays.

4.C.7. Prototype and Test Beam Program

There will be both functional and mechanical prototypes of the EMC barrel modules constructed early in the program. These include a small 2 × 2 tower prototype, one or two full-size prototype modules, and a full-size engineering model. Additional engineering modules to test various concepts may also be built.

The small, four-tower prototype EM calorimeter is presently being constructed. The main purpose of this prototype is to measure its response to low energy hadrons, to check the optical readout system, and to test the prototype shower maximum detectors for performance and optimum depth in the calorimeter. Tests will be carried out with cosmic rays and low energy protons at Michigan State University (MSU), and with pions and electrons at TRIUMF, BNL, and IHEP, Protvino. Michigan State University will assemble the detector with parts and materials purchased and prepared at several other institutions. The scintillators for this detector were prepared at UCLA using a diamond mill to test this procedure as a possible means to reduce the labor cost associated with fabricating scintillator tiles. The waveshifter fibers used for readout were cut and aluminized at UCLA as well. The lead absorber plates will be fabricated at Argonne National Laboratory with the final design, engineering, and machining of structural elements being performed at MSU. Photomultipliers and bases will be supplied by UCLA. Electronics are being supplied by several institutions, and data acquisition

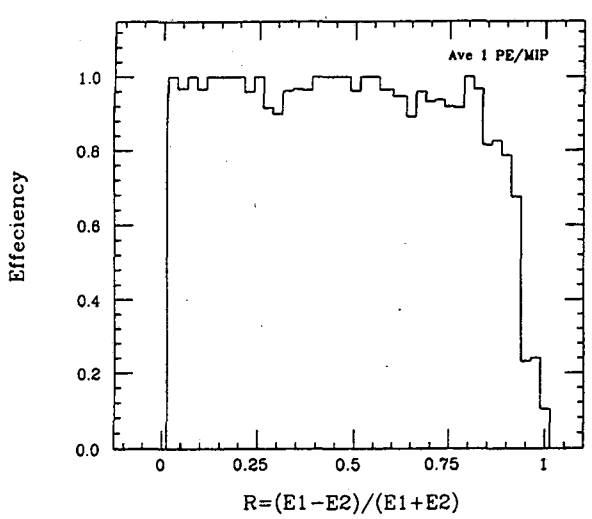

Figure 4C-19. The detection efficiency of a one-dimensional scintillator strip shower maximum detector as a function of the asymmetry R = (E1 – E2)/(E1 + E2) in the decay energies E1 and E2 of photons from π° decay. The threshold for detection is set at three photoelectrons, while the average light output is assumed to be one photoelectron per minimum ionizing particle. The actual light output is expected to be higher.

programming may be done by Johns Hopkins University, MSU, and UCLA. Construction of the small prototype will be completed early in 1994, at which point testing will begin.

At least one, and perhaps two, full-scale prototype barrel modules will also be built. These may not be fully instrumented initially because of costs. The goal of constructing the full-scale prototypes will be to demonstrate that modules can be assembled and installed as planned, to demonstrate the capabilities of collaborating institutions, and to estimate more accurately the true cost of parts and labor. Additional physics testing will be directed at measuring the energy resolution possible with this detector, determining the spatial resolution of the shower maximum detector for showers which are close together, and studying the uniformity of response near boundaries in η or ϕ. If the full-scale prototypes perform satisfactorily, they may also be used in the final barrel calorimeter. Tests will be performed with various low and high energy beams at BNL, TRIUMF, and IHEP, Protvino.

A full-scale engineering prototype module will be built without scintillator or fibers. The purpose of this prototype will be to verify deflections and stresses computed with finite element calculations, to test methods of fastening various structural members together, and to identify potential problems with the mechanical design. Lumped loads will probably be used for testing instead of a full set of lead plates. This prototype will be constructed in the fall of 1993 at Argonne National Laboratory.

4.C.8. Future Decisions/Schedule

Three technical decisions are required before proceeding to a full preliminary design of the barrel electromagnetic calorimeter. The first concerns the mechanical design of the EMC modules.

Four options are currently under consideration. The first design incorporates stacked sheets of clad lead separated by spacers. Scintillator tiles are placed between the spacers to form pseudo-projective towers. Gravitational loads are supported by the front and back plates, as well as side covers, end plates, and a central bulkhead. The second design is similar, except the use of spacers has been eliminated. In this instance, compression of the scintillator by the weight of the lead would result in pressures $\leq$0.02 MPa. A third design utilizes stacked sheets of clad lead without spacers. Lead sheets are placed directly on top of the scintillator in this option, and the lead-scintillator stack is held together by friction using compressive loads. Compression of the stack in this design results in a pressure of ~0.10 MPa on the scintillator tiles. Although this pressure is low enough to prevent significant "creep" of the lead, concern exists over possible changes in the performance of the scintillator over the lifetime of the calorimeter. The fourth design calls for cast lead absorber sheets, reinforced with steel bulkheads and tubes. This design has been adopted for the electromagnetic calorimeter for SDC. Preliminary cost estimates indicate that this option is the most expensive, primarily as a consequence of the labor required to machine and construct a mold. Considerable maintenance is also required to ensure the quality of the mold for multiple castings. It is presently envisioned that sufficient engineering and cost-gathering will have been conducted by July 1993 to decide between these options.

The second technical decision is whether to use scintillator strips or wire/strip chambers for the shower maximum detector. Since it is presently thought that the information from the shower maximum detector will not be used in the trigger, wire chambers of appropriate design may be fast enough for this application even at the highest pp luminosities. The relevant issues entering into this consideration are cost per channel, spatial resolution, and signal per minimum ionizing particle. Additionally, the possible use of existing components and issues related to the

mechanical interface between the shower maximum detector and the EMC modules must also be taken into account.

The third decision necessary to proceed to a full preliminary design is related to the second, and concerns the type of readout electronics for the shower maximum detector. The possible use of electronics similar to those planned for the STAR TPC and SVT is being considered.

Both the latter decisions will be made in close consultation with the group at IHEP, Protvino which has expressed interest in the construction of the shower maximum detector. Sufficient engineering, cost-gathering, and simulation should be accomplished to make these decisions by the fall of 1993.

A small, four-tower prototype calorimeter is currently being assembled at Michigan State University, using parts constructed at a number of participating institutions. Completion of the prototype is expected by the spring of 1994, at which time it will be placed in an accelerator beam (BNL, MSU, IHEP) to test its response to low energy (200–600 MeV) pions, electrons, and protons.

A full-scale engineering model of a barrel calorimeter module will be constructed in the fall of 1993, following the decision noted above as to the optimum mechanical design. The model will be used to test various aspects of the design, including finite element calculations concerning stresses, deflections, and module stability.

4.D. The Endcap Calorimeter

4.D.1. Choice of Technology

A sampling calorimeter constructed of alternating layers of lead and plastic scintillator was also chosen for the endcap electromagnetic calorimeter. The basic concept is similar to that for the barrel EMC, although the mechanical support is necessarily different. In considering this decision, inorganic crystals such as NaI, CsI, BGO, etc., were again found to be too expensive in view of the large acceptance to be covered. Considerations of space, noise, and timing response ruled out the use of liquid argon. It was also hoped that significant costs savings might be realized by using electronics and mechanical elements similar to those for the barrel EMC.

The total absorber thickness in this instance is ~23 X_0 This is thicker than for the barrel EMC, and accounts for the fact that electrons and photons entering this acceptance will generally be of higher energy. In order to match the barrel EMC design, sampling will be accomplished using alternating layers of 5-mm-thick lead absorber plates and 4-mm-thick scintillator tiles. A shower maximum detector located at a depth of ~5 X_0 will again be used to distinguish between direct photons and photons resulting from π^0 decay. Since the space available between the TPC electronics and the magnet poletip represents a severe constraint on the depth of the endcap calorimeter, the photomultipliers will be located outside the magnet pole tip. This has the advantage that to first order the photomultipliers are outside the magnetic field. It also has the disadvantage that fibers attached to the scintillator tiles must be routed to the exterior of the magnet. The fibers to be used will be plastic optical fibers of 1-mm diameter.

Details of the endcap calorimeter conceptual design are presented in the sections that follow.

4.D.2. Mechanical Structure

The mechanical structure of the STAR endcap EMC is constrained by the amount of space available between the end of the time projection chamber (TPC) and the inside of the magnet poletip iron. Severe constraints also occur near $\eta = 1$, where the barrel and endcap EMCs meet. Cables from detectors inside the EMC, including those from the TPC, will exit from STAR near $\eta = 1$. The detailed routing of these cables is presently under study. The following discussion includes details of the conceptual design, and analytical and finite element calculations of the stresses in various structural members of the endcap EMC.

Constraints on the Endcap Electromagnetic Calorimeter Design

Figure 4D-1 shows a cross-sectional view through one-quarter of the STAR detector. The detector is cylindrical with the beamline on the cylinder axis. It is also symmetric left and right of the nominal beam-interaction point. The space available for the endcap EMC ranges from z = 2712 to z = 3087 mm, with z along the beam direction. The inner and outer edges of the endcap calorimeter subtend polar angles of $\theta = 15.4°$ and $\theta = 38.3°$, respectively. The magnet poletip is retractable for servicing detector components inside the barrel. The endcap EMC is mounted to it.

Gaps separating adjacent scintillator tiles are generally undesirable and should be minimized. Particles traveling in these gaps do not give signals in the scintillators, a condition that can lead to a degradation in the energy resolution. This problem is expected to be especially serious near $\eta = 1$, the boundary between the endcap and barrel EMCs. This boundary region will contain many cables, as well as the TPC supports, cooling lines for electronics, etc.

Conceptual Design

The ϕ segmentation of the endcap calorimeter was chosen to match the barrel EMC. Consequently, $\Delta\phi = 6°$ and there are 60 ϕ towers. This segmentation is an integral multiple (5) of the number of TPC sectors. The segmentation in η corresponds to $\Delta\eta = 0.05$ near $\eta = 1.0$, but increases to $\Delta\eta = 0.1$ near $\eta = 1.4$. This increase avoids scintillation tiles with dimensions less than 80 mm in the η direction. A scale drawing showing the planned η and θ segmentation is shown in Fig. 4D-2. The coarser η segmentation for $\eta \sim 1.4$ also reduces the number of photomultipliers, fibers, and associated readout electronics.

Each of the scintillator tiles shown in Fig. 4D-2 is part of a tower of alternating layers of lead and scintillator, with boundaries that project to the nominal beam-interaction point. This is shown in Fig. 4D-3 for a section of the endcap EMC. A total of 25 layers of lead and 26 scintillator tiles are present in each tower. A 25-mm gap is present for a finely segmented strip detector (shower maximum detector) near the depth corresponding to the maximum number of particles in electromagnetic showers of 2–5 GeV. The total weight per endcap EMC is approximately 27.3 tonnes.

An early design for the endcap EMC consisted of a number of $\Delta\phi = 6°$ modules, one of which is shown in Fig. 4D-4. In this design, the lead plates were held in place by the sides of the module as well as inner and outer radial end supports. Tabs in the sides were used to support the lead sheets when the module was horizontal and to maintain an approximately constant separation of the lead sheets when the module was vertical and mounted on the magnet poletip. In this design, there was essentially no pressure on the scintillator tiles or optical fibers. An aluminum front plate and stainless steel back plate provided additional structural support for the modules.

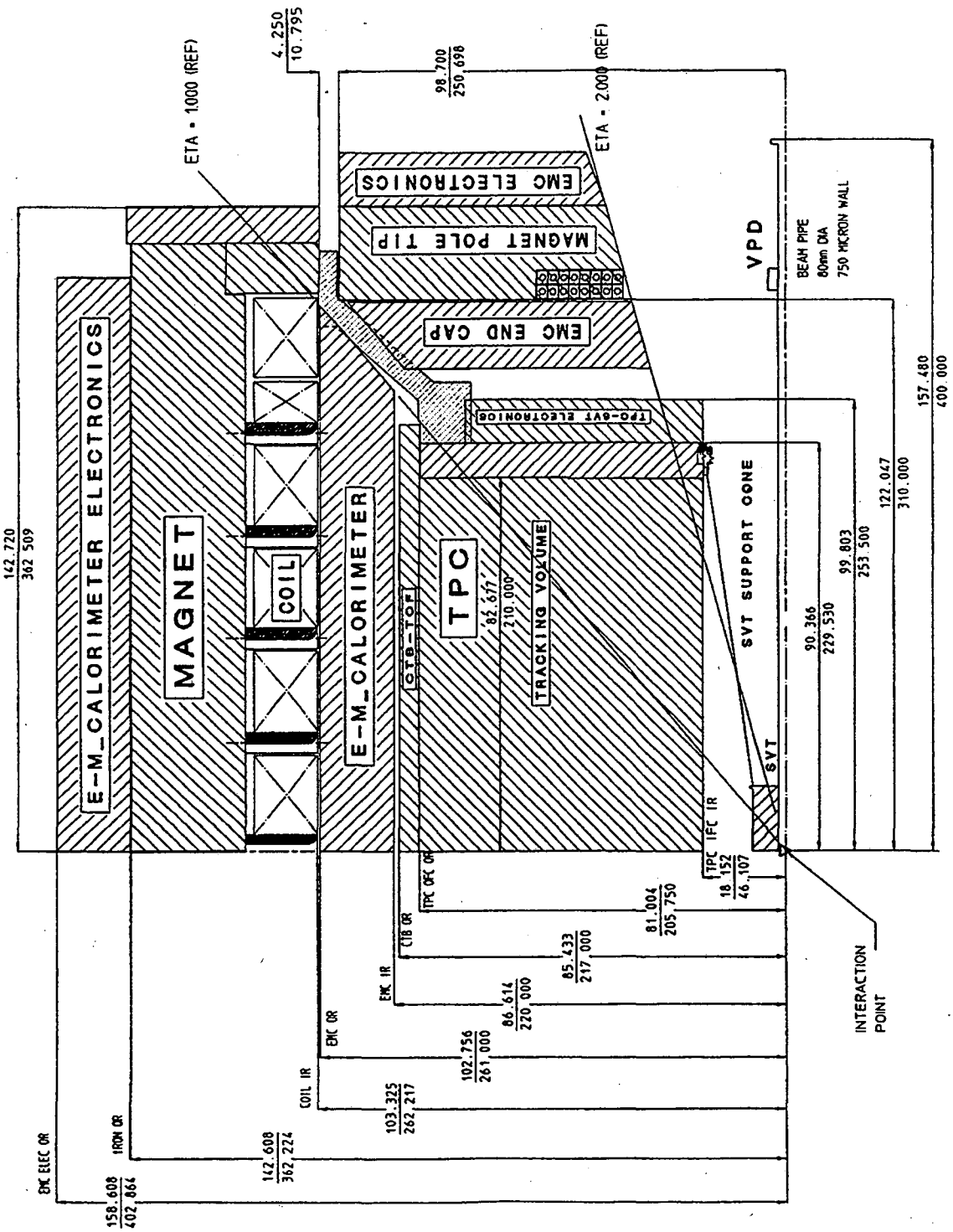

Figure 4D-1. A quarter section of the STAR detector showing the radial and longitudinal location of various detector systems.

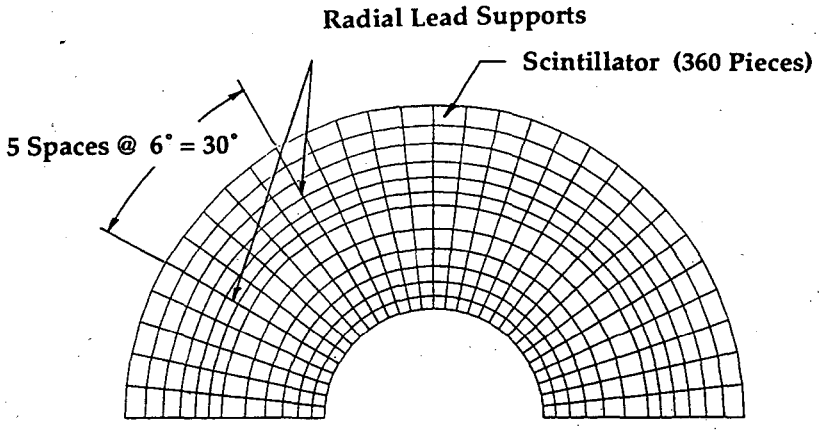

Figure 4D-2. A scale drawing showing the segmentation in η and ϕ of the endcap electromagnetic calorimeter. There are 360 tiles in a single sampling layer. Radial lead supports are located at intervals of 30°.

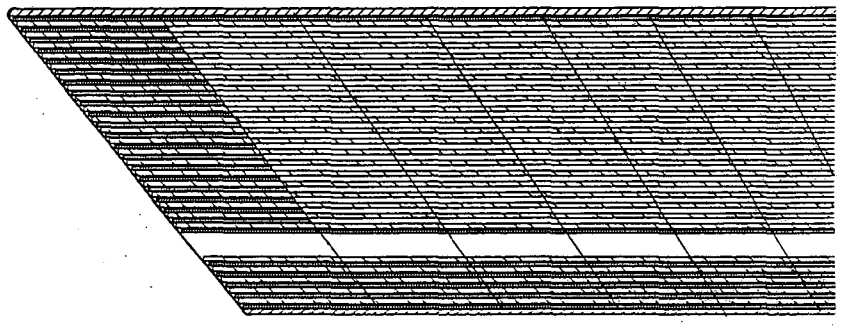

Figure 4D-3. A cross-sectional view of one 180° endcap EMC module. The scintillators are positioned so as to form pseudo-projective towers pointing to the interaction region. A shower maximum detector to distinguish between direct photons and photons from π^0 decay is located at a depth of ~5X_0. The diagonal lines indicate the tower boundaries.

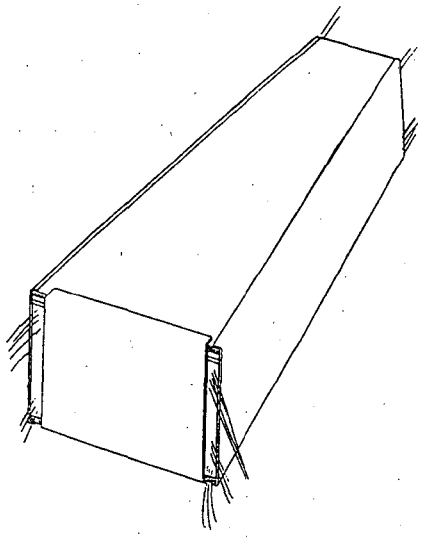

Figure 4D-4. A conceptual design for one of the 6° modules first investigated for possible use in the endcap EMC. This design was abandoned because of the relatively large gap created between adjacent modules by the side plates necessary for support.

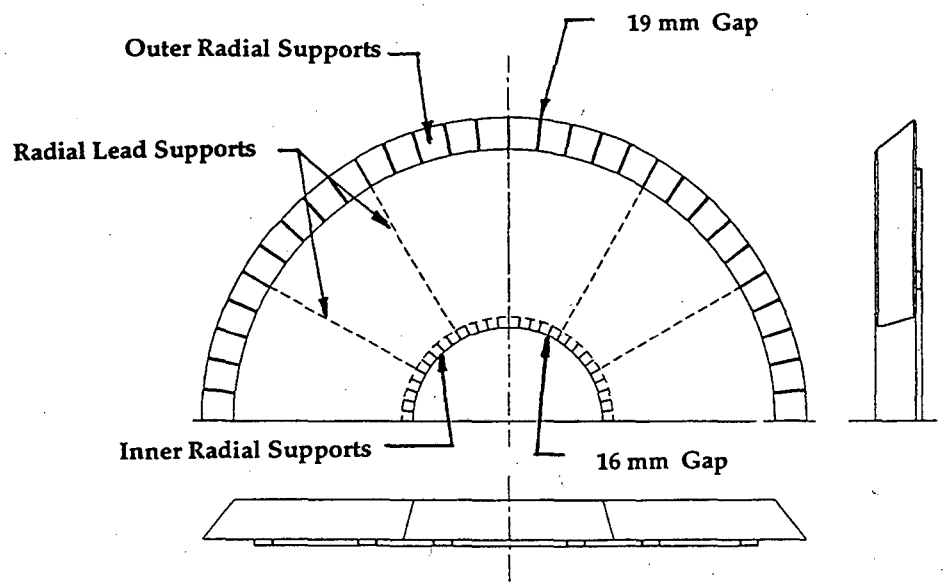

Figure 4D-5. A perspective view of one of the 180° modules used for the endcap electromagnetic calorimeter.

The $\Delta\phi = 6°$ module design was abandoned because of the relatively large gaps in the ϕ direction between adjacent scintillator tiles caused by the module side plates. Various other options were considered before developing the present design which consists of two $\Delta\phi = 180°$ sections per endcap. These sections may be mounted to the magnet poletips in the experimental hall without removing the accelerator beam pipe. The weight of each is expected to be well within the crane capacity of ~18 tonnes. A drawing of one 180° section is shown in Fig. 4D-5. A cross-sectional view with dimensions is shown in Fig. 4D-6.

Preliminary structural analyses suggested the need for additional lead supports besides the inner and outer radial ends or supports and the two sides separated by 180°. The present conceptual design has additional radial lead supports every $\Delta\phi = 30°$ in the shadow of the TPC sector boundaries (see Fig. 4D-7). These sector boundaries correspond to support members on the ends of the TPC and are thus already regions of lower efficiency for the detection of charged particles. The radial lead supports and the sides contain tabs to support the lead.

Between each of the radial lead supports are five rows of towers. The lead sheets receive additional support in these regions from extruded aluminum "z-brackets" as shown in Fig. 4D-8. The height of the z-brackets is 6 mm, while that of the scintillator and fiber is ~5.5 mm. The I-beam spacers considered for use in the barrel EMC could not be used because of limitations in the space available and the need for 23 radiation lengths of lead. The fibers are embedded in the scintillator tile and then routed on the surface of adjacent tiles as shown in Fig. 4D-9.

The endcap sections are reinforced on the back with stainless steel channel and mounted to the magnet pole tip with locating pins and mounting bolts (see Fig. 4D-10). The support blocks receiving the pins and bolts will be bolted to the magnet pole tip. This will avoid possible distortions to the magnetic field caused by welding. An alternative design employs a solid, thick back plate with regions machined out for locating pins, mounting bolts, and support blocks.

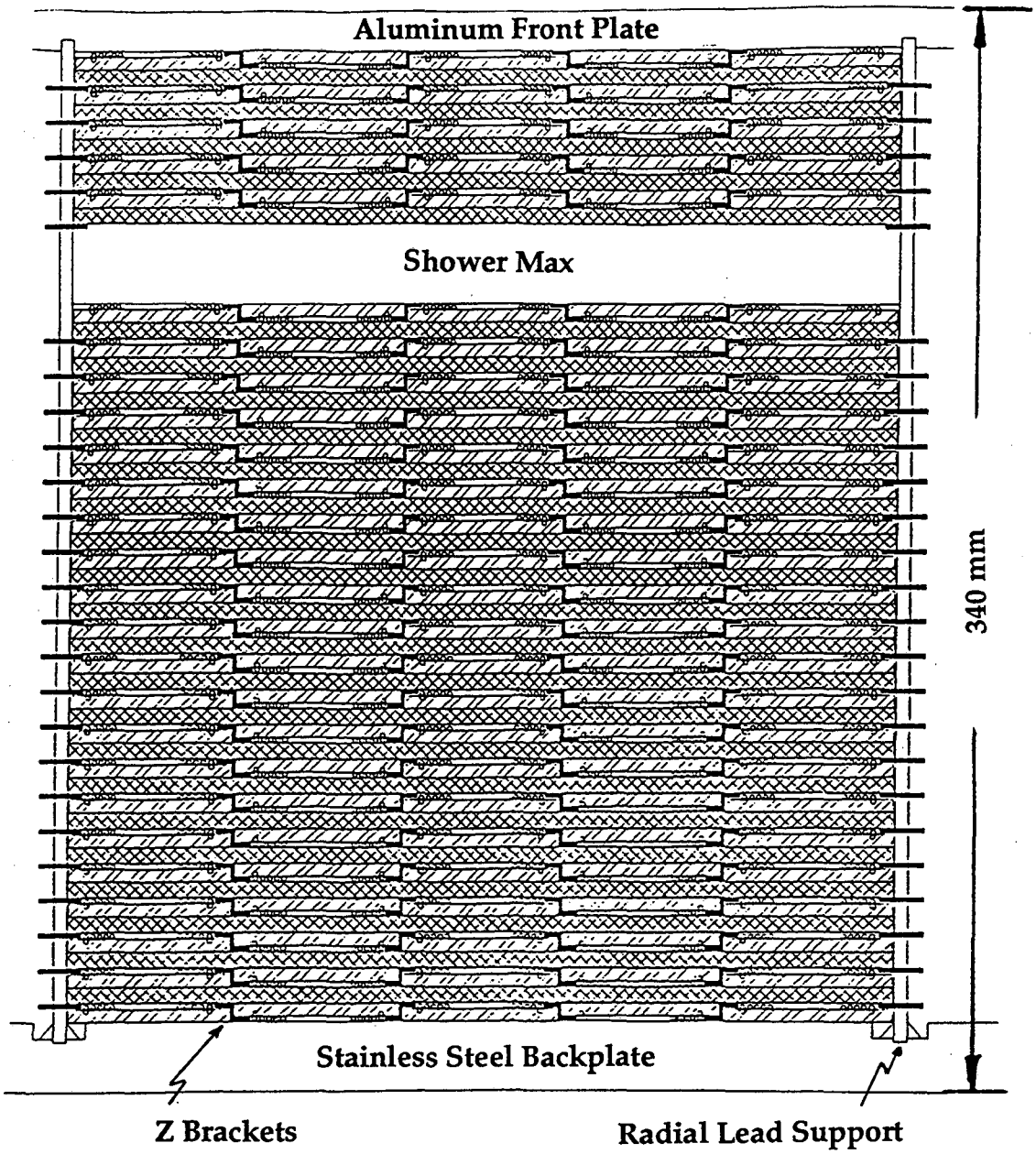

Figure 4D-6. A cross section showing the location and arrangement of scintillator tiles in the endcap calorimeter. Structural support is provided by an aluminum front plate and a stainless steel back plate. At a depth of ~5 X_o, approximately 25 mm is allocated for a shower maximum detector. To allow for fibers to exit the assembly, "z" brackets are used to offset adjacent towers in depth by 1–1.5 mm, affording space for the routing of fibers between the tiles and the layers of lead absorber. Radial lead supports provide shelf support for the absorber plates.

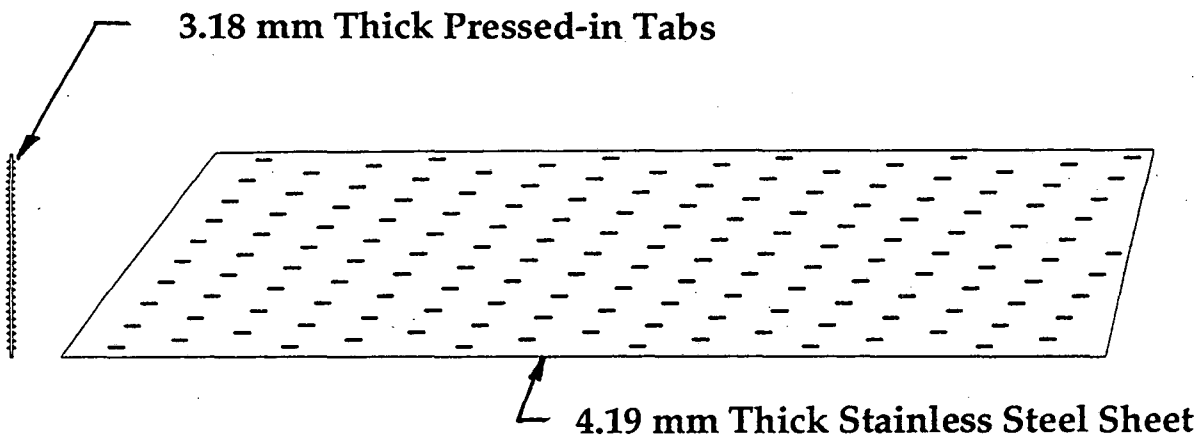

Figure 4D-7. A schematic drawing of the stainless steel sheets used as radial lead supports in the endcap electromagnetic calorimeter. Pressed-in tabs provide shelf support for the plates of lead absorber. The radial lead supports are located at intervals of 30° in the 180° endcap modules.

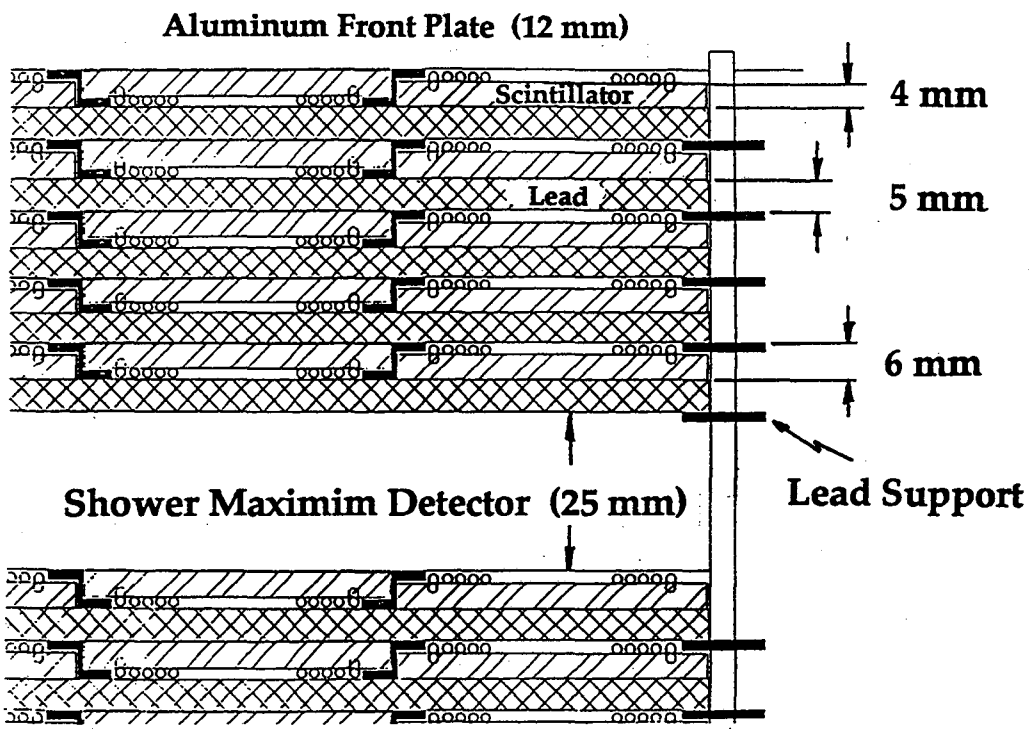

Figure 4D-8. A cross section of part of an endcap EMC tower. To provide space for fibers to exit the module, "z" brackets are used to offset the scintillators in adjacent towers by 1–1.5 mm, so that fibers may pass between the scintillator tiles and lead absorber plates.

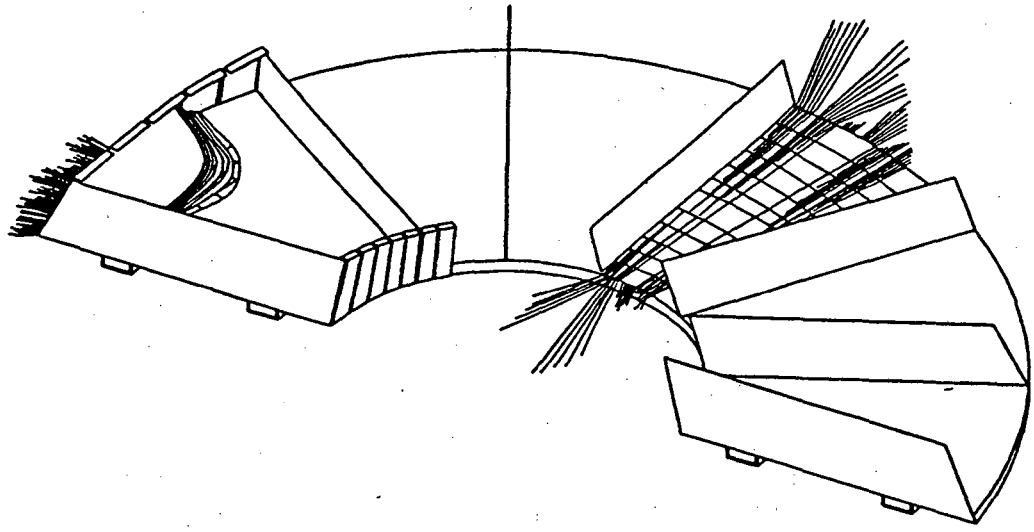

Figure 4D-9. A schematic drawing showing the routing of fibers in the endcap electromagnetic calorimeter.

A sketch of one endcap section during assembly is given in Fig. 4D-11. Optical fibers are routed as shown and exit between the inner and outer end supports. The total number of optical fibers per endcap for the towers is (60 in ϕ) × (12 in η) × (26 scintillators/tower) × (2 fibers/scintillator) = 37,440. The 26 optical fibers from each side of a single tower will be bundled together inside flexible tubing for further routing and protection. If commercial shrink-tubing is used, then the outside diameter will be 7.7 mm per bundle of 26 fibers. The total cross-sectional area of the fiber bundles for each $\Delta\phi = 6°$ row of towers will be ~8.3 cm^2 for fibers that exit at $\eta = 1$ and ~5.92 cm^2 for fibers that exit at $\eta = 2$, not including fibers from the shower maximum detector.

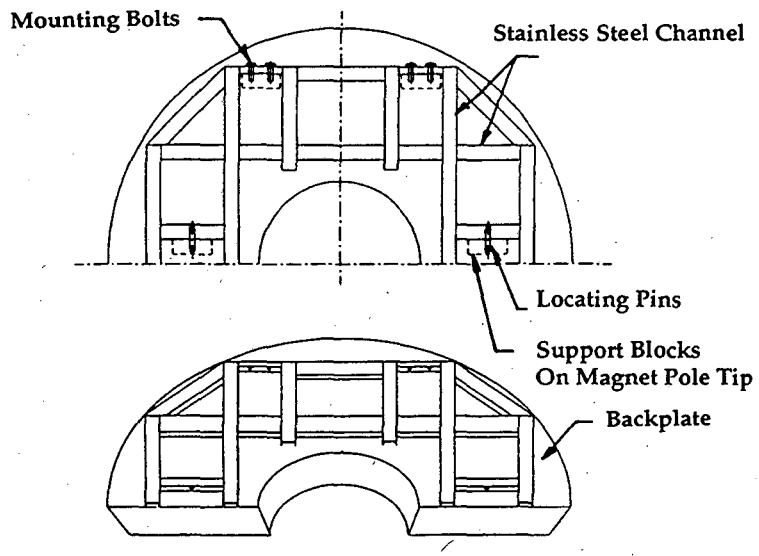

Figure 4D-10. A perspective view showing the location and arrangement of the mounting brackets for one of the four 180° endcap modules.

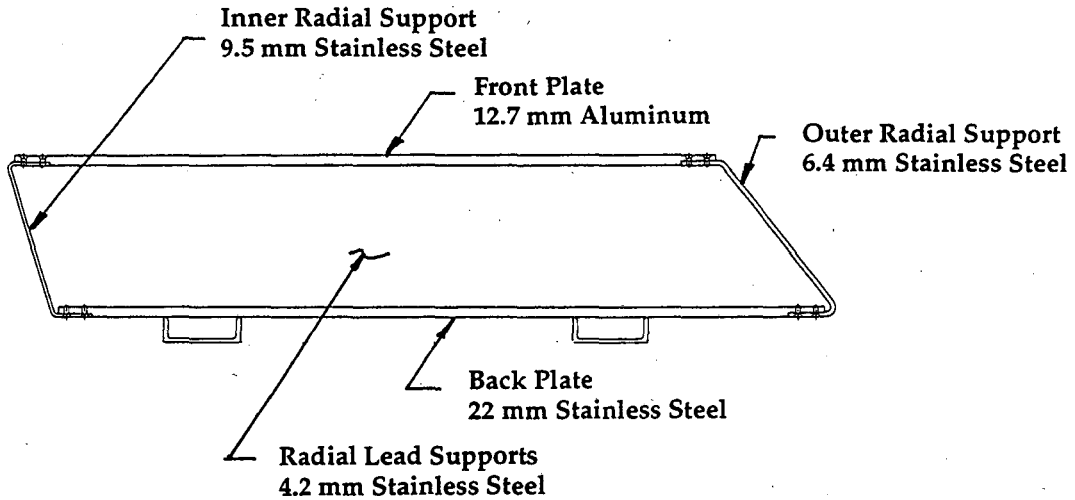

Figure 4D-11. A perspective view showing the location and arrangement of the internal mechanical support for the endcap EMC. Radial lead supports are located at intervals of 30°. Fibers from the scintillator tiles are routed through slots in the walls of the inner and outer circumference. These fibers are connected to photomultipliers located on the exterior of the magnet poletip.

The shower maximum detector will contribute about 7,500 fibers per endcap. This assumes 7-mm-wide scintillator strips oriented at 45° to the center line of each $\Delta\phi = 30°$ section, as shown in Fig. 4D-12. Two sets of strips perpendicular to each other are assumed, with one fiber mounted in a groove in each scintillator strip. Approximately half of the strips will be split to keep the scintillator length less than 60 cm in order to avoid light-attenuation problems.

The total number of fibers per endcap will be 37,440 + 7,500 ≅ 45,000. Assuming that the fibers from the outer seven towers are routed to the outer radius of the endcap, and those from the inner five towers are routed to the inner radius, then the total area required for fibers will be 600 cm^2 and 430 cm^2, respectively. The estimated uncertainty on the area required for fibers is ±20%.

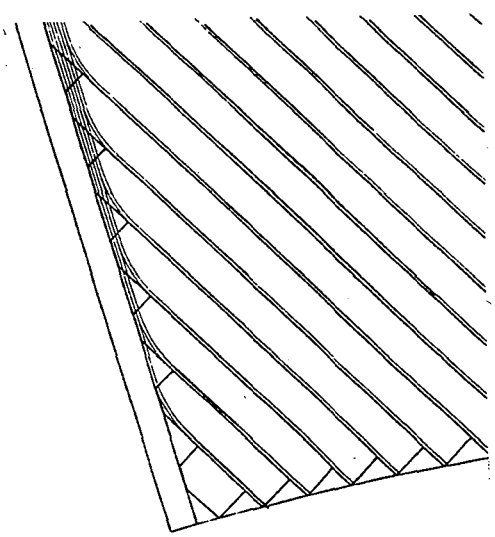

Figure 4D-12. A schematic drawing showing the location and arrangement of scintillator strips for the shower maximum detector for the endcap EMC. This technology is one of two being considered for this application.

Analytical Calculations

A number of analytical calculations were performed to estimate the required thicknesses of various structural elements in the endcap EMC.

Inner Radial Supports

These supports are assumed to be narrow in order to allow fibers to exit at the endcap EMC inner radius. They are at an angle ~15.5° relative to the beam. The maximum stress is expected to occur for the topmost inner radial support. For the stress calculation, the inner radial support was assumed to be fixed to rigid front and back plates with a separation distance of 33.0 cm. It was assumed, however, to be free at the sides. A load of 408 kg was assumed to be carried normal to the inner radial support (considered to be a beam). This is conservative since the support is 15.5° to the horizontal. In reality, 96% (cos 15.5°) of the load is normal to the beam, with the remainder generating tension parallel with the beam. The computed stress was 119.28 MPa for a 9.5-mm-thick support. This stress is near the maximum allowable for Type 304 stainless steel. The corresponding maximum deflection in the steel was estimated to be 0.4 mm.

Outer Radial Supports

Similar assumptions and calculations were performed for the outer radial supports. In this instance, the angle relative to the beam is 38.5°. The span between the front and back plates is 39.9 cm, and the maximum stress and deflection is expected to occur at the 6 o'clock position. The load of 408 kg was again assumed to be carried normal to the outer radial support (considered to be a beam). This is conservative since the support is 38.5° to the horizontal. In reality 88% (cos 38.5°) of the load is normal to the beam, with the remainder generating tension parallel with the beam. A 6.4-mm-thick outer radial support gives a maximum stress near 93.77 MPa, which is too high for aluminum. For Type 304 stainless steel outer radius supports, the maximum deflection was calculated to be 0.74 mm.

180° Assembly Back Plate

The geometry of the back plate for the 180° assembly was approximated by a rectangular plate. A particular concern was the stress in the back plate under gravitational loading from the lead and scintillator as the assembly is lifted from a horizontal position to a vertical mounting orientation. For this study, the back plate was uniformly loaded (12,245 kg) and was simply supported on two edges, being free on the other two sides. The estimated stress was quite low (~6.895 MPa) for a 22.2-mm-thick back plate. However, very sizable maximum deflections (~2–3 cm) were computed, even with a Type 304 stainless steel back plate. As a consequence, reinforcing steel channel welded to the back plate on the side away from the lead and scintillator was included in the conceptual design. An alternative possibility is the use of a significantly thicker back plate of aluminum. For example, a 51-mm-thick aluminum plate would reduce the deflection by approximately a factor of four. It is also noted that these large deflections only occur when the assembly is being rotated to the vertical. Thus, a specially reinforced support for the endcap assembly could be designed that would not be permanently attached to the endcap. This type of temporary support might reduce the total cost for the endcap EMC.

180° Assembly End Plates and Internal Lead Radial Supports

The total gravitational load on the 180° assembly end plates was determined to be 2041 kg. This load was applied uniformly, although in reality it would vary linearly with

position. The maximum stress and deflection would be expected for the end plates located at 3 and 9 o'clock for the upper 180° endcap assembly. The end plate was assumed to be fixed to the front and back plates and free on the other two sides. The maximum stress and deflection for 4.3-mm Type 304 stainless steel end plates were estimated to be ~119.28 MPa and 0.9 mm, respectively. Smaller deflections and stresses would be present for the internal lead radial supports, leading to the possibility of different thicknesses, depending on the location within the 180° endcap assembly.

Finite Element Calculations

A finite element model of one-quarter of the endcap EMC was made to evaluate stresses and deflections in more detail for the case when the calorimeter is mounted on the magnet pole tip. Plate elements were used to represent all structural members. The upper and lower 180° endcap assemblies were studied separately by changing the gravitational loading on the model. All structural members except the front plate were assumed to be Type 304 nonmagnetic stainless steel. The thicknesses were initially chosen based on the analytical calculations. The inner and outer radial supports were 9.5 mm and 6.4 mm, and the ends and lead radial supports were 4.2 mm. Each of these items was assumed to be fixed to both the back stainless steel plate of thickness 22.2 mm and to the front aluminum plate of thickness 12.7 mm, but no connections were assumed between any other pair of elements. In particular, the individual inner radial supports were not connected in order to allow fibers to exit from the endcap assembly.

Gravitational loads were taken to be uniform across the various supports. The loads for each 30° section (≅2041 kg) were split, depending on the horizontal projection of the support areas. For example, for the bottom 30° region, the loading was assumed uniform on the outer radial support. Also, the top 30° region has approximately 65% or 1332 kg on the radial lead supports, and the remaining 35% or 709 kg on the inner radial support. The lead radial supports at the 6 and 12 o'clock positions were constrained to remain in the vertical plane.

The estimated stresses from the finite element calculations for the bottom 180° endcap assembly were less than 75.85 MPa everywhere, with the largest stress occurring at the outer radius of one of the radial lead supports (Fig. 4D-13). The maximum deflection was 0.8 mm at the outer edge of the first radial lead support down from the horizontal.

For the top 180° assembly, the stresses on the front plate and the inner and outer radial supports were all estimated from the finite element calculations to be less than 34.48 MPa. The largest estimated stresses were for the end plates at the 3 and 9 o'clock positions, where the gravitational loading from the lead and scintillator would be expected to be the largest. Different element meshes were used for these end plates in an attempt to obtain an accurate stress determination. The estimated maximum stress was computed to be over 137.9 MPa for 4.2-mm-thick end plates. The maximum deflection was approximately independent of the element mesh and was 1.2 mm. For final runs, the two end plates were increased in thickness from 4.2 mm to 4.75 mm in order to reduce the stresses. With the finest mesh above, the maximum stress in the thicker ends was 110.32 MPa, and the maximum deflection was 0.9 mm.

Cross checks of the finite element and the analytical calculations were also performed. The maximum stress and deflection for the top inner radial support (at the 12 o'clock position) from the finite element model were 29.65 MPa and 0.1 mm respectively. For the analytical calculation, the inner radial support was assumed to be fixed to rigid front and back plates with a separation distance of 33 cm, but to be free at the sides to allow the optical fibers to exit the calorimeter. Since the support is 15.4° to the horizontal, 96% (cos 15.4°) of the load is normal to

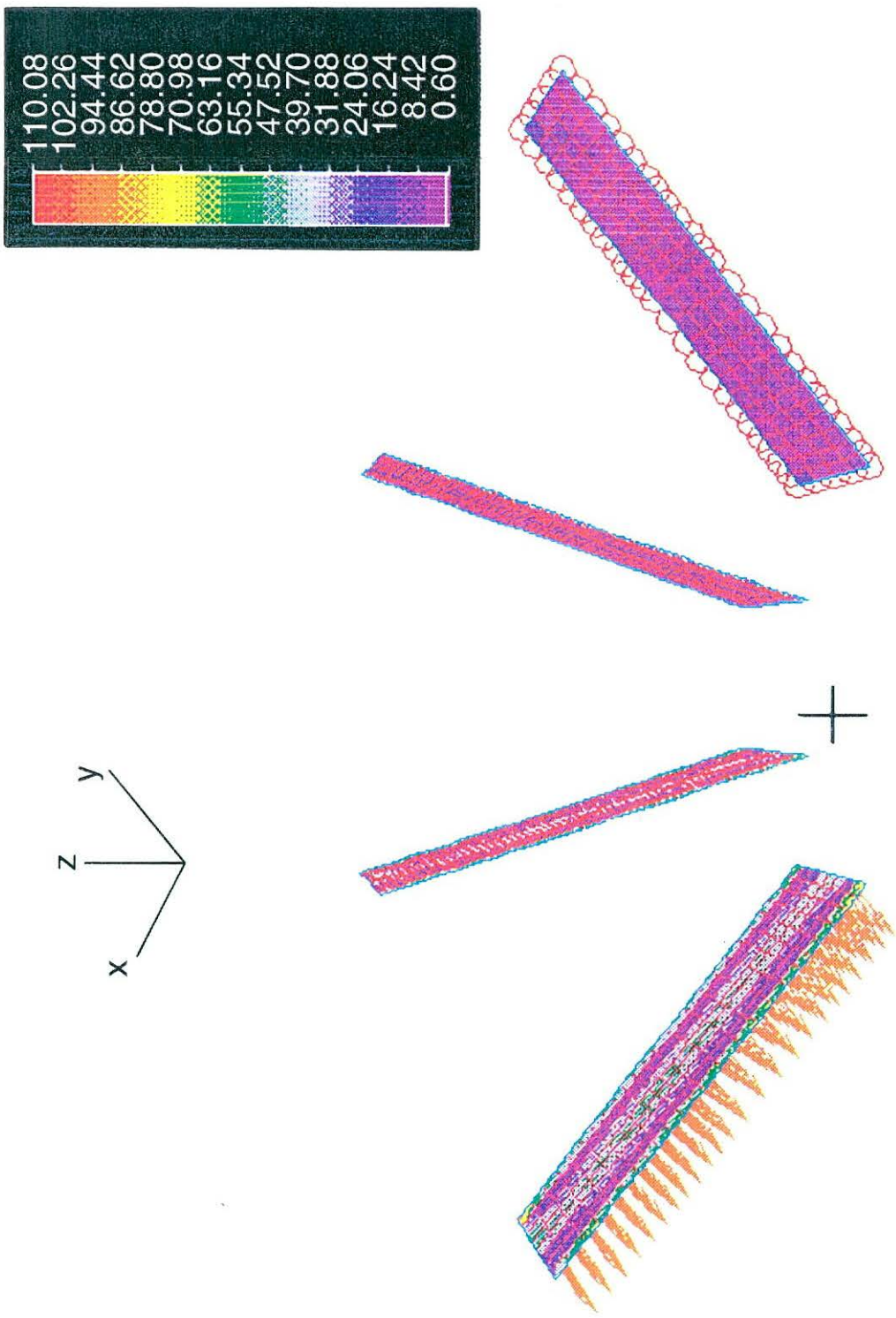

Figure 4D-13. A finite element analysis showing the stresses in the radial lead supports. The assumed loading of the 30° sections is discussed in the text. The largest stress occurs at the outer radius of one of the radial lead supports.

the beam, with the remainder generating tension parallel with the beam. The total gravitational load on the five inner radial supports is 709 kg, and the computed stress and deflection are 40.0 MPa and 0.13 mm, respectively.

The maximum stress and deflection for the bottom outer radial support (at the 6 o'clock position) were 59.30 MPa and 0.4 mm, respectively. Similar assumptions and analytical calculations were performed for the outer radial supports. The angle relative to the beam in this case is 38.3°, and the span between the front and back plates is 39.9 cm. A load of (2041 kg) × (cos 38.3°) was applied normal to the outer radial support. The computed maximum stress and deflection were 73.78 MPa and 0.58 mm respectively. When the original element mesh for the outer radial support at the 6 o'clock position of 2 × 8 plate elements was subdivided to 4 × 16 and 8 × 32 elements, the computed stress increased to 67.57 and 72.40 MPa, respectively. These values are much closer to the analytical estimate. These results suggest further work is needed in the preliminary design to estimate the stresses more accurately. The basic endcap conceptual design is still thought to be adequate, however.

Additional calculations were performed to test the feasibility of a 51-mm-thick aluminum back plate instead of the thinner stainless steel back plate. The stresses are within acceptable limits, and the maximum calculated deflection was 0.8 mm. These results indicate that the thick aluminum back plate is a viable option for the endcap EMC design. The cost and weight for the aluminum would be expected to be less than for the stainless steel back plate.

4.D.3. Optical System

The optical system for the endcap calorimeter is similar to that for the barrel EMC. The primary differences are related to the geometry which must be accommodated. In particular, the scintillator tiles to be used will be smaller and trapezoidal in shape. In addition, due to concern over the gaps in coverage that would be created by the amount of space required to couple fibers to the edge of the scintillator tiles, fibers will be constrained to lie in a straight groove cut into the surface of each scintillator (Fig. 4D-14). They will subsequently be routed out of the active region of the calorimeter, by traversing the surface of neighboring scintillators, passing through a space created by the introduction of "z brackets." The fibers will finally exit the calorimeter at the inner and outer circumference of the module, with ~60% leaving the body of the calorimeter at $\eta = 1$ and ~40% leaving at $\eta = 2$.

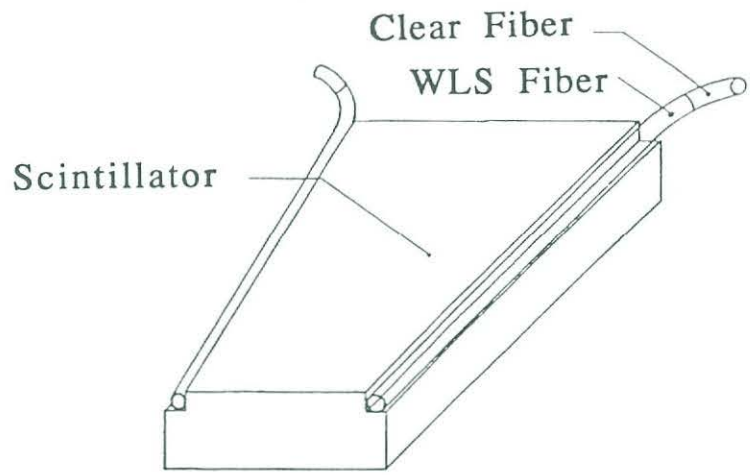

Figure 4D-14. A schematic drawing showing the coupling of the wavelength shifting fibers to the trapezoidal-shaped scintillator tiles in the endcap electromagnetic calorimeter. Due to considerations of space, the fibers are constrained to lie in straight grooves cut along the edge of the tiles.

The present design incorporates straight grooves cut into the face of each scintillator tile in order to couple the optical fibers to the plastic. The use of a straight groove should reduce the cost of machining compared to that for a loop-shaped groove as was used in the CDF endcap upgrade.

Similar considerations for the endcap shower maximum detector may drive the final choice of technology. There is room on the exterior of the magnet pole piece for the photomultipliers of the endcap towers, but not for the relatively large number (~7,000) that would be required if the shower maximum detector is constructed of scintillator strips coupled to individual photomultipliers. Moreover, for this option, the per channel cost of providing high voltage and high voltage control is prohibitive. Multi-anode phototubes require much less space, but in general are expensive and have problems with channel-to-channel cross-talk and gain uniformity. Wire-strip MWPC technology is presently being considered as a possible solution to this problem.

4.D.4. Electronics

The electronics for the endcap EMC towers will be identical to those for the barrel EMC towers. It is preferable to use the same technology (wire-strip chambers or scintillator strips) for both the barrel and endcap shower maximum detectors as well, in which case, the electronics for this detector component would also be identical. One possible advantage of selecting a standard technology is that in the event there were insufficient electronics to fully instrument the shower maximum detectors in both the endcap and the barrel calorimeters, the existing electronics could be periodically moved to maximize the physics from the STAR detector during different running periods.

4.D.5. Calibration

The calibration system for the endcap and barrel EMC are expected to be identical. In particular, to calibrate the energy scale for the towers, radioactive source tubes will be routed radially from the inner to outer periphery of the endcap EMC at a depth corresponding to the location of the shower maximum detector.

4.D.6. Shower Maximum Detector

The purpose of the endcap shower maximum detector is to provide the spatial resolution necessary to measure inclusive direct-γ's and inclusive $W^{\pm}$ and Z° production. In general, for example, π^{o}s headed in the forward direction have a higher longitudinal momenta than those at mid-rapidity for a fixed p_t, and thus the minimum opening angle between the decay photons will be smaller. Hence, a more finely segmented detector is required for the endcap.

It is likely that the same technology will be chosen for both the barrel and endcap shower maximum detectors. In the event that only a limited number of electronics channels can be instrumented, this would allow moving the electronics to the area of most interest for a specific physics goal. Having the same technology also avoids the complications and development costs associated with supporting two different systems.

A CDF-style wire-strip detector (Fig. 4D-15) would probably give the finest segmentation for a fixed cost. The electron drift distance to the wire in the gas should be $\lesssim 3$ mm to be commensurate with the minimum crossing time of 110 ns envisioned for RHIC. If the same aluminum extrusions discussed in Section 4.C.6 were used for both the endcap and barrel,

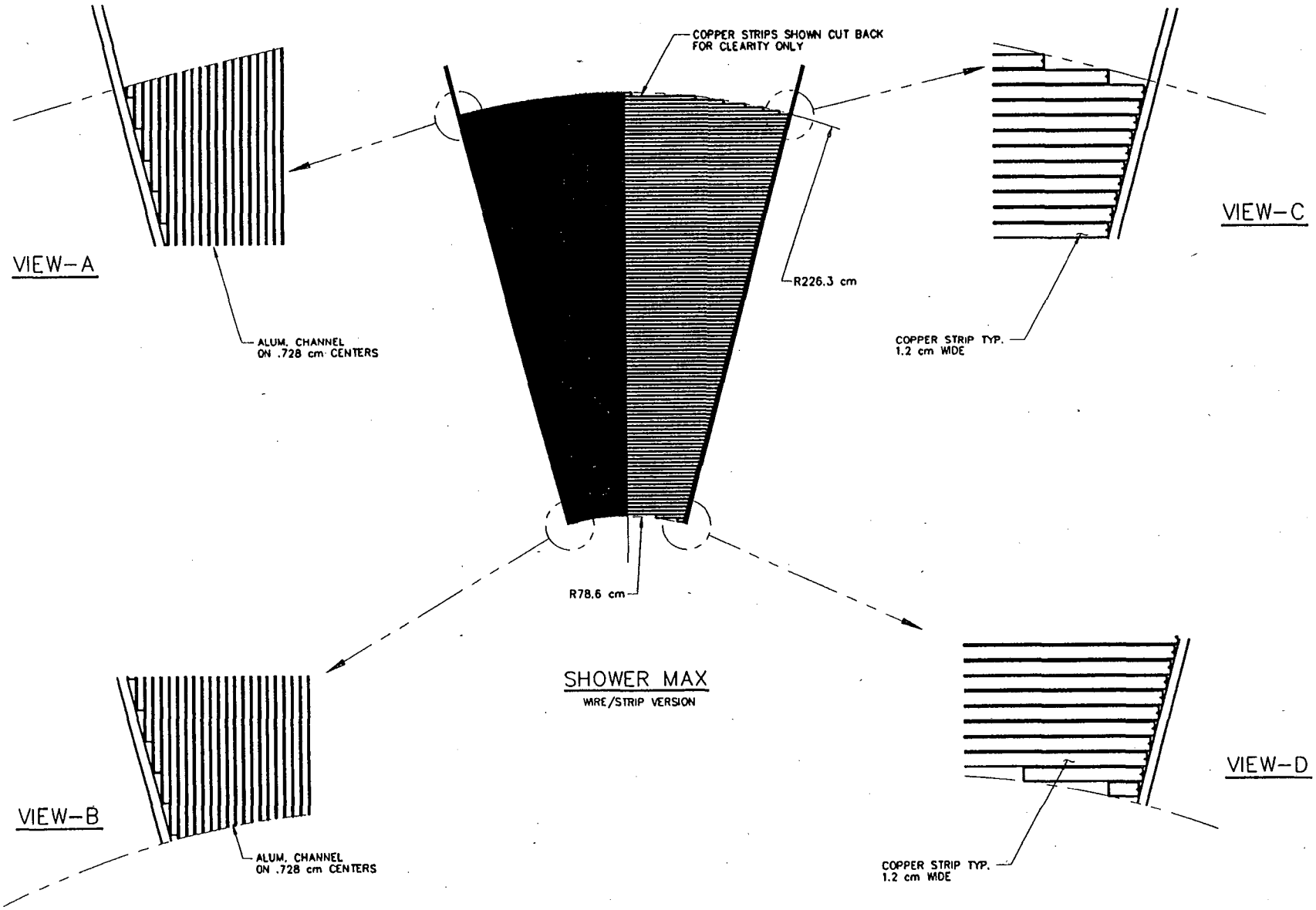

Figure 4D-15. A schematic view showing the layout of a CDF-style wire/strip shower maximum detector for the endcap electromagnetic calorimeter. The electron drift distance to the wire in the gas must be ≤3 mm to be commensurate with the minimum crossing time of 110 ns envisioned for RHIC. Aluminum extrusions similar to those discussed in Section 4.C.6 may be used for this application.

and each wire was instrumented individually in the endcap, this criterion could be met and the detector would be more finely segmented than in the barrel. Additional Monte Carlo simulations are required to understand how to optimize the performance of the endcap wire-strip chambers. As in the barrel, small insensitive regions for the high voltage blocking capacitors and current-limiting resistors will be located near the ends of the wires.

A scintillator strip shower maximum detector would reduce potential problems with rate limitations at the highest RHIC luminosities. However, there appears to be insufficient space for the ~7,500 individual photomultipliers required if standard PMTs are used. Multi-anode photomultipliers may be a solution to the problem with space. In this instance, there would be one fiber per pixel and the costs for photomultiplier tube bases and high voltage generation and control circuits would be considerably reduced. However, certain other problems generally experienced with multi-anode photomultipliers (cross-talk, channel-to-channel gain variations, etc.) would still need to be addressed.

As noted in Section 4.C.6, the choice of technology for the shower maximum detector has not yet been made.

4.D.7. Prototype and Test Beam Program

It is not anticipated that a dedicated prototype for the endcap EMC sections would be constructed, since the technology is quite close to the barrel EMC modules. However, various engineering models may need to be constructed to verify analytical and finite element calculations of stresses and deflections in the 180° endcap EMC sections.

4.D.8. Future Decisions/Schedule

Two technical decisions are required before proceeding to a full preliminary design of the endcap electromagnetic calorimeter. One decision is whether to use wire-strip chambers or scintillator strips for the construction of the endcap shower maximum detector. The other concerns the related electronics. These same issues were discussed for the barrel EMC in Section 4.C.8, and are closely coupled to similar decisions for the barrel shower maximum detector. Given the present design effort, choices concerning these technologies will be made in the fall of 1993.

The engineering models for the endcap EMC will be constructed in mid-1994, after the barrel EMC design effort is complete.

5.

Integration into STAR

5. INTEGRATION INTO STAR

5.A. Integration of the Mechanical Structure

A thin superconducting solenoidal magnet was originally planned for the STAR detector, as described in the STAR Conceptual Design Report (CDR).[1] The barrel EMC was to be mounted outside the magnet coil and inside iron bars or "backleg steel" used for the magnet flux return. This design had relatively little coupling of the requirements for the magnet and EMC. After the CDR was written, it was decided to use a conventional solenoidal magnet with aluminum coils, primarily on the basis of construction costs. In this configuration, the large thickness of coil material was expected to seriously degrade the calorimeter performance, so the coil was moved outside the EMC. In the process, the magnet and barrel calorimeter designs became much more closely coupled.

In order to lower costs for the baseline STAR detector, the magnet inner radius had to be minimized. Thus the space available for the barrel EMC was restricted. It was also decided that the solenoidal coil would be constructed of a number of coil pancakes to reduce manufacturing costs. As a consequence, the magnet became segmented along its length. Finally, it was considered essential to be able to install the EMC modules after the magnet, TPC, and barrel trigger scintillation counters were assembled, since the EMC is not part of the baseline STAR detector and its schedule for completion is unknown. Consequently, given the magnet and TPC geometry, the EMC modules must be installed from the ends of the STAR detector on "ways" or rails parallel to the solenoidal axis. The weight of the calorimeter and the restricted space led to the requirement of multiple supports for the ways along their length.

The solution adopted to support the calorimeter, allow installation of the EMC modules, and fit in the restricted space, is to incorporate nine equally spaced gaps of approximately 121 mm between magnet coil segments (Fig. 5A-1) and to transmit the light from the calorimeter scintillators to the photomultipliers with 1-mm-diameter optical fibers. In each gap there would be a 70-mm-thick aluminum ring attached to both the magnet flux return bars and the ways that serve as supports for the barrel calorimeter (Fig. 5A-2). The remaining space would allow routing of the optical fibers to the photomultipliers mounted on the outside of the magnet flux return bars. Geometrical constraints require small bending radii for the fibers ($\lesssim$30 mm), which in turn requires 1-mm-diameter fibers. The minimum bending radius of 1.5-mm-diameter fibers is much too large. These fibers could be routed around the ends of the barrel, but light attenuation effects would cause unacceptable degradation of the calorimeter energy resolution. Additionally, there would be problems with space limitations between the magnet end ring and poletip. Consequently, the optical fibers must be routed between the magnet coil segments and pulled through the gaps as the barrel EMC modules are installed. This process has been tested successfully for a simplified routing, using groups of fibers bundled together and enclosed in plastic tubing.

A number of analytical and finite element calculations have been performed in the process of deciding the magnet inner radius, the number and size of the gaps, and the dimensions and shape of the ways. For example, the deflection of a module at the 12 o'clock position under gravitational loading was studied for various numbers of rings supporting the modules and as a function of the dimensions of the strongback support. Specifically, for a 70-mm-thick by 200-mm-wide stainless steel strongback, the maximum deflection in the module for supports only at $\eta = 0$ and $\eta = 1$, is 5.3 mm. The corresponding deflection using nine

[1]The STAR Collaboration, The STAR Conceptual Design Report, LBL PUB-5347 (1992).

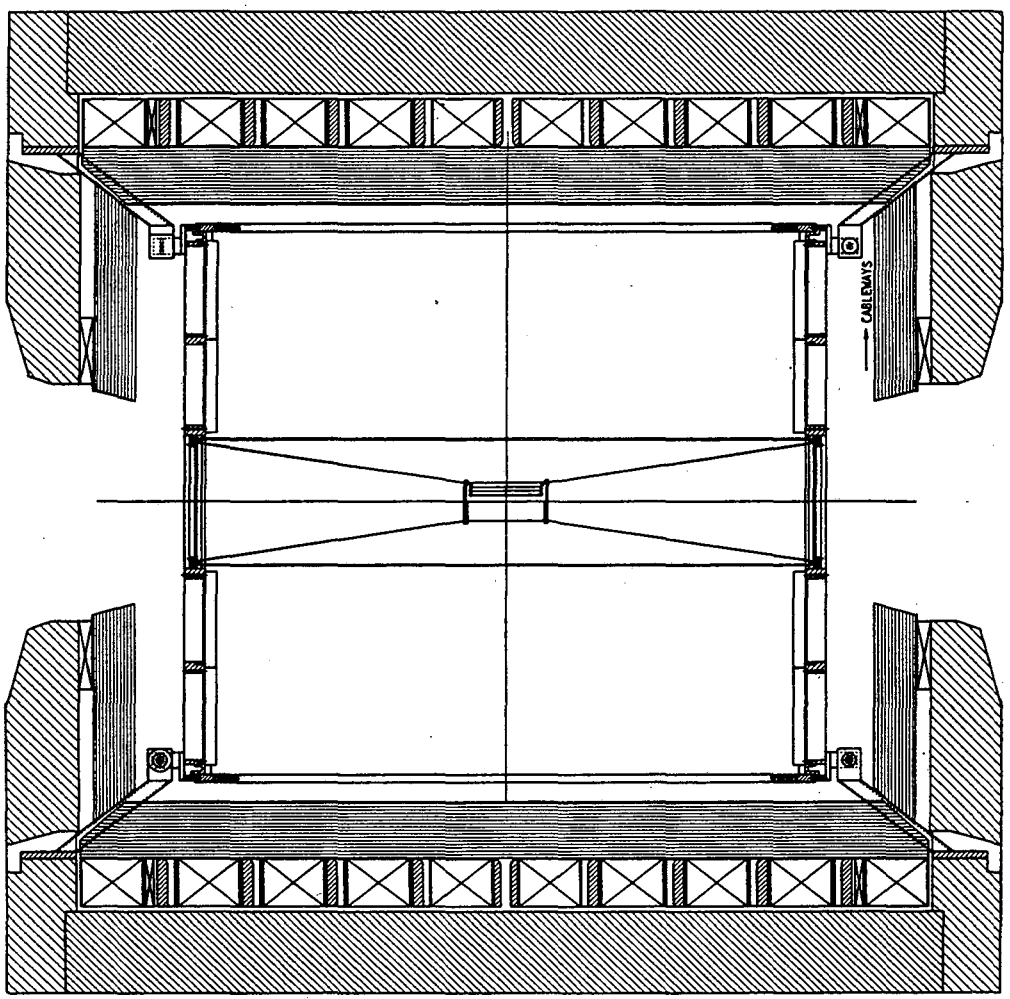

Figure 5A-1. A cross-sectional view of the STAR detector showing the location and arrangement of the TPC, SVT, EMC, and magnet return iron. The magnet coil is constructed of ten individual packages, each of which contains four two-conductor pancakes. There are nine equally spaced gaps of ~121 mm between the coil packages to allow optical fibers to transmit light from the EMC to photomultipliers on the exterior of the magnet return iron. Each gap also contains a 70-mm-thick aluminum ring attached to both the magnet flux return bars and the ways that serve as support for the barrel calorimeter.

aluminum rings to which the strongback is fixed is 0.01 mm. In the former case, the large deflection would require sizeable gaps between adjacent modules, significantly degrading the calorimeter performance. Finite element calculations of a number of key and way shapes and sizes indicated that stresses could be kept low ($\lesssim$68.95 MPa) for a strongback of 70-mm radial dimension and trapezoidal/dovetail, "L," or "T" shaped ways. For the conceptual design, a single dovetail way is planned for each module, with a height of 35 mm, and minimum and maximum widths of 70 and 100 mm respectively. Figure 5A-3 shows the stresses in this way/strongback from the finite element calculation.

Calculations were also performed for the rings.[2] It was demonstrated that if the gravitational loading in the rings resulted in deflections greater than 10 mm, the clearance

[2]T. Fornek *et al.*, "Calculations on the STAR Conventional Magnet Design," STAR Note No. 115.

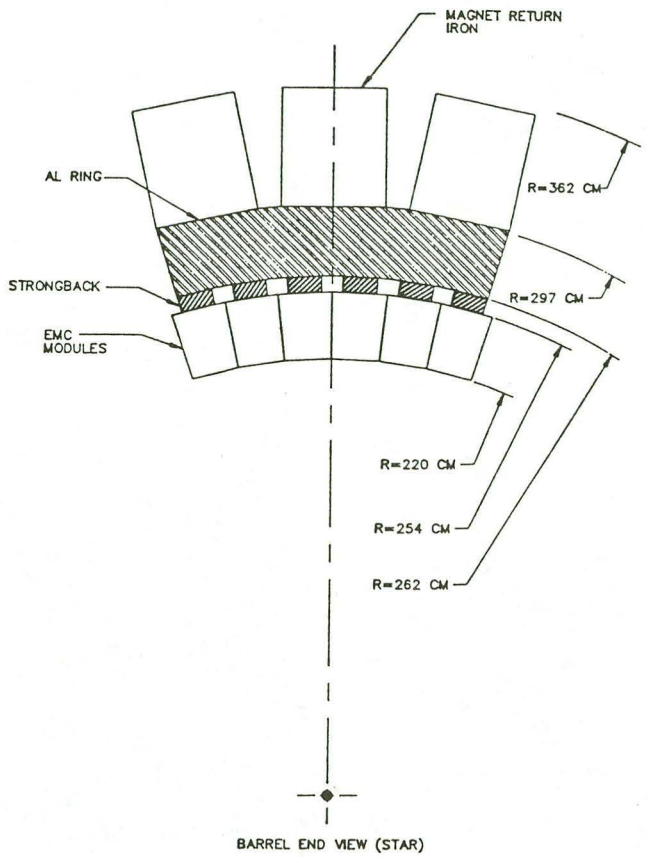

Figure 5A-2. An end view of several modules of the EMC barrel showing the location and arrangement of the aluminum ring and strongback supports.

between modules would need to increase by approximately 1 mm. This was considered an upper limit, since noninstrumented gaps between modules reduce the calorimeter performance because particles cannot be detected in the gaps. The method of supporting the rings was also studied. Both finite element and analytical calculations indicated that stresses were acceptable for 76-mm-thick aluminum or stainless steel rings, but that maximum deflections exceeded 10 mm when the rings were supported at the bottom only. If the rings are supported from each of the magnet flux return bars, stresses and deflections in the bars and the rings are estimated to be small ($\lesssim$8.96 MPa and $\lesssim$0.5 mm), including the effects of gravitational loads from the bars, aluminum rings, and barrel electromagnetic calorimeter. Various concepts are presently being considered to attach the rings to the magnet flux return bars and to fabricate the aluminum rings inexpensively.

A conceptual design for the installation fixture is shown in Figs. 5A-4 and 5A-5. A module would first be attached to the way on the fixture and then rotated into the desired orientation for installation. After moving the fixture and module to the desired location with the overhead crane, the fixture would be bolted to the magnet iron end ring. A short section of the trapezoidal way would be inserted between the barrel and the fixture ways, and final adjustments would be made to the relative alignment. Then the module would be pushed into position with a hand-operated drivescrew mechanism. Binding of the module would be sensed easily and the problem corrected before damaging either the module or the way. Figure 5A-5 shows the temporary section of way being installed near the top of the barrel.

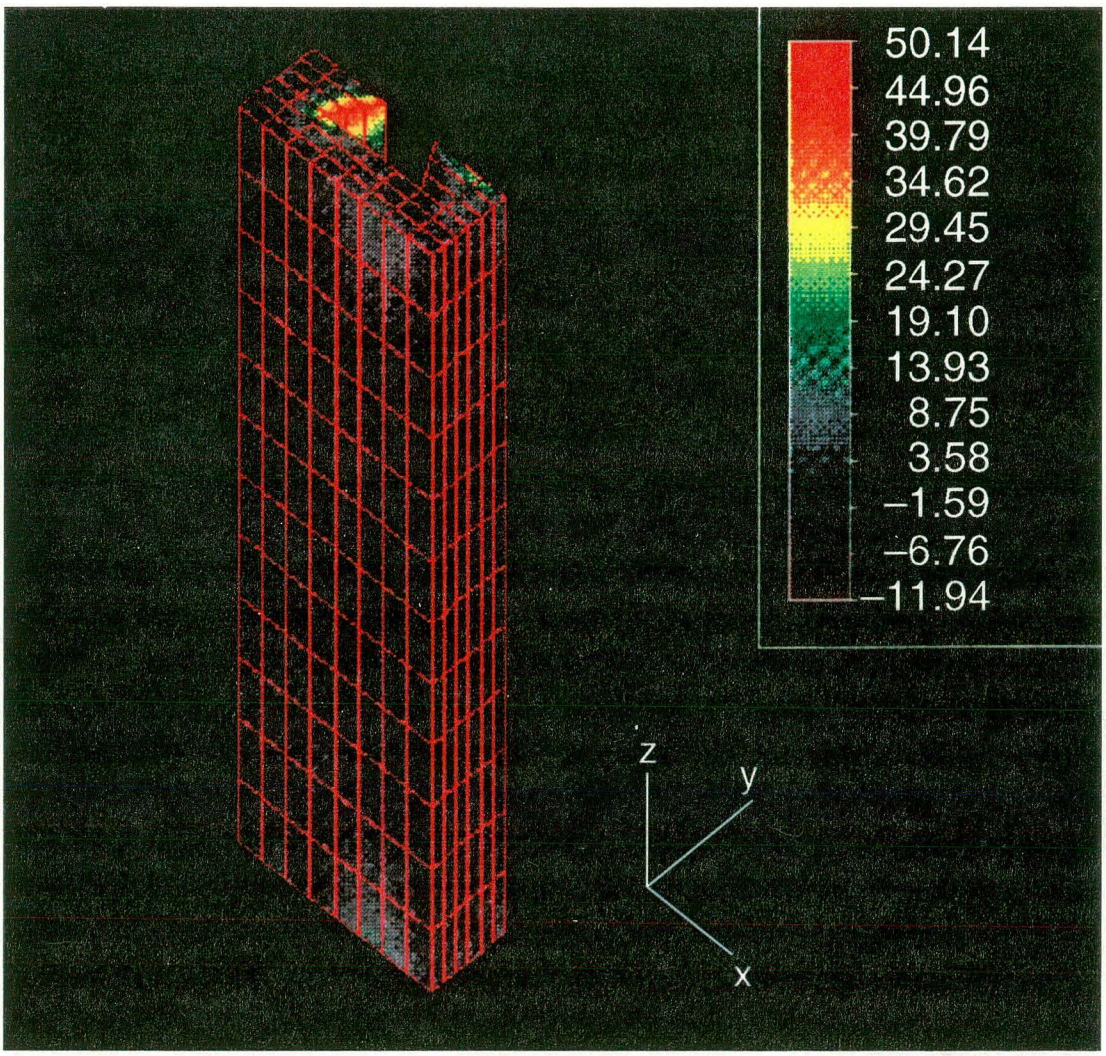

Figure 5A-3. The results of a finite element calculation showing the stresses in a strongback support for one of the EMC barrel calorimeter modules under gravitational loading. For this calculation, the strongback is assumed to be supported at nine locations along its length, corresponding to the nine aluminum rings located in the gaps between the coil packages for the STAR magnet. The units of stress are MPa.

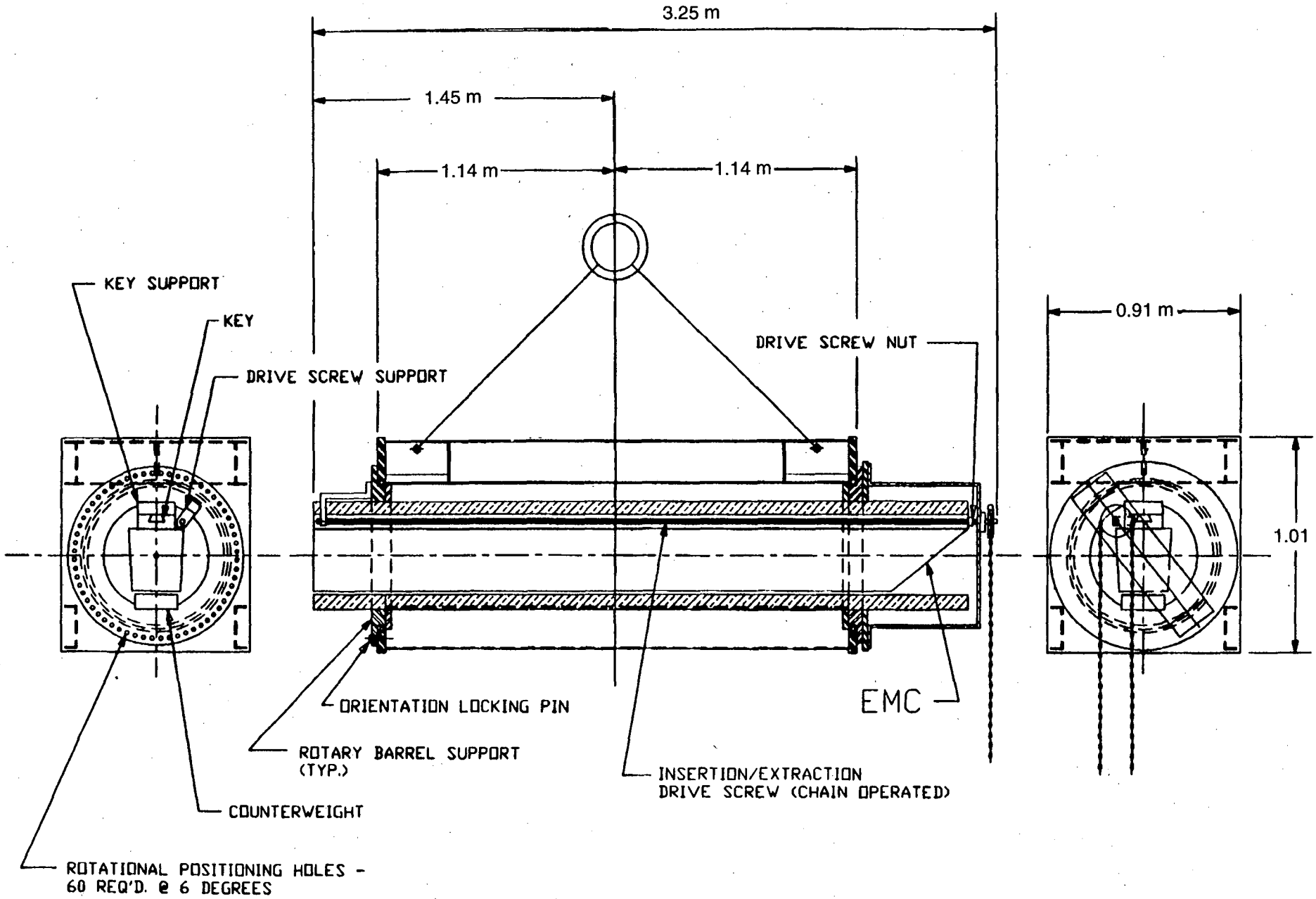

Figure 5A-4. The installation fixture used to insert modules of the EMC barrel.

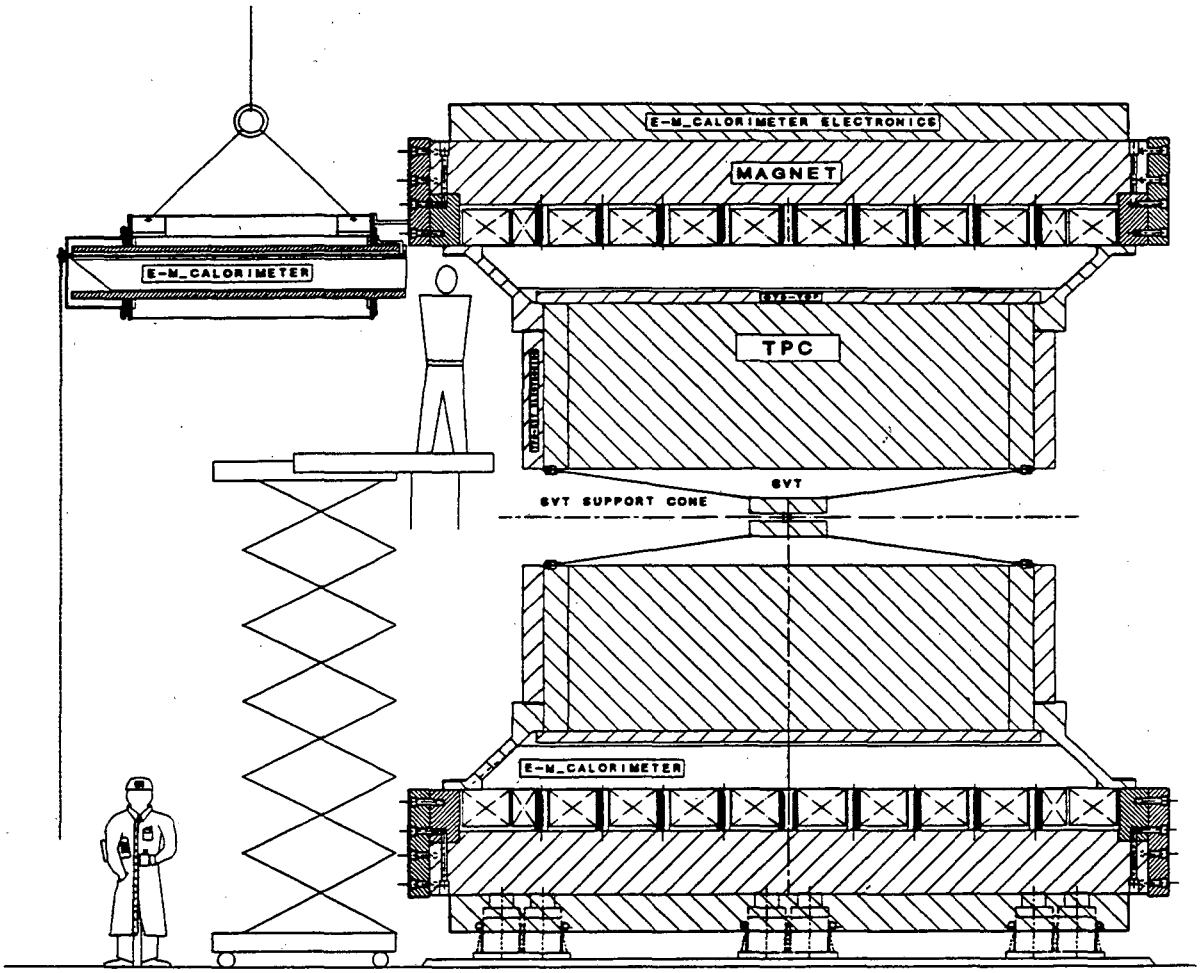

Figure 5A-5. A module of the barrel EMC being installed in the STAR detector. The module would first be inserted onto the temporary way of the fixture and then put in the proper position using the overhead crane. Upon being placed in the correct orientation using a counterbalance, the EMC module would be pushed onto the permanent way using a hand-operated, drivescrew mechanism. Alignment would be maintained during insertion by bolting the temporary way to the face of the magnet end ring.

Four or eight special barrel calorimeter modules will need to be constructed for locations near the TPC supports. These supports are planned to mount to the magnet iron end rings, interfering with the installation of some modules. Hence, either these special modules will need to be in place before the TPC is installed, or the TPC will have to be removed when the special modules are installed. These modules will probably be one tower in eta shorter than the rest of the barrel EMC modules.

The photomultipliers for the towers, and perhaps also those for the shower maximum detector, will be mounted inside iron boxes used for magnetic shielding on the outside of the magnet flux return bars. All the photomultipliers can fit radially on the surface area of the bars. However, on the bottom of the barrel, there will be interference with the major supports for the STAR detector. For one bar on the side, there will be interference with water cooling lines for the conventional solenoidal magnet coils. Finally, on the top of the barrel, the iron boxes may

interfere with the overhead door into the experimental hall. Special locations for the photomultipliers affected by these interferences will be arranged as necessary.

The endcap calorimeter 180° sections will mount to the inner face of the magnet poletip. The iron boxes containing the endcap photomultipliers will mount to the corresponding outside surface. The conceptual design for the mounting of the sections includes blocks bolted to the poletip, with pins and screws into brackets on the back plate of the endcap EMC sections (Fig. 5A-6). The blocks cannot be welded because of possible distortions of the poletip and resulting changes to the desired magnetic field configuration. A special fixture may be needed to raise the sections from the horizontal to the vertical in order to prevent large deflections; this depends on the type and reinforcing of the endcap back plate. Details of the iron boxes for magnetic shielding of the endcap photomultipliers will depend on the location and sizes of the magnet poletip supports.

The endcap EMC sections as well as the barrel EMC modules could be installed in the experimental hall without removing the accelerator beam pipe, or in the assembly building (Fig. 5A-7). It is presently thought that RHIC will be shut down for several months each year for maintenance. It is possible therefore that even if the calorimeter elements are not ready at the start of RHIC operations, they could be installed in either the assembly hall or the experimental hall during such a period.

5.B. Facility Requirements

The primary requirements placed upon RHIC and the Wide Angle Hall (WAH) in which the STAR detector will be located concern the availability of power and space. The space required for the mechanical support of the barrel and endcap calorimeters has already been discussed. In addition, however, there will be a need for space for electronics racks containing, for example, optical or ECL receiver cards and trigger electronics. Ideally, this space would be

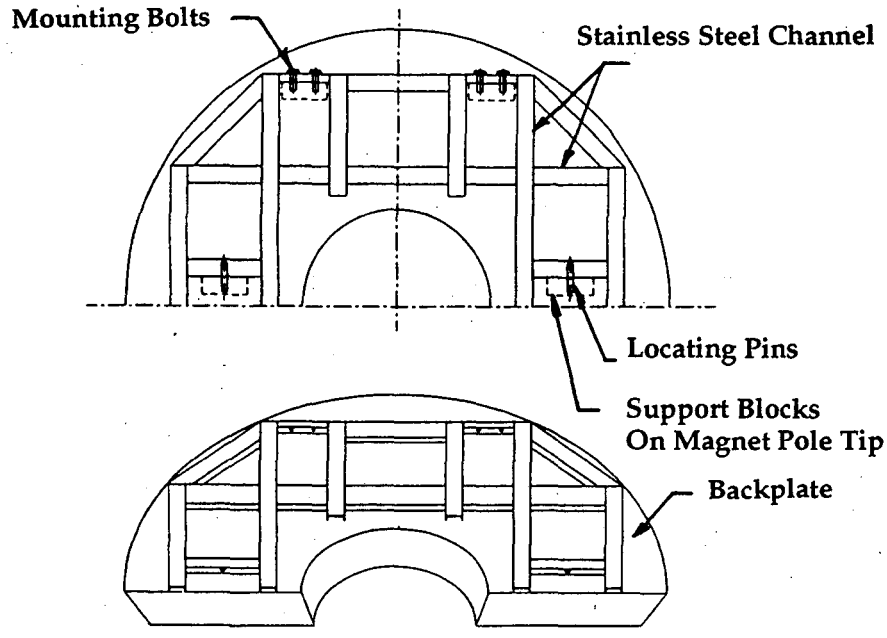

Figure 5A-6. A perspective view showing the location and arrangement of the mounting brackets for one of the four 180° endcap EMC modules.

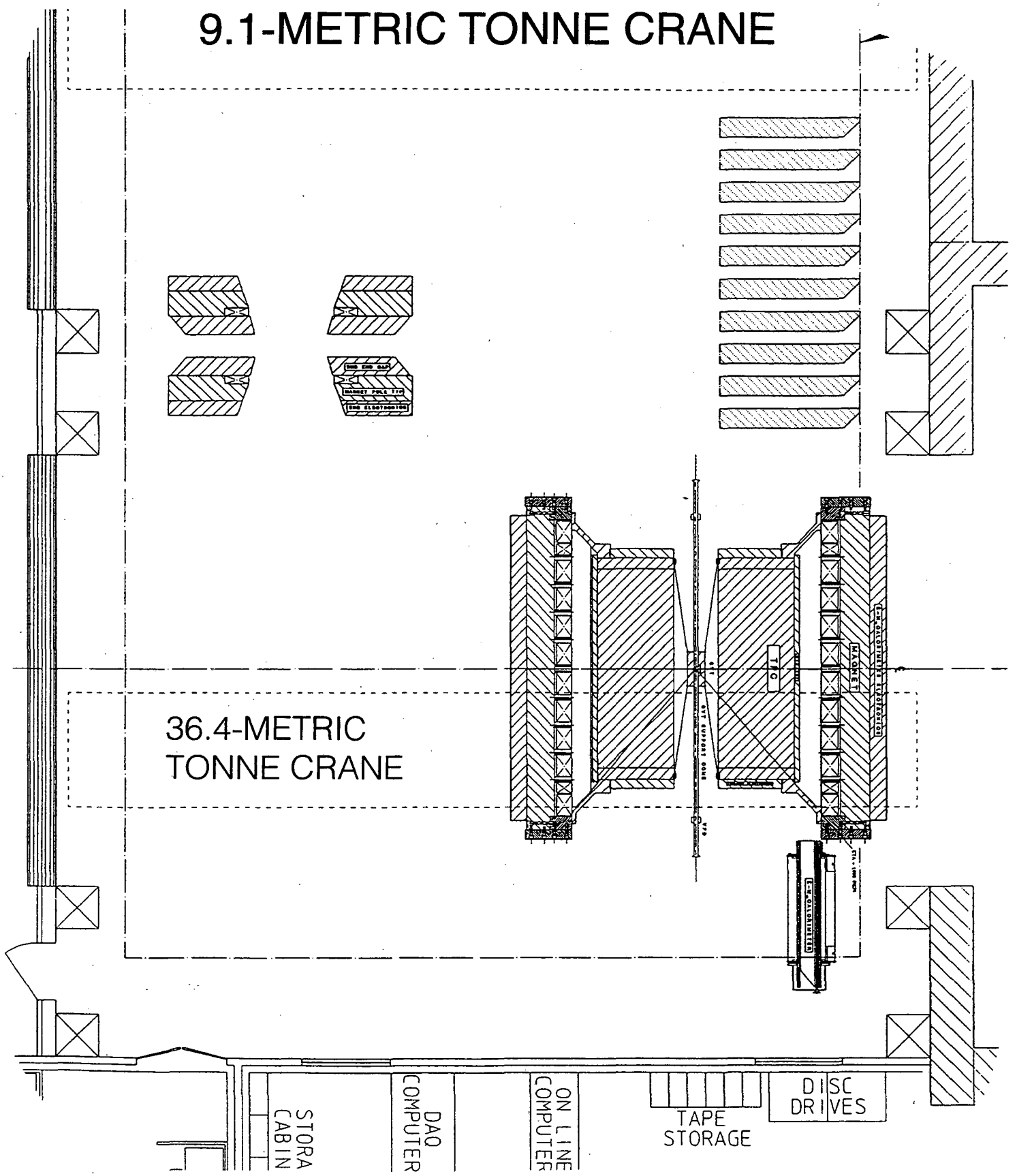

Figure 5A-7. A plan view showing the installation of modules of the barrel electromagnetic calorimeter in the STAR assembly hall.

allocated on the electronics cart for STAR which is shielded from radiation during normal RHIC operations and therefore accessible. The space available in this location has recently been reduced, however, due to the need for thicker shielding. Consequently, as the design for this aspect of the calorimeter project matures, a second option that will be considered is placing all EMC electronics on or near the detector. As discussed in Section 4.C.4, it is already planned that the photomultipliers, photomultiplier bases, and components necessary for high voltage generation and distribution will be located on the detector. The electronics for digitization are also envisioned to reside in this location. The question that remains is whether to locate the trigger electronics away from the detector and send digitized information to this component from a remote location or whether to locate the trigger electronics on the detector as well. This decision will be made by fall of 1993.

The power requirements for the EMC are indicated in Table 5B-1, along with the corresponding channel counts for various implementations of the calorimeter. The total power reserve requested by STAR for upgrade detectors is 250 KVA. As noted in Table 5B-1, although the total power required by the full calorimeter system is ~80 KVA, it is well within the requested reserve.

Table 5B-1. Estimated Power Requirements for Components of the Barrel and Endcap Calorimeters.

Detector	Channels	Power Required
Barrel EMC	300	2.4 KVA
Barrel EMC upgrade	4,500	36.0 KVA
Barrel SMD	30,000 wires/pads	8.0 KVA
Endcap EMC	720	5.8 KVA
Endcap SMD	13,000 wires/pads	4.0 KVA
VME crates	6	9.0 KVA
Power supplies		13.0 KVA

5.C. Safety and Environmental Protection Issues

The safety issues related to the STAR EMC are the same as for many other components of the STAR detector and do not constitute any special or high-hazard concerns. All components of the STAR EMC will conform to all applicable RHIC/BNL safety standards. Some typical areas in which normal standards would apply are discussed below. They include access control, fire protection, laser safety, and electrical and mechanical hazards. An internal STAR Safety Committee will review all systems from initial design to final operation to ensure that the system conforms to all applicable safety standards. Inspection of systems that have been disassembled for repair is required prior to operation in order to ensure that the safety-related components are fully functional.

5.C.1. Shielding and Access Control

During the operation of RHIC, the main components of the STAR EMC will be inaccessible. These include the EMC mechanical structure, the light-transmitting fibers, and the transducers used for readout. The photomultiplier tube (PMT) bases used for high-voltage generation and the flash ADC system used for digitization will also be located on the detector

and will also be inaccessible during normal operation. Occasional access for periods of short duration may be possible depending upon the maintenance and fill schedules for RHIC. During these periods, it is envisioned that minor repairs to components that are normally inaccessible might be made (e.g., phototube replacement). Personnel making such repairs would be familiar with and proceed according to all BNL/RHIC safety procedures relating to radiation, electrical, magnetic safety, and possible suffocation hazards. Access to the experimental area under these circumstances would be in accordance with established RHIC/BNL procedures.

During operation, there must be access to an area as close to the detector as possible. Presently,[3] there is a plan to build a shielded room for electronic racks that reaches from a few meters from the detector to the outside of the interaction hall (e.g., Fig. 5C-1). Exact distances from the detector and the shield-wall requirements will be determined by RHIC in accordance with RHIC/BNL radiation safety requirements. Electronics components necessary for the first-, second-, and third-level triggers generated from information provided by the electromagnetic calorimeter will be located in this shielded room. It is presently envisioned that access to this

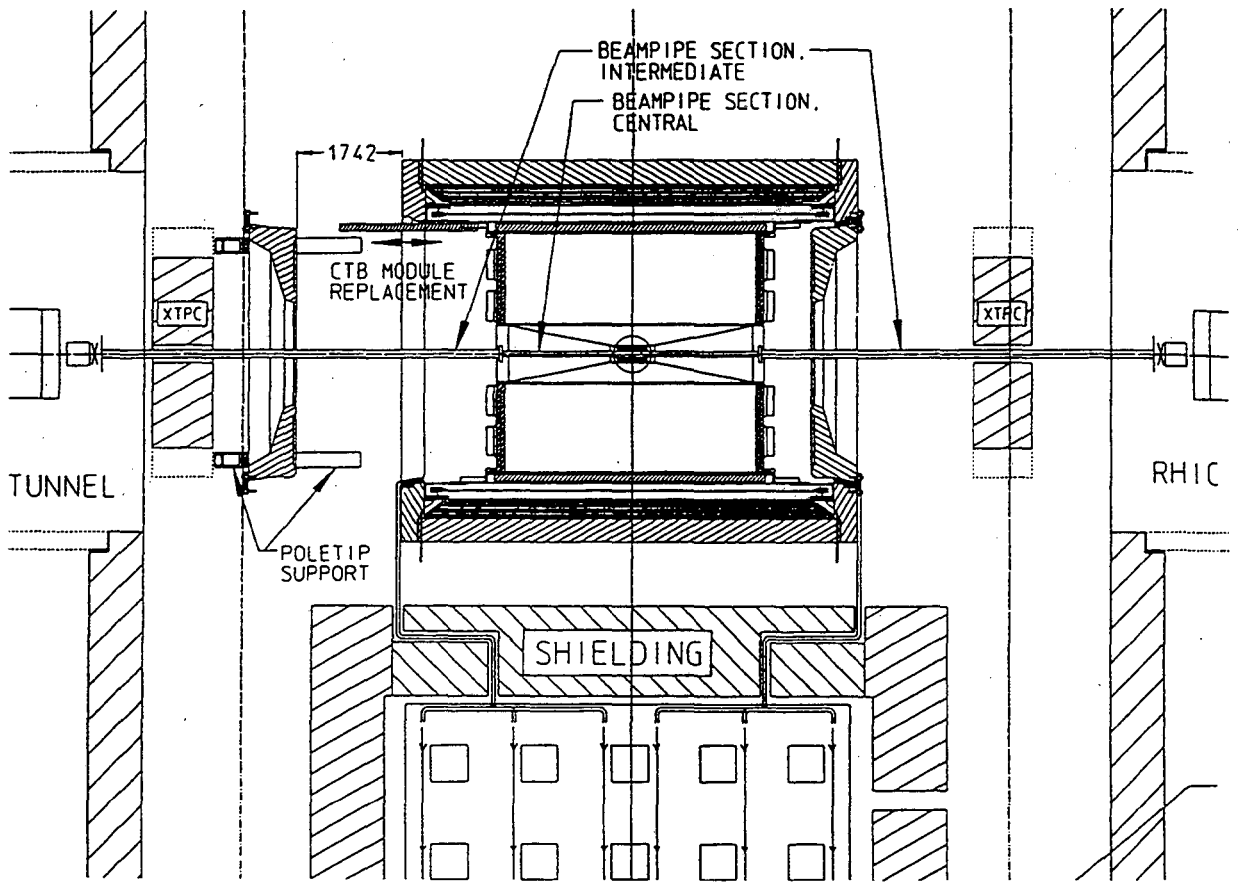

Figure 5C-1. A plan view of the STAR detector in the Wide Angle Hall during RHIC operation. A shielded room extending from a few meters from the detector to outside the interaction hall will allow access to essential components during run periods.

[3]Since the time of this writing, the size of the shielded room has been greatly reduced due to the thickness of concrete required for radiation safety. It is presently thought that most electronics will be located on a platform which moves with the detector but is not accessible during periods when the beam is in operation.

area will not be restricted during normal RHIC operation, although the monitoring of personnel for exposure to radiation in accordance with RHIC/BNL safety procedures will be required.

All other areas that are to be occupied during operation meet the standards for a low-radiation environment.

5.C.2. Hazardous Materials and Systems

Fire Protection

The main mechanical structures of the barrel and endcap electromagnetic calorimeters are constructed of aluminum. These structures support alternating layers of lead absorber and polystyrene scintillator that are effectively enclosed completely within an aluminum light-tight barrier. Small (1.0-mm) optical fibers connect the enclosed scintillator tiles via pathways through the magnet coils and the magnet return steel to photomultiplier tubes located in magnetically shielded boxes attached to the exterior surface of the magnet return steel.

There are no sources of ignition in the interior components of the barrel and endcap electromagnetic calorimeters. Therefore, the primary fire-safety concern for these structures is the possibility of the enclosed polystyrene scintillator acting as a source of fuel in the event of an external fire. An additional concern is that the EMC structure contains lead, which could represent a possible contamination hazard if a fire in this structure were extinguished with water. A preliminary analysis indicates that these concerns are addressed both by isolating these elements in the enclosed mechanical structure of the calorimeter and by the fire-prevention system planned for the interior of the STAR detector. Since the interior region of the detector will be enclosed to provide a controlled environment and will not be occupied during operation, it will be filled with dry nitrogen gas supplied from a liquid source. It is assumed that the system used to fill the central detector with nitrogen gas will require a small modification to the environmental-control system. This area will require oxygen-deficiency hazard (ODH) monitors and alarms, and an access procedure that utilizes the information provided by these elements. Final evaluation of fire safety for these components will be made by STAR and RHIC/BNL safety personnel to certify that the interior calorimeter components meet all applicable RHIC/BNL material and fire-safety standards.

Optical fibers traversing the magnet coils to the exterior of the detector will be enclosed in an approved fire-retardant jacket or sleeve. The average temperature of the environment through which the fibers pass will be ~75°F under normal conditions to ensure the long-term optical integrity of the fibers.

Low-voltage power (20 V) will be cabled into the magnetically shielded boxes on the exterior of the return steel to generate the high voltage necessary for the photomultipliers used for readout (see Section 4.C.4). The power supplies used to generate low-voltage power will be appropriately fused to eliminate the possibility of ignition as a result of an accidental short circuit.

Presently existing requirements of the BNL ES&H fire-safety standards will be incorporated into all aspects of the design of EMC components, and any additional requirements of the RHIC Safety and Environmental Administrative Policy and Procedures Manual (SEAPPM) will be satisfied. This area will be supervised by a senior member of the BNL staff associated with STAR.

Lasers and Radioactive Sources

At least one laser will be used for calibration and monitoring of light output. The laser will be supervised by a senior member of the collaboration, and its optical path will be totally enclosed. The laser system will be operated in accordance with the BNL ES&H standards and the RHIC SEAPPM.

There will be radioactive sources used for calibration, monitoring, and setup purposes throughout the experiment. Many of these will be installed into individual detectors and will be supervised by a senior collaborator. General-use sources will be secured in an approved storage area when not in use, and handling of sources will be supervised by the STAR safety coordinator.

5.C.3. Cryogenics

Cryogenic Fluids

There are no cryogenic systems incorporated in the design of the STAR electromagnetic calorimeter and no cryogenic hazards from other STAR components near the location of any EMC component.

Several hundred liters of liquid argon and nitrogen will be used in the TPC gas supply system and for fire protection. These supplies will be located next to a remote gas-mixing area and will be supervised by a senior member of the BNL staff associated with STAR in accordance with the applicable RHIC/BNL safety codes.

5.C.4. High Voltage/ High Current Power

Electrical Hazards

Several low-voltage, high-current supplies will be used to power the EMC electronics located in magnetically shielded boxes attached to the exterior surface of the magnet return iron. The output of these supplies will be distributed to many individual circuit boards. These supplies will include fuses or other devices that will limit the current in each lead to a safe operating range. All high-current conductors will be insulated independent of voltage to prevent accidental contact with other conductive surfaces.

High voltage for use by the photomultipliers employed for optical readout will be generated locally inside individual photomultiplier bases via the Cockroft-Walton technique (see Section 4.C.4). The design of the PMT bases will incorporate appropriate shielding to eliminate the possibility of accidental contact with other electronics or conductors in proximity and will include appropriate safeguards to eliminate possible shock hazards.

All electrical systems will be designed, built, and operated in accordance with NEC and BNL ES&H standards and RHIC SEAPPM.

5.C.5. Mechanical Hazards

The major mechanical hazards are associated with heavy objects. It is required that people who handle them be properly trained and certified to operate equipment with the required rating.

6.

Cost, Schedule, Manpower, and Funding

6. COST, SCHEDULE, MANPOWER, AND FUNDING

6.A. Detector Scope

The detector configuration necessary in order to accomplish all the physics goals encompassed in this report includes the following:

- Full EMC barrel
- One endcap calorimeter
- Shower maximum detector

In nucleus-nucleus collisions, the barrel calorimeter provides the means to measure the neutral transverse electromagnetic energy. In addition to affording a more detailed understanding of the transfer of energy from the projectile frame to midrapidity, the improved resolution in determining the total transverse energy deposition will allow the creation of highly selective triggers in order to search for rare events predicted to result if a color deconfined plasma of quarks and gluons is produced. Since both the coverage of the barrel calorimeter and measurement of the neutral energy are necessary for the detection of jets, the barrel EMC is also necessary to utilize the interaction of hard-scattered partons with the surrounding medium as a penetrating probe of the early stages of the collision. Additionally, the measurement of jets within the coverage of the barrel is necessary for the study of gluon shadowing in pp and pA interactions, which is essential if the particle production in nucleus-nucleus collisions at RHIC is to be understood.

The acceptance of the endcap calorimeter is necessary to study gluon shadowing in pp and pA interactions, and to detect gluon and quark jets in polarized pp interactions in order to determine the contribution to the proton spin from the angular momentum carried by gluons. Since both of these studies are most easily carried out by studying the $qg \rightarrow \gamma q$ Compton subprocess, efficient detection of direct photons above $p_t \sim 10$ GeV/c is essential. The shower maximum detector provides the fine spatial resolution necessary to distinguish direct photons from photons emanating from π° and η° decay.

The modular nature of the calorimeter design makes it possible to stage the construction of this detector in a number of ways. Depending upon which staging plan is adopted, the physics capabilities of the EMC also vary. The present report addresses two possible options, both of which extend the reach of the STAR physics program significantly.

The first option (Option 1) is to construct the 120 modules necessary to complete the full EMC barrel. Due to the difficulty of retrofitting the EMC modules with a shower maximum detector at a later date, each module constructed would contain the hardware for the shower maximum detector. However, the corresponding electronics would not be added until further funding became available. Construction of the endcap calorimeter would also be deferred. In addition, to reduce the initial cost, fiber bundles from towers adjacent within $\Delta\eta \sim 0.2$ would be coupled to the same photomultiplier. As a consequence, the total number of photomultipliers and electronics channels would be ~600. The cost of this option is $7.5M in FY93 dollars. Several areas have been identified in which contributions from participating institutions could result in significant savings. These include machining of mechanical components, labor for module assembly, and fabrication of the shower maximum detector. The estimated total cost of components and labor which could be contributed is ~$1.5M in FY93 dollars.

The physics provided by this implementation of the calorimeter is significant. Specifically, with the full EMC barrel, the resolution on the reconstructed global transverse energy for AuAu interactions, for example, will improve to ~2%. The resolution available at the trigger level for the global neutral transverse energy would be ~2.5%. With this resolution, STAR will be able to search at the trigger level for events exhibiting unusual isospin abundances or unusual correlations between energy density and entropy density. Additionally, the improved resolution provided by the EMC will afford a more detailed understanding of the transfer of energy from projectile rapidity to mid-rapidity. As the EMC barrel is large compared to a jet radius ($\sqrt{(\Delta\eta)^2 + (\Delta\phi)^2} \leq .7$), it will also be possible to measure inclusive jets and high p_t π^os from parton scatters within $|\eta| \lesssim 0.3$. This will allow STAR to study the energy loss of hard-scattered partons using inclusive jets as well as γ-jet and jet-jet coincidences.

The assembly scenario for this implementation of the EMC leads naturally to a descoped configuration in the event of reduced funding. As the mechanical supports for the TPC capture the modules within $\Delta\phi \sim 12^\circ$ at two locations which are back-to-back, the modules located in these regions of the barrel would be constructed first. A natural consequence is that the EMC barrel would be built up from two sections that are 180° apart. In the event of reduced funding, it would be possible to complete two back-to-back sections comprising half of the EMC barrel for ~$4.5M before contributions. This would allow STAR some capability for all of the physics discussed previously, with some reduction in resolution, sensitivity, and acceptance.

The second option (Option 2) is to construct the full EMC barrel and one of the endcap calorimeters. The EMC barrel would be instrumented with 1,200 channels of tower electronics. The number of electronics channels for the endcap would be ~720. The shower maximum hardware would be completed for installation in both the barrel and endcap calorimeters, but would only be instrumented with electronics in the endcap. The estimated cost for this option before contributions is $13M in FY93 dollars.

This implementation of the STAR EMC provides essentially all the capabilities discussed in Section 1.A. In particular, with the addition of the endcap calorimeter instrumented with shower max, the measurement of gluon shadowing in pA collisions would be possible. This would allow STAR to determine the initial conditions in AA interactions and make full use of perturbative QCD in predicting the pre-equilibrium phase of the collision.

6.B. Detector Summary Cost Estimates

The projected cost of the barrel and endcap calorimeters is based on independent engineering estimates from Lawrence Berkeley Laboratory and Argonne National Laboratory.

The starting point for costing the barrel electromagnetic calorimeter was an estimate developed by LBL engineers for submission with the STAR CDR. However, the cost estimates presented below have been refined since the submission of the STAR CDR, insofar as the design of many items has become more fully developed. Thus, for example, the estimated cost of the insertion fixture used to install the barrel EMC modules was reduced from $500 K to $100 K after the completion of a preliminary design.

Various elements of the barrel EMC have also evolved in concept. As noted above, it is presently thought, for example, that all the shower maximum hardware will be included in the initial module construction with electronics added later. To reduce the initial cost, it has been decided that all fibers from towers adjacent within $|\Delta\eta| \lesssim 0.2$ will be coupled to a single photomultiplier. The longitudinal and transverse segmentation will be upgraded as necessary, and as funding permits. The cost of trigger electronics, which was not included in the original

estimate, has been included in the present estimate. Finally, some of the costs for mechanical engineering and prototyping have been reduced, since some of these tasks have already occurred as part of R&D funded by STAR or by the Argonne National Laboratory High Energy Physics Division.

The present cost estimate reflects the changes in design and concept that have occurred since the submission of the STAR CDR. These data were developed from an independent analysis by engineers at Argonne National Laboratory. The total cost from this estimate is approximately 10% higher than the original estimate from LBL, with most of the increase resulting from the projected cost for the mechanical construction. The costs presented for the barrel electromagnetic calorimeter include EDIA, labor, materials, and contingency. The average contingency for the EMC barrel is ~25% with an approximately equal amount of contingency being included for each fiscal year. The cost projection below does not include funding for installation of the EMC modules. Funds for installation have also not been included in the budget for the STAR baseline detector. It is presently thought that by the time the calorimeter modules are ready for installation, STAR will be eligible for support from RHIC operations. In this instance, most of the installation of the barrel EMC modules would be performed by riggers and technicians supported by RHIC with supervision provided by STAR personnel.

The cost estimate for the endcap calorimeter was developed by engineers at Argonne National Laboratory. Since the design of this detector is not as mature as that for the barrel EMC, the average contingency included in this case is 35%. The costs presented for the endcap calorimeter also assume that installation will be performed by riggers and technicians supported by RHIC.

The summary costs estimates in FY93 dollars for the two detector configurations addressed in this report are identified in Table 6B-1.

Table 6B-1. The Estimated Cost for Various Components of the Electromagnetic Calorimeter Detectors Encompassed in Option 1 and Option 2.

	Option 1	Option 2
Item	Full EMC barrel, 600 towers	Full EMC barrel plus one endcap, 1920 towers
Barrel tower hardware and EDIA	$4680 K	$7110 K
Shower maximum hardware	$900 K	$1430 K
Tower and SMD front end electronics	$690 K	$2370 K
Computing, DAQ, trigger electronics	$450 K	$720 K
Prototypes and fixtures	$1070 K	$1270 K
Subtotal	$7790 K	$12900 K
EDIA already funded	$300 K	$300 K
Total Funds Required	$7490 K	$12600 K

The costs for the endcap calorimeter broken out separately are identified in Table 6B-2. It is noted that for the Option 2 costs presented in Table 6B-1, the number of electronics channels required is 1200 for the barrel EMC and 720 for the endcap.

Some significant cost savings through the use of contributed resources is anticipated. The use of mechanical and electronics shops, as well as student labor at collaborating institutions, is expected to reduce the cost of some items considerably. The barrel module front and back plates, for example, are estimated to cost $1.8 M if machined at typical laboratory rates. However, savings of ~$1.4 M may be realized using the machine shops at several collaborating institutions (e.g., University of Texas at Austin, Wayne State University, IHEP, Protvino). The cost of the shower maximum hardware may also be reduced considerably (~$400 K) if it is constructed at IHEP, Protvino. Additional savings for engineering and design may be realized through R&D support in FY94 and FY95. The overall cost savings from these and other sources is conservatively estimated to be ~$1.5M. For the purpose of discussion, this credit has been assumed in developing the funding profile presented in the following section.

Based on experience with the construction of the ZEUS electromagnetic calorimeter, it should be possible to assemble 2–3 modules per month. This effort is estimated to require 16–17 full-time personnel. Much of the effort would be devoted to the preparation and calibration of the tile/fiber assemblies, which would be accomplished at collaborating universities. The assembly of the electronics could also be performed at collaborating institutions as well. The final assembly of the 1.3-tonne modules would require the use of high bay facilities, and would therefore most probably be done at Michigan State University or Argonne National Laboratory.

The cost of building 24 modules per year is ~$1M, once the necessary engineering has been completed. Assuming a level funding profile, the full barrel calorimeter would require ~6 years to build at this rate. Given a construction start in FY94, this would mean that ~90% of the barrel could be completed by the start of RHIC operations.

Table 6B-2. The Estimated Cost of Various Components of the Endcap Electromagnetic Calorimeter.

Item	One EMC endcap (720 Towers)
Barrel tower hardware and EDIA	$2430 K
Shower maximum hardware	$530 K
Tower front end electronics	$690 K
Computing, DAQ, trigger electronics	$270 K
Prototypes and fixtures	$200 K
Shower maximum front end electronics	$300 K
Total	$4420 K

6.C. Funding Profile and Schedule Estimate

Much of the engineering required to interface the barrel and endcap calorimeters to the STAR detector has already been carried out. In addition, considerable engineering directed at the choice of technology has been accomplished. As a consequence, given an appropriate funding profile, it is possible for all of the EMC construction to be completed for the start of RHIC operations. Specifically, it is envisioned that given the choice of technology in the summer of 1993, a full-scale prototype could be constructed and tested within a year. Upon completion of this phase, construction of modules would commence. Schedule estimates based upon the construction of similar modules for ZEUS suggest that modules could be completed at the rate of ~30 per year. Consequently, based upon feasibility alone, the full barrel calorimeter would be available for assembly at RHIC in mid-1998. Assuming a level funding profile of ~$1M, ~24 modules could be completed per year. In this instance, the construction of all the modules for the full EMC barrel, including front-end electronics, trigger electronics, and data acquisition, would require approximately six years.

Using the data presented for Option 1 in Section 6.B, the costs for computing/DAQ, electronics, engineering, module construction, and fixtures are presented by fiscal year in Fig. 6C-1. The total profile is assumed to be constant at the level of $1 M per year. In the initial stages, engineering and fixtures comprise most of the cost, while module construction accounts for the majority of expenditures through the remainder of the construction phase. As finished modules become ready for installation, the costs for computing/DAQ and electronics increase as a percentage of the total.

The corresponding schedule estimate is shown in Fig. 6C-2. What is evident from this figure is that for the assumed profile, module construction continues over a relatively long period, with several major procurements being staged to avoid periods of discontinuity. Under the assumed profile and schedule estimate, the last modules arrive at BNL after the start of RHIC operations in the second quarter of FY99. The remaining modules would be installed during the first scheduled RHIC shutdown. It is estimated that with a level profile ~25% higher in FY94-FY98, modules could be completed at the rate of ~30 per year, and the total time required for module construction could be shortened by ~1 year.

6.D. Project Effort

The estimated level of effort required to complete the full barrel calorimeter (Option 1) according to the schedule presented in Fig. 6C-2 is indicated by fiscal year in Fig. 6D-1. The engineering required after FY94 is assumed to be provided by staff engineers and designers at Michigan State University or Argonne National Laboratory. The total effort required from physicists, engineers/designers, and technicians/students is approximately constant at 30 FTEs per year from FY96-FY99. The total effort required to complete the project is ~180 man-years. What is evident from this estimate, is that given the funding and schedule estimates presented above, on-time completion of the barrel electromagnetic calorimeter will require heavy commitments of time from physicists and students.

Presently this project involves 11 institutions and ~80 physicists and engineers. These institutions include national laboratories, university laboratories, and university research groups. Among the participants are physicists who have extensive experience in constructing calorimeters. Much of the engineering and R&D for this project is presently being carried out at Argonne National Laboratory.

It is envisioned that components of the barrel and endcap calorimeters will be constructed at a number of collaborating institutions with final assembly taking place at Michigan State University and Argonne National Laboratory.

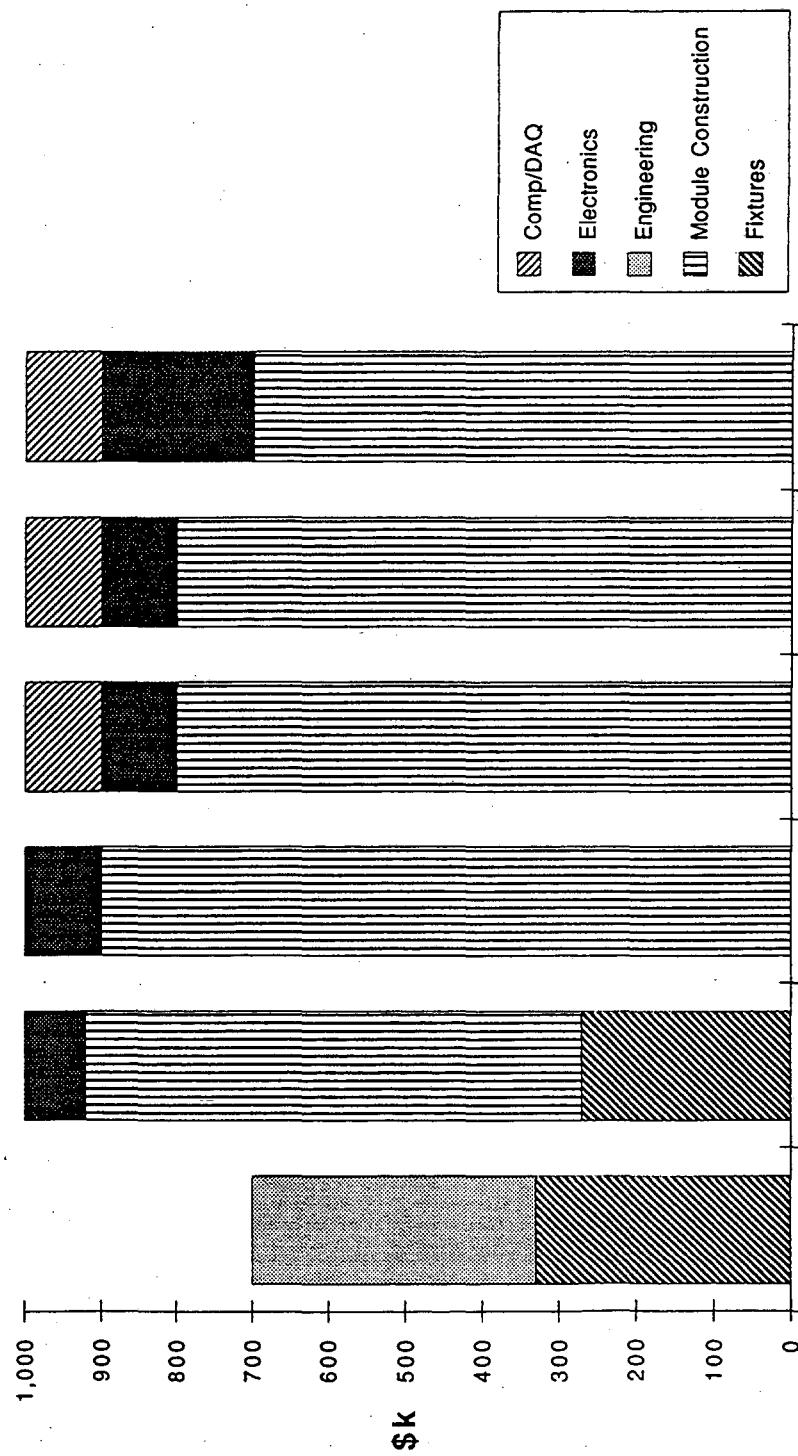

Figure 6C-1. The cost, projected as a function of fiscal year, for various components of the STAR barrel electromagnetic calorimeter. A credit of ~$1.5M for contributions from collaborating institutions has been assumed. The profile shown assumes that module construction will be completed in 1999. Modules not installed by the start of RHIC operations would be put in place during the first scheduled RHIC shutdown.

EM Calorimeter WBS 4.5

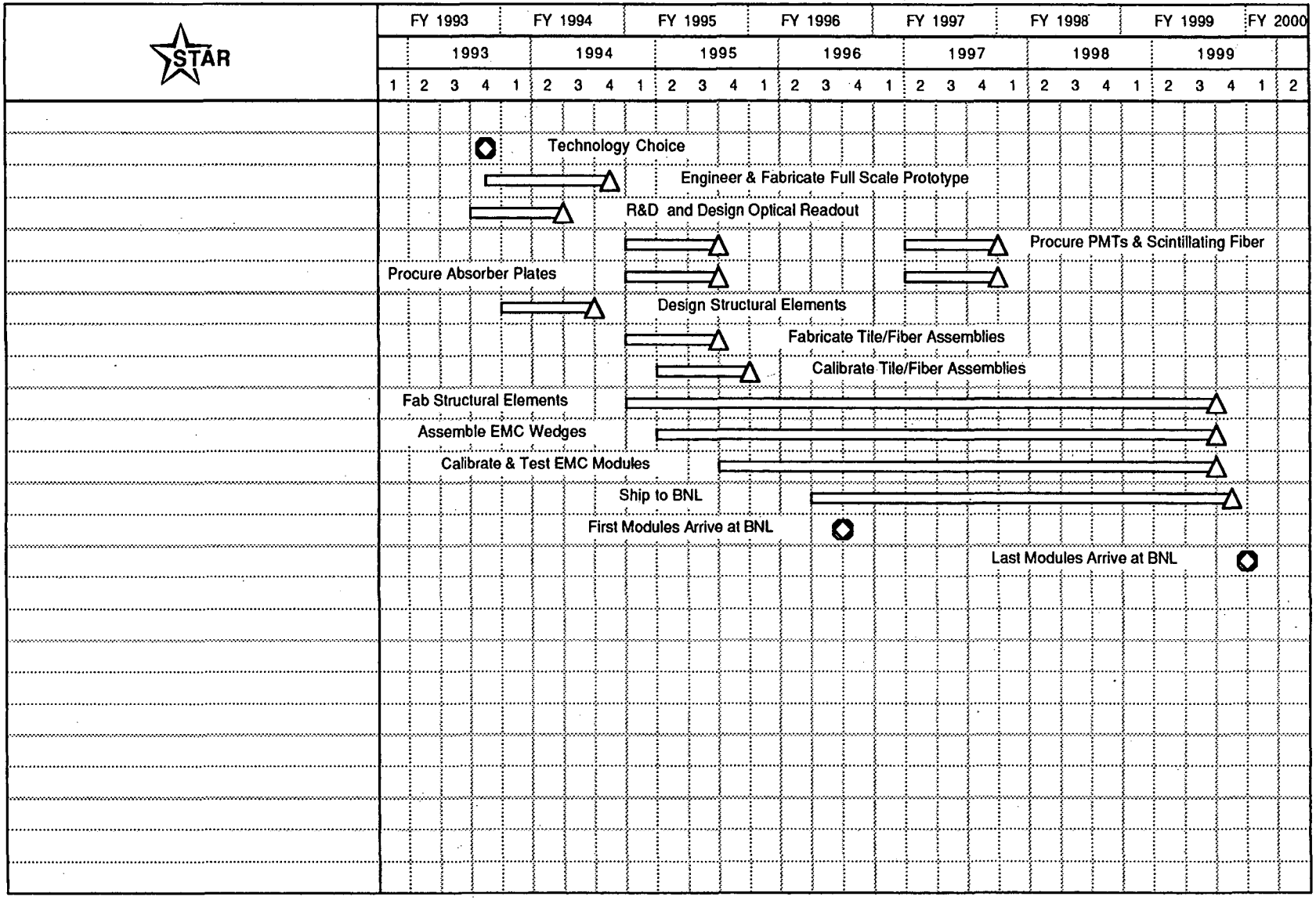

Figure 6C-2. The schedule projected for construction of the STAR barrel electromagnetic calorimeter, given the funding profile shown in Fig. 6C-1.

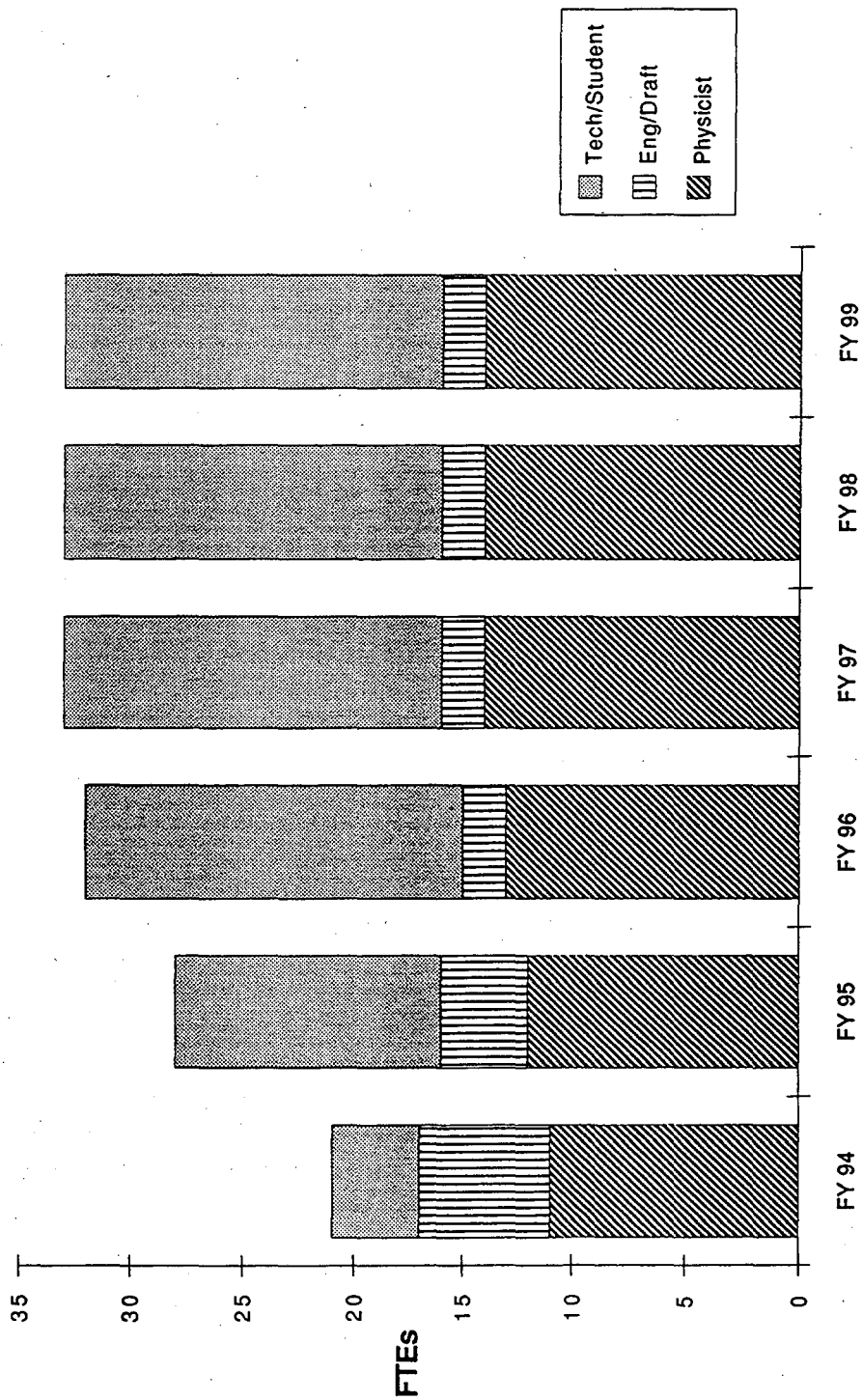

Figure 6D-1. The estimated level of effort necessary for construction of the STAR barrel electromagnetic calorimeter.

LAWRENCE BERKELEY LABORATORY
UNIVERSITY OF CALIFORNIA
TECHNICAL INFORMATION DEPARTMENT
BERKELEY, CALIFORNIA 94720